Faculty of Mechanical Engineering
Institute of Physical Engineering
Brno University of Technology

Habilitation Thesis

Electron-Photon Interaction at the Nanoscale

Ing. Andrea Konečná, Ph.D.

Brno, May 2023

Contents

Acknowledgements

I am very grateful to my PhD advisors **Prof. Javier Aizpurua** and **Prof. Rainer Hillenbrand** who introduced me in the world of nanophotonics and with whom I developed my first works dealing with electron energy-loss spectroscopy applied to optical and infrared excitations in nanostructures. I was then extremely lucky to work as a postdoctoral researcher with **Prof. Javier García de Abajo**, from whom I could learn so much about electron-photon interaction and who was involved in a substantial portion of publications included in this thesis. Thank you, Javier, for the opportunity to work with you on such interesting projects, for all the help and inspiration.

Over the years, I could interact and collaborate with many outstanding researchers. I am particularly thankful to **Dr. Tomáš Neuman**, who has been a great friend, talented colleague and who is always here to share both ups and downs of (not only) academic life. **Prof. Peter Rez** and **Prof. Juan Carlos Idrobo** have been not only collaborators, but and also mentors giving me valuable advice on my future scientific steps.

I am very happy to work at the Institute of Physical Engineering (IPE) and Central European Institute of Technology in an inspiring and friendly environment. My special thanks go to **Assoc. Prof. Vlastimil Křápek**, who taught me everything I wanted to know about proposal writing and many other things, for the fun discussions and support. I thank **Dr. Michal Horák** for his patience with STEM-EELS experiments and for his willingness to collaborate on challenging projects. At IPE, I met many talented students, and I am happy that several of them decided to develop their thesis under my supervision or join a newly established team dealing with electron-light interactions: **Martin Ošmera**, **Jiří Kabát**, **Jan Krpenský**, **Tereza Špičáková**, **Martin Hájek**, **Dr. Martin Hrtoň**, **Zdeněk Nekula** and **Jakub Urban**. And I am looking forward to interact with those who are going to start working with us very soon!

I would also like to thank **Prof. Petr Dub** and **Prof. Bohumila Lencová** for mentoring, and also for inspiring and fun discussions. **Prof. Tomáš Šikola** deserves my gratitude for his continuous support, trust and for tolerating the reverse mentoring.

Mé velké poděkování patří **Stanislavu Petrášovi**, mým rodičům, prarodičům a strýci za lásku a podporu. Tuto práci bych ráda věnovala mým dědečkům Jaroslavovi a An-

tonínovi, kteří už tu s námi bohužel nejsou, ale kteří by, doufám, měli velkou radost.

About the Author

Andrea Konečná is currently a researcher and lecturer at the Institute of Physical Engineering (IPE) of Faculty of Mechanical Engineering (FME), Brno University of Technology (BUT). She is leading a newly established research group **AR**t of **T**heory in **E**lectron **MI**croscopy and **S**pectroscopy (ARTEMIS), under a prestigious Junior Star funding scheme of the Czech Science Foundation.

After obtaining the Engineering Physics Master's degree at FME, BUT, Andrea Konečná pursued PhD studies within the programme "Physics of Nanostructures and Advanced Materials" of the University of the Basque Country under the supervision of Javier Aizpurua and Rainer Hillenbrand. She defended her PhD thesis entitled "Theoretical Description of Low-Energy Excitations in Nanostructures as Probed by Fast Electrons" in May 2019. She further developed her expertise in theory of electron-matter interaction at the Institute of Photonic Sciences in Barcelona (Spain) and spent two years as a post-doctoral researcher in the Nanophotonics Theory Group led by Javier García de Abajo.

Research topics of Andrea Konečná are at the interface of nanophotonics and state-of-the-art electron microscopy and spectroscopy. In particular, she has been dealing with theoretical description of the interaction of fast electron beams with nanostructured matter and optical fields at the nanoscale within the following topics:

- Probing optical excitations (phonons and vibrations, plasmons and excitons) by electron energy-loss spectroscopy (EELS) in scanning transmission electron microscopy (STEM). She has been modelling and interpreting various STEM-EELS experiments that involved understanding hyperbolic phonon polaritons in thin films of hexagonal boron nitride, plasmons in metallic nanoparticles, low-energy nanoparticle plasmons in unconventional plasmonic materials such as MXenes or highly-doped semiconductors.

- Shaping electron beams via the interaction with optical fields. She has contributed to suggestions of versatile and fast setups using structured light beams whose phase and intensity profile can be imprinted on electron beams. Such optical phase plates for electrons could be implemented in future electron microscopes.
- Use of shaped electron beams in probing symmetries of excitations in matter and for low-dose imaging.
- Thermal effects in EELS, spatial dependence of thermally-driven phase transitions.

To address the research interests above, Andrea Konečná combines analytical and numerical methods (boudary- and finite-element methods) to describe electromagnetic fields emerging in the interaction of fast electrons, arbitrarily shaped nanostructures and nanoscale optical fields.

Papers authored by Andrea Konečná

1 Papers Discussed in the Habilitation Thesis

This thesis presents brief commentaries of the publications listed below. In all these publications, Andrea Konečná participated in at least one of the mentioned activities: development of theoretical formalism, numerical calculations, interpretation of experimental results, manuscript writing.

1. Konečná, A., Iyikanat, F. & García de Abajo, F. J. Theory of Atomic-Scale Vibrational Mapping and Isotope Identification with Electron Beams. *ACS Nano* **15,** 9890–9899 (2021).
2. Maciel-Escudero, C., Konečná, A., Hillenbrand, R. & Aizpurua, J. Probing and steering bulk and surface phonon polaritons in uniaxial materials using fast electrons: Hexagonal boron nitride. *Phys. Rev. B* **102,** 115431 (2020).
3. Konečná, A., Li, J., Edgar, J. H., García de Abajo, F. J. & Hachtel, J. A. Revealing Nanoscale Confinement Effects on Hyperbolic Phonon Polaritons with an Electron Beam. *Small* **17,** 2103404 (2021).
4. Yang, H., Konečná, A., Xu, X., Cheong, S.-W., Garfunkel, E., García de Abajo, F. J. & Batson, P. E. Low-Loss Tunable Infrared Plasmons in the High-Mobility Perovskite (Ba, La) SnO3. *Small* **18,** 2106897 (2022).
5. Yang, H., Konečná, A., Xu, X., Cheong, S.-W., Batson, P. E., García de Abajo, F. J. & Garfunkel, E. Simultaneous Imaging of Dopants and Free Charge Carriers by Monochromated EELS. *ACS Nano* **16,** 18795–18805 (2022).
6. Gallina, P., Konečná, A., Liška, J., Idrobo, J. C. & Šikola, T. Strongly Coupled Plasmon and Phonon Polaritons as Seen by Photon and Electron Probes. *Phys. Rev. Appl.* **19,** 024042 (2023).

7. Reidy, K., Majchrzak, P. E., Haas, B., Thomsen, J. D., Konečná, A., Park, E., Klein, J., Jones, A. J. H., Volckaert, K., Biswas, D., Watson, M. D., Cacho, C., Narang, P., Koch, C. T., Ulstrup, S., Ross, F. M. & Idrobo, J. C. Direct Visualization of Subnanometer Variations in the Excitonic Spectra of 2D/3D Semiconductor/Metal Heterostructures. *Nano Lett.* **23,** 1068–1076 (2023).
8. Sannomiya, T., Konečná, A., Matsukata, T., Thollar, Z., Okamoto, T., García de Abajo, F. J. & Yamamoto, N. Cathodoluminescence Phase Extraction of the Coupling between Nanoparticles and Surface Plasmon Polaritons. *Nano Lett.* **20,** 592–598 (2020).
9. Konečná, A., Di Giulio, V., Mkhitaryan, V., Ropers, C. & García de Abajo, F. J. Nanoscale Nonlinear Spectroscopy with Electron Beams. *ACS Photonics* **7,** 1290–1296 (2020).
10. Konečná, A. & García de Abajo, F. J. Electron Beam Aberration Correction Using Optical Near Fields. *Phys. Rev. Lett.* **125,** 030801 (3 2020).
11. García de Abajo, F. J. & Konečná, A. Optical Modulation of Electron Beams in Free Space. *Phys. Rev. Lett.* **126,** 123901 (12 2021).
12. Konečná, A., Rotunno, E., Grillo, V., García de Abajo, F. J. & Vanacore, G. M. Single-Pixel Imaging in Space and Time with Optically Modulated Free Electrons. *ACS Photonics* **10,** 1463–1472 (2023).
13. Konečná, A., Iyikanat, F. & García de Abajo, F. J. Entangling free electrons and optical excitations. *Sci. Adv.* **8,** eabo7853 (2022).

2 Other papers

The following papers were published either as a part of the author's Ph.D. studies or are not tightly related to the topics discussed within this thesis.

1. Lagos, M. J., Reyes-Coronado, A., Konečná, A., Echenique, P. M., Aizpurua, J. & Batson, P. E. Attosecond and femtosecond forces exerted on gold nanoparticles induced by swift electrons. *Phys. Rev. B* **93,** 205440 (2016).
2. Govyadinov, A. A., Konečná, A., Chuvilin, A., Vélez, S., Dolado, I., Nikitin, A. Y., Lopatin, S., Casanova, F., Hueso, L. E., Aizpurua, J. & Hillenbrand, R. Probing low-energy hyperbolic polaritons in van der Waals crystals with an electron microscope. *Nat. Commun.* **8,** 95 (2017).

3. Konečná, A., Neuman, T., Aizpurua, J. & Hillenbrand, R. Surface-enhanced molecular electron energy loss spectroscopy. *ACS Nano* **12,** 4775–4786 (2018).
4. Jokisaari, J. R., Hachtel, J. A., Hu, X., Mukherjee, A., Wang, C., Konecna, A., Lovejoy, T. C., Dellby, N., Aizpurua, J., Krivanek, O. L., Idrobo, J.-C. & Klie, R. F. Vibrational spectroscopy of water with high spatial resolution. *Adv. Mater.* **30,** 1802702 (2018).
5. Konečná, A., Venkatraman, K., March, K., Crozier, P. A., Hillenbrand, R., Rez, P. & Aizpurua, J. Vibrational electron energy loss spectroscopy in truncated dielectric slabs. *Phys. Rev. B* **98,** 205409 (2018).
6. Horák, M., Křápek, V., Hrtoň, M., Ligmajer, F., Stöger-Pollach, M., Šamořil, T., Paták, A., Édes, Z., Metelka, O., Babock7, J. & Šikola, T. Limits of Babinet's principle for solid and hollow plasmonic antennas. *Sci. Rep.* **9,** 4004 (2019).
7. Křápek, V., Konečná, A., Horák, M., Ligmajer, F., Stöger-Pollach, M., Hrtoň, M., Babocký, J. & Šikola, T. Independent engineering of individual plasmon modes in plasmonic dimers with conductive and capacitive coupling. *Nanophotonics* **9,** 623–632 (2020).
8. Hrtoň, M., Konečná, A., Horák, M., Šikola, T. & Křápek, V. Plasmonic Antennas with Electric, Magnetic, and Electromagnetic Hot Spots Based on Babinet's Principle. *Phys. Rev. Appl.* **13,** 054045 (2020).
9. Yu, R., Konečná, A. & García de Abajo, F. J. Inelastic Scattering of Electron Beams by Nonreciprocal Nanotructures. *Phys. Rev. Lett.* **127,** 157404 (2021).
10. Iyikanat, F., Konečná, A. & García de Abajo, F. J. Nonlinear Tunable Vibrational Response in Hexagonal Boron Nitride. *ACS Nano* **15,** 13415–13426 (2021).
11. Gallina, P., Kvapil, M., Liška, J., Konečná, A., Křápek, V., Kalousek, R., Zlámal, J. & Šikola, T. Strong coupling in an Au plasmonic antenna–SiO_2 layer system: A hybrid-mode analysis. *Phys. Rev. B* **107,** 125144 (2023).
12. Chen, S., Leng, P. L., Konečná, A., Modin, E., Gutierrez-Amigo, M., Vicentini, E., Martín-García, B., Barra-Burillo, M., Niehues, I., Maciel Escudero, C., Xie, X. Y., Hueso, L. E., Artacho, E., Aizpurua, J., Errea, I., Vergniory, M. G., Chuvilin, A., Xiu, F. X. & Hillenbrand, R. Real-space observation of ultraconfined in-plane anisotropic acoustic terahertz plasmon polaritons. *Nat. Mater.* **ASAP,** – (2023).

1 Introduction

This habilitation thesis stands topically at the interface of two seemingly distinct fields: **electron microscopy and spectroscopy**, aiming at developing methods for materials analysis with electron beams, and **nanophotonics** dealing with confined optical fields and low-energy excitations in nanostructures. However, one of the main motivations stimulating developments in both fields is identical – to inspect samples with better spatial resolution than we can achieve with conventional light microscopes.

The smallest resolvable details in an image are restricted according to the Abbe diffraction limit $d = \lambda/(2\mathrm{NA})$, where λ is the probing wavelength and NA is the numerical aperture. A possible solution to overcome the limit is to decrease λ. In nanophotonics, we reduce photon wavelength by tightly confining the optical fields at interfaces, thin films, or specifically designed nanostructures. On the other hand, electron microscopes rely on the fact that electrons accelerated to energies $\sim 10^4 - 10^5$ eV can be associated with wavelengths as small as units of picometers and can be used to probe matter at single-atom resolution. Both fields, however, go well beyond "just" improved imaging and have many other applications.

In Section 1.1 and Section 1.2, we will separately introduce electron microscopy and spectroscopy, and nanophotonics. This will provide a basis for discussing the possible synergy between the two fields in Section 1.3, which is essential for this thesis.

1.1 Electron Microscopy and Spectroscopy

Since the invention and construction of the first electron microscope by Max Knoll and Ernst Ruska in 1931[1], electron microscopes have evolved into irreplaceable instruments in many areas of research and technology. Due to the sustainable development of electron-microscope instrumentation and related imaging and spectroscopic techniques, modern instruments are powerful analytical tools in material, physical and chemical sciences, as well as in biology or nanotechnology. The electron beams are not only passive probes but can also be used as fabrication tools to sculpt nanostructures and nanodevices. State-of-the-art microscopes can operate at sub-Ångstrom spatial resolution[2], attosecond time resolution[3], and can resolve sample excitations with few-meV spectral resolution[4].

Electron microscopes are commonly divided into two main categories: **scanning electron microscopes** (SEMs) are typically operated at acceleration voltages up to 30 kV, and we usually collect secondary electrons (SEs) emitted due to the interaction of the sample atoms with a focused primary electron beam. On the other hand, in **transmission electron microscopes** (TEMs) operated at higher voltages (between ~ 30 and 300 kV), we detect the primary-beam electrons after their transmission through the sample. Electron beams in TEM can be transversely extended, resembling plane waves, or tightly focused and scanned across the sample. In the latter case, we talk about **scanning transmission electron microscopes** (STEMs).

The interaction between an energetic electron beam and the sample can generate a "zoo" of signals and excitations. Part of the signal comprises electrons: primary electrons transmitted through the sample, back-scattered primary electrons (BSEs), and secondary and Auger electrons (SEs and AEs) emitted from the sampled material. Moreover, the interaction process can lead to the emission of photons, either in the visible-ultraviolet spectral range (cathodoluminescence (CL) process) or in the X-ray region. The electron-sample interaction processes can also be sorted based on the difference between initial and final electron beam energy (energy loss ΔE) as elastic ($\Delta E = 0$) or inelastic ($\Delta E \neq 0$). The inelastic processes can involve excitations in the sample, such as magnons, vibrational excitations, plasmons or excitons.

Having the microscope capable of operating with a focused beam (SEM or STEM) allows not only for imaging but also for highly localized spectroscopy. By analyzing the energy distribution of SEs, AEs, or X-rays, we can retrieve the sample's elemental composition. The CL signal can provide characteristics of material band gaps or optical excitations. Spatial localization of these signals is highly dependent on the type of material, primary beam energy and focus, but nanometric details are often routinely resolved. The most essential spectroscopic technique for this habilitation thesis is **electron energy-loss spectroscopy** (EELS), which analyses the energy of the primary electron beam after the interaction with the sample with the help of an electron energy-loss spectrometer, typically a magnetic prism[5].

After recent instrumental developments in electron monochromation, determining the initial primary-beam energy more precisely, and in energy-loss spectrometers, EELS can achieve a few-meV energy resolution, unlocking the energy region where phonons and molecular vibrations appear[6]. It is equally interesting to study valence electron excitations in the energy range $\sim 1-50$ eV, such as plasmons, excitons, and electronic transitions governing matter's optical and electronic properties[7]. Chemical composition can be determined from EELS at energies of hundreds of eVs corresponding to core electron excitations[8]. The unprecedented combined spectral/spatial meV/sub-Ångstrom resolution, breadth of the analysable energy region ($10^{-3} - 10^{3}$ eV), and richness of analytic possibilities achievable with modern STEM-EELS instruments facilitate the correlation of various material and functional properties and make STEM-EELS a unique technique.

Another development direction of state-of-the-art electron microscopes goes towards improvements in time resolution. Conventional microscopes and related spectroscopic techniques rely on the accumulation of electron and photon counts over relatively long time periods ($10^{-3} - 10^{2}$ s), which averages many dynamical processes in the studied samples, such as dynamics of phase transitions or optical excitations. These typical time-resolution limits can be overcome by preparing a pulse of primary electrons whose arrival towards the sample is synchronized with an external stimulus pre-exciting the sample within a "pump-probe" experiment. We currently distinguish between **dynamic TEM** (DTEM) and **ultrafast TEM** (UTEM) used to probe irreversible or reversible processes, respectively. UTEM is closely linked to the so-called **photon-induced near-field electron microscopy** (PINEM), which probes the evolution of near-fields associated with the optical excitation in nanostructured samples in a stroboscopic way by varying the delay between the arrival of the electrons and the sample stimulated by a laser pulse.

Besides improvements in spectral and time resolution, there have been many efforts to achieve high spatial resolution in all microscope types and to develop new imaging techniques. A key aspect determining the microscope's resolving power is our capability to eliminate aberrations of electron lenses to form and image the electron beams perfectly. The electron beam distortions can be significantly reduced nowadays by involving aberration correctors[2,9].

The constant development of new imaging techniques, either improving the resolution or introducing new capabilities, is also responsible for making electron microscopes so powerful. For instance, samples that are thin and composed of light elements (such as 2D materials or biological specimens) impose mainly a phase modulation in the transmitted electron wave function in TEM, while the contrast in the conventional setup mostly provides amplitude information (*i.e.*, we detect intensity $I \propto |\psi_{\mathrm{f,prop}}|^2$, where $\psi_{\mathrm{f,prop}}$ is the post-interaction and propagated electron wave function). This limitation have been overcome by introducing electron holography[10], or phase plates[11], using the concepts adopted from light optics to retrieve the phase information. Another possibility to reconstruct the sample phase is electron ptychography[12].

1.2 Nanophotonics

To introduce one of the main concepts of nanophotonics, we can start with basic considerations of waves propagating in a bulk, homogeneous, and isotropic medium. An electric field describing a harmonic plane wave of light in such an environment can be expressed as $\mathbf{E}(\mathbf{r},t) = \mathrm{Re}\,|\mathbf{E}_0 \exp(\mathrm{i}\mathbf{k}\cdot\mathbf{r} - \mathrm{i}\omega t)|$, where $(\mathbf{r},t)$ are spatial coordinates and time, $\mathbf{E}_0$ is a vector describing amplitude and polarization, $\mathbf{k}$ is a wave vector determining the direction of propagation, and ω is the angular frequency. To ensure fulfillment of the wave equation in an isotropic medium described by relative permittivity ε and relative permeability μ, we have $k = \sqrt{\varepsilon\mu}\omega/c$, where c is the speed of light in vacuum.

Nanophotonics very often deals with materials and frequency ranges, where $\mu = 1$, and $\mathrm{Re}\{\varepsilon\} < 0 \wedge \mathrm{Im}\{\varepsilon\} \ll \mathrm{Re}\{\varepsilon\}$, which can take place, *e.g.*, in noble metals in the visible spectral range[13], or ionic crystals in the infrared[14]. Such dielectric properties imply purely imaginary k and thus no propagation of plane waves in bulk. However, solutions taking the form of evanescent waves propagating along interfaces with such materials exist. For a planar interface between vacuum ($\varepsilon = 1$) and material described by the permittivity ε, the wave vector component in the direction of propagation along the interface has to fulfill $k_{\|} = \omega/c\sqrt{\varepsilon/(\varepsilon+1)}$.

One can easily check that the wave vector component perpendicular to the plane of propagation yields an exponential decay of the field from the interface and, importantly, $\mathrm{Re}\{k_{\|}\} > \omega/c$ if the dielectric response fulfills the abovementioned conditions. The evanescent waves corresponding to the so-called polaritons, hybrid light-matter waves, are thus associated with an effective wavelength $\lambda = 2\pi/k_{\|}$, which is smaller than the wavelength of a photon in free space $\lambda_0 = 2\pi c/\omega$. This result suggests that the polaritons could break the conventional Abbe diffraction limit and "shrink" light to much smaller dimensions compared to photon wavelengths in free space or in an infinitely extended homogeneous medium.

The flat interface represents only one of the many arrangements to achieve light confinement due to the surface polaritons. Other geometries often used in nanophotonics are flat or corrugated thin films, edges, or variously shaped nanoparticles, ranging from spheres to nanostars, where the so-called localized surface plasmons (LSPs) reside[13]. It is nowadays possible to tailor the confined optical field almost on demand by choosing the suitable material and designing the particular geometry concerning the operating frequency ranging from far infrared to ultraviolet region of the electromagnetic spectrum.

Our understanding of the behavior of light at the nanoscale, together with improvements in nanofabrication and chemical synthesis of specifically shaped nanoparticles, leads to a broad scope of applications, *e.g.*, in light nanofocusing and waveguiding[15–17], energy storage and conversion[18], biosensing[19], or quantum computing[20]. Other efforts of the nanophotonics community are in the development of near-field-based imaging and spectroscopic techniques, such as scanning-near field optical microscopy and nano Fourier Transform Infrared spectroscopy (nano-FTIR)[21] or tip-enhanced Raman spectroscopy[22].

1.3 Marriage of electrons and photons

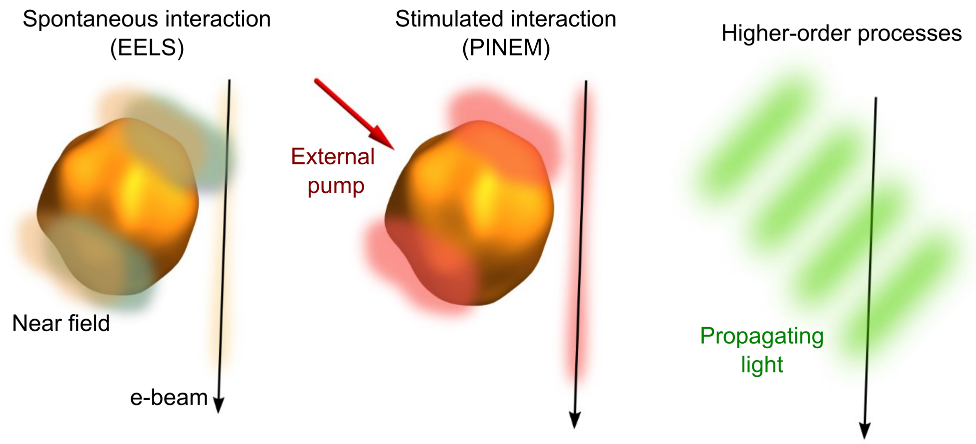

Figure 1.1: Three scenarios of electron-light interaction discussed in this Thesis. Left: electron beams can induce optical near fields, which results in energy losses visible in electron spectra. Middle: if an electron beam passes close to an already excited near field (*e.g.,* by an external light source), it can experience multiple photon exchanges. Right: electrons can also interact with freely propagating photons through higher-order processes. Such interaction is thus possible, but rather inefficient.

As the confined near field features spatial details much smaller than the free-space photon wavelength, it is understandable that the "conventional" photons cannot probe the spatial characteristics of such nanoscale optical fields. And very often, the free-space photon cannot even excite such fields. On the other hand, a beam of fast electrons is accompanied by an evanescent field, thus representing a natural excitation source and/or probe for polaritons in nanophotonics structures. The interaction of fast electrons with confined polaritonic near fields is then imprinted in electron spectra. Interestingly, this interaction can be either spontaneous or stimulated if an external source is used to pre-excited the sample, as schematically visualized in FIGURE 1.1.

In CHAPTER 2 and CHAPTER 3, we introduce several works discussing how fast electrons probe the polaritonic waves in the infrared (IR) and visible (VIS) energy range, respectively. We will discuss several material platforms, ranging from ionic crystals supporting phonon polaritons (PhPs) to doped semiconductors and metals where free-charge carriers yield plasmon polaritons (PPs). One of the commented publications describes the excitation of localized vibrational modes of both optical and acoustic nature in an isolated inorganic molecule.

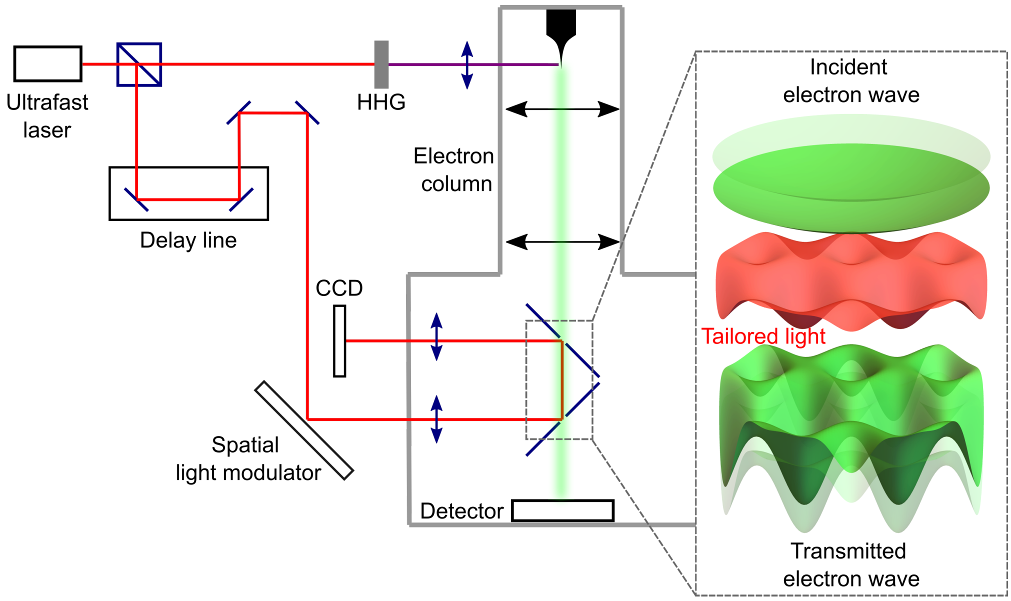

Figure 1.2: Implementation of electron-light interaction in an electron microscope. A schematic of a possible experimental setup as introduced in Ref.[23]. The setup is based on a femtosecond laser source attached to a SEM. The laser extracts electrons from the electron gun and in the second path it is structured by a spatial light modulator to modify the electron wave function as visualized in the inset.

Although our description of the capabilities of electron microscopy and spectroscopy in Section 1.1 might result in the impression that everything we need has already been developed and all issues are resolved, but the opposite is true. Many solutions or techniques mentioned are complex regarding instrumentation, operation and/or post-processing[12]. Therefore, there is still a search for alternative and out-of-the-box solutions. Exploiting the electron-photon interaction could be one of them: in Chapter 4 we discuss how the optical fields can be used to actively modify the electron beams in different scenarios and suggest setups to correct for electron-beam aberrations and generate on-demand electron beam shapes.

The electron-photon interaction could be introduced in an electron microscope in two (or even more) steps: in the first one, we could perform the on-demand tailoring of electron wave functions, as shown in FIGURE 1.2, while in the second step, the tailored electrons would interact with a sample. CHAPTER 5 outlines several possible applications of the shaped electron beams in both imaging and spectroscopy and finally, in CHAPTER 6 we summarize the presented work and present an outlook and personal viewpoint of the future development of electron spectro-microscopy hand in hand with (nano)photonics.

2 Vibrational electron energy-loss spectroscopy

When energetic primary electrons in STEM interact with a sample without any other external stimulation, the probability of nonzero energy exchange between the electrons and the sample is very low. If we employ an electron energy-loss spectrometer, most of the electrons contribute to the so-called zero-loss peak (ZLP) with a natural width determined by the primary electrons' monochromaticity (energy spread). As the energy spread limits the resolution over the entire EEL spectrum, the aim is to reduce it. The best results can be achieved by employing cold field-emission guns producing the smallest $\sim$ 250-meV broadening[24] and by further improving the energy spread with monochromators.

So far, the most successful STEM-EELS design can reach the ZLP width as small as a few meV[4,6]. Such resolution yields unprecedented details in the EEL spectra in core-loss and valence-loss regions that can be simultaneously linked with the precisely defined electron-beam position. Notably, the narrowness of the ZLP also uncovers the spectral region, where magnons, phonons, low-energy plasmons, and molecular vibrations exist. Although the ultra-low-energy or high-resolution STEM-EELS is a relatively young technique, it has already been applied to various material systems where either localized vibrational excitations or low-energy quasi-particles emerge.

Molecular vibrations

Konečná, A., Iyikanat, F. & García de Abajo, F. J. Theory of Atomic-Scale Vibrational Mapping and Isotope Identification with Electron Beams. *ACS Nano* **15,** 9890–9899 (2021).

Localized vibrational modes have been detected by STEM-EELS in molecular crystals, particularly in guanine[26,27], in clusters or alanine molecules, where different isotopes were distinguished[28], in molecular adsorbates on surfaces[29], and even in liquid water encapsulated in a liquid cell[30]. Fast electrons are typically quite harmful to sensitive organic molecules, which has been experimentally overcome by taking advantage of long-range interaction with optical-like vibrational modes featuring non-zero net dipole moment. Such vibrations are detectable even with an electron beam placed in aloof geometry, probing the molecules remotely. We confirm and extend these observations with a case study of an inorganic h-BN-like molecule, where we observe different localization of the acoustic- and optical-like vibrations and suggest that single-isotope impurities could be detected down to the single-atom level.

Phonon polaritons

Maciel-Escudero, C., Konečná, A., Hillenbrand, R. & Aizpurua, J. Probing and steering bulk and surface phonon polaritons in uniaxial materials using fast electrons: Hexagonal boron nitride. *Phys. Rev. B* **102,** 115431 (2020).

Konečná, A., Li, J., Edgar, J. H., García de Abajo, F. J. & Hachtel, J. A. Revealing Nanoscale Confinement Effects on Hyperbolic Phonon Polaritons with an Electron Beam. *Small* **17,** 2103404 (2021).

Solid-state systems with periodic atomic lattices feature acoustic and optical phonon branches. It turns out that the largest energy-loss probability arises when the electrons interact with ionic crystals featuring optical modes with a non-zero net dipole moment. In such a scenario, the crystal can support PhPs[33], which can be, similarly to the optically active molecular vibrations, excited even with aloof electrons[34]. As we mentioned, the electrons naturally couple to the polaritons and can be used to map the associated near field and its confinement.

Even the first STEM-EELS spectra in the infrared[6] showed the PhPs in different ionic crystals, including hexagonal BN (h-BN), SiO_2, SiC, and TiH_2. However, the complete and correct interpretation of the spectra was presented in follow-up works, which could get some inspiration from works published a few decades earlier[35]. Several studies demonstrated the emergence of rather damped PhPs in thin films and at edges of SiO_2[36–38]. Confined PhPs were observed in MgO nanocubes[39] and ZnO nanowires[40].

PhPs in h-BN represent a special case because of the material anisotropy. Due to the covalent in-plane and weak out-of-plane van-der-Waals bonds, h-BN features distinct vibrational properties in the two directions. The anisotropy then yields a peculiar propagation of waves on h-BN surfaces in different frequency regions when excited by focused electron beams.

When the h-BN crystal takes the form of a thin film, waveguide-like modes that offer promising applications in nanophotonic devices can be excited and probed[41]. Interestingly, by precisely positioning the electron beam with respect to thin-film boundaries, we can control the preferred polariton wavelength to be probed by the electrons, which allows us to reconstruct the polariton dispersion. We first suggested this polariton interferometry scheme in Ref.[42], but we were able to exploit its full potential only in the more recent work[32]. We were able to reconstruct dispersions of polaritonic modes propagating along sheet or edge surfaces, where we revealed that an exact edge geometry plays a significant role in determining the resulting polaritonic properties.

Plasmon polaritons

Yang, H., Konečná, A., Xu, X., Cheong, S.-W., Garfunkel, E., García de Abajo, F. J. & Batson, P. E. Low-Loss Tunable Infrared Plasmons in the High-Mobility Perovskite (Ba, La) SnO3. *Small* **18,** 2106897 (2022).

Yang, H., Konečná, A., Xu, X., Cheong, S.-W., Batson, P. E., García de Abajo, F. J. & Garfunkel, E. Simultaneous Imaging of Dopants and Free Charge Carriers by Monochromated EELS. *ACS Nano* **16,** 18795–18805 (2022).

Compared to ionic crystals, where the PhPs are formed due to the lattice vibrations, materials with free-charge carriers can feature PPs. In the infrared, PPs emerge either in large metallic cavities (*e.g.*, micrometer-sized particles)[45,46] or in doped semiconductors[47], where the free-carrier oscillations naturally occur at lower frequencies due to smaller carrier concentrations.

We investigated a perovskite material $BaSnO_3$ (BSO) which becomes plasmonic due to the doping by La atoms (BLSO). In particular, we performed spatially-resolved EELS mapping of BLSO nanoparticles forming nanocubes or nanoblocks and thoroughly analyzed the localized plasmonic modes formed in these nanoresonators. We focused on evaluating the resonance broadenings $\Delta\omega_\mathrm{r}$ and quality factors $Q = \omega_\mathrm{r}/(\Delta\omega_\mathrm{r})$, where ω_r denotes the resonant frequency. These quantities are tightly related to the energy loss associated with the resonances and, thus, the potential applicability of the plasmonic nanoparticles. Interestingly, we found out that the plasmonic resonances in the smallest particles are more damped than initially expected due to additional scattering and very tight confinement of the conduction electrons.

We also investigated the effects of inhomogeneous La doping in some of the fabricated nanoparticles. We used the full potential of STEM-EELS and correlated the information from high-resolution imaging, EEL spectra in the core-loss, valence, and vibrational energy regions. Although the images did not reveal any apparent inhomogeneities, we could extract dopant densities by analyzing ratios of the peaks associated with La and Ba atoms in the core-loss EELS. In the visible range, we could evaluate the band gap, which, together with Hall measurements, led to our estimation of the Burstein-Moss (B-M) shift. We could also observe local energies of bulk plasmons in the (near)infrared spectral range, which correlated with the dopant densities and values with the most significant B-M shifts. Very interestingly, the inhomogeneities in doping led to non-trivial localized plasmon modes, and we could even observe waveguiding-like modes arising between areas with a local increase of doping. We also concluded that not all La atoms provide carriers and found a carrier-activation percentage of about 50 %.

Coupled plasmon-phonon polaritons

Gallina, P., Konečná, A., Liška, J., Idrobo, J. C. & Šikola, T. Strongly Coupled Plasmon and Phonon Polaritons as Seen by Photon and Electron Probes. *Phys. Rev. Appl.* **19,** 024042 (2023).

If we deal with a system composed of several elements (*e.g.*, nanoparticles), each supporting a polaritonic excitation, we must consider a possible coupling between the elements. Such coupling occurs via the electromagnetic near field associated with each polaritonic excitation and can influence all other elements yielding a new modal structure[49]. We can imagine a system of coupled oscillators, where each oscillator represents one polaritonic excitation, and the springs emerge due to the electromagnetic interaction between them[50]. Coupled polaritonic systems are extensively studied in nanophotonics[51,52]. The coupling offers more degrees of freedom to tailor the nanoscale fields on demand and brings applications in energy transport, sensing, or field enhancement[53].

The coupling of two or more plasmonic particles has also been studied in various STEM-EELS works, which revealed both the energy structure of the new hybridized modes and the related near field distributions[45,54–56]. As the infrared frequency range become accessible only recently in STEM-EELS, only a few pioneering works[57,58] addressed the coupling between PhPs, residing exclusively in the infrared, and low-energy PPs. Our contribution deals with the interaction of previously studied infrared polaritons in SiO_2 and localized plasmonic excitations in micron-sized gold particles[52]. We revealed that by precisely positioning the electron beam, we could actively control the coupling, which could be used to characterize both the coupled system and individual system constituents without any need to prepare several samples. We also compared the spatially-resolved STEM-EELS measurements to far-field optical spectra, which lack spatial information and, on the other hand, bring better spectral resolution.

ACS NANO
www.acsnano.org
ARTICLE

Theory of Atomic-Scale Vibrational Mapping and Isotope Identification with Electron Beams

Andrea Konečná, Fadil Iyikanat, and F. Javier García de Abajo*

Cite This: *ACS Nano* 2021, 15, 9890−9899 Read Online

ACCESS | Metrics & More | Article Recommendations | Supporting Information

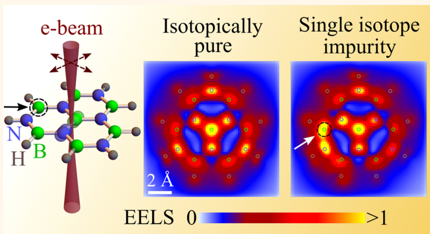

ABSTRACT: **Transmission electron microscopy and spectroscopy currently enable the acquisition of spatially resolved spectral information from a specimen by focusing electron beams down to a sub-angstrom spot and then analyzing the energy of the inelastically scattered electrons with few-meV energy resolution. This technique has recently been used to experimentally resolve vibrational modes in 2D materials emerging at mid-infrared frequencies. Here, on the basis of first-principles theory, we demonstrate the possibility of identifying single isotope atom impurities in a nanostructure through the trace that they leave in the spectral and spatial characteristics of the vibrational modes. Specifically, we examine a hexagonal boron nitride molecule as an example of application, in which the presence of a single isotope impurity is revealed through changes in the electron spectra, as well as in the space-, energy-, and momentum-resolved inelastic electron signal. We compare these results with conventional far-field spectroscopy, showing that electron beams offer superior spatial resolution combined with the ability to probe the complete set of vibrational modes, including those that are optically dark. Our study is relevant for the atomic-scale characterization of vibrational modes in materials of interest, including a detailed mapping of isotope distributions.**

KEYWORDS: *electron energy-loss spectroscopy (EELS), isotope identification, vibrational spectroscopy, atomically resolved infrared spectroscopy, infrared microscopy*

The ability of exciting vibrational modes in crystals and molecules with localized probes has attracted much attention over the past decade because of the possibility of investigating chemical composition and atomic bonding with high spatial resolution. Numerous theoretical and experimental works have demonstrated that vibrational spectroscopy is feasible with nanoscale or even atomic-scale resolution using tip-based spectroscopic techniques, such as scanning near-field optical microscopy[1−3] and tip-enhanced Raman spectroscopy.[4−7] These approaches rely on the electromagnetic optical-field enhancement produced at the probed sample area by introducing sharp metallic tips, such as those that are commonly used in atomic force and scanning tunneling microscopes. However, despite the substantial efforts made in engineering the geometric properties of the probing tip to improve resolution and sensitivity,[8−10] tip-based microscopies are still unable to map atomic vibrations, can only examine a fixed orientation of the specimen, and generally require complex analyses to subtract the undesired effects associated with tip−sample coupling. In addition, these techniques are only sensitive to vibrational modes that are optically or Raman active, while dark excitations without a net dipole moment remain difficult to detect.

Enabled by recent advances in instrumentation,[11,12] electron energy-loss spectroscopy (EELS) performed in scanning transmission electron microscopes (STEMs) has emerged as an alternative, versatile technique capable of mapping vibrational modes with an atomic level of detail. In STEM-EELS, the sample is probed by a beam of fast electrons (typically with energies of 30−300 keV) focused below 1 Å, thus allowing for the identification of individual atoms. Early theoretical predictions[13−17] were followed by experimental studies

Received: February 4, 2021
Accepted: May 7, 2021
Published: May 19, 2021

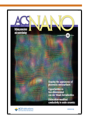

https://doi.org/10.1021/acsnano.1c01071
ACS Nano 2021, 15, 9890−9899

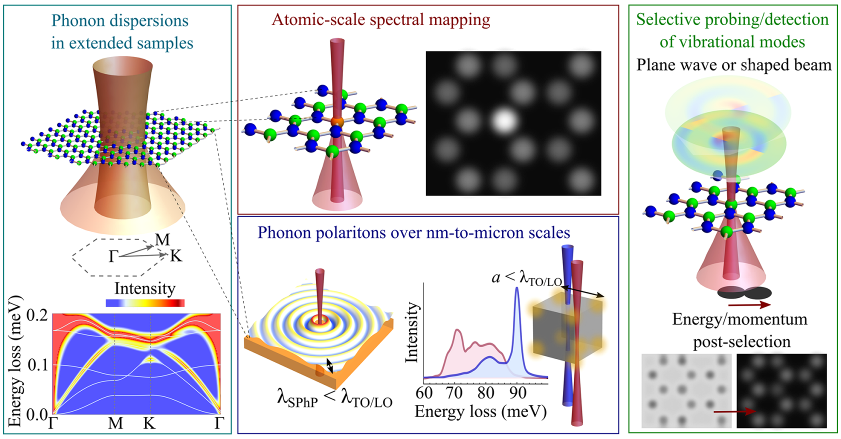

Figure 1. Experimental approaches to probing vibrational excitations by EELS. Left: phonon dispersion in bulk materials can be studied through momentum-resolved EELS using an extended electron beam (e-beam) with a focal size of tens of nm.[22,25] Middle top: localized vibrational modes in finite or defective structures can be probed at atomic resolution with tightly focused e-beams.[32−34] Middle bottom: phonon polaritons—electromagnetic waves coupled to the optical phonons of ionic crystals—can be efficiently excited by e-beams to probe their spatial (nm-to-μm scale) and spectral (10s-to-100s meV) properties, which strongly depend on sample and probing geometry.[16,19,20] Right: preshaping and post-selection of the electron transverse wave function enables the identification of specific vibrational-mode profiles and symmetries in the inelastic signal. Images are illustrations taken from our calculations.

demonstrating the spectral and spatial characterization of low-energy excitations (10s−100s meV), such as phonons in general, phonon polaritons in nanostructured polar crystals,[12,18−26] molecular vibrations,[27−30] and hybrid modes resulting from the coupling between vibrational and plasmonic excitations.[31] Recent achievements include the detection of vibrations at truly atomic resolution in hexagonal boron nitride (h-BN),[32] silicon,[33] graphene,[34] and silicon carbide,[35] as well as the visualization of single-atom impurities in extended samples.[34,35]

We depict common STEM-EELS experimental arrangements and types of probed infrared (IR) excitations in Figure 1. Dispersion relations of vibrational modes can be retrieved under broad electron beam (e-beam) irradiation of extended crystals combined with angle- and energy-resolved electron detection[22,25] (left panel). In addition, localized vibrational modes (upper middle panel) can be probed with atomic detail using focused e-beams,[32−34] while the spatial and spectral distribution of phonon polaritons—hybrids of atomic vibrations and photons—can also be mapped in structured samples[16,19,20] (lower middle panel). Interestingly, by changing the collection conditions or the orientation of the specimen, one can filter different contributions to the inelastic signal,[14,36−38] and similarly, selected excitations of specific symmetry may be addressed by shaping the electron wave function (right panel) in coordination with energy and momentum post-selection, as shown in a proof-of-principle experiment at higher excitation energies for the triggered detection of plasmons with dipolar and quadrupolar character.[39]

Here, we present first-principles calculations demonstrating the potential of e-beams for atomic-scale vibrational mapping, including the identification of single isotope-atom impurities in a finite molecular sample. Specifically, we follow previous theoretical works relying on molecular dynamics[37,40] and first-principles calculations of extended systems,[18,22,25,41] and introduce a general computational methodology based on density-functional theory that can be applied to model spatially resolved EELS spectra with an atom-sized probe. Such an approach goes beyond the macroscopic dielectric formalism, which is successfully used to simulate low-loss EELS without atomic detail,[42,43] but fails to model the microscopic characteristics of the EELS signal. We show that e-beams are capable of exciting both bright and dark vibrational modes, while the latter are missed by far-field IR spectroscopy, as we illustrate by comparing our results to simulated optical extinction spectra. Additionally, we discuss polarization selectivity for different e-beam orientations with respect to the sample.

We note that atomically resolved vibrational mapping has so far been demonstrated only in samples that are resistant to e-beam damage, which is not the case of organic molecules, for which aloof EELS needs to be considered.[27−30] However, we foresee that less energetic electrons together with expected improvements in the sensitivity of electron analyzers may eventually allow us to probe molecular vibrations with high spatial resolution (see upper-mid-panel in Figure 1). In preparation for these advances, we analyze here a rather stable h-BN-like molecule, which is purposely chosen as a model system that can naturally incorporate different boron isotopes (in particular ^{10}B and ^{11}B),[44] so it serves to study the effect of a single isotope defect on the resulting high-resolution EELS maps. In particular, we demonstrate that such impurity can significantly affect the vibrational modes and produce clearly discernible variations in the energy-filtered maps compared to those obtained for an isotopically pure sample. We thus

https://doi.org/10.1021/acsnano.1c01071
ACS Nano 2021, 15, 9890−9899

conclude the feasibility of isotope identification at the single-atom level in a finite nanostructure. In addition, we show that post-selection of scattered electrons depending on the acceptance angle of the spectrometer can improve these capabilities for isotope site recognition.

RESULTS AND DISCUSSION

Theoretical Description of Spatially Resolved Vibrational EELS. For swift electrons of kinetic energy > 30 keV interacting with thin specimens (<10s nm) or under aloof conditions (*i.e.*, without actually traversing any material), coupling to each sampled mode is sufficiently weak as to be described within first-order perturbation theory, so that the EELS spectrum is contributed by electrons that have experienced single inelastic scattering events. As a safe assumption for e-beams, the initial (i) and final (f) electron wave functions can be separated as $\psi_{i|f}(\mathbf{r}) = (1/\sqrt{L}) \times e^{ip_{i|f,z}z}\psi_{i|f\perp}(\mathbf{R})$, where $\mathbf{R} = (x,y)$ denotes the transverse coordinates, L is the quantization length along the e-beam direction z, the longitudinal wave functions are plane waves of wave vectors $p_{i|f,z}$, and $\psi_{i|f\perp}(\mathbf{R})$ are the transverse wave functions. In addition, we focus on scattering events that produce negligible changes in the electron momentum relative to the initial value, such that the electron velocity vector $\mathbf{v}$ can be considered to remain constant (nonrecoil approximation). Finally, the atomic vibrations under study take place over small spatial extensions compared to the wavelength of light with the same frequency, so we adopt the quasistatic limit to describe the electron−sample interaction. Under these approximations, the EELS probability is given by[42] (see Methods)

$$\Gamma_{\mathrm{EELS}}(\omega) = \frac{e^2}{\pi\hbar v^2}\sum_f \int d^2\mathbf{R} \int d^2\mathbf{R}'\, \psi_{i\perp}(\mathbf{R})\psi^*_{f\perp}(\mathbf{R})\, \psi^*_{i\perp}(\mathbf{R}')\, \psi_{f\perp}(\mathbf{R}') \times \int_{-\infty}^{\infty} dz \int_{-\infty}^{\infty} dz'\, e^{i\omega(z-z')/v}\, \mathrm{Im}\{-W(\mathbf{r},\mathbf{r}',\omega)\} \quad (1)$$

where we sum over final transverse states f and the specimen enters through the screened interaction $W(\mathbf{r},\mathbf{r}',\omega)$, defined as the potential created at $\mathbf{r}$ by a unit charge placed at $\mathbf{r}'$ and oscillating with frequency ω. For atomic vibrations, the screened interaction reduces to a sum over the contributions of different vibrational modes, as shown in eqs 10 and 11 in Methods. Inserting these expressions into eq 1 and using the identity[45] $\int_{-\infty}^{\infty} dz\, e^{iqz}/r = 2K_0(|q|R)$, where K_0 is the modified Bessel function of the second kind and order 0, we find

$$\Gamma_{\mathrm{EELS}}(\omega) = \frac{4e^2}{\pi\hbar v^2}\sum_{nf} \mathrm{Im}\left\{\frac{|N_{nfi}(\omega/v)|^2}{\omega_n^2 - \omega(\omega + i\gamma)}\right\} \quad (2)$$

where

$$N_{nfi}(q) = \int d^2\mathbf{R}\, \psi_{i\perp}(\mathbf{R})\, \psi^*_{f\perp}(\mathbf{R})\, I_n(\mathbf{R}, q)$$

$$I_n(\mathbf{R}, q) = \sum_l \frac{1}{\sqrt{M_l}} \int d^3\mathbf{r}'\, K_0(|q||\mathbf{R} - \mathbf{R}'|)\, e^{iqz'}[\mathbf{e}_{nl}\cdot\vec{\rho}_l(\mathbf{r}')] \quad (3)$$

The n sum runs over the sampled vibrational modes, ω_n and $\mathbf{e}_{nl}$ are the associated frequencies and normalized atomic displacement vectors, respectively, the l sum extends over the atoms in the structure, M_l is the mass of atom l, the gradient of the charge distribution with respect to displacements of that atom is denoted $\vec{\rho}_l(\mathbf{r})$, and we have incorporated a phenomenological damping rate γ. As described in Methods, we use density-functional theory to obtain $\vec{\rho}_l(\mathbf{r})$ and the dynamical matrix. The latter is then used to find the natural vibration-mode frequencies ω_n and eigenvectors $\mathbf{e}_{nl}$ by solving the corresponding secular equation of motion. Because core electrons in the specimen are hardly affected by the swift electron, we assimilate them together with the nuclei to positive ionic point charges eZ_l (= $3e$ for B and $5e$ for N atoms) located at the equilibrium atomic positions $\mathbf{r}_l$, so that they contribute to $\vec{\rho}_l(\mathbf{r})$ with a term $\vec{\rho}_l^{\,\mathrm{nucl}}(\mathbf{r}) = eZ_l\nabla_{\mathbf{r}_l}\delta(\mathbf{r} - \mathbf{r}_l)$, which upon insertion into eq 3 leads to

$$I_n(\mathbf{R}, q) = I_n^{\mathrm{val}}(\mathbf{R}, q) + \sum_l \frac{eZ_l}{\sqrt{M_l}} e^{iqz_l}\mathbf{e}_{nl}\cdot\left[|q|\frac{(\mathbf{R} - \mathbf{R}_l)}{|\mathbf{R} - \mathbf{R}_l|} K_1(|q||\mathbf{R} - \mathbf{R}_l|) + iqK_0(|q||\mathbf{R} - \mathbf{R}_l|)\hat{\mathbf{z}}\right]$$

Here, $I_n^{\mathrm{val}}(\mathbf{R},q)$ is computed from eq 3 by substituting $\vec{\rho}_l(\mathbf{r}) = \vec{\rho}_l^{\,\mathrm{nucl}}(\mathbf{r}) + \vec{\rho}_l^{\,\mathrm{val}}(\mathbf{r})$ by the gradient of the valence-electron charge density $\vec{\rho}_l^{\,\mathrm{val}}(\mathbf{r})$ and carrying out the integral over a fine spatial grid. Incidentally, close encounters with the atoms in the structure produce an unphysical divergent contribution to the loss probability, which is avoided when accounting for the maximum possible momentum transfer[42] and also when averaging over the finite width of the e-beam. For simplicity, we regularize this divergence in this work by making the substitution $|\mathbf{R} - \mathbf{R}'| \to \sqrt{|\mathbf{R} - \mathbf{R}'|^2 + \Delta^2}$ with $\Delta = 0.2$ Å in the argument of the Bessel functions of the above equations. We have chosen Δ such that $1/\Delta$ approximately corresponds to the typical maximal range of collection angles in experiments.

Measurement of the inelastic electron signal in the Fourier plane corresponds to a selection of transmitted electron wave functions $\psi_{f\perp}(\mathbf{R}) = e^{i\mathbf{Q}_f\cdot\mathbf{R}}/\sqrt{A}$ (normalized by using the transverse quantization area A), having a well-defined final transverse wave vector $\mathbf{Q}_f \perp \hat{\mathbf{z}}$. Inserting this expression into eq 2 and making the substitution $\sum_f \to [A/(2\pi)^2]\int d^2\mathbf{Q}_f$, we find $\Gamma_{\mathrm{EELS}}(\omega) = \int d^2\mathbf{Q}_f\, [d\Gamma_{\mathrm{EELS}}(\omega)/d\mathbf{Q}_f]$, where

$$\frac{d\Gamma_{\mathrm{EELS}}(\omega)}{d\mathbf{Q}_f} = \frac{e^2}{\pi^3\hbar v^2}\sum_n \left|\int d^2\mathbf{R}\, \psi_{i\perp}(\mathbf{R})\, e^{-i\mathbf{Q}_f\cdot\mathbf{R}}\, I_n(\mathbf{R}, \omega/v)\right|^2 \times \mathrm{Im}\left\{\frac{1}{\omega_n^2 - \omega(\omega + i\gamma)}\right\} \quad (4)$$

is the momentum-resolved EELS probability. A dependence on the initial electron wave function is observed, which is however known to be lost when performing the integral over the entire $\mathbf{Q}_f$ space,[42,46] leading to $\Gamma_{\mathrm{EELS}}(\omega) = \int d^2\mathbf{R}\, |\psi_{i\perp}(\mathbf{R})|^2\, \Gamma_{\mathrm{EELS}}(\mathbf{R},\omega)$, where

$$\Gamma_{\mathrm{EELS}}(\mathbf{R}, \omega) = \frac{4e^2}{\pi\hbar v^2}\sum_n \mathrm{Im}\left\{\frac{|I_n(\mathbf{R}, \omega/v)|^2}{\omega_n^2 - \omega(\omega + i\gamma)}\right\} \quad (5)$$

(*i.e.*, the loss probability reduces to that experienced by a classical point electron averaged over the transverse e-beam density profile $|\psi_{i\perp}(\mathbf{R})|^2$).

https://doi.org/10.1021/acsnano.1c01071
ACS Nano 2021, 15, 9890−9899

The above results are derived at zero temperature. When the vibrational modes are in thermal equilibrium at a finite temperature T, the loss probabilities given by eqs 2, 4, and 5 need to be corrected as $\Gamma^T_{\mathrm{EELS}}(\omega) = \Gamma_{\mathrm{EELS}}(|\omega|)[n_T(\omega) + 1]\,\mathrm{sign}(\omega)$, where $n_T(\omega) = 1/(e^{\hbar\omega/k_BT} - 1)$ is the Bose−Einstein distribution function and $\omega > 0$ ($\omega < 0$) describes electron energy losses (gains). This expression, which has been used to determine phononic[21,24] and plasmonic[47] temperatures with nanoscale precision using EELS, can be derived from first principles for bosonic modes,[48] whose excitation and de-excitation probabilities are proportional to the quantum-harmonic-oscillator factors $n_T(\omega_n) + 1$ and $n_T(\omega_n)$, respectively. In what follows, we ignore thermal corrections as a good approximation for energy losses $\hbar\omega \gtrsim 50$ meV at room temperature ($k_BT \sim 25$ meV).

Valence-Electron Charge Gradients. We focus on the model system sketched in Figure 2a, which consists of 7 boron (green) and 6 nitrogen (blue) atoms arranged in a h-BN-like configuration, and includes 9 hydrogen edge atoms (gray) to passivate the edges and give stability to the structure[49] (see Methods and Supporting Information Figure S7). Molecules such as this one are likely produced during chemical vapor deposition before a continuous h-BN film is formed,[49] and they can also emerge when destroying continuous h-BN layers using physical methods.[50] In what follows, we compare the EELS signal from the isotopically pure molecule (taking all boron atoms as ^{11}B) with that obtained when one of the boron atoms is replaced by the isotope ^{10}B either at the edge or the center of the molecule. The isotopic composition affects the vibrational modes, but not the valence-electron charge density, which is represented for the unperturbed molecule in the underlying color plot of Figure 2a (integrated over the z direction, normal to the $x-y$ atomic plane). We observe electron accumulation around nitrogen atoms that reflects the ionic nature of the N−B bonds, similar to what is observed in extended h-BN monolayers. Coupling to the electron probe is mediated by the charge gradients $\vec{\rho}_l(\mathbf{r})$ entering eq 3, the valence contribution of which is shown in Figure 2b after integration over the out-of-plane direction (*i.e.*, $\int dz\, \vec{\rho}_l^{\,\mathrm{val}}(\mathbf{r})$) for l running over the three types of atoms under consideration. Each atomic displacement leads to a dipole-like pattern centered around the displaced atom and is qualitatively similar for other atoms of the same kind. As valence electrons pile up around nitrogen atoms, their displacements lead to the highest values of $\vec{\rho}_l^{\,\mathrm{val}}(\mathbf{r})$.

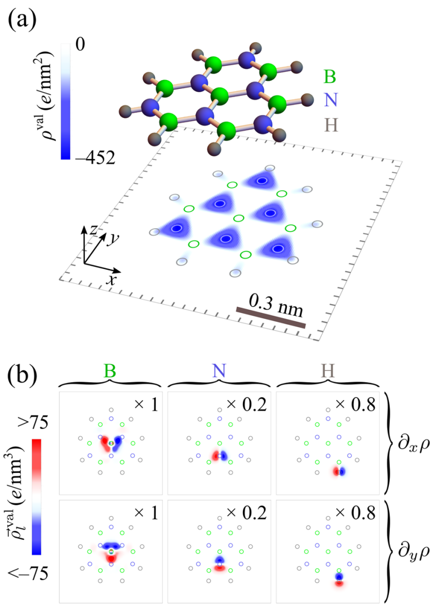

Figure 2. Charge density and its gradients in a h-BN-like molecule. (a) We show the unperturbed valence-electron charge density integrated over the direction *z* normal to the atomic plane for the molecular structure overlaid above the density plot. (b) Gradients are shown of the *z*-integrated valence charge density with respect to in-plane atomic displacements along *x* and *y* for selected B, N, and H individual atoms (identified by the rapid variations of the gradient in these plots). The gradient is multiplied by a different factor in each plot (see labels) to maintain a common color scale. We note that the charge density does not change when introducing the isotope impurity.

Vibrational EELS *vs* Infrared Spectroscopy. The gradients of the charge distribution in the nanostructure together with a vibrational eigenmode analysis provide the elements needed to calculate EELS and optical-extinction spectra in the IR range. In Figure 3a, we show EELS spectra obtained by using eq 5 for 60 keV electrons focused at four different positions within the $x-y$ atomic plane. We compare results for the isotopically pure molecule (solid curves) and the same structure with an isotopic impurity (dashed curves and symbols). The presence of the impurity leads to slight energy shifts of the mode energies (up to ∼2 meV; see details in Supporting Information Figures S1−S3 and S6), as well as substantial changes in the corresponding spectral weights. In addition, we observe that most features are enhanced when the e-beam is moved closer to the atomic positions, while several of them persist even when the beam passes outside the molecule (*cf.* green spectra). Such persisting features are associated with modes that exhibit a net dipole moment, so they can also be revealed through far-field optical spectroscopy, as shown in the extinction cross-sections plotted in Figure 3c (see Methods for details of the calculation). Dipole-active modes couple to the e-beam over long distances, and consequently, they can be detected in the aloof configuration, which has been recently employed in EELS experiments to study beam-sensitive molecules.[27−30] Indeed, we corroborate a strong resemblance of the optical extinction (Figure 3c) and the aloof EELS (Figure 3a, green curves) spectra. Modes with a net dipole therefore couple more efficiently to light and also to distant electrons under the aloof configuration than dark modes, while the latter, although making a vanishing contribution to EELS at large distances, can still be detected by electrons passing close to the structure. Incidentally, the 3-fold symmetry of the molecules renders the optical cross-section independent of the orientation of the polarization vector within the plane of the atoms. The most intense EELS peaks are observed at around 130 meV and 170−180 meV, corresponding to modes involving B−N bond vibrations (see Supporting Information Figures S1−S3 for details of the

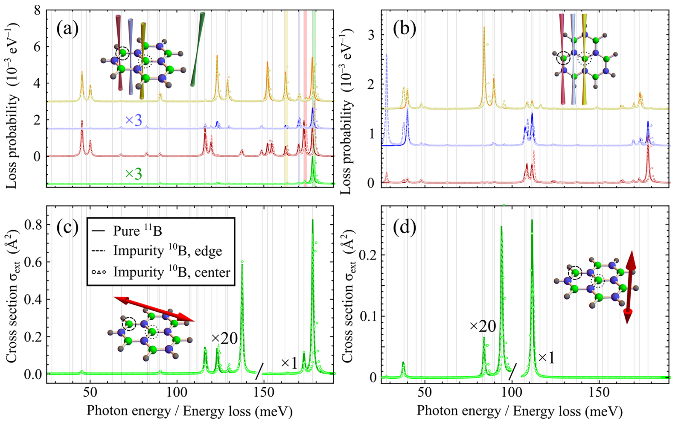

Figure 3. Effect of an isotope impurity in EELS and infrared (IR) extinction. We compare calculated EELS (a, b) and optical-extinction (c, d) spectra for an isotopically pure molecule (solid curves, only ^{11}B atoms) and a molecule containing a single isotope atom impurity (dashed curves for a ^{10}B impurity placed at the edge; symbols for the impurity positioned at the center). For EELS (a, b), we take 60 keV electrons and consider different e-beam positions (see color-coordinated vertically offset curves) and orientations (normal to the plane of the atoms in panel a; parallel to and 1 Å away from that plane in panel b). For optical IR spectroscopy (c, d), we consider in-plane (c) and out-of-plane (d) light polarization (see red arrows in the insets). All vibrational mode energies obtained in the displayed energy range for the isotopically pure structure are indicated by vertical gray lines. We incorporate a spectral broadening of 1 meV to account for intrinsic losses and instrument resolution.

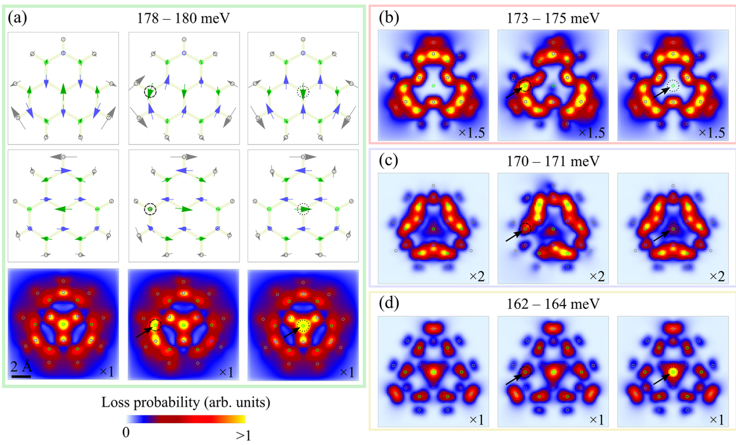

Figure 4. Isotope-impurity determination through energy-filtered EELS imaging. We plot the calculated EELS probability integrated over different energy-loss ranges (see labels) as a function of e-beam position under the conditions of Figure 3a for the isotopically pure molecule (left plots in each panel) and a molecule with an isotope atom defect (middle and right plots, ^{10}B atomic impurity at the edge or in the center of the molecule, as indicated by black arrows and circles). In panel a, we show the atomic displacements associated with the involved vibrational modes. The probability is multiplied by a different factor in each density plot (see lower-right labels) to maintain a common color scale. Frame colors are coordinated with the vertical bands indicated in Figure 3a. We spatially average the probability over a transverse Gaussian e-beam profile of 0.8 Å fwhm.

atomic displacement vectors associated with different vibrational modes). Weaker features above 300 meV (see Supporting Information Figure S5) arise from N−H and B−H bond stretches. Interestingly, the presence of the isotope

https://doi.org/10.1021/acsnano.1c01071
ACS Nano 2021, 15, 9890−9899

impurity dominantly affects modes that involve the motion of the atom substituted by the impurity. For such modes, we observe both slight blue shifts in their energies (further summarized in Supporting Information Figure S6) and changes in the peak intensities following modifications and distortions of the vibrational eigenvectors.

By rotating the nanoflake with respect to the e-beam direction (or analogously, the light polarization for optical measurements), a different set of modes contributes to the spectral features, dominated by out-of-plane atomic motion under the conditions of Figure 3b,d. In EELS, the strengths of these features strongly depend on e-beam position and orientation; such polarization sensitivity of EELS was also analyzed in ref 51 for anisotropic crystalline material. In particular, the spectra shown in Figure 3b (with the electrons passing parallel to and 1 Å away from the plane of the atoms) reveal several peaks that are absent under normal electron incidence (Figure 3a). Some of these modes are also missed in the optical extinction for out-of-plane polarization (Figure 3d), which confirms their dark nature, in contrast to the dominant excitations observed around ∼110 meV energy.

Vibrational Mapping at the Atomic Scale. To visualize the complete spatial dependence of the vibrational EELS signal at specific energies corresponding to selected modes, we calculate energy-filtered maps by scanning the beam position over an area covering the studied structure (placed in the $x-y$ plane). In Figure 4, we show maps calculated for a beam of 0.8 Å fwhm focal size and selected modes in isotopically pure and defective molecules (see Supporting Information Figure S4 for additional maps on the isotopically pure molecule). By inspecting the results for ∼179 meV (Figure 4a) energy losses, together with the corresponding atomic displacement vectors (two degenerate modes around this energy), we observe a strong correlation in symmetry and strength between the mode displacements and the EELS map, thus corroborating that the latter provides a solid basis to reconstruct the contribution of each atom to the vibrational modes. In addition, by introducing a boron isotope impurity at the edge of the molecule (indicated by black arrows), the 3-fold symmetry of the mode displacements and the resulting EELS maps are severely distorted. The impurity can produce either depletion or enhancement of the EELS intensity around its position, but in general, it influences the inelastic electron signal over the entire area of interest. Importantly, even if the impurity is placed in the center of the molecule, and thus, it does not distort the symmetry of the vibrational modes, it produces changes in the EELS intensities for those modes involving movement of the central atom. A slightly smaller mass of the central atom gives rise to larger vibrational amplitudes and consequently, higher EELS intensities. These findings suggest that although small frequency changes may be difficult to detect, the isotopic impurities could be identified *via* intensity changes in EELS maps integrated over an affordably large energy window. We also note that the ratio of inelastic to elastic electron signals is rather small (e.g., the loss probability is $\lesssim 10^{-3}$ for electrons focused close to atomic nuclei, or $\sim 10^{-5}$ for *aloof* beam positions), but such signals should still be detectable, especially in STEM-EELS setups equipped with direct electron detectors.[52]

In Figure 5, we explore the effect of post-selection on the resulting EELS intensity, as calculated for transverse-momentum-resolved scattered electrons using eq 4. The incident e-beam is taken to have a Gaussian density profile

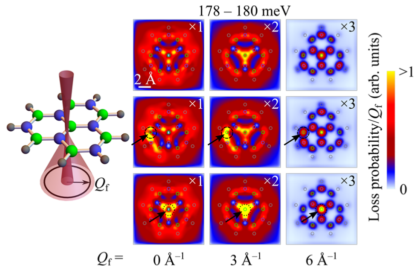

Figure 5. Isotope-impurity determination through momentum-resolved EELS. Under the conditions of Figure 3a, we plot the calculated EELS probability as a function of e-beam position for the isotopically pure molecule (upper plots) and a molecule with an isotope atom defect (lower plots, ^{10}B atomic impurity indicated by black arrows) after integration over both the specified energy-loss range (around ∼179 meV) and the transverse wave vector of the transmitted electrons within a narrow annular aperture centered around the e-beam direction. Different radii of the latter (Q_f) are considered in each column, as indicated by the lower labels. The probability is multiplied by a different factor in each color plot (see labels) and normalized to the same area of the collection aperture to maintain a common color scale. The incident e-beam has a transverse Gaussian profile of 0.8 Å fwhm.

$|\psi_i(\mathbf{R})|^2$ of 0.8 Å fwhm. We present calculations for the most prominent feature in EELS at energies around ∼179 meV, and compare results from isotopically pure (top row) and defective (middle and bottom rows) samples. The obtained momentum-dependent energy-filtered maps clearly demonstrate that the directly transmitted electrons ($Q_f = 0$) carry long-range information associated with the polarization of valence-electron charges (see Supporting Information Figure S4, showing the separate contributions of valence-electron and nuclear charges). Such long-range signal is particularly prominent for the ∼179 meV modes, which are dipole-active (see IR spectra in Figure 3b). In general, when collecting electrons experiencing larger transverse momentum transfers, the spatial localization of the signal is increased, enabling a better determination of the atomic positions and their contributions to the observed modes with a resolution limited by the finite size of the e-beam spot. Incidentally, we can link the energy-integrated low- and large-angle signal to bright- and dark-field images, respectively, as collected with different apertures in STEMs.[32,37] We note that elastic scattering by the molecule and its surroundings could potentially mask the inelastic signal, so one should focus on angular regions for which the latter makes a larger relative contribution, for example, by exploring different collection conditions.

CONCLUSIONS

STEM-EELS has evolved into a leading technique enabling both atomic-resolution imaging and spectroscopy over a broad frequency range extending down to the mid-IR. In particular, atomic-scale mapping of IR vibrational modes, which has recently become accessible,[32−34] is important for understanding and manipulating the optical response in such a spectral range, as well as for determining the effect of phonons and phonon-polaritons in the electrical and thermal conductivities of nanostructured materials. We have shown that

https://doi.org/10.1021/acsnano.1c01071
ACS Nano 2021, 15, 9890−9899

STEM-EELS can probe the complete set of vibrational modes, including optically bright and dark modes, the polarization characteristics of which can be addressed by tilting the sample relative to the e-beam or by resolving the inelastic electron signal as a function of scattering angle. The latter can benefit from recent advances in hybrid pixel detection technology.[52] As an application of these methods, we have demonstrated through first-principles calculations that an individual isotope impurity in a h-BN-like molecule produces radical changes in the spectral and spatial characteristics of the electron signal associated with the excitation of its vibrational modes. Although the emergence of localized vibrational signatures associated with single isotopic impurities in extended samples might be more complicated from a theoretical viewpoint (they require the use of larger supercells, while an interesting panorama may emerge from hybridization between localized vibrations and extended phonons) and is yet to be explored, our study supports the use of STEM-EELS to map isotope distributions with atomic precision in finite nanostructures. In general, studying the influence of isotopic impurities can be important for understanding phononic lifetimes, as well as thermal and electrical transport at the nanoscale.

METHODS

EELS Probability. Under the assumptions discussed in the main text, the loss rate reduces to[42]

$$\frac{\Gamma_{\mathrm{EELS}}(\omega)}{\mathrm{d}t} = \frac{2e^2}{\hbar} \sum_f \int \mathrm{d}^3\mathbf{r} \int \mathrm{d}^3\mathbf{r}'\, \psi_i(\mathbf{r})\, \psi_f^*(\mathbf{r})\, \psi_i^*(\mathbf{r}')\, \psi_f(\mathbf{r}') \times \mathrm{Im}\{-W(\mathbf{r}, \mathbf{r}', \omega)\}\, \delta(\varepsilon_f - \varepsilon_i + \omega)$$

where $\psi_i(\mathbf{r})$ and $\psi_f(\mathbf{r})$ denote initial and final electron wave functions of energies $\hbar\varepsilon_i$ and $\hbar\varepsilon_f$, respectively. We now separate longitudinal and transverse components as specified in the main text (*i.e.*, $\psi_{i|f}(\mathbf{r}) = (1/\sqrt{L})\mathrm{e}^{\mathrm{i}p_{i|f,z}z}\psi_{i|f\perp}(\mathbf{R})$), use the nonrecoil approximation to write $\varepsilon_f - \varepsilon_i \approx (p_{f,z} - p_{i,z})v$, transform the sum over final states through the prescription $\sum_f \to (L/2\pi)\int \mathrm{d}p_{f,z}\sum_f$ (*i.e.*, the remaining sum over f now refers to transverse degrees of freedom), carry out the $p_{f,z}$ integral using the δ function, and multiply the result by the interaction time L/v to convert the loss rate into a probability. Following these steps, we readily find eq 1.

Optical Response Associated with Atomic Vibrations. The quasistatic limit is adopted here under the assumption that the studied structures are small compared with the light wavelength at the involved oscillation frequencies. We consider a perturbation potential $\phi^{\mathrm{ext}}(\mathbf{r},t)$ due to externally incident light or a swift electron, in response to which the atoms in the structure (labeled by $l = 1, ..., N$) oscillate around their equilibrium positions $\mathbf{r}_l$ with time-dependent displacements $\mathbf{u}_l(t)$. The charge density $\rho(\{\mathbf{u}\},\mathbf{r})$, which obviously depends on $\{\mathbf{u}\} \equiv \{\mathbf{u}_1,...,\mathbf{u}_N\}$, is calculated from first principles as discussed below. Following a standard procedure to describe atomic vibrations,[53] we Taylor-expand the configuration energy (also calculated from first principles) for small displacements and only retain the lowest-order $\mathbf{u}$-dependent contribution $(1/2)\sum_{ll'} \mathbf{u}_l(t)\cdot\mathcal{D}_{ll'}\cdot\mathbf{u}_{l'}(t)$, where $\mathcal{D}_{ll'}$ is the so-called dynamical matrix. We now write the Lagrangian of the system as

$$\mathcal{L} = (1/2)\sum_l M_l |\dot{\mathbf{u}}_l(t)|^2 - (1/2)\sum_{ll'} \mathbf{u}_l(t)\cdot\mathcal{D}_{ll'}\cdot\mathbf{u}_{l'}(t) - \int \mathrm{d}^3\mathbf{r}\, \rho(\{\mathbf{u}\}, \mathbf{r})\, \phi^{\mathrm{ext}}(\mathbf{r}, t)$$

where M_l is the mass of atom l and the rightmost term accounts for the potential energy in the presence of the perturbing electric potential $\phi^{\mathrm{ext}}(\mathbf{r},t)$. The equation of motion then follows from $\partial_t\nabla_{\dot{\mathbf{u}}_l}\mathcal{L} = \nabla_{\mathbf{u}_l}\mathcal{L}$, which leads to

$$M_l\ddot{\mathbf{u}}_l(t) = -\sum_{l'} \mathcal{D}_{ll'}\cdot\mathbf{u}_{l'}(t) - \int \mathrm{d}^3\mathbf{r}\, \vec{\rho}_l(\mathbf{r})\, \phi^{\mathrm{ext}}(\mathbf{r}, t) \tag{6}$$

where we have used the property $\mathcal{D}_{ll'}^{\mathrm{T}} = \mathcal{D}_{l'l}$, while the vector field $\vec{\rho}_l(\mathbf{r}) = \nabla_{\mathbf{u}_l}\rho(\{\mathbf{u}\},\mathbf{r})$ represents the gradient of the electric charge density with respect to displacements of atom l. Linear response is assumed by using the dynamical matrix. In addition, to be consistent with this approximation, we evaluate $\vec{\rho}_l(\mathbf{r})$ at the equilibrium position $\mathbf{u} = 0$. It is then convenient to treat each frequency component separately to deal with the corresponding external potential $\phi^{\mathrm{ext}}(\mathbf{r},\omega) = \int_{-\infty}^{\infty} \mathrm{d}t\, \mathrm{e}^{\mathrm{i}\omega t}\phi^{\mathrm{ext}}(\mathbf{r},t)$, so that eq 6 becomes

$$\omega(\omega + \mathrm{i}\gamma)M_l\mathbf{u}_l(\omega) = \sum_{l'} \mathcal{D}_{ll'}\cdot\mathbf{u}_{l'}(\omega) + \int \mathrm{d}^3\mathbf{r}\, \vec{\rho}_l(\mathbf{r})\, \phi^{\mathrm{ext}}(\mathbf{r}, \omega) \tag{7}$$

where we have introduced a phenomenological damping rate γ. The solution to eq 7 can be found by first considering the symmetric eigenvalue problem for the free oscillations,

$$\sum_{l'} \frac{1}{\sqrt{M_l M_{l'}}}\mathcal{D}_{ll'}\cdot\mathbf{e}_{nl'} = \omega_n^2\mathbf{e}_{nl} \tag{8}$$

where n labels the resulting vibration modes of frequencies ω_n. The eigenvectors $\mathbf{e}_{nl}$ form a complete ($\sum_n \mathbf{e}_{nl}^* \otimes \mathbf{e}_{nl'} = \delta_{ll'}\mathcal{I}_3$, where $\mathcal{I}_3$ is the 3×3 unit matrix) and orthonormal ($\sum_l \mathbf{e}_{nl}^*\cdot\mathbf{e}_{n'l} = \delta_{nn'}$) basis set, which we use to write the atomic displacements as

$$\mathbf{u}_l(\omega) = \frac{1}{\sqrt{M_l}}\sum_n c_n(\omega)\mathbf{e}_{nl}$$

with expansion coefficients

$$c_n(\omega) = \frac{1}{\omega(\omega + \mathrm{i}\gamma) - \omega_n^2}\sum_l \frac{1}{\sqrt{M_l}}\mathbf{e}_{nl}^*\cdot\int \mathrm{d}^3\mathbf{r}\, \vec{\rho}_l(\mathbf{r})\, \phi^{\mathrm{ext}}(\mathbf{r}, \omega)$$

Incidentally, because the dynamical matrix is real and symmetric, the eigenvectors $\mathbf{e}_{nl}$ can be chosen to be real, but we consider a more general formulation using complex eigenvectors that are convenient to describe extended crystals, where the mode index n may naturally incorporate a well-defined Bloch momentum. Now, introducing the above expression for $\mathbf{u}_l$ in the induced charge density $\rho^{\mathrm{ind}}(\mathbf{r},\omega) = \sum_l \mathbf{u}_l\cdot\vec{\rho}_l(\mathbf{r})$, we can obtain the susceptibility

$$\chi(\mathbf{r}, \mathbf{r}', \omega) = \sum_{nll'} \frac{1}{\sqrt{M_l M_{l'}}}\frac{[\mathbf{e}_{nl}\cdot\vec{\rho}_l(\mathbf{r})][\mathbf{e}_{nl'}^*\cdot\vec{\rho}_{l'}(\mathbf{r}')]}{\omega(\omega + \mathrm{i}\gamma) - \omega_n^2} \tag{9}$$

which is implicitly defined by the relation $\rho^{\mathrm{ind}}(\mathbf{r},\omega) = \int \mathrm{d}^3\mathbf{r}'\, \chi(\mathbf{r},\mathbf{r}', \omega)\, \phi^{\mathrm{ext}}(\mathbf{r}',\omega)$. Finally, the screened interaction, defined by $W(\mathbf{r},\mathbf{r}',\omega) = \int \mathrm{d}^3\mathbf{r}_1 \int \mathrm{d}^3\mathbf{r}_2\, \chi(\mathbf{r}_1,\mathbf{r}_2,\omega)\, |\mathbf{r} - \mathbf{r}_1|^{-1}|\mathbf{r}' - \mathbf{r}_2|^{-1}$, reduces to

$$W(\mathbf{r}, \mathbf{r}', \omega) = \sum_n \frac{S_n(\mathbf{r})\, S_n^*(\mathbf{r}')}{\omega(\omega + \mathrm{i}\gamma) - \omega_n^2} \tag{10}$$

where

$$S_n(\mathbf{r}) = \sum_l \frac{1}{\sqrt{M_l}}\int \mathrm{d}^3\mathbf{r}'\, \frac{\mathbf{e}_{nl}\cdot\vec{\rho}_l(\mathbf{r}')}{|\mathbf{r} - \mathbf{r}'|} \tag{11}$$

Eqs 10 and 11 are used to evaluate eq 1 and produce eqs 2, 4, and 5.

Optical-Extinction Cross-Section. For a small structure such as that considered in Figure 2, we describe the far-field response in terms of the polarizability tensor, which we in turn calculate from the susceptibility by writing the dipole induced by a unit electric field; that is, $\overline{\overline{\alpha}}(\omega) = -\int \mathrm{d}^3\mathbf{r} \int \mathrm{d}^3\mathbf{r}'\, \chi(\mathbf{r},\mathbf{r}',\omega)\mathbf{r}\otimes\mathbf{r}'$. Using eq 9, we find

$$\overline{\overline{\alpha}}(\omega) = \frac{2}{\hbar}\sum_n \frac{\omega_n\mathbf{d}_n \otimes \mathbf{d}_n^*}{\omega_n^2 - \omega(\omega + \mathrm{i}\gamma)}$$

where

https://doi.org/10.1021/acsnano.1c01071
ACS Nano 2021, 15, 9890−9899

$$\mathbf{d}_n = \sum_l \sqrt{\frac{\hbar}{2\omega_n M_l}} \int d^3\mathbf{r}\, [\mathbf{e}_{nl}\cdot\vec{\rho}_l(\mathbf{r})]\mathbf{r} \tag{12}$$

is the transition dipole associated with mode n. We then calculate the optical-extinction cross-section as[54] $\sigma_{\rm ext}(\omega) = (4\pi\omega/c){\rm Im}\{\alpha_{ii}(\omega)\}$ for light polarization along either an in-plane ($i = x$) or an out-of-plane ($i = z$) symmetry direction. In practice, as described earlier in the text, we separate the charge gradient $\vec{\rho}_l(\mathbf{r}) = \vec{\rho}_l^{\rm nucl}(\mathbf{r}) + \vec{\rho}_l^{\rm val}(\mathbf{r})$ into the contributions of valence electrons ($\vec{\rho}_l^{\rm val}(\mathbf{r})$) and the rest of the system ($\vec{\rho}_l^{\rm nucl}(\mathbf{r})$, that is, nuclei and core electrons), so the transition dipoles reduce to $\mathbf{d}_n = \mathbf{d}_n^{\rm val} + e\sum_l Z_l\sqrt{\hbar/(2\omega_n M_l)}\,\mathbf{e}_{nl}$, where $\mathbf{d}_n^{\rm val}$ is calculated from eq 12 by replacing $\vec{\rho}_l(\mathbf{r})$ by $\vec{\rho}_l^{\rm val}(\mathbf{r})$.

DFT Calculations. We perform density functional theory (DFT) calculations using the projector-augmented-wave (PAW) method[55] as implemented in the Vienna *ab initio* simulation package (VASP)[56−58] within the generalized gradient approximation in the Perdew−Burke−Ernzerhof (PBE) form to describe electron exchange and correlation.[59] The cutoff energy for the plane waves is set to 500 eV. The atomic positions of the molecular structures under consideration with and without an isotopic impurity are determined by minimizing total energies and atomic forces by means of the conjugate gradient method. Atomic positions are allowed to relax until the atomic forces are less than 0.02 eV/Å and the total energy difference between sequential steps in the iteration is below 10^{-5} eV. The edges of the molecule are passivated with hydrogen terminations to maintain structural stability, leading to a nearly hexagonal structure (see Supporting Information Figure S7). Additionally, hydrogen passivation eliminates a strong effect associated with the dangling bonds observed in the vibrational spectra. We calculate the dynamical matrix $\mathcal{D}_{ll'}$ using the small displacement method: each atom in the unit cell is initially displaced by 0.01 Å, and the resulting interatomic force constants are then determined to fill the corresponding matrix elements. Vibrational eigenmodes and eigenfrequencies are obtained by diagonalizing the dynamical matrix, as discussed above. We assimilate nuclear and core-electron charges in each atom to a point charge. However, the distribution of the valence-electron charge density is incorporated using a dense grid in the unit cell to tabulate the charge gradients $\vec{\rho}_l^{\rm val}(\mathbf{r}')$ from the change in the valence-electron density produced for each small atomic displacement.

ASSOCIATED CONTENT

Supporting Information

The Supporting Information is available free of charge at https://pubs.acs.org/doi/10.1021/acsnano.1c01071.

(Figures S1−S3) Vibrational eigenenergies and eigenvectors; (Figure S4) nuclear + core-electron and valence-electron charge contributions to energy-filtered EELS probability maps; (Figure S5) spatially resolved EELS and IR absorption spectra overview; (Figure S6) mode energy differences; (Figure S7) relaxed atomic structures (PDF)

AUTHOR INFORMATION

Corresponding Author

F. Javier García de Abajo − *ICFO-Institut de Ciencies Fotoniques, The Barcelona Institute of Science and Technology, 08860 Castelldefels, Barcelona, Spain; ICREA-Institució Catalana de Recerca i Estudis Avançats, 08010 Barcelona, Spain;* orcid.org/0000-0002-4970-4565; Email: javier.garciadeabajo@nanophotonics.es

Authors

Andrea Konečná − *ICFO-Institut de Ciencies Fotoniques, The Barcelona Institute of Science and Technology, 08860 Castelldefels, Barcelona, Spain;* orcid.org/0000-0002-7423-5481

Fadil Iyikanat − *ICFO-Institut de Ciencies Fotoniques, The Barcelona Institute of Science and Technology, 08860 Castelldefels, Barcelona, Spain;* orcid.org/0000-0003-1786-3235

Complete contact information is available at: https://pubs.acs.org/10.1021/acsnano.1c01071

Notes

The authors declare no competing financial interest.

ACKNOWLEDGMENTS

This work has been supported in part by the European Research Council (Advanced Grant 789104-eNANO), the European Commission (Horizon 2020 Grants 101017720 FET-Proactive EBEAM and 964591-SMART-electron), the Spanish MINECO (Grants MAT2017-88492-R and Severo Ochoa CEX2019-000910-S), the Catalan CERCA Program, and Fundaciós Cellex and Mir-Puig.

REFERENCES

(1) Hillenbrand, R.; Taubner, T.; Keilmann, F. Phonon-Enhanced Light-Matter Interaction at the Nanometer Scale. *Nature* **2002**, *418*, 159−162.

(2) Huth, F.; Govyadinov, A.; Amarie, S.; Nuansing, W.; Keilmann, F.; Hillenbrand, R. Nano-FTIR Absorption Spectroscopy of Molecular Fingerprints at 20 nm Spatial Resolution. *Nano Lett.* **2012**, *12*, 3973−3978.

(3) Amenabar, I.; Poly, S.; Nuansing, W.; Hubrich, E. H.; Govyadinov, A. A.; Huth, F.; Krutokhvostov, R.; Zhang, L.; Knez, M.; Heberle, J.; Bittner, A. M.; Hillenbrand, R. Structural Analysis and Mapping of Individual Protein Complexes by Infrared Nanospectroscopy. *Nat. Commun.* **2013**, *4*, 2890.

(4) Kneipp, K.; Wang, Y.; Kneipp, H.; Perelman, L. T.; Itzkan, I.; Dasari, R. R.; Feld, M. S. Single Molecule Detection Using Surface-Enhanced Raman Scattering (SERS). *Phys. Rev. Lett.* **1997**, *78*, 1667−1670.

(5) Zhang, R.; Zhang, Y.; Dong, Z.; Jiang, S.; Zhang, C.; Chen, L.; Zhang, L.; Liao, Y.; Aizpurua, J.; Luo, Y.; Yang, J. L.; Hou, J. G. Chemical Mapping of a Single Molecule by Plasmon-Enhanced Raman Scattering. *Nature* **2013**, *498*, 82−86.

(6) Lee, J.; Crampton, K. T.; Tallarida, N.; Apkarian, V. A. Visualizing Vibrational Normal Modes of a Single Molecule with Atomically Confined Light. *Nature* **2019**, *568*, 78−82.

(7) Jaculbia, R. B.; Imada, H.; Miwa, K.; Iwasa, T.; Takenaka, M.; Yang, B.; Kazuma, E.; Hayazawa, N.; Taketsugu, T.; Kim, Y. Single-Molecule Resonance Raman Effect in a Plasmonic Nanocavity. *Nat. Nanotechnol.* **2020**, *15*, 105−110.

(8) Yeo, B.-S.; Zhang, W.; Vannier, C.; Zenobi, R. Enhancement of Raman Signals with Silver-Coated Tips. *Appl. Spectrosc.* **2006**, *60*, 1142−1147.

(9) Asghari-Khiavi, M.; Wood, B. R.; Hojati-Talemi, P.; Downes, A.; McNaughton, D.; Mechler, A. Exploring the Origin of Tip-Enhanced Raman Scattering; Preparation of Efficient TERS Probes with High Yield. *J. Raman Spectrosc.* **2012**, *43*, 173−180.

(10) Mastel, S.; Govyadinov, A. A.; Maissen, C.; Chuvilin, A.; Berger, A.; Hillenbrand, R. Understanding the Image Contrast of Material Boundaries in IR Nanoscopy Reaching 5 nm Spatial Resolution. *ACS Photonics* **2018**, *5*, 3372−3378.

(11) Krivanek, O. L.; Ursin, J. P.; Bacon, N. J.; Corbin, G. J.; Dellby, N.; Hrncirik, P.; Murfitt, M. F.; Own, C. S.; Szilagyi, Z. S. High-Energy-Resolution Monochromator for Aberration-Corrected Scanning Transmission Electron Microscopy/Electron Energy-Loss Spectroscopy. *Philos. Trans. R. Soc., A* **2009**, *367*, 3683−3697.

(12) Krivanek, O. L.; Lovejoy, T. C.; Dellby, N.; Aoki, T.; Carpenter, R. W.; Rez, P.; Soignard, E.; Zhu, J.; Batson, P. E.; Lagos,

M. J.; Egerton, R. F.; Crozier, P. A. Vibrational Spectroscopy in the Electron Microscope. *Nature* **2014**, *514*, 209−214.
(13) Rez, P. Is Localized Infrared Spectroscopy Now Possible in the Electron Microscope? *Microsc. Microanal.* **2014**, *20*, 671−677.
(14) Dwyer, C. Localization of High-Energy Electron Scattering from Atomic Vibrations. *Phys. Rev. B: Condens. Matter Mater. Phys.* **2014**, *89*, 054103.
(15) Saavedra, J. R. M.; García de Abajo, F. J. Phonon Excitation by Electron Beams in Nanographenes. *Phys. Rev. B: Condens. Matter Mater. Phys.* **2015**, *92*, 115449.
(16) Lourenço-Martins, H.; Kociak, M. Vibrational Surface Electron-Energy-Loss Spectroscopy Probes Confined Surface-Phonon Modes. *Phys. Rev. X* **2017**, *7*, 041059.
(17) Konečná, A.; Neuman, T.; Aizpurua, J.; Hillenbrand, R. Surface-Enhanced Molecular Electron Energy Loss Spectroscopy. *ACS Nano* **2018**, *12*, 4775−4786.
(18) Dwyer, C.; Aoki, T.; Rez, P.; Chang, S. L. Y.; Lovejoy, T. C.; Krivanek, O. L. Electron-Beam Mapping of Vibrational Modes with Nanometer Spatial Resolution. *Phys. Rev. Lett.* **2016**, *117*, 256101.
(19) Lagos, M. J.; Trügler, A.; Hohenester, U.; Batson, P. E. Mapping Vibrational Surface and Bulk Modes in a Single Nanocube. *Nature* **2017**, *543*, 529−532.
(20) Govyadinov, A. A.; Konečná, A.; Chuvilin, A.; Vélez, S.; Dolado, I.; Nikitin, A. Y.; Lopatin, S.; Casanova, F.; Hueso, L. E.; Aizpurua, J.; Hillenbrand, R. Probing Low-Energy Hyperbolic Polaritons in van der Waals Crystals with an Electron Microscope. *Nat. Commun.* **2017**, *8*, 95.
(21) Idrobo, J. C.; Lupini, A. R.; Feng, T.; Unocic, R. R.; Walden, F. S.; Gardiner, D. S.; Lovejoy, T. C.; Dellby, N.; Pantelides, S. T.; Krivanek, O. L. Temperature Measurement by a Nanoscale Electron Probe Using Energy Gain and Loss Spectroscopy. *Phys. Rev. Lett.* **2018**, *120*, 095901.
(22) Hage, F. S.; Nicholls, R. J.; Yates, J. R.; McCulloch, D. G.; Lovejoy, T. C.; Dellby, N.; Krivanek, O. L.; Refson, K.; Ramasse, Q. M. Nanoscale Momentum-Resolved Vibrational Spectroscopy. *Sci. Adv.* **2018**, *4*, eaar7495.
(23) Konečná, A.; Venkatraman, K.; March, K.; Crozier, P. A.; Hillenbrand, R.; Rez, P.; Aizpurua, J. Vibrational Electron Energy Loss Spectroscopy in Truncated Dielectric Slabs. *Phys. Rev. B: Condens. Matter Mater. Phys.* **2018**, *98*, 205409.
(24) Lagos, M. J.; Batson, P. E. Thermometry with Subnanometer Resolution in the Electron Microscope Using the Principle of Detailed Balancing. *Nano Lett.* **2018**, *18*, 4556−4563.
(25) Senga, R.; Suenaga, K.; Barone, P.; Morishita, S.; Mauri, F.; Pichler, T. Position and Momentum Mapping of Vibrations in Graphene Nanostructures in the Electron Microscope. *Nature* **2019**, *573*, 247−250.
(26) Qi, R.; Wang, R.; Li, Y.; Sun, Y.; Chen, S.; Han, B.; Li, N.; Zhang, Q.; Liu, X.; Yu, D.; Gao, P. Probing Far-Infrared Surface Phonon Polaritons in Semiconductor Nanostructures at Nanoscale. *Nano Lett.* **2019**, *19*, 5070−5076.
(27) Rez, P.; Aoki, T.; March, K.; Gur, D.; Krivanek, O. L.; Dellby, N.; Lovejoy, T. C.; Wolf, S. G.; Cohen, H. Damage-Free Vibrational Spectroscopy of Biological Materials in the Electron Microscope. *Nat. Commun.* **2016**, *7*, 10945.
(28) Haiber, D. M.; Crozier, P. A. Nanoscale Probing of Local Hydrogen Heterogeneity in Disordered Carbon Nitrides with Vibrational Electron Energy-Loss Spectroscopy. *ACS Nano* **2018**, *12*, 5463−5472.
(29) Jokisaari, J. R.; Hachtel, J. A.; Hu, X.; Mukherjee, A.; Wang, C.; Konecna, A.; Lovejoy, T. C.; Dellby, N.; Aizpurua, J.; Krivanek, O. L.; Idrobo, J.-C.; Klie, R. F. Vibrational Spectroscopy of Water with High Spatial Resolution. *Adv. Mater.* **2018**, *30*, 1802702.
(30) Hachtel, J. A.; Huang, J.; Popovs, I.; Jansone-Popova, S.; Keum, J. K.; Jakowski, J.; Lovejoy, T. C.; Dellby, N.; Krivanek, O. L.; Idrobo, J. C. Identification of Site-Specific Isotopic Labels by Vibrational Spectroscopy in the Electron Microscope. *Science* **2019**, *363*, 525−528.
(31) Tizei, L. H. G.; Mkhitaryan, V.; Lourenço-Martins, H.; Scarabelli, L.; Watanabe, K.; Taniguchi, T.; Tencé, M.; Blazit, J. D.; Li, X.; Gloter, A.; Zobelli, A.; Schmidt, F. P.; Liz-Marzán, L. M.; García de Abajo, F. J.; Stéphan, O.; Kociak, M. Tailored Nanoscale Plasmon-Enhanced Vibrational Electron Spectroscopy. *Nano Lett.* **2020**, *20*, 2973−2979.
(32) Hage, F. S.; Kepaptsoglou, D. M.; Ramasse, Q. M.; Allen, L. J. Phonon Spectroscopy at Atomic Resolution. *Phys. Rev. Lett.* **2019**, *122*, 016103.
(33) Venkatraman, K.; Levin, B. D.; March, K.; Rez, P.; Crozier, P. A. Vibrational Spectroscopy at Atomic Resolution with Electron Impact Scattering. *Nat. Phys.* **2019**, *15*, 1237−1241.
(34) Hage, F. S.; Radtke, G.; Kepaptsoglou, D. M.; Lazzeri, M.; Ramasse, Q. M. Single-Atom Vibrational Spectroscopy in the Scanning Transmission Electron Microscope. *Science* **2020**, *367*, 1124−1127.
(35) Yan, X.; Liu, C.; Gadre, C. A.; Gu, L.; Aoki, T.; Lovejoy, T. C.; Dellby, N.; Krivanek, O. L.; Schlom, D. G.; Wu, R.; Pan, X. Single-Defect Phonons Imaged by Electron Microscopy. *Nature* **2021**, *589*, 65−69.
(36) Asenjo-Garcia, A.; García de Abajo, F. J. Dichroism in the Interaction between Vortex Electron Beams, Plasmons, and Molecules. *Phys. Rev. Lett.* **2014**, *113*, 066102.
(37) Zeiger, P. M.; Rusz, J. Efficient and Versatile Model for Vibrational STEM-EELS. *Phys. Rev. Lett.* **2020**, *124*, 025501.
(38) Rez, P.; Singh, A. Lattice Resolution of Vibrational Modes in the Electron Microscope. *Ultramicroscopy* **2021**, *220*, 113162.
(39) Guzzinati, G.; Beche, A.; Lourenço-Martins, H.; Martin, J.; Kociak, M.; Verbeeck, J. Probing the Symmetry of the Potential of Localized Surface Plasmon Resonances with Phase-Shaped Electron Beams. *Nat. Commun.* **2017**, *8*, 14999.
(40) Hohenester, U.; Trügler, A.; Batson, P. E.; Lagos, M. J. Inelastic Vibrational Bulk and Surface Losses of Swift Electrons in Ionic Nanostructures. *Phys. Rev. B: Condens. Matter Mater. Phys.* **2018**, *97*, 165418.
(41) Forbes, B. D.; Allen, L. J. Modeling Energy-Loss Spectra Due to Phonon Excitation. *Phys. Rev. B: Condens. Matter Mater. Phys.* **2016**, *94*, 014110.
(42) García de Abajo, F. J. Optical Excitations in Electron Microscopy. *Rev. Mod. Phys.* **2010**, *82*, 209−275.
(43) Radtke, G.; Taverna, D.; Lazzeri, M.; Balan, E. First-Principles Vibrational Electron Energy Loss Spectroscopy of β-Guanine. *Phys. Rev. Lett.* **2017**, *119*, 027402.
(44) Giles, A. J.; Dai, S.; Vurgaftman, I.; Hoffman, T.; Liu, S.; Lindsay, L.; Ellis, C. T.; Assefa, N.; Chatzakis, I.; Reinecke, T. L.; Tischler, J. G.; Fogler, M. M.; Edgar, J. H.; Basov, D. N.; Caldwell, J. D. Ultralow-Loss Polaritons in Isotopically Pure Boron Nitride. *Nat. Mater.* **2018**, *17*, 134−139.
(45) Gradshteyn, I. S.; Ryzhik, I. M. *Table of Integrals, Series, and Products*, 7th ed.; Academic Press: London, 2007; DOI: 10.1016/C2009-0-22516-5.
(46) Ritchie, R. H.; Howie, A. Inelastic-Scattering Probabilities in Scanning-Transmission Electron-Microscopy. *Philos. Mag. A* **1988**, *58*, 753−767.
(47) Mkhitaryan, V.; March, K.; Tseng, E.; Li, X.; Scarabelli, L.; Liz-Marzán, L. M.; Chen, S.-Y.; Tizei, L. H. G.; Stéphan, O.; Song, J.-M.; Kociak, M.; García de Abajo, F. J.; Gloter, A. Can Copper Nanostructures Sustain High-Quality Plasmons? *Nano Lett.* **2021**, *21*, 2444−2452.
(48) García de Abajo, F. J.; Di Giulio, V. Optical Excitations with Electron Beams: Challenges and Opportunities. *ACS Photonics* **2021**, *8*, 945−974.
(49) Maruyama, M.; Okada, S. Energetics and Electronic Structure of Triangular Hexagonal Boron Nitride Nanoflakes. *Sci. Rep.* **2018**, *8*, 16657.
(50) Valerius, P.; Herbig, C.; Will, M.; Arman, M. A.; Knudsen, J.; Caciuc, V.; Atodiresei, N.; Michely, T. Annealing of Ion-Irradiated Hexagonal Boron Nitride on Ir(111). *Phys. Rev. B: Condens. Matter Mater. Phys.* **2017**, *96*, 235410.

(51) Radtke, G.; Taverna, D.; Menguy, N.; Pandolfi, S.; Courac, A.; Le Godec, Y.; Krivanek, O. L.; Lovejoy, T. C. Polarization Selectivity in Vibrational Electron-Energy-Loss Spectroscopy. *Phys. Rev. Lett.* **2019**, *123*, 256001.
(52) Plotkin-Swing, B.; Corbin, G. J.; De Carlo, S.; Dellby, N.; Hoermann, C.; Hoffman, M. V.; Lovejoy, T. C.; Meyer, C. E.; Mittelberger, A.; Pantelic, R.; Piazza, L.; Krivanek, O. L. Hybrid Pixel Direct Detector for Electron Energy Loss Spectroscopy. *Ultramicroscopy* **2020**, *217*, 113067.
(53) Ashcroft, N. W.; Mermin, N. D. *Solid State Physics*; Harcourt College: Philadelphia, 1976.
(54) van de Hulst, H. C. *Light Scattering by Small Particles*; Dover: New York, 1981.
(55) Blöchl, P. E. Projector Augmented-Wave Method. *Phys. Rev. B: Condens. Matter Mater. Phys.* **1994**, *50*, 17953.
(56) Kresse, G.; Hafner, J. *Ab Initio* Molecular Dynamics for Liquid Metals. *Phys. Rev. B: Condens. Matter Mater. Phys.* **1993**, *47*, 558−561.
(57) Kresse, G.; Furthmüller, J. Efficient Iterative Schemes for *ab Initio* Total-Energy Calculations Using a Plane-Wave Basis Set. *Phys. Rev. B: Condens. Matter Mater. Phys.* **1996**, *54*, 11169−11186.
(58) Kresse, G.; Furthmüller, J. Efficiency of ab Initio Total Energy Calculations for Metals and Semiconductors Using a Plane-Wave Basis Set. *Comput. Mater. Sci.* **1996**, *6*, 15−50.
(59) Perdew, J. P.; Burke, K.; Ernzerhof, M. Generalized Gradient Approximation Made Simple. *Phys. Rev. Lett.* **1996**, *77*, 3865−3868.

https://doi.org/10.1021/acsnano.1c01071
ACS Nano 2021, 15, 9890−9899

PHYSICAL REVIEW B **102**, 115431 (2020)

Probing and steering bulk and surface phonon polaritons in uniaxial materials using fast electrons: Hexagonal boron nitride

C. Maciel-Escudero,[1,2] Andrea Konečná,[1] Rainer Hillenbrand,[2,3] and Javier Aizpurua[1,4,*]
[1]*Materials Physics Center, CSIC-UPV/EHU, 20018, Donostia-San Sebastián, Spain*
[2]*CIC NanoGUNE BRTA and Department of Electricity and Electronics, UPV/EHU, 20018, Donostia-San Sebastián, Spain*
[3]*IKERBASQUE, Basque Foundation for Science, 48009 Bilbao, Spain*
[4]*Donostia International Physics Center DIPC, 20018 Donostia-San Sebastián, Spain*

(Received 9 June 2020; revised 5 August 2020; accepted 7 August 2020; published 23 September 2020)

We theoretically describe how fast electrons couple to polaritonic modes in uniaxial materials by analyzing the electron energy-loss spectra. We show that in the case of a uniaxial medium with hyperbolic dispersion, bulk and surface modes can be excited by a fast electron traveling through the volume or along an infinite interface between the material and vacuum. Interestingly, and in contrast to excitations in isotropic materials, bulk modes can be excited by fast electrons traveling outside the uniaxial medium. We demonstrate our findings with the representative uniaxial material hexagonal boron nitride. We show that the excitation of bulk and surface phonon polariton modes is strongly related to the electron velocity and highly dependent on the angle between the electron beam trajectory and the optical axis of the material. Our work provides a systematic study for understanding bulk and surface polaritons excited by a fast electron beam in hyperbolic materials and sets a way to steer and control the propagation of the polaritonic waves by changing the electron velocity and its direction.

DOI: 10.1103/PhysRevB.102.115431

I. INTRODUCTION

Polar materials have become of high interest in the field of nanophotonics due to their ability to support phonon polaritons, quasiparticles which result from the coupling between electromagnetic waves and crystal lattice vibrations [1,2] with a characteristic wavelength lying in the mid-infrared region. These quasiparticles can enhance the electromagnetic field deep below the diffraction limit with large quality factors compared to infrared plasmons [3–6], making them promising building blocks for infrared nanophotonics applications [7–10].

One interesting two-dimensional (2D) polar material is hexagonal boron nitride (h-BN) because of its high-quality phonon polaritons and the easy preparation of the single atomic layers made by exfoliation [11–16]. Aside from being widely used in heterostructures [17], h-BN is emerging by itself as a versatile material offering novel optical and electro-optical functionalities. The crystal layer structure that constitues h-BN, mediated via interlayer van der Waals forces, produces a uniaxial optical response of the material. This implies that the dielectric function of h-BN needs to be described by a diagonal tensor $\overleftrightarrow{\varepsilon}$ with two principal axes [12,13]: $\varepsilon_x = \varepsilon_y = \varepsilon_\perp$ and $\varepsilon_z = \varepsilon_\parallel$. When $\mathrm{Re}(\varepsilon_\parallel)\mathrm{Re}(\varepsilon_\perp) < 0$, phonon polaritons can propagate inside the material and exhibit a hyperbolic dispersion [7,18], that is, the relationship between the different components of the polariton wave vector $\mathbf{k}(\omega) = (k_x, k_y, k_z)$ traces a surface in momentum space which corresponds to hyperboloids. For h-BN, one can find two energy bands (the reststrahlen bands) where one of the principal components of the dielectric tensor is negative. Each reststrahlen band is defined by the energy region between the transverse and longitudinal optical phonon energy, TO and LO, respectively ($\mathrm{TO}_\perp$ and $\mathrm{LO}_\perp$ for the upper reststrahlen band and $\mathrm{TO}_\parallel$ and $\mathrm{LO}_\parallel$ for the lower Reststrahlen band, see Fig. 1). On the other hand, when $\mathrm{Re}(\varepsilon_\parallel)\mathrm{Re}(\varepsilon_\perp) > 0$, the isofrequency surfaces traced by the polariton wave vector in momentum space are ellipsoids.

Figure 1 depicts $\varepsilon_\perp$ and $\varepsilon_\parallel$ (see Appendix A for expressions and parameters of the dielectric tensor components), which represent the in-plane and out-of-plane dielectric components of h-BN, respectively. The energy range in Fig. 1, shaded in red, corresponds to the lower reststrahlen band (94.2–102.3 meV) where the real part of the out-of-plane permittivity is negative, leading to isofrequency surfaces in the form of two-sheet hyperboloids (inset type I). The energy region shaded in gray corresponds to the upper reststrahlen band (168.6–200.1 meV), where the real part of the in-plane permittivity is negative and the isofrequency surfaces correspond to one-sheet hyperboloids (inset type II).

Hyperbolic phonon polaritons excitable in h-BN within the range of 90–200 meV might be a key to many novel photonic technologies relying on the nanoscale confinement of light and its manipulation. As a result, efficient design and utilization of h-BN structures require spectroscopic studies with adequate spatial resolution. This can be provided, for instance, by electron energy-loss spectroscopy (EELS) using electrons as localized electromagnetic probes. Recently, instrumental improvements in EELS performed in a scanning transmission electron microscope (STEM) allowed to spatially map phonon polaritons [19] and hyperbolic phonon polaritons in h-BN [20,21]. The focused electron beam in STEM has thus become a suitable probe to access the spectral information of low-energy excitations in technologically relevant materials, with nanoscale spatial resolution. Thus, EEL spectra in

*aizpurua@ehu.eus

2469-9950/2020/102(11)/115431(20)

phononic materials can be of paramount importance to reveal the properties of phonon polariton excitations.

In this work we first show that a fast electron traveling through bulk h-BN can excite volume phonon polaritons inside and outside the h-BN reststrahlen bands. Our analysis reveals that the excitation of the volume polariton modes is strongly dependent on the electron velocity and also on the orientation between the electron beam trajectory and the h-BN optical axis. We then study the formation of wake patterns in the field distribution induced by the electron beam at h-BN. Our methodology allows us to connect the excitation of these wake fields with the different electron energy-loss mechanisms experienced by the fast electron in the medium: (i) excitation of phonon polaritons or (ii) Cherenkov radiation. We also discuss the emergence of asymmetric wake patterns exhibited by the induced electromagnetic field when the electron beam trajectory sustains an angle relative to the h-BN optical axis. Finally, in the last two sections of the paper we show that a fast electron beam interacting with a semi-infinite h-BN interface excites Dyakonov surface phonon polaritons within the h-BN upper reststrahlen band. We further demonstrate that the probing electron traveling above h-BN in aloof trajectories excites volume phonon polaritons (remotely activation). All these findings offer a way to steer and control the propagation of the polaritonic waves and reveal the importance of the anisotropic optical response of the material in the EELS analysis.

II. EXCITATION OF INFRARED BULK MODES IN H-BN BY A FOCUSED FAST ELECTRON BEAM

A. Bulk modes in h-BN

According to Maxwell's equations in momentum-frequency $(\mathbf{k}, \omega)$ space, the dispersion relation for a wave propagating in the volume of an anisotropic material can be found from the following relationship [22,23]:

$$\det[\overleftrightarrow{\mathbf{G}}^{-1}(\mathbf{k};\omega)] = \det\big[\mathbf{k}\otimes\mathbf{k} - k^2\overleftrightarrow{\mathbf{I}} + k_0^2\overleftrightarrow{\varepsilon}\big] = 0, \quad (1)$$

where $\overleftrightarrow{\mathbf{G}}^{-1}$ is the inverse of the Green's tensor, $\mathbf{k}(\omega) = (k_x, k_y, k_z)$ is the wave vector of the wave, $k_0 = \omega/c$ is the magnitude of the wave vector in vacuum, c is the speed of light, $\det[\overleftrightarrow{\mathbf{x}}]$ stands for the determinant of a matrix, $\otimes$ is the tensor product, and $\overleftrightarrow{\mathbf{I}}$ is the identity tensor. Particularly, for a uniaxial medium, the dielectric response can be described in tensor form as $\overleftrightarrow{\varepsilon}(\omega) = \mathrm{diag}[\varepsilon_\perp, \varepsilon_\perp, \varepsilon_\parallel]$. For this case, two solutions (modes) arise from Eq. (1), yielding the dispersion relation for ordinary waves

$$k^2 = k_0^2\varepsilon_\perp, \quad (2)$$

and the dispersion relation for extraordinary waves

$$\frac{k_x^2 + k_y^2}{\varepsilon_\parallel} + \frac{k_z^2}{\varepsilon_\perp} = k_0^2. \quad (3)$$

Equation (2) represents concentric spheres in $\mathbf{k}$ space for a given energy $\hbar\omega$ (with $\varepsilon_\perp > 0$), while Eq. (3) represents hyperboloids or ellipsoids in the reciprocal space depending on the sign of the dielectric components $\varepsilon_\parallel$ and $\varepsilon_\perp$. Altogether, the isofrequency surfaces of the polariton wave vector $\mathbf{k}(\omega)$ in momentum space (for a uniaxial medium) constitute the dispersion relation of the phonon-polariton modes and, as observed in Eqs. (2) and (3), are represented geometrically by spheres, ellipsoids, or hyperboloids. Note that these modes are independent of the exciting probe used. For h-BN, the insets in Fig. 1 depict the isofrequency surfaces for each energy region inside and outside the reststrahlen bands. As we will show in the following, fast electron beams are effective probes capable of exciting the different phonon-polariton modes sustained in h-BN.

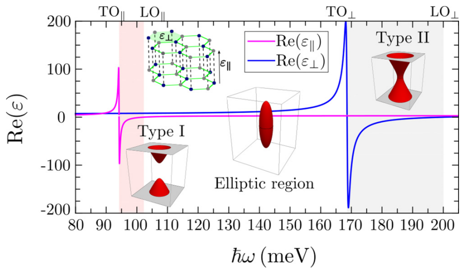

FIG. 1. Real parts of the components of the h-BN dielectric function. The shaded red area marks the lower reststrahlen band and the gray area the upper reststrahlen band. Insets illustrate the elliptic and the hyperbolic (type I and type II) isofrequency surfaces and the crystal lattice structure of h-BN.

B. Electron energy-loss probability

Fast electron beams can couple to bulk polaritonic modes sustained in anisotropic media. We can observe this by analyzing the energy losses experienced by the electron when traveling in such media. Electron energy losses, ΔE_{EELS}, can be calculated within classical electrodynamics as the work performed by the induced electromagnetic field $\mathbf{E}^{\mathrm{ind}}(\mathbf{r};t)$ on the probing electron [24–28]

$$\Delta E_{\mathrm{EELS}} = e\int d\mathbf{r}_e \cdot \mathbf{E}^{\mathrm{ind}}(\mathbf{r}_e;t), \quad (4)$$

where the integration is performed along the electron beam trajectory $\mathbf{r}_e(t)$, e is the elementary charge, and $\mathbf{E}^{\mathrm{ind}}(\mathbf{r};t)$ is evaluated along $\mathbf{r}_e(t)$. Notice that we approximate the electron beam as a classical point charge. The relatively low currents used in typical EELS experiments justify this approximation [29–31]. If we Fourier transform $\mathbf{E}^{\mathrm{ind}}(\mathbf{r};t) \mapsto \mathbf{E}^{\mathrm{ind}}(\mathbf{r};\omega)$ in Eq. (4), the electron energy losses can be written as

$$\begin{aligned}\Delta E_{\mathrm{EELS}} &= \frac{e}{2\pi}\int d\mathbf{r}_e \cdot \int_{-\infty}^{\infty} d\omega\, \mathbf{E}^{\mathrm{ind}}(\mathbf{r}_e;\omega)\, e^{-i\omega t}\\ &= \int_0^{\infty} d\omega \int dL\, \hbar\omega\, \Gamma(\omega),\end{aligned} \quad (5)$$

where one identifies the electron energy-loss (EEL) probability per unit path $\Gamma(\omega)$ as

$$\Gamma(\omega) = \frac{e}{\pi\hbar\omega}\mathrm{Re}[\mathbf{E}^{\mathrm{ind}}(\mathbf{r}_e;\omega)\cdot\hat{\mathbf{v}}\, e^{-i\omega t_e}], \quad (6)$$

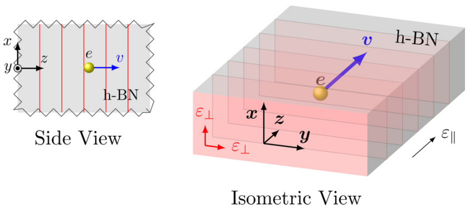

FIG. 2. Schematics of the electron traveling through the h-BN with velocity $\mathbf{v} = v\hat{\mathbf{z}}$ parallel to the h-BN optical axis (z direction).

with $\hat{\mathbf{v}}$ the unit vector in the same direction as the electron velocity $\mathbf{v}$ and t_e is the time for the electron to travel a distance dL. Hence, to calculate $\Gamma(\omega)$ one needs to know the induced electric field $\mathbf{E}^{\text{ind}}(\mathbf{r};\omega)$. We derive below the expressions of the total electric field $\mathbf{E}^{\text{tot}}(\mathbf{r};\omega)$ and $\Gamma(\omega)$ for an electron beam trajectory parallel to the optical axis of h-BN, as depicted in Fig. 2.

It follows from Maxwell's equations that the field produced by the fast electron plus the induced electric field, namely, the total electric field $[\mathbf{E}^{\text{tot}}(\mathbf{r};\omega)]$ is given by

$$\mathbf{E}^{\text{tot}}(\mathbf{r};\omega) = -i\frac{\omega}{(2\pi)^3 c^2 \varepsilon_0}\int d^3\mathbf{k}\,\rho(\mathbf{k};\omega)\,\overleftrightarrow{\mathbf{G}}(\mathbf{k};\omega)\cdot\mathbf{v}\,e^{i\mathbf{k}\cdot\mathbf{r}}, \tag{7}$$

with ε_0 the vacuum permittivity and $\rho(\mathbf{k};\omega) = -2\pi\, e\delta(\omega - \mathbf{k}\cdot\mathbf{v})$ the charge density of the probing electron. The integration in Eq. (7) extends over the whole reciprocal space and the delta function introduced by the charge density ensures conservation of energy and momentum. Indeed, one finds that in the no-relativistic limit the energy that the electron with initial velocity $\mathbf{v}$ transfers to the medium upon losing momentum $\hbar\mathbf{k}$ is

$$\hbar\omega = \frac{(\mathbf{p}+\hbar\mathbf{k})^2}{2m} - \frac{p^2}{2m} = \hbar\mathbf{v}\cdot\mathbf{k} + \frac{\hbar^2}{2m}k^2, \tag{8}$$

with $\mathbf{p} = m\mathbf{v}$ the initial momentum of the fast electron. By neglecting recoil of the incident electron, from Eq. (8) one arrives to the so-called nonrecoil approximation where $\omega = \mathbf{k}\cdot\mathbf{v}$. Note that the z component of the wave vector is fixed by $k_z = \omega/v$ when the electron travels in the z direction.

To calculate the bulk loss probability $\Gamma^{\text{bulk}}(\omega)$ experienced by the fast electron in the anisotropic medium we substitute Eq. (7) into Eq. (6). Notice that a fast electron traveling in vacuum loses no energy, thus we can use $\mathbf{E}^{\text{tot}}(\mathbf{r};\omega)$ instead of $\mathbf{E}^{\text{ind}}(\mathbf{r};\omega)$ in Eq. (6). Using the cylindrical symmetry of the field produced by the fast electron one finds that

$$\Gamma^{\text{bulk}}(\omega) = \int_0^{k_\perp^c} dk_\perp\, P^{\text{bulk}}(k_\perp;\omega), \tag{9}$$

where

$$P^{\text{bulk}}(k_\perp;\omega) = -\frac{2e^2 k_\perp v}{(2\pi)^3\hbar c^2\varepsilon_0 v_z}\int_0^{2\pi} d\phi\,\text{Im}[\hat{\mathbf{v}}\cdot\overleftrightarrow{\mathbf{G}}_{k_z}\cdot\hat{\mathbf{v}}] \tag{10}$$

is the probability for the electron to transfer a transverse momentum $\hbar k_\perp$ (to the electron trajectory) upon losing energy $\hbar\omega$. We will refer to this quantity as the momentum-resolved loss probability. In Eq. (10) $\overleftrightarrow{\mathbf{G}}_{k_z} = \overleftrightarrow{\mathbf{G}}(k_\perp,\phi,k_z = \omega/v_z - \mathbf{k}_\perp\cdot\mathbf{v}/v_z)$, and ϕ is the angle between $\mathbf{k}_\perp$ and the k_x axis, with $\hbar k_\perp^c$ the maximum perpendicular momentum of the electrons selected by the collection aperture of the EELS spectrometer.

Particularly, when the electron beam trajectory points out in the same direction as the h-BN optical axis ($\mathbf{v} = v\hat{\mathbf{z}}$), expressions for $\mathbf{E}^{\text{tot}}(\mathbf{r};\omega)$ and thus for $\Gamma^{\text{bulk}}(\omega)$ can be found in a closed form (see Appendix B for the analytical formula of the Green's tensor in uniaxial anisotropic media):

$$\mathbf{E}^{\text{tot}}(\mathbf{r};\omega) = \frac{e}{2\pi\varepsilon_0}\frac{\omega}{v^2\gamma_\perp\varepsilon_\perp}\mathbf{g}(\mathbf{r};\omega), \tag{11}$$

where

$$\mathbf{g}(\mathbf{r};\omega) = e^{i\omega z/v}\left[\frac{i}{\gamma_\perp}K_0\left(\sqrt{\frac{\varepsilon_\parallel}{\varepsilon_\perp}}\frac{|\omega|}{\gamma_\perp v}R\right)\hat{\mathbf{z}} - \text{sgn}(\omega)\sqrt{\varepsilon_\parallel\varepsilon_\perp}K_1\left(\sqrt{\frac{\varepsilon_\parallel}{\varepsilon_\perp}}\frac{|\omega|}{\gamma_\perp v}R\right)\hat{\mathbf{R}}\right] \tag{12}$$

is written in cylindrical coordinates $\mathbf{r} = (\mathbf{R}, z) = (x, y, z)$, $R = \sqrt{x^2+y^2}$, $K_0(x)$, $K_1(x)$ are the zero- and first-order modified Bessel functions of the second kind, sgn stands for the sign function, and $\gamma_\perp = 1/\sqrt{1 - v^2\varepsilon_\perp/c^2}$ is the Lorentz factor.

The momentum-resolved loss probability becomes

$$P^{\text{bulk}}(k_\perp;\omega) = -\frac{2e^2}{(2\pi)^2\omega^2\hbar\varepsilon_0}\text{Im}\left\{\left[k_0^2\varepsilon_\perp - \frac{\omega^2}{v^2}\right] \times \frac{k_\perp}{\varepsilon_\parallel\left[\varepsilon_\perp k_0^2 - \omega^2/v^2\right] - \varepsilon_\perp k_\perp^2}\right\}, \tag{13}$$

and, substituting Eq. (13) into Eq. (9), one finds that

$$\Gamma^{\text{bulk}}(\omega) = \frac{e^2}{(2\pi)^2\omega^2\hbar\varepsilon_0}\text{Im}\left\{\left[k_0^2 - \frac{\omega^2}{\varepsilon_\perp v^2}\right] \times \ln\left[\frac{\varepsilon_\parallel\varepsilon_\perp k_0^2 - \varepsilon_\parallel\omega^2/v^2 - \varepsilon_\perp\left(k_\perp^c\right)^2}{\varepsilon_\parallel\varepsilon_\perp k_0^2 - \varepsilon_\parallel\omega^2/v^2}\right]\right\}. \tag{14}$$

The nonretarded versions of $P^{\text{bulk}}(k_\perp;\omega)$ and $\Gamma^{\text{bulk}}(\omega)$ can be obtained by setting k_0 equal to zero in Eqs. (13) and (14).

The spectrum of the momentum-resolved loss probability and the EEL probability provide valuable information which reveals the properties of the modes of the anisotropic material. We thus explore in the following the connection between the dispersion relation of the h-BN excitations in the upper reststrahlen band with these two quantities.

C. Upper reststrahlen band

In the following we address the electron energy losses in h-BN and the connection of these losses with the isofrequency surfaces of the material. We first show in Fig. 3(a) the isofrequency curve of a h-BN phonon polariton for an energy in the upper reststrahlen band (red curve). We chose 195 meV as a representative value of this band. When a fast electron beam is used to probe these excitations in the medium, the velocity of the electron determines the momentum transfer, as $\mathbf{k}\cdot\mathbf{v} = \omega$ [Eq. (8) in the nonrecoil approximation]. If the electron is traveling along the z direction, then $k_z = \omega/v$ [blue horizontal line in Fig. 3(a)]. Following Eq. (3), this also sets the value of the $\hbar k_\perp$ momentum component ($k_\perp^2 = \varepsilon_\parallel k_0^2 - \varepsilon_\parallel k_z^2/\varepsilon_\perp$) of the excited phonon polariton.

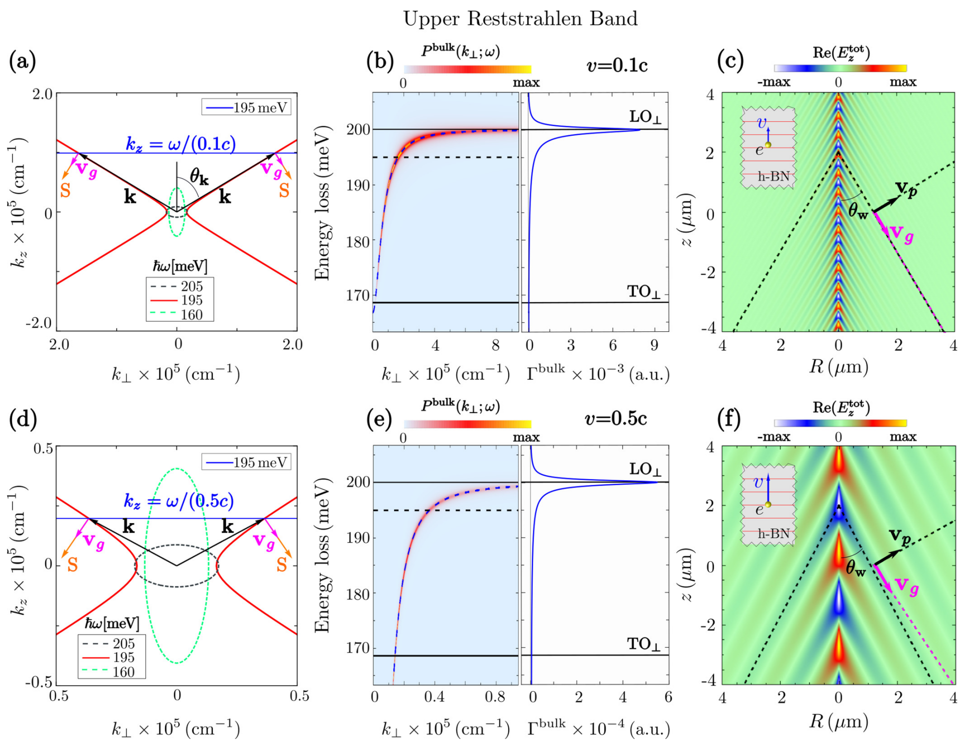

FIG. 3. (a) Isofrequency curves for energies inside (195 meV, red solid line) and outside (160 and 205 meV, green and black dashed lines) the upper reststrahlen band plotted for the wave vector k_z versus $k_\perp = \sqrt{k_x^2 + k_y^2}$. The horizontal blue line represents the momentum $\hbar k_z = \hbar\omega/(0.1c)$ transferred by the fast electron to the polaritons when it travels along the z direction with $v = 0.1c$. The blue line is evaluated at energy 195 meV (caption at the top right of the figure). The black arrows represent the polariton wave vector $\mathbf{k}(\omega)$, $\theta_{\mathbf{k}}$ is the angle between $\mathbf{k}(\omega)$ and the k_z axis, the magenta arrows represent the group velocity $\mathbf{v}_g$, and the orange arrows the Poynting vector $\mathbf{S}$. (d) Shows a zoom into (a). In (d) the horizontal blue line represents $k_z = \omega/(0.5c)$. The contour plot (left panel) in (b) shows the momentum-resolved loss probability $P^{\rm bulk}(k_\perp;\omega)$ normalized to the maximum value (3 a.u.) for $v = 0.1c$. The right panel in (b) shows the energy-loss probability $\Gamma^{\rm bulk}(\omega)$ obtained by integrating $P^{\rm bulk}(k_\perp;\omega)$ over $k_\perp$ up to $k_\perp^c = 0.05$ Å^{-1}. (e) Same as in (b) but considering $v = 0.5c$. (c), (f) Depict the real part of the z component of the total electric field induced by the fast electron along the cylindrical coordinates (R, z) for the energy 195 meV. The field plots are normalized to the maximum value in each case: (c) 1×10^{-5} a.u. and (f) 7.5×10^{-7} a.u. The insets in (c) and (f) illustrate the electron beam trajectory and orientation of the h-BN crystal planes.

The intersections between $k_z = \omega/v$ and the isofrequency curves in the upper reststrahlen band establish a relationship between the energy $\hbar\omega$ of the hyperbolic phonon polariton and its perpendicular momentum component $\hbar k_\perp$. In the left panel of Fig. 3(b) we plot this relationship (blue dashed line) and the momentum-resolved loss probability $P^{\rm bulk}(k_\perp;\omega)$ (light blue-yellow contour plot) for $v = 0.1c$. We note that the highest values of $P^{\rm bulk}(k_\perp;\omega)$ coincide with the blue dashed line and its asymptotic behavior approaches LO$_\perp$ for large $k_\perp$. This demonstrates that electron energy losses in the upper band are due to phonon polariton excitations. We confirm this by integrating $P^{\rm bulk}(k_\perp;\omega)$ over $k_\perp$ up to a cutoff momentum $\hbar k_\perp^c$, which yields the EEL probability $\Gamma^{\rm bulk}(\omega)$ [right panel of Fig. 3(b)]. A clear peak can be observed at the longitudinal optical phonon. This energy-loss peak is slightly asymmetric with a broader tail inside the reststrahlen band compared to that outside the band. Importantly, at energies above LO$_\perp$ no losses are found. This can be understood with the help of the isofrequency curves in Fig. 3(a). For instance, at energy 205 meV (black dashed line, above the upper reststrahlen band) the ellipse does not intersect the blue horizontal line and therefore there is no excitation above the upper band. For energies below TO$_\perp$, the ellipses may intersect or not the blue horizontal line of k_z depending on the particular energy. For instance, at an energy of 160 meV [green dashed line, below the upper reststrahlen band in Fig. 3(a)] the ellipse does not cut $k_z = \omega/(0.1c)$ and therefore there is no excitation induced in that case. However, for other energies the isofrequency surfaces can cut the k_z line, and therefore an anisotropic dielectric mode can be excited [tail below 170 meV in Fig. 3(b)]. We learn from this analysis that the excitation of the phonon polariton modes close to the upper reststrahlen band is highly dependent on the topology (hyperbolic or elliptic) of the isofrequency surfaces.

The dependency of phonon polaritons excitation on the isofrequency surface allows to control the polaritonic modes as we discuss now in Fig. 3(c), where we show the real part of the z component of the total electric field at $\hbar\omega =$ 195 meV (representing the energy within the hyperbolic dispersion regime in the upper reststrahlen band), induced by a fast electron with velocity $v = 0.1c$. A schematic representation of such electron beam trajectory is displayed in the inset of Fig. 3(c). We observe two important features: the formation of a wake pattern and an oscillatory behavior of the field in the z direction. This spatial periodicity is connected with the parallel momentum component ($\hbar k_z = \hbar\omega/v$) transferred by the electron since the observed wavelength along the z axis is $\lambda_z = 2\pi/k_z$. This implies that the wavelength λ_z decreases with increasing energy of the phonon polariton. Furthermore, the direction of the wake pattern is governed by the polariton phase velocity [$\mathbf{v}_p$ parallel to $\mathbf{k}(\omega)$, black arrow]. The outward direction (relative to the electron beam trajectory) of the wavefronts is determined by the sign of the radial component of $\mathbf{v}_p$ relative to the radial component of the energy flow (given by the Pointing vector $\mathbf{S} = \mathbf{E} \times \mathbf{H}$ parallel to the group velocity $\mathbf{v}_g = \nabla_{\mathbf{k}}\omega$ [32–36], magenta arrow). We recognize in Fig. 3(a) that the group and the phase velocities are nearly perpendicular, and their projection onto the radial axis are parallel, leading to a wave propagating away from the electron beam trajectory (positive phase and positive group velocity with respect to the energy propagation direction). It is worth noting that the projection of the group and the phase velocities onto the beam trajectory direction (z direction) leads to negative phase and positive group velocities relative to S_z [Fig. 3(a)].

As pointed out, for each energy $\hbar\omega$, the velocity of the fast electron determines (primarily) the polariton wave vector parallel to the beam trajectory k_z and, consequently, the perpendicular wave vector $k_\perp$ [according to Eq. (3)]. To emphasize the velocity dependency, we perform the same analysis [Figs. 3(d)–3(f)] as in Figs. 3(a)–3(c) but increasing the electron velocity to $v = 0.5c$. In Fig. 3(d) a zoom into the isofrequency curve of Fig. 3(a) is presented, together with the value k_z (horizontal blue line) determined by the electron velocity $v = 0.5c$. The increase of the electron velocity leads to the excitation of 195-meV polaritons with reduced momentum (determined by the intersection of the blue horizontal line and the red isofrequency curve). By calculating the momentum-resolved loss probability $P^{\mathrm{bulk}}(k_\perp;\omega)$ [left panel of Fig. 3(e)] and the EEL probability $\Gamma^{\mathrm{bulk}}(\omega)$ [right panel of Fig 3(e)] we find the same behavior as in Fig. 3(b) for $v = 0.1c$, except for a one order of magnitude reduction in both $k_\perp$ and the magnitude of the loss probability.

The differences in the properties of the phonon polaritons launched by the fast electron at both electron velocities are distinguishable in Fig. 3(f), where we show the real part of the z component of the total electric field induced by the fast electron with $v = 0.5c$ at energy 195 meV. The spatial period λ_z of the polariton is longer compared to that in Fig. 3(c) as a result of the increase in the electron velocity (smaller $\hbar k_z$ transferred). The direction of the wake field is quite similar to that of Fig. 3(c). This behavior is a specific feature of hyperbolic polaritons since the intersection of the blue line both for $v = 0.1c$ and $v = 0.5c$ occurs at the asymptote of the hyperbola which results in polariton wave vectors that have very similar propagation direction but different absolute values.

D. Lower reststrahlen band

In Fig. 4(a) we show the isofrequency curve of h-BN phonon polaritons for an energy in the lower reststrahlen band (red line). Note that the hyperbolas are rotated by 90° as compared to the upper reststrahlen band [see Figs. 3(a) and 3(d)]. However, the momentum $\hbar k_z$ transferred by the fast electron to the phonon polaritons is still given by the crossing of the hyperbolas with the horizontal blue line [representing $k_z = \omega/v$ for $v = 0.1c$ in Fig. 4(a)]. From Eq. (3) we obtain the polariton perpendicular momentum $\hbar k_\perp$, which is shown in Fig. 4(b) as a function of energy $\hbar\omega$ (dashed blue curve). We also plot the momentum-resolved loss probability $P^{\mathrm{bulk}}(k_\perp;\omega)$ for energies within the lower reststrahlen band. Notice that the highest values of $P^{\mathrm{bulk}}(k_\perp;\omega)$ (red and yellow colors in the contour plot) coincide perfectly with the blue dashed curve, demonstrating that the electron energy losses in the lower band are also governed by polariton excitations. However, in contrast to the upper band, we find that the dashed blue curve has a negative slope, $d\omega/dk_\perp < 0$, indicating that the group and the phase velocities are antiparallel (have opposite sign) along the radial direction. We will show below with Fig. 4(c) that the phase velocity in the radial direction is indeed antiparallel (negative) relative to the Poynting vector (energy flow) while the group velocity in the radial direction is parallel (positive), which is a consequence of the phase and group velocity vectors being perpendicular to each other and rotated by 90° compared to the upper reststrahlen band.

To obtain spectroscopic information on the excitations in the lower reststrahlen band, we calculate the EEL probability $\Gamma^{\mathrm{bulk}}(\omega)$ by integration of $P^{\mathrm{bulk}}(k_\perp;\omega)$ in momentum space [right panel in Fig. 4(b)]. Contrary to the upper reststrahlen band, we observe a uniform and relatively small loss probability between $\mathrm{TO}_\parallel$ and $\mathrm{LO}_\parallel$ without the appearance of a sharp peak around $\mathrm{LO}_\parallel$. We explain this finding by (i) the large cutoff momenta ($\hbar k_\perp^c$) imposed by the aperture of the microscope detector and (ii) the relationship between the energy and the transverse momentum of the polaritons in the lower band [see Fig. 4(b), left panel]. Indeed, we observe in Fig. 4(b) that the asymptotic behavior of the blue dashed line tends to $\mathrm{TO}_\parallel$ for large $k_\perp$. This shows that low-energy hyperbolic phonon polaritons, close to $\mathrm{TO}_\parallel$, largely contribute to the energy losses for large $k_\perp^c$ values. Contrary to the upper band, where the high-momenta contribution to the electron energy losses comes from polaritons with high energy, close to

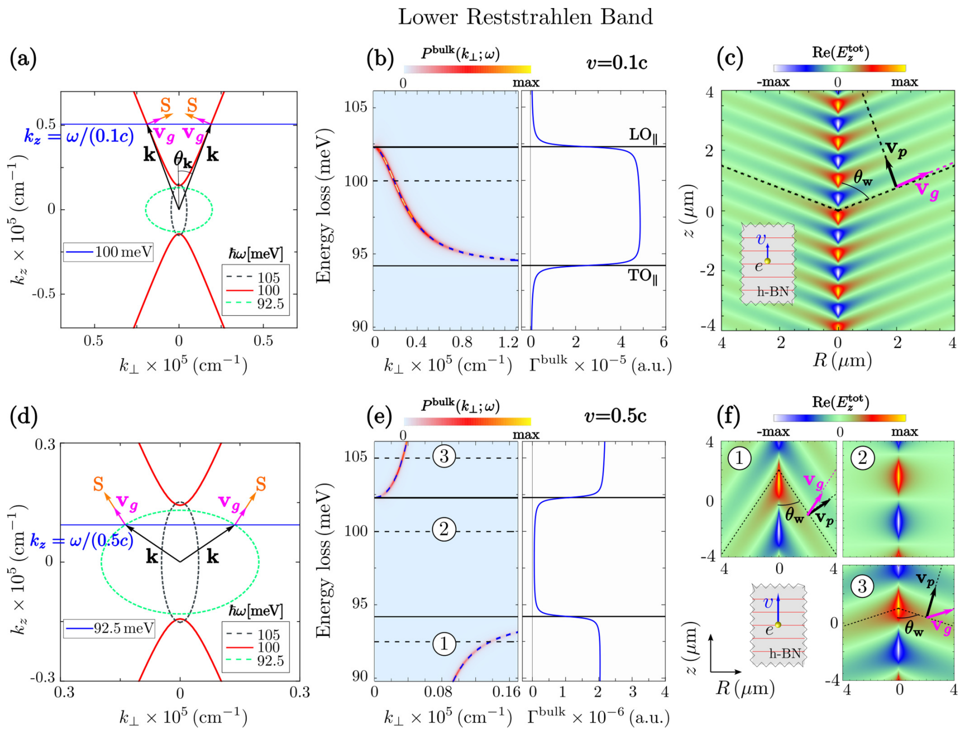

FIG. 4. (a) Isofrequency curves for energies inside (100 meV, red solid line) and outside (92.5 and 105 meV, green and black dashed lines) the lower reststrahlen band plotted for the wave vector k_z against $k_\perp = \sqrt{k_x^2 + k_y^2}$. The horizontal blue line represents the momentum $\hbar k_z = \hbar\omega/(0.1c)$ transferred by the fast electron to the polaritons when it travels along the z direction with velocity $0.1c$. The blue line is evaluated at energy 100 meV. The black arrows represent the polariton wave vector $\mathbf{k}(\omega)$, $\theta_{\mathbf{k}}$ is the angle between $\mathbf{k}(\omega)$ and the k_z axis, the magenta arrows represent the group velocity $\mathbf{v}_g$, and the orange arrows the Poynting vector $\mathbf{S}$. (d) Shows a zoom into (a). In (d) the horizontal blue line represents $k_z = \omega/(0.5c)$ evaluated at energy 92.5 meV. The contour plot (left panel) in (b) shows the momentum-resolved loss probability $P^{\text{bulk}}(k_\perp;\omega)$ normalized to the maximum value (3 a.u) for $v = 0.1c$. The right panel in (b) shows the energy-loss probability $\Gamma^{\text{bulk}}(\omega)$ obtained by integrating $P^{\text{bulk}}(k_\perp;\omega)$ over $k_\perp$ up to $k_\perp^c = 0.05$ Å^{-1}. (e) Same as in (b) but considering $v = 0.5c$. For this case the maximum of $P^{\text{bulk}}(k_\perp;\omega)$ is 2.5 a.u. (c), (f) Depict the real part of the z component of the total electric field induced by the fast electron along the cylindrical coordinates (R, z) for the energies: (c) 100 meV (for $v = 0.1c$) and (f) 92.5, 100, and 105 meV (for $v = 0.5c$). The field plots are normalized to the maximum value in each case: (c) 1×10^{-6} a.u. and (f) 7.5×10^{-8} a.u.. The insets in (c) and (f) illustrate the electron beam trajectory.

$\text{LO}_\perp$ [Fig. 3(b), left panel]. We address the reader to Appendix C where we show $\Gamma^{\text{bulk}}(\omega)$ in the lower reststrahlen band for different $k_\perp^c$ cutoff values.

The excitation of phonon polaritons (within the lower reststrahlen band) by the probing electron can be observed in Fig. 4(c), where we show the real part of the z component of the total electric field induced at energy $\hbar\omega = 100$ meV. Analogously to the upper band, the oscillatory behavior of the field distribution along the z direction is governed by the transferred momentum $\hbar k_z$. Interestingly, the wake pattern is reversed compared to that for the upper reststrahlen band [Figs. 3(c) and 3(f)], i.e., the wavefronts are propagating toward the electron beam [33,37,38]. By plotting the group and phase velocity vectors onto the field plots [magenta and black arrows, respectively; also plotted in Fig. 4(a)], we can clearly recognize that the projections of both vectors onto the radial axis (perpendicular to the electron beam trajectory) are antiparallel. This leads to a negative phase and positive group velocity relative to the Poynting vector direction (which points always away from the electron beam to preserve causality) along the radial axis. The negative phase velocity in the radial direction is a direct result of the phase velocity vector being nearly perpendicular to the Poynting vector, both being rotated by 90° as compared to the upper reststrahlen band [where both phase and group velocities are positive relative to energy propagation in the radial direction, see Figs. 3(c) and 3(f)].

When the velocity of the electron is increased up to 50% the speed of light, the k_z component of the wave vector parallel to the beam trajectory is reduced. In this case, the matching between the red hyperbola and the horizontal blue line is prevented as observed in Fig. 4(d). This mismatch of energy and momentum forbids the excitation of hyperbolic phonon polaritons. However, the blue line intersects the elliptical isofrequency surface of anisotropic bulk phonon polaritons (dielectric) above and below the lower reststrahlen band (black and green dashed curves calculated for 105 and 92.5 meV, respectively). The matching of energy and momentum at the intersections of the elliptical isofrequency surfaces leads to the excitation of the dielectric modes, as demonstrated by calculating the momentum-resolved loss probability $P^{\text{bulk}}(k_\perp;\omega)$ [left panel of Fig. 4(e)]. This loss probability is determined by the relationship between the energy of the elliptical polaritons and the perpendicular momentum component [dashed blue lines, showing $\omega(k_\perp)$ of the elliptical polaritons]. The integration of $P^{\text{bulk}}(k_\perp;\omega)$ in the reciprocal space subsequently yields small energy-loss probabilities outside the reststrahlen band, whereas inside the reststrahlen band the loss probability is negligible due to absence of polariton excitations.

In Fig. 4(f) we show the total electric field induced by the electron beam for energies inside (marked 2) and outside (marked 1 and 3) the lower reststrahlen band. We can observe the formation of wake patterns only for those energies where the dielectric modes are excited (marked as 1 and 3). Importantly, the wake wavefronts propagate outward the beam trajectory as a consequence of the group ($\mathbf{v}_g$) and phase velocities ($\mathbf{v}_p$) being parallel (positive) relative to the Poynting vector in the radial direction [Fig. 4(d)]. We can also notice that the projection of these velocity vectors onto the z direction is positive. This demonstrates that the radial and z projections of $\mathbf{v}_p$ and $\mathbf{v}_g$ for elliptical polaritons are positive, contrary to the hyperbolic regime (reststrahlen bands) where one of the components is negative [Figs. 3(c), 3(f), and 4(c)].

E. Induced wake patterns and Cherenkov radiation

We have shown in Secs. II C [Figs. 3(c) and 3(f)] and II D [Figs. 4(c) and 4(f)] that the field distributions produced by a fast electron traveling through h-BN can exhibit wake patterns. The excitation of these patterns (for energies inside and outside the reststrahlen bands) is connected to the different mechanisms of energy losses experienced by the fast electron in the h-BN. In the following we discuss this connection.

First, it is worth noting that the excitation of the wake fields inside the reststrahlen bands occurs for energies where electron losses appear [compare Fig. 4(c) with the image in Fig. 4(f) labeled as 2]. As we pointed out, the electron energy losses within the reststrahlen bands correspond to the excitation of hyperbolic phonon polaritons. This implies that the wake fields are associated to the excitation of coherent-charge density fluctuations [38–43] in the h-BN, namely, the phonon polaritons.

In contrast to the wake fields inside the reststrahlen bands, the emergence of the wake patterns outside the bands (see Fig. 4, images labeled as 1 and 3) occurs due to a different physical process to that of the excitation of hyperbolic phonon polaritons. Outside the reststrahlen bands the h-BN dielectric function is purely dielectric and thus the electron energy losses correspond to the radiation emitted by the electron when it passes through the medium with velocity larger than the speed of light (in the h-BN). This mechanism is known as Vavilov-Cherenkov radiation [44–51]. We have confirmed that the losses in this energy range are present even in the absence of damping in the material (not shown), confirming that the losses are due to Cherenkov radiation in this case. This only happens for electron velocities which fulfill

$$v > \frac{c}{\sqrt{\varepsilon_\perp}}, \tag{15}$$

being consistent with the condition for excitation of Cherenkov radiation [52,53].

Finally, one can also note that the excitation of the wake fields in the lower reststrahlen band depends on the electron velocity [compare Figs. 4(c) and 4(f) label 2]. Indeed, for energies in the lower band one can deduce from Eqs. (11)–(12) that the wake patterns appear under the following condition:

$$\frac{\varepsilon_\parallel}{\varepsilon_\perp} < \frac{v^2}{c^2}\varepsilon_\parallel \quad \text{or equivalently} \quad v < \frac{c}{\sqrt{\varepsilon_\perp}}, \tag{16}$$

where only the real part of the dielectric function is considered. Interestingly, one can observe that the velocity of the fast electron fulfills different conditions for the appearance of wake patterns in different energy ranges [compare Eqs. (15) and (16)]. This difference is a direct consequence of the distinct physical processes in the excitation of the wake fields.

The different nature of the excitation of the wake fields outside and inside the reststrahlen bands is also reflected in the angle $\theta_{\text{w}} = 90^\circ - \theta_{\mathbf{k}}$ that the wake patterns sustain with respect to the electron beam trajectory. An analysis of this angle and its relationship with Eqs. (15) and (16) is developed at the end of Appendix D.

F. Asymmetric wake patterns induced by tilting the electron beam trajectory

As we pointed out in the last sections, the excitation of hyperbolic phonon polaritons can be controlled by the velocity of the fast electrons. In the following, we study how steering of phonon polaritons can be controlled via the angle α between the electron beam trajectory and the h-BN optical axis.

When the electron travels at an angle α relative to the h-BN optical axis (illustrated in Fig. 5), the condition for the conservation of energy and momentum given by Eq. (8) in the nonrecoil approximation ($\mathbf{k}\cdot\mathbf{v} = k_y v_y + k_z v_z = \omega$) is represented by an inclined plane in momentum space [blue planes in Figs. 6(a) and 6(d)]. The magnitude of the momentum transferred by the electron to the phonon polaritons (along the beam trajectory given by $\hat{\mathbf{v}}$) is still given by $\hbar k_{\hat{\mathbf{v}}} = \hbar\omega/v$. The polariton wave vector can be obtained from the intersection between the blue plane $\mathbf{k}\cdot\mathbf{v} = \omega$ and the isofrequency

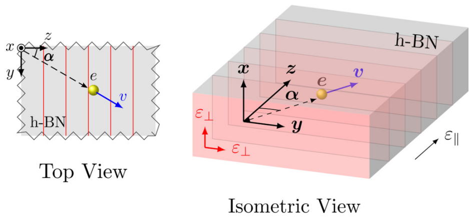

FIG. 5. Schematics of the electron traveling through the h-BN with velocity $\mathbf{v} = v(0, \sin\alpha, \cos\alpha)$ at an angle α with respect to the optical (z) axis of h-BN.

surfaces [red hyperboloids in Figs. 6(a) and 6(d)]. Interestingly, we observe that the intersections are not cylindrically symmetric with respect to the k_z axis [Figs. 6(a) and 6(d)]. This implies that the polaritonic wave will propagate asymmetrically with respect to the electron beam trajectory. Indeed, depending on the direction of propagation, the intersection between the blue planes and the red hyperboloids in Figs. 6(a) and 6(d) will occur at wave vectors $\mathbf{k}^{(1)}$ and $\mathbf{k}^{(2)}$ whose z component can be the same (symmetrical case) or different (asymmetrical case). To better understand the different asymmetries in the propagation of the polaritonic wave we refer the reader to Appendix D, where we show the intersection of the blue plane and the red hyperboloids [Figs. 6(a) and 6(d)] for selected directions of the wave vector. Notice that the symmetric case is similar to the one we discussed in Secs. II C and II D. Therefore, we will focus here on the analysis of the polariton propagation direction which shows the largest asymmetry, that is, the k_yk_z plane.

We show in Fig. 6(a) the plane $\mathbf{k}\cdot\mathbf{v} = \omega$ for $v = 0.1c$ (blue surface) and the isofrequency hyperboloid (red surface) for a representative energy in the upper reststrahlen band ($\hbar\omega = 180$ meV). In Fig. 6(b), we plot the projection of the intersection between the blue plane and the red hyperboloid in the k_yk_z plane. The blue dashed line represents the electron beam trajectory and the black dashed line the k_z axis. One can notice that the matching between the blue solid line and the red hyperbola [Fig. 6(b)] occurs at wave vectors $\mathbf{k}^{(1)}$ and $\mathbf{k}^{(2)}$ whose z component is different. Thus, the projections onto the z axis of the phase velocities $\mathbf{v}_p^{(1)}$ and $\mathbf{v}_p^{(2)}$ (parallel to $\mathbf{k}^{(1)}$ and $\mathbf{k}^{(2)}$, black arrows) are also different. Due to the hyperbolic shape of the isofrequency curve the z component of the group velocities $\mathbf{v}_g^{(1)}$ [parallel to the Poynting vector $\mathbf{S}^{(1)}$, right orange arrow in Fig. 6(b)] and $\mathbf{v}_g^{(2)}$ [parallel to the Poynting vector $\mathbf{S}^{(2)}$, left orange arrow in Fig. 6(b)] are also asymmetric. This difference (asymmetry) in the components of the two phase and group velocities leads to a highly asymmetric propagation of the polaritonic wave with respect to the electron beam trajectory.

The dependency of the polaritonic waves on the angle α can be observed in Fig. 6(c), where we plot the real part of the z component of the total electric field produced by the fast electron at energy $\hbar\omega = 180$ meV and $v = 0.1c$ when $\alpha = 20^\circ$ and 45°. Similar to the parallel trajectory (Secs. II C and II D), one can notice the formation of wake patterns and the spatial periodicity of the field along the electron beam trajectory. This periodicity is determined by the momentum transferred along the beam trajectory ($\hbar k_{\hat{\mathbf{v}}} = \hbar\omega/v$) since the corresponding wavelength is $\lambda_{\hat{\mathbf{v}}} = 2\pi/k_{\hat{\mathbf{v}}}$. Thus, the higher the energy of the polariton is, the smaller $\lambda_{\hat{\mathbf{v}}}$ will be. The wake patterns formed by the field distribution are clearly asymmetric with respect to the beam trajectory. We observe [Fig. 6(c)] that the wake fields exhibit largest asymmetry as α is increased from 20° [Fig. 6(c), left panel] to 45° [Fig. 6(c), right panel]. This is a direct consequence on how the electron transfers different momentum components $\hbar k_y$ and $\hbar k_z$ to the polaritonic excitation [see Fig. 6(b)]. One can notice from Fig. 6(b) that as α is increased, $k_z^{(1)} \approx 0$ and $\mathbf{k}^{(2)}$ tends to the asymptote of the red hyperbola. Therefore, for large angles α the polaritonic wave will propagate relative to the beam trajectory with a phase velocity close to zero on one side of the beam trajectory and with a non-zero phase velocity on the other side of the beam trajectory. These findings explain the tilting of the wavefronts in Fig. 6(c) for $\alpha = 45^\circ$ at the left side of the electron beam. It is worth noting that Fig. 6(c) corresponds to the propagation of the polaritonic wave in the yz plane. However, for other propagation directions, the field distributions will be different.

In Figs. 6(d)–6(f) we show the same analysis (electron beam trajectory tilted an angle α with respect to the h-BN optical axis) for a representative energy within the lower reststrahlen band (100 meV). Importantly, for this case the projections onto the y axis of the phase velocities $\mathbf{v}_p^{(1)}$ and $\mathbf{v}_p^{(2)}$ are antiparallel (negative) to the y component of the Poynting vectors $\mathbf{S}^{(1)}$ and $\mathbf{S}^{(2)}$. This yields an asymmetric wave propagating with negative phase velocity [Fig. 6(f)].

Additionally, the electron velocity v allows to control the momentum transfer by the fast electron to the phonon polaritons [Eq. (8)]. Indeed, one can obtain the relationship between v and the excitation of the asymmetric wake patterns by analyzing the wake angles $\theta_{\mathrm{w}}^{(1)} = 90^\circ - \theta_{\mathbf{k}}^{(1)}$ and $\theta_{\mathrm{w}}^{(2)} = 90^\circ - \theta_{\mathbf{k}}^{(2)}$ [Figs. 6(c) and 6(f)]. We refer the reader to Appendix D where we derived this relationship. For completeness, we show in Appendix E the electron energy losses experienced by a fast electron traveling through h-BN in tilted trajectories with respect to the h-BN optical axis.

We have found that the excitation of the polaritonic wave is highly dependent on the orientation of the electron beam trajectory with respect to the h-BN crystallographic arrangement. Thus, while the speed of the electron serves as a means to excite the polaritonic wave or not, the orientation of the electron beam trajectory can serve to control the direction of the polaritonic excitation.

III. EXCITATION OF DYAKONOV SURFACE PHONON POLARITONS IN H-BN BY A LOCALIZED BEAM OF FAST ELECTRONS

We next study the EELS signal when the electron beam is traveling above an h-BN semi-infinite surface. The interface between vacuum and h-BN lies on the yz plane, as depicted in Fig. 7, with the y axis in the direction of $\varepsilon_\perp$ and the z axis in the direction of the h-BN optical axis. The electron travels in vacuum at a distance x_0 from the surface (we will refer to this distance as the impact parameter) with velocity

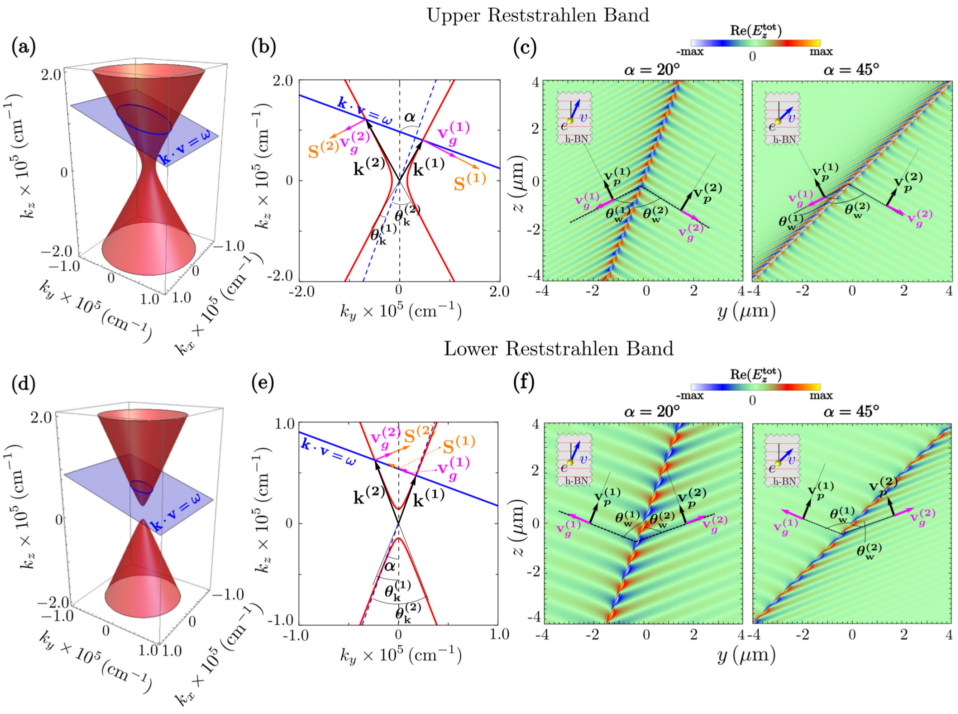

FIG. 6. Isofrequency surfaces for (a) the upper and (d) the lower reststrahlen bands for representative energies in each band: (a) 180 meV and (d) 100 meV. The blue inclined plane represents the condition for the conservation of energy and momentum in the nonrecoil approximation: $\mathbf{k} \cdot \mathbf{v} = \omega$ for an electron with $v = 0.1c$ and $\alpha = 20^\circ$. Panels (b) and (e) next to each hyperboloid depict the intersection between the blue plane and the hyperboloids in the $k_y k_z$ plane. In these projections, the black arrows represent the two wave-vector solutions $\mathbf{k}^{(1)}$, $\mathbf{k}^{(2)}$ with angles $\theta_{\mathbf{k}}^{(1)}$, $\theta_{\mathbf{k}}^{(2)}$ with respect to the beam trajectory (blue dashed line), the magenta arrows represent the group velocities $\mathbf{v}_g^{(1)}$, $\mathbf{v}_g^{(2)}$ and the orange arrows the Poynting vectors $\mathbf{S}^{(1)}$, $\mathbf{S}^{(2)}$. The contour plots in (c) and (f) show the normalized real part of the z component of the total electric field in the yz plane for the energies: (c) 180 meV and (f) 100 meV. We plot the field distributions for two different angles of the electron beam trajectory: 20° (left panels) and 45° (right panels). The maximum values of the field plots are (c) 4×10^{-6} a.u. and (f) $>1.5 \times 10^{-6}$ a.u.

v parallel to the optical axis of the h-BN. A schematic representation of the probing electron-surface system is shown in Fig. 7.

Surfaces of uniaxial materials with optical axis parallel to the surface support a specific kind of surface waves, the so-called Dyakonov waves [54,55]. When either $\varepsilon_\perp$ or $\varepsilon_\parallel$ is negative (as in the case of the reststrahlen bands in h-BN), Dyankonov surface polaritons [56] can propagate along the surface. Recently, Dyakonov surface phonon polaritons have been observed by scattering-type scanning near-field optical microscopy (s-SNOM) at the edges of h-BN flakes [14,57] as well as by STEM-EELS [20,58]. In the latter experiments, the probing electrons were passing outside the flake edge in a perpendicular trajectory. However, the excitation and detection of Dyakonov surface phonon polaritons with an electron beam parallel to an extended surface has not been described yet.

In the following, we first describe the Dyakonov surface phonon polariton modes that exist at the interface between h-BN and vacuum. We then show that a localized beam of fast electrons can couple to these polaritons and we analyze the corresponding EEL spectra and their polariton wake patterns. Importantly, we find that surface Dyakonov phonon polaritons are excited only in the upper reststrahlen band. Therefore, our analysis and calculations are restricted to this energy range.

A. Surfaces modes in h-BN

According to Dyakonov's theory [54], the interface described in Fig. 7 supports electromagnetic waves that propagate along it and their associated electromagnetic fields decay exponentially perpendicular to the interface [54,55,59,60]. These surface waves can be expressed as a linear superposition of the four following modes propagating along the

C. MACIEL-ESCUDERO *et al.* PHYSICAL REVIEW B **102**, 115431 (2020)

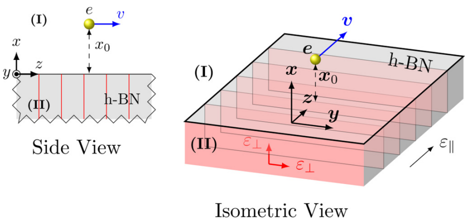

FIG. 7. Schematics of the probing electron traveling with velocity v at a distance x_0 parallel to a h-BN surface. The optical axis of the h-BN crystal lattice is parallel to the h-BN surface. Label I refers to vacuum, while label II refers to h-BN.

interface: (i) a transverse electric (TE) mode, (ii) a transverse magnetic (TM) mode (the corresponding fields decay into the vacuum, upper half space in Fig. 7 labeled I), (iii) an ordinary mode, and (iv) an extraordinary mode (the corresponding fields decay exponentially into h-BN, lower half space in Fig. 7 labeled II). Following this scheme the electric field in each media can be written as

$$\mathbf{E}_{\mathrm{I}}(x>0,y,z) = (\mathbf{A}_{\mathrm{TE}}+\mathbf{A}_{\mathrm{TM}})e^{-\kappa_{\mathrm{I}}x}e^{i(k_y y+k_z z)}, \quad (17a)$$

$$\mathbf{E}_{\mathrm{II}}(x<0,y,z) = (\mathbf{A}_{\mathrm{o}}e^{\kappa^o_{\mathrm{II}}x}+\mathbf{A}_{\mathrm{e}}e^{\kappa^e_{\mathrm{II}}x})e^{i(k_y y+k_z z)}, \quad (17b)$$

where harmonic dependency in time has been assumed, and $\mathbf{A}_{\mathrm{TE}}, \mathbf{A}_{\mathrm{TM}}, \mathbf{A}_{\mathrm{o}}, \mathbf{A}_{\mathrm{e}}$ are the amplitudes of each aforementioned mode. The wave vector of each mode is given by

$$\mathbf{k}_d = (i\kappa_{\mathrm{I}}, k_y, k_z) \quad \text{TE, TM}, \quad (18a)$$

$$\mathbf{k}_o = \left(-i\kappa^o_{\mathrm{II}}, k_y, k_z\right) \quad \text{ordinary}, \quad (18b)$$

$$\mathbf{k}_e = \left(-i\kappa^e_{\mathrm{II}}, k_y, k_z\right) \quad \text{extraordinary}, \quad (18c)$$

where $\kappa_{\mathrm{I}}, \kappa^o_{\mathrm{II}}, \kappa^e_{\mathrm{II}} > 0$ and $k_y, k_z \in \mathbb{C}$ need to fulfill the following conditions:

$$\kappa_{\mathrm{I}}^2 = k_y^2 + k_z^2 - (\omega/c)^2 \quad \text{vacuum}, \quad (19a)$$

$$\left(\kappa^o_{\mathrm{II}}\right)^2 = k_y^2 + k_z^2 - \varepsilon_\perp(\omega/c)^2 \quad \text{ordinary}, \quad (19b)$$

$$\left(\kappa^e_{\mathrm{II}}\right)^2 = k_y^2 + \frac{\varepsilon_\parallel}{\varepsilon_\perp}k_z^2 - \varepsilon_\parallel(\omega/c)^2 \quad \text{extraordinary}. \quad (19c)$$

Applying boundary conditions imposed by Maxwell's equations at the interface between vacuum and h-BN, one obtains the following relationship [54,60,61]:

$$\left(\kappa_{\mathrm{I}}+\kappa^e_{\mathrm{II}}\right)\left(\kappa_{\mathrm{I}}+\kappa^o_{\mathrm{II}}\right)\left(\kappa_{\mathrm{I}}+\varepsilon_\perp\kappa^e_{\mathrm{II}}\right) = (\omega/c)^2(\varepsilon_\parallel-1)(1-\varepsilon_\perp)\kappa_{\mathrm{I}}, \quad (20)$$

which together with the set of Eqs. (19a)–(19c) determines the in-plane wave vector (k_y, k_z) of the Dyakonov waves.

It is worth noting that Dyakonov's original work [54] was derived for positive $\varepsilon_\perp$ and $\varepsilon_\parallel$. However, Eq. (20) is still valid when $\varepsilon_\perp < 0$ and $\varepsilon_\parallel > 0$ [59,61]. Since negative values in the real part of the dielectric components support the excitation of polaritonic states, Dyakonov surface waves sustained in h-BN in the mid-infrared region are thus called Dyakonov surface phonon polaritons.

In Fig. 8 we plot the isofrequency contour (red curve) of the h-BN surface polariton for an energy within the upper reststrahlen band (193 meV), obtained from Eqs. (19a)–(19c) and (20). For comparison, we show a cut (k_yk_z plane) of the isofrequency surface of the hyperbolic volume polariton [black dashed line obtained from Eq. (3)]. We find that the isofrequency curve of the surface polariton is a hyperbola, similar to that of the volume polariton particularly for small momenta. At large momenta, on the other hand, the opening angle of the isofrequency contour of the surface polariton θ_s is smaller than that of the volume polariton θ_v, demonstrating that the dispersion of Dyakonov phonon polaritons is different to the one obtained for the bulk hyperbolic phonon polaritons.

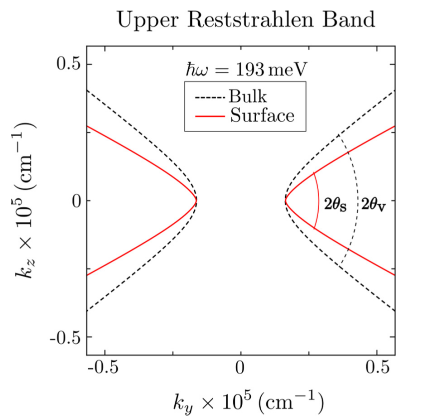

FIG. 8. The red solid hyperbola represents the isofrequency curve obtained with Eqs. (19a)–(19c) and (20) for the surface phonon polariton, while the black dashed hyperbola represents the isofrequency curve obtained using Eq. (3) (setting $k_x = 0$) for the bulk phonon polariton. Both curves are calculated for a representative energy in the upper reststrahlen band, 193 meV.

B. Electron energy-loss probability

The excitation of Dyakonov surface phonon polaritons by fast electron beams can be revealed by the electron energy-loss spectra. In the following we describe the strategy to obtain the momentum-resolved loss probability $P^{\mathrm{surf}}(k_y;\omega)$ and the EEL probability $\Gamma^{\mathrm{surf}}(\omega)$, when the probing electron travels above the h-BN surface (see Fig. 7).

To calculate $\Gamma^{\mathrm{surf}}(\omega)$, following Eq. (6), one needs to obtain the induced electric field $\mathbf{E}^{\mathrm{ind}}(\mathbf{r}_e;\omega)$ along the electron beam trajectory. To that end we obtain $\mathbf{E}^{\mathrm{ind}}(\mathbf{r};\omega)$ by solving Maxwell's equations in the presence of vacuum–h-BN interface, assuming that the electron travels in vacuum with constant velocity v and impact parameter x_0 (Fig. 7). Considering the boundary conditions at the interfaces ($x = 0$), one finds the induced electric field in vacuum (region I in Fig. 7):

$$\mathbf{E}^{\mathrm{ind}}_{\mathrm{I}}(x,k_y,k_z;\omega) = (b_{\mathrm{I}}, d_{\mathrm{I}}, g_{\mathrm{I}})\,\tilde{\rho}\,e^{-\kappa_{\mathrm{I}}x}, \quad (21)$$

with $b_{\mathrm{I}}, d_{\mathrm{I}}, g_{\mathrm{I}}$ being the coefficients involving the dielectric functions at both sides of the interface and $\tilde{\rho} = -2\pi e\delta(\omega - k_z v)e^{-\kappa_{\mathrm{I}}x_0}/\varepsilon_0$. We refer to Appendices F and G for a detailed

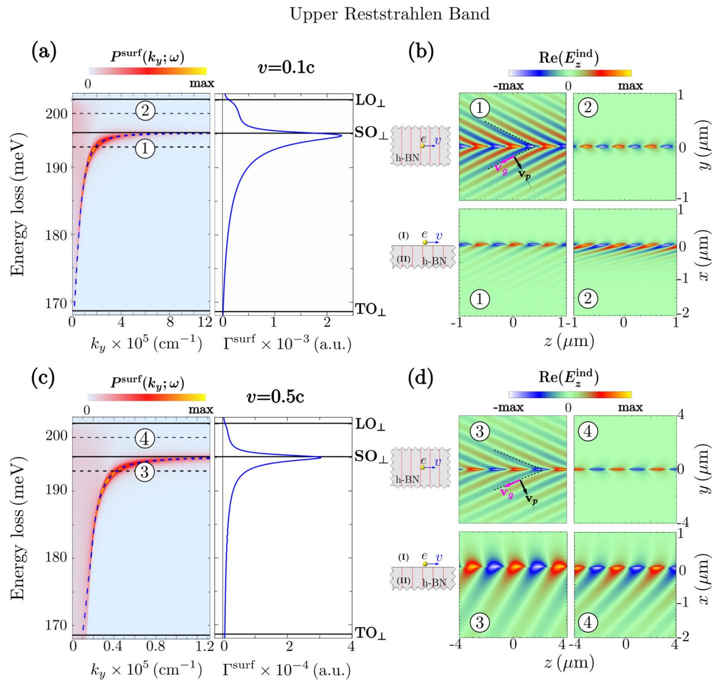

FIG. 9. The left panel in (a) displays the momentum-resolved loss probability $P^{\rm surf}(k_y;\omega)$ normalized to the maximum value (3 a.u.) in the vicinity of the upper reststrahlen band for $x_0 = 10$ nm and $v = 0.1c$. The right panel in (a) shows the EEL probability $\Gamma^{\rm surf}(\omega)$ obtained by integrating $P^{\rm surf}(k_y;\omega)$ over k_y up to $k_y^c = 0.09$ Å^{-1}. (c) Same as in (a) but considering $v = 0.5c$. For this case the maximum value of the momentum-resolved loss probability is 1 a.u. The color maps in (b) and (d) show the real part of the z component of the induced electric field for the energies: 193 (marked 1, 3) and 198 meV (marked 2, 4). The top panels in (b) and (d) correspond to the in-plane views (yz plane) of the induced field, while the bottom panels correspond to the out-of-plane views (xz plane). The field plots are normalized with respect to the maximum value in each case. For the top panels the maximum values are (b.1) 1×10^{-4} a.u., (b.2) 7.5×10^{-5} a.u., (d.3) 7.5×10^{-6} a.u., and (d.4) 5×10^{-6} a.u. For the bottom panels the maximum values are (b.1) 4×10^{-5} a.u., (b.2) 2×10^{-5} a.u., and (d) 1.5×10^{-6} a.u.

description of the coefficients of the total and induced electric fields at each half-space (vacuum and h-BN).

By Fourier transforming $\mathbf{E}_{\rm I}^{\rm ind}(x, k_y, k_z; \omega) \mapsto \mathbf{E}_{\rm I}^{\rm ind}(\mathbf{r}; \omega)$ in Eq. (21) and inserting its value into Eq. (6), we find that $\Gamma^{\rm surf}(\omega)$ can be written as

$$\Gamma^{\rm surf}(\omega) = \int_0^{k_y^c} dk_y\, P^{\rm surf}(k_y;\omega), \tag{22}$$

where

$$P^{\rm surf}(k_y;\omega) = -\frac{e^2}{\pi^2 \varepsilon_0 \hbar \omega v} {\rm Re}[g_{\rm I}\, e^{-2\kappa_{\rm I} x_0}]|_{k_z=\omega/v} \tag{23}$$

is the probability that the electron transfers a transverse momentum $\hbar k_y$ (y component of the momentum) upon losing energy $\hbar\omega$. Notice that the z component of the wave vector in $P^{\rm surf}(k_y;\omega)$ is fixed by $k_z = \omega/v$, implying that the electron still transfers a parallel momentum equal to $\hbar\omega/v$. The integration of Eq. (22) is performed up to the cutoff value k_y^c, which is determined by the aperture of the EELS detector.

As we discussed in Sec. II, the spectrum of the momentum-resolved loss probability and the EEL probability provides information on the properties of the excited modes in the anisotropic medium. We thus show in the following the relationship between these two quantities and the excitation of Dyakonov surface phonon polaritons.

C. Excitation of surface phonon polaritons

As pointed out above, the parallel momentum $\hbar k_z$ transferred by the fast electron to the phonon polaritons is determined by the relation $k_z = \omega/v$. Similarly to the bulk analysis of Sec. II, this relationship represents a horizontal line in the $k_y k_z$ representation of Fig. 8. Thus, the transferred momentum can be determined by the crossing between this horizontal line ($k_z = \omega/v$) and the isofrequency hyperbolas obtained from Eqs. (19a)–(19c) and (20). From the latter equations one can further obtain the relationship between the y component of the polariton wave vector (k_y) and $\hbar\omega$, which is shown in the left panel of Fig. 9(a) (dashed blue curve). We also plot the momentum-resolved loss probability $P^{\text{surf}}(k_y;\omega)$ for energies around the upper reststrahlen band. The probing electron is traveling above the h-BN surface with an impact parameter of 10 nm and velocity $v = 0.1c$. Some similarities between $P^{\text{surf}}(k_y;\omega)$ and $P^{\text{bulk}}(k_\perp;\omega)$ [Fig. 3(b), left panel] become apparent. For instance, the highest values of $P^{\text{surf}}(k_y;\omega)$ [red and yellow colors in Fig. 9(a)] coincide perfectly with the blue dashed curve, demonstrating that the electron energy losses in the upper band are caused mainly due to the excitation of hyperbolic phonon polaritons. However, by comparing Figs. 3(b) and 9(a) we recognize that the asymptotic behavior (at large momenta) of $P^{\text{surf}}(k_y;\omega)$ occurs at a lower energy compared to the asymptotic behavior of $P^{\text{bulk}}(k_\perp;\omega)$. While $P^{\text{bulk}}(k_\perp;\omega)$ tends to the $\text{LO}_\perp$ phonon energy, $P^{\text{surf}}(k_y;\omega)$ tends to the surface optical ($\text{SO}_\perp$) phonon energy given by the condition $\varepsilon_\perp(\omega_{\text{SO}_\perp}) = -1$ [derived from Eqs. (19a)–(19c) and (20) for large momenta]. Importantly, the latter is a fingerprint of the excitation of surface polariton modes. In our case (electron traveling in vacuum above the h-BN surface) these surface modes correspond to Dyakonov surface phonon polaritons. We confirm this by integrating $P^{\text{surf}}(k_y;\omega)$ over k_y up to a cutoff momentum $\hbar k_y^c$, which yields the EEL probability $\Gamma^{\text{surf}}(\omega)$ [right panel of Fig. 9(b)]. A clear peak can be observed at the $\text{SO}_\perp$ phonon energy. This loss peak is slightly asymmetric with a broader tail for lower energies in the reststrahlen band compared to that for larger energies in the band. Notice that for energies above $\text{SO}_\perp$ the loss spectrum displays a shoulder arising from background losses present in the entire upper band at small momentum [red blurred area for small momentum in the left panel of Fig. 9(a)].

The excitation of Dyakonov surface phonon polaritons (within the upper reststrahlen band) by the probing electron can be observed in real space in Fig. 9(b), where we show the real part of the z component of the induced electric field at energies 193 meV (marked as 1) and 198 meV (marked as 2). The top panels correspond to the evaluation of $\text{Re}[E_z^{\text{ind}}(\mathbf{r};\omega)]$ in the yz plane (in plane at the interface), and the bottom panels to the evaluation in the xz plane (lateral view, containing the electron trajectory). One can recognize from the in-plane views [Fig. 9(b) marked as 1] the formation of wake patterns and the oscillatory behavior of the induced field in the z direction. Similarly to the field distribution shown in Fig. 3(c), the spatial periodicity along the z direction is connected with the parallel wave vector component $k_z = \omega/v$ since $\lambda_z = 2\pi/k_z$. Moreover, the wake wavefronts show interesting propagation patterns both in the transverse direction from the beam trajectory as well as into the h-BN.

In the top panel of Fig. 9(b) (image labeled as 1), the wavefronts along the y direction propagate with positive phase and group velocities relative to the Poynting vector. Indeed, we find that the dashed blue curve in Fig. 9(a) has a positive slope ($d\omega/dk_y > 0$), indicating that the projections onto the y axis of the group and phase velocities are parallel (positive). We also notice that Dyakonov surface phonon polaritons are confined to the interface with penetration of the field into the h-BN interface [Fig. 9(b), bottom image labeled as 1]. For energies larger than that of the $\text{SO}_\perp$ phonon, Dyakonov surface phonon polaritons are not excited [Fig. 9(b), image labeled as 2]. Thus, the induced field distributions for those energies correspond to the reflection of the electron electromagnetic field at the h-BN surface [Fig. 9(b), top image labeled as 2]. We can also notice that the field penetrates into the h-BN [bottom panels of Fig. 9(b)], which is connected with the presence of the red blurred region corresponding to the losses appearing for lower momenta in Fig. 9(a) (left panel).

When the velocity of the probing electron is increased up to 50% the speed of light, the momentum parallel to the beam trajectory $\hbar k_z$ is reduced and so does the k_y component of the Dyakonov surface phonon polariton. By calculating the momentum-resolved loss probability $P^{\text{surf}}(k_y;\omega)$ [left panel of Fig. 9(c)] and the EEL probability $\Gamma^{\text{surf}}(\omega)$ one obtains a similar behavior as in Fig. 9(a) for $v = 0.1c$, except for a one order of magnitude reduction of both k_y and the value of the loss probability.

The differences in the properties of the Dyakonov surface phonon polaritons launched by the fast electron beam can be observed in Fig. 9(d), where we show the real part of the z component of the induced electric field for $v = 0.5c$ at energies 193 and 200 meV. Notice that the spatial periodicity λ_z of the polariton is longer in this situation compared to that in Fig. 9(b) as a result of the increased electron velocity. Also, the penetration of the field into the h-BN medium is larger compared to that in Fig. 9(b). This increase in the penetration depth can be attributed to the increase of the background losses present in the entire upper band [blurred red are in the left panel of Fig. 9(c)].

For completeness and similar to the analysis presented above, we study in Appendix H the excitation of phonon polaritons in the lower reststrahlen band by a fast electron traveling in aloof trajectory. In the Appendix we show the momentum-resolved loss probability [$P^{\text{surf}}(k_y;\omega)$], the EEL probability [$\Gamma^{\text{surf}}(\omega)$], and the wake patterns for this energy range.

IV. REMOTE EXCITATION OF BULK PHONON POLARITONS

We have shown in Figs. 9(b) and 9(d) that the electric field penetrates into the bulk of the h-BN semi-infinite surface, which is surprising, as one does not expect the excitation of volume modes in isotropic materials for electron beam trajectories outside the material. By comparing the angles of the wake patterns, we demonstrate that indeed volume modes are excited in h-BN with external beam trajectories.

We first calculated the angle θ_{w} of the wake wavefronts produced by the fast electron traveling through bulk h-BN with $v = 0.5c$ at $\hbar\omega = 193$ meV [Figs. 10(a) and 10(c)], obtaining a value of $\theta_{\text{w}} = 32.35°$. We compare θ_{w} with the angles of the wake wavefronts produced by the fast electron traveling in an aloof trajectory 10 nm above the h-BN surface [Figs. 10(b) and 10(d)]. From this comparison we find that (i) the angle $\theta_{\text{w}_\text{s}} = 24.67°$ of the wake pattern at the h-BN surface [Fig. 10(b)] is different from θ_{w}, and (ii) the angle of the wake pattern excited inside the h-BN is the same as θ_{w} [Fig. 10(d)]. This implies that volume modes are excited by the fast electron traveling in trajectories outside the anisotropic medium.

Importantly, these findings open the possibility of remotely exciting volume phonon polaritons. In contrast to isotropic

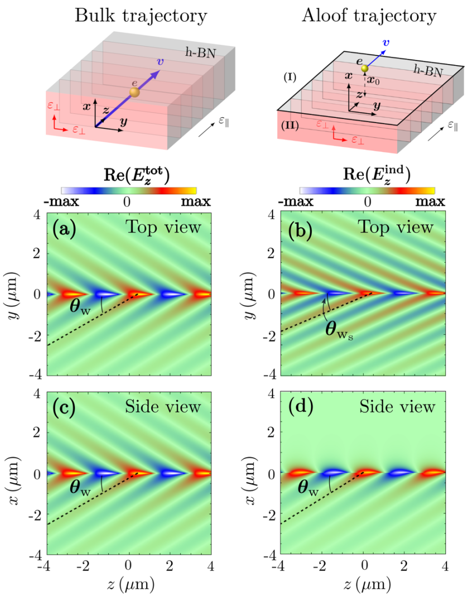

FIG. 10. (a) Real part of the z component of the total electric field in the yz plane produced by a fast electron traveling through h-BN parallel to its optical axis. (c) Shows Re(E_z^{tot}) evaluated in the xz plane and θ_w is the angle between the z axis and the wake patterns formed by the bulk polariton. (b) Shows the real part of the z component of the induced electric field in the yz plane produced by a fast electron traveling in vacuum 10 nm above a semi-infinite h-BN surface. (d) Shows Re(E_z^{ind}) evaluated in the xz plane and θ_{w_s} is the angle between the z axis and the wake patterns formed by the Dyakonov surface phonon polariton. We used for the calculation of the fields an electron velocity equal to $v = 0.5c$ at energy $\hbar\omega = 193$ meV. The field plots are normalized with respect to the maximum value in each case: (a) 5×10^{-7} a.u., (b) 7.5×10^{-6} a.u., (c) 5×10^{-7} a.u., and (d) 1.5×10^{-6} a.u. The insets above (a) and (b) illustrate the geometry under consideration for each case.

materials, where an aloof electron beam only couples to surface modes, for anisotropic materials the energy and momentum matching between the electron and the polaritons allows for launching of bulk excitations.

V. SUMMARY

We have thoroughly analyzed the excitation of optical phonon polaritons in hexagonal boron nitride by focused electron beams for two relevant situations: when the electron travels through the h-BN bulk and when it travels in vacuum above a semi-infinite h-BN surface. For the bulk situation, we have observed that the electron couples to volume phonon polaritons. We demonstrated that the excitation of these polaritonic modes is strongly dependent on the electron velocity and on the angle between the optical axis of h-BN and the trajectory of the electron beam. Furthermore, we have shown that Dyakonov surface phonon polaritons can be excited by a fast electron traveling above the h-BN surface. Interestingly, aloof electron beams are capable of exciting volume polaritons in the h-BN.

By a detailed mode analysis, we showed that the electron beam transfers a specific momentum to the modes. This momentum transfer determines the properties of the excited phonon polaritons, and thus controls their phase and group velocities, as well as their propagation direction. Importantly, we found that the propagation of the polaritonic waves is highly asymmetric with respect to the electron beam trajectory when the trajectory sustains an angle relative to the h-BN optical axis.

Our findings may offer a way to steer and control the propagation of the polaritonic waves excited in hyperbolic materials. Although we studied the specific material h-BN, our findings can be generalized and can serve as a guide for the correct interpretation of the different excited modes and loss channels encountered in EELS experiments of uniaxial materials.

ACKNOWLEDGMENTS

C.M.-E. thanks Á. Nodar for his help in the parallelization of the programming codes. J.A. and R.H. acknowledge Grant No. IT1164-19 for research groups of the Basque University system from the Department of Education of the Basque Government. R.H. further acknowledges financial support from the Spanish Ministry of Science and Innovation (national Project No. RTI2018-094830-B-100 and the Project No. MDM-2016-0618 of the María de Maeztu Units of Excellence Program). J.A. acknowledges financial support from the Spanish Ministry of Science and Innovation (national Project No. PID2019-107432GB-I00).

APPENDIX A: h-BN DIELECTRIC FUNCTION

The two components of the h-BN dielectric function can be described by a Drude-Lorentz model as [12]

$$\varepsilon(\omega) = \varepsilon_\infty\left(1 + \frac{\omega_{LO}^2 - \omega_{TO}^2}{\omega_{TO}^2 - \omega^2 - i\omega\gamma}\right), \qquad (A1)$$

with $\hbar\omega_{LO}$, $\hbar\omega_{TO}$ the phonon LO, TO energies, respectively, ε_∞ is the high-frequency dielectric permittivity, and γ is the damping constant. The values used for each constant are presented in Table I.

TABLE I. Parameters used for the in-plane and out-of-plane dielectric components within the Drude-Lorentz model taken from [14].

	In plane ($\varepsilon_\perp$)	Out of plane ($\varepsilon_\parallel$)
ε_∞	4.90	2.95
$\hbar\omega_{TO}$	168.6 meV	94.2 meV
$\hbar\omega_{LO}$	200.1 meV	102.3 meV
γ	0.87 meV	0.25 meV

APPENDIX B: GREEN'S TENSOR DECOMPOSITION IN AN ANISOTROPIC MEDIUM

In this work we use the following Fourier transform convention:

$$\hat{\mathbf{F}}(\mathbf{k};\omega) = \int_{-\infty}^{\infty} dt \int_V d^3\mathbf{r}\,\mathbf{F}(\mathbf{r};t)\,e^{i(\omega t-\mathbf{k}\cdot\mathbf{r})}, \tag{B1}$$

where $\mathbf{F}(\mathbf{r};t)$ is a smooth vector field representing the electric or magnetic fields and V stands for the volume in the Euclidean space $\mathbb{R}^3$. Thus, the Green's tensor satisfying the wave equation [62–65]

$$\nabla^2\overleftrightarrow{\mathbf{G}}(\mathbf{r};\omega) + k_0^2\overleftrightarrow{\varepsilon}\overleftrightarrow{\mathbf{G}}(\mathbf{r};\omega) - \nabla[\nabla\cdot\overleftrightarrow{\mathbf{G}}(\mathbf{r};\omega)] = \overleftrightarrow{\mathbf{I}}\delta(\mathbf{r}) \tag{B2}$$

can be expressed in $k-\omega$ space as follows:

$$\overleftrightarrow{\mathbf{G}}(\mathbf{k};\omega) = \left[\mathbf{k}\otimes\mathbf{k} - k^2\overleftrightarrow{\mathbf{I}} + k_0^2\overleftrightarrow{\varepsilon}\right]^{-1}. \tag{B3}$$

From Eq. (B3) one can deduce that the inverse of the Green's tensor for a uniaxial medium can be decomposed in the form $\overleftrightarrow{\mathbf{G}}^{-1} = (k_0^2\varepsilon_\perp - k^2)\,\overleftrightarrow{\mathbf{I}} + \mathbf{k}\otimes\mathbf{k} + k_0^2(\varepsilon_\parallel - \varepsilon_\perp)\,\hat{\mathbf{z}}\otimes\hat{\mathbf{z}}$ where $\varepsilon_\perp = \varepsilon_x = \varepsilon_y$ and $\varepsilon_\parallel = \varepsilon_z$. This tensor decomposition allows for finding the following closed expression for $\overleftrightarrow{\mathbf{G}}(\mathbf{k};\omega)$ [22,23]:

$$\overleftrightarrow{\mathbf{G}}(\mathbf{k};\omega) = \frac{1}{k_0^2\varepsilon_\parallel\varepsilon_\perp - \mathbf{k}\cdot\overleftrightarrow{\varepsilon}\cdot\mathbf{k}}\Bigg[\varepsilon_\parallel\overleftrightarrow{\mathbf{I}} - (\varepsilon_\parallel - \varepsilon_\perp)\hat{\mathbf{z}}\otimes\hat{\mathbf{z}} - \frac{\mathbf{k}\otimes\mathbf{k}}{k_0^2} + \frac{\varepsilon_\parallel - \varepsilon_\perp}{k_0^2\varepsilon_\perp - k^2}(\mathbf{k}\times\hat{\mathbf{z}})\otimes(\mathbf{k}\times\hat{\mathbf{z}})\Bigg], \tag{B4}$$

where we used that the inverse of the Green's tensor can be obtained as $\overleftrightarrow{\mathbf{G}}^{-1} = \mathrm{adj}[\overleftrightarrow{\mathbf{G}}]/\det[\overleftrightarrow{\mathbf{G}}]$, with $\mathrm{adj}[\overleftrightarrow{\mathbf{G}}]$ the adjoint of the Green's tensor.

APPENDIX C: BULK EEL PROBABILITY FOR DIFFERENT CUTOFF VALUES $k_\perp^c$

In Fig. 11 we show the EEL probability [$\Gamma^{\mathrm{bulk}}(\omega)$, given by Eq. (14)] in the vicinity of the lower reststrahlen band for different cutoff values $k_\perp^c$: (a) 1×10^{-2} Å^{-1}, (b) 1×10^{-3} Å^{-1}, (c) 1×10^{-4} Å^{-1}, and (d) 1×10^{-5} Å^{-1}. For the calculation of $\Gamma^{\mathrm{bulk}}(\omega)$ we consider $v = 0.1c$.

One can observe that for small cutoff momentum the EEL probability of the $\mathrm{LO}_\parallel$ phonon energy is better defined. Whereas for large cutoff momenta the sharp peak in Fig. 11(d) broadens. However, cutoff values of 1×10^{-4} Å^{-1} or 1×10^{-5} Å^{-1} are not experimentally feasible.

APPENDIX D: ANALYSIS OF THE ASYMMETRIES OF BULK POLARITONIC WAVES

When the electron beam trajectory makes an angle α relative to the h-BN optical axis, the propagation of the phonon polaritons (excited by the fast electron) is highly asymmetric with respect to the beam trajectory. We analyze these asymmetries in the following.

The propagation of the polaritonic wave is governed by its phase velocity and, thus, by the polariton wave vector

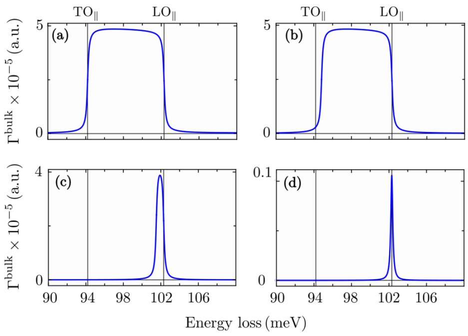

FIG. 11. Electron energy-loss probability $\Gamma^{\mathrm{bulk}}(\omega)$ for energies around the lower reststrahlen band for four different $k_\perp^c$: (a) 1×10^{-2} Å^{-1}, (b) 1×10^{-3} Å^{-1}, (c) 1×10^{-4} Å^{-1}, and (d) 1×10^{-5} Å^{-1}. The electron travels through h-BN parallel to the optical axis with velocity $v = 0.1c$.

$\mathbf{k}(\omega) = (k_x, k_y, k_z)$ which fulfills Eq. (3). When the hyperbolic phonon polaritons are excited by an electron beam, the components of $\mathbf{k}(\omega)$ have also to fulfill Eq. (8), that is, the components of $\mathbf{k}(\omega)$ can be obtained from the following two expressions:

$$\frac{k_x^2 + k_y^2}{\varepsilon_\parallel} + \frac{k_z^2}{\varepsilon_\perp} = k_0^2, \tag{D1a}$$

$$k_y\sin\alpha + k_z\cos\alpha = \omega/v, \tag{D1b}$$

where we assume that the electron velocity is $\mathbf{v} = v(0, \sin\alpha, \cos\alpha)$. Moreover, if we decompose $\mathbf{k}(\omega)$ in cylindrical coordinates as $\mathbf{k}(\omega) = (q\cos\phi, q\sin\phi, k_z)$, with ϕ the azimuthal angle of the symmetry axis, and substitute it into Eqs. (D1a) and (D1b), we obtain the following system of equations:

$$\frac{q^2}{\varepsilon_\parallel} + \frac{k_z^2}{\varepsilon_\perp} = k_0^2, \tag{D2a}$$

$$q\sin\phi\,\sin\alpha + k_z\cos\alpha = \omega/v, \tag{D2b}$$

for q, ϕ, and k_z. Notice that the variable q corresponds to $k_\perp$ for trajectories parallel to the h-BN optical axis. However, for the oblique trajectory $\hbar\mathbf{q} = (\hbar k_x, \hbar k_y)$ is no longer orthogonal to the beam trajectory and thus we avoid referring to it as the transverse momentum. One can deduce from Eqs. (D2a) and (D2b) that the solutions have cylindrical symmetry (symmetric with respect to the k_z axis) when $\alpha = 0°$. For cases where $\alpha \neq 0°$, this symmetry is broken and the solutions depend on the azimuthal angle ϕ. We explore this dependency below.

In Fig. 12 we show the intersection between the h-BN isofrequency hyperboloids [red surfaces, Figs. 12(a) and 12(c)] and the plane $\mathbf{k}\cdot\mathbf{v} = \omega$ determined by the electron beam trajectory [blue surfaces, Figs. 12(a) and 12(c)]. Notice that the direction of the electron beam trajectory is orthogonal to the blue plane $\mathbf{k}\cdot\mathbf{v} = \omega$. We analyze an electron beam with velocity $v = 0.1c$ and a trajectory angle of $\alpha = 20°$. Finally,

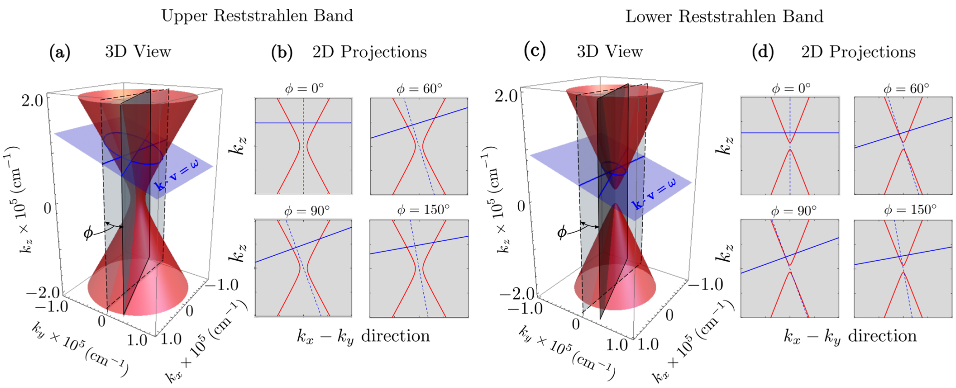

FIG. 12. (a) Isofrequency surface (red hyperboloid) for a representative energy in the upper reststrahlen band (180 meV). The blue inclined plane depicts Eq. (D1b) for an electron beam with $v = 0.1c$ and trajectory angle of $\alpha = 20°$. The gray plane represents the different directions set by the azimuthal angle ϕ. The 2D plots in (b) show the intersection between the red hyperboloid and the blue plane in the four different directions determined by ϕ: $0°,\ 60°,\ 90°$, and $150°$. The blue dashed lines in the 2D projections depict the trajectory of the electron beam, as viewed along each direction determined by the angle ϕ. (c), (d) The same as (a) and (b) but for a representative energy in the lower reststrahlen band (100 meV).

we chose two representative energies, one in the upper reststrahlen band at 180 meV [Fig. 12(a)] and the other one in the lower reststrahlen band at 100 meV [Fig. 12(c)]. The gray 2D plots in Figs. 12(b) and 12(d) show the intersection between the red hyperboloid and the blue plane along four different directions determined by the azimuthal angle ϕ: $0°,\ 60°,\ 90°$, and $150°$. In the 2D projections the blue dashed lines depict the beam trajectory, as viewed from the direction determined by ϕ. The polariton wave vector along each particular direction can be obtained from the intersection between the blue lines and the red hyperbolas. Importantly, one can recognize the following from the 2D projections:

(1) The intersection between the blue line and the red hyperbola is asymmetric with respect to the k_z axis for $\phi \in (0°, 180°)$, as we observe in Figs. 12(b) and 12(d) for $\phi = 60°,\ 90°,\ 150°$.

(2) The direction of largest asymmetry occurs at $\phi = 90°$ ($k_y k_z$ plane) and the direction of symmetric propagation occurs at $\phi = 0°$ ($k_x k_z$ plane).

(3) The intersections between the blue lines and the red hyperbolas are also asymmetric (or symmetric) with respect to the electron beam trajectory (blue dashed line).

To better understand the asymmetries in the propagation of the polaritonic waves, we focus on the direction of largest asymmetry: $\phi = 90°$ (equivalently, the $k_y k_z$ plane). From Eqs. (D1a) and (D1b) one can obtain the following two solutions for the polariton wave vector in the $k_y k_z$ plane:

$$\mathbf{k}^{(1)} = \frac{\omega}{v}\left[\frac{\varepsilon_\parallel \sin\alpha + \sqrt{\varepsilon_\parallel \varepsilon_\perp \Delta}\cos\alpha}{\varepsilon_\perp \cos^2\alpha + \varepsilon_\parallel \sin^2\alpha}\right]\hat{\mathbf{y}} + \frac{\omega}{v}\left[\frac{\varepsilon_\perp \cos\alpha - \sqrt{\varepsilon_\parallel \varepsilon_\perp \Delta}\sin\alpha}{\varepsilon_\perp \cos^2\alpha + \varepsilon_\parallel \sin^2\alpha}\right]\hat{\mathbf{z}}, \tag{D3a}$$

$$\mathbf{k}^{(2)} = \frac{\omega}{v}\left[\frac{\varepsilon_\parallel \sin\alpha - \sqrt{\varepsilon_\parallel \varepsilon_\perp \Delta}\cos\alpha}{\varepsilon_\perp \cos^2\alpha + \varepsilon_\parallel \sin^2\alpha}\right]\hat{\mathbf{y}} + \frac{\omega}{v}\left[\frac{\varepsilon_\perp \cos\alpha + \sqrt{\varepsilon_\parallel \varepsilon_\perp \Delta}\sin\alpha}{\varepsilon_\perp \cos^2\alpha + \varepsilon_\parallel \sin^2\alpha}\right]\hat{\mathbf{z}} \tag{D3b}$$

with

$$\Delta = \left(\frac{v}{c}\cos\alpha\right)^2 \varepsilon_\perp + \left(\frac{v}{c}\sin\alpha\right)^2 \varepsilon_\parallel - 1. \tag{D4}$$

From Eqs. (D3a) and (D3b) one can recognize that $k_z^{(1)} \neq k_z^{(2)}$, showing the asymmetry in the propagation of the polaritonic wave. Moreover, the angles $\theta_{\mathbf{k}}^{(1)}$ and $\theta_{\mathbf{k}}^{(2)}$ defined by $\mathbf{k}^{(1)}$, $\mathbf{k}^{(2)}$ vectors with respect to the electron beam trajectory [see Figs. 6(b) and 6(e)] satisfy the following relations:

$$\tan\left(\theta_{\mathbf{k}}^{(1)} + \alpha\right) = \frac{\varepsilon_\parallel \sin\alpha + \sqrt{\varepsilon_\parallel \varepsilon_\perp \Delta}\cos\alpha}{\varepsilon_\perp \cos\alpha - \sqrt{\varepsilon_\parallel \varepsilon_\perp \Delta}\sin\alpha}, \tag{D5a}$$

$$\tan\left(\theta_{\mathbf{k}}^{(2)} - \alpha\right) = \frac{\varepsilon_\parallel \sin\alpha - \sqrt{\varepsilon_\parallel \varepsilon_\perp \Delta}\cos\alpha}{\varepsilon_\perp \cos\alpha + \sqrt{\varepsilon_\parallel \varepsilon_\perp \Delta}\sin\alpha}. \tag{D5b}$$

When $\alpha = 0°$, one can deduce from Eqs. (D5a) and (D5b) that

$$\tan\theta_{\mathbf{k}}^{(1)} = \sqrt{\left(\frac{v}{c}\right)^2 \varepsilon_\parallel - \frac{\varepsilon_\parallel}{\varepsilon_\perp}}, \tag{D6a}$$

$$\tan\theta_{\mathbf{k}}^{(2)} = -\sqrt{\left(\frac{v}{c}\right)^2 \varepsilon_\parallel - \frac{\varepsilon_\parallel}{\varepsilon_\perp}}. \tag{D6b}$$

Therefore, $\theta_{\mathbf{k}}^{(1)} = \theta_{\mathbf{k}}^{(2)} = \theta_{\mathbf{k}}$ for this particular case of symmetric propagation. Notice that $\theta_{\mathbf{k}}$ is also preserved in any other azimuthal direction.

We can observe from Eqs. (D3a) and (D3b) that $\mathbf{k}^{(1)}, \mathbf{k}^{(2)}$ depend on the electron velocity v. This dependency provides information on the condition that the electron velocity needs to satisfy for the electron beam to excite the polaritonic waves. Indeed, by imposing real value solutions to Eqs. (D5a) and (D5b), one obtains the following condition on v:

$$\frac{v^2}{c^2}[\varepsilon_\perp^2\varepsilon_\parallel \cos^2\alpha + \varepsilon_\parallel^2\varepsilon_\perp \sin^2\alpha] > \varepsilon_\perp\varepsilon_\parallel. \tag{D7}$$

This last relationship results in the inequality

$$\frac{v^2}{c^2}\varepsilon_\parallel > \frac{\varepsilon_\parallel}{\varepsilon_\perp}, \tag{D8}$$

when $\alpha = 0^\circ$, which coincides exactly with the first inequality in Eq. (16) obtained in the main text. As we discuss in Sec. II E, Eq. (D8) reveals the condition on the electron velocity for exciting phonon polaritons or emitting Cherenkov radiation.

We show now that we can recover the properties of the excited wave in an isotropic dielectric medium from the previous expressions. Assuming that the medium has dielectric function equal to $\varepsilon_\perp = \varepsilon_\parallel = \varepsilon > 0$, the condition (D8) results in the canonical relation for Cherenkov radiation: $v > c/\sqrt{\varepsilon}$. Moreover, the two wave-vector solutions $\mathbf{k}^{(1)}, \mathbf{k}^{(2)}$ given by Eqs. (D3a) and (D3b) result in

$$\mathbf{k}^{(1)} = \frac{\omega}{v}\mathbb{M}\,(\hat{\mathbf{y}} - \sqrt{\Delta}\,\hat{\mathbf{z}}), \tag{D9a}$$

$$\mathbf{k}^{(2)} = \frac{\omega}{v}\mathbb{M}\,(\hat{\mathbf{y}} + \sqrt{\Delta}\,\hat{\mathbf{z}}), \tag{D9b}$$

with

$$\mathbb{M} = \begin{bmatrix} \sin\alpha & -\cos\alpha \\ \cos\alpha & \sin\alpha \end{bmatrix}. \tag{D10}$$

It is worthwhile noting that $\mathbb{M}$ is an orthogonal matrix. This implies that the angles $\theta_{\mathbf{k}}^{(1)}$ and $\theta_{\mathbf{k}}^{(2)}$ are always equal. Thus, the propagation of the wake patterns excited in an isotropic dielectric media is always cylindrically symmetric with respect to the electron beam trajectory.

APPENDIX E: MOMENTUM-RESOLVED LOSS AND EEL PROBABILITIES FOR ELECTRON TRAJECTORIES OBLIQUE TO THE OPTICAL AXIS OF h-BN

As we show in Appendix D, the cylindrical symmetry in the propagation of the phonon polariton wave is broken when the electron beam trajectory is not parallel to the h-BN optical axis. This break in symmetry means that the momentum-resolved loss probability $P^{\text{bulk}}(\mathbf{q};\omega)$ is no longer constant along the azimuthal direction but it depends on the angle ϕ [66]. Notice also that the momentum $\hbar\mathbf{q} = (\hbar k_x, \hbar k_y)$ is no longer perpendicular to the beam trajectory $\mathbf{r}_e(t) = vt(0, \sin\alpha, \cos\alpha)$. In fact, the two orthogonal directions to $\mathbf{r}_e(t)$ are (i) the x direction and (ii) the direction set by the unit vector $\hat{\mathbf{n}}_\alpha = (0, \cos\alpha, -\sin\alpha)$. Thus, the two transverse components (to the beam trajectory) of the polariton wave vector are k_x and

$$k_\alpha = \mathbf{k}\cdot\hat{\mathbf{n}}_\alpha = k_y\cos\alpha - k_z\sin\alpha. \tag{E1}$$

Furthermore, the components of the polariton wave vector $\mathbf{k}(\omega)$ excited by the fast electron beam need to satisfy Eq. (D1b). By solving Eqs. (D1b) and (E1) one finds that k_y and k_z can be written in terms of k_α as

$$k_y = k_y^{(\alpha)} = k_\alpha\cos\alpha + \frac{\omega}{v}\sin\alpha, \tag{E2a}$$

$$k_z = k_z^{(\alpha)} = -k_\alpha\sin\alpha + \frac{\omega}{v}\cos\alpha. \tag{E2b}$$

Following Eq. (10), we can define the probability for the fast electron to transfer a transverse momentum $(\hbar k_x, \hbar k_\alpha)$ upon losing energy $\hbar\omega$ as

$$P_\alpha^{\text{bulk}}(k_x, k_\alpha;\omega) = -\frac{2e^2}{(2\pi)^3\hbar c^2\varepsilon_0\cos\alpha}\text{Im}[\hat{\mathbf{v}}\cdot\overleftrightarrow{\mathbf{G}}_{k_\alpha}\cdot\hat{\mathbf{v}}], \tag{E3}$$

where $\overleftrightarrow{\mathbf{G}}_{k_\alpha} = \overleftrightarrow{\mathbf{G}}(k_x, k_y^{(\alpha)}, k_z^{(\alpha)})$ and $k_y^{(\alpha)}$, $k_z^{(\alpha)}$ are given by Eqs. (E2a) and (E2b), respectively. On the other hand, the electron energy-loss probability $\Gamma_\alpha^{\text{bulk}}(\omega)$ can be obtained by integrating $P_\alpha^{\text{bulk}}(k_x, k_\alpha;\omega)$ over the momentum coordinates [Eq. (9)]

$$\begin{aligned}\Gamma_\alpha^{\text{bulk}}(\omega) &= \int dk_x \int dk_y\, P_\alpha^{\text{bulk}}(k_x, k_y;\omega) \\ &= \int dk_x \int dk_\alpha \cos\alpha P_\alpha^{\text{bulk}}(k_x, k_\alpha;\omega) \\ &= \int_0^{q^c} q\,dq \int_0^{2\pi} d\phi\, P_\alpha^{\text{bulk}}(q,\phi;\omega),\end{aligned} \tag{E4}$$

where the last equality follows by expressing $\mathbf{q}$ in cylindrical coordinates. Notice that the integration over the magnitude of $\mathbf{q}$ is performed up to the cutoff value q^c.

In Fig. 13 we show the momentum-resolved loss probability $P_\alpha^{\text{bulk}}(k_x, k_\alpha;\omega)$ and the EEL probability $\Gamma_\alpha^{\text{bulk}}(\omega)$ for representative energies inside the reststrahlen bands when $v = 0.1c$ and two different trajectory angles α: 20° and 45°. One can observe in the figure that the EEL features are similar but the momentum-resolved loss probability shows asymmetries for different energies in the reststrahlen bands.

APPENDIX F: INDUCED ELECTROMAGNETIC FIELD FOR AN ELECTRON TRAJECTORY ABOVE THE SURFACE OF A UNIAXIAL ANISOTROPIC SEMI-INFINITE MEDIUM

To obtain the induced electromagnetic field when the electron is traveling above the surface of an anisotropic media, we solve the following wave equation (derived from Maxwell's equations) satisfied by the total electric field [67]

$$\begin{aligned}\nabla^2\mathbf{E}^{\text{tot}}(\mathbf{r};t) - \mu_0\varepsilon_0\frac{\partial^2}{\partial t^2}[\overleftrightarrow{\varepsilon}\mathbf{E}^{\text{tot}}(\mathbf{r};t)] \\ = \mu_0\frac{\partial}{\partial t}\mathbf{J}(\mathbf{r};t) + \nabla[\nabla\cdot\mathbf{E}^{\text{tot}}(\mathbf{r};t)],\end{aligned} \tag{F1}$$

where ε_0 and μ_0 stand for the vacuum permittivity and permeability, respectively, and $\mathbf{J}(\mathbf{r};t) = \rho(\mathbf{r};t)\mathbf{v} = -e\delta(x - x_0, 0, z - vt)(0, 0, v)$ is the current density corresponding to the electron traveling with velocity $\mathbf{v} = v\hat{\mathbf{z}}$ and impact parameter x_0. We show in Fig. 7 of the main text a schematics of the considered geometry.

By Fourier transforming Eq. (F1) with respect to the variables y, z, and t and solving for the electric field separately outside (label I) and inside (label II) the anisotropic medium,

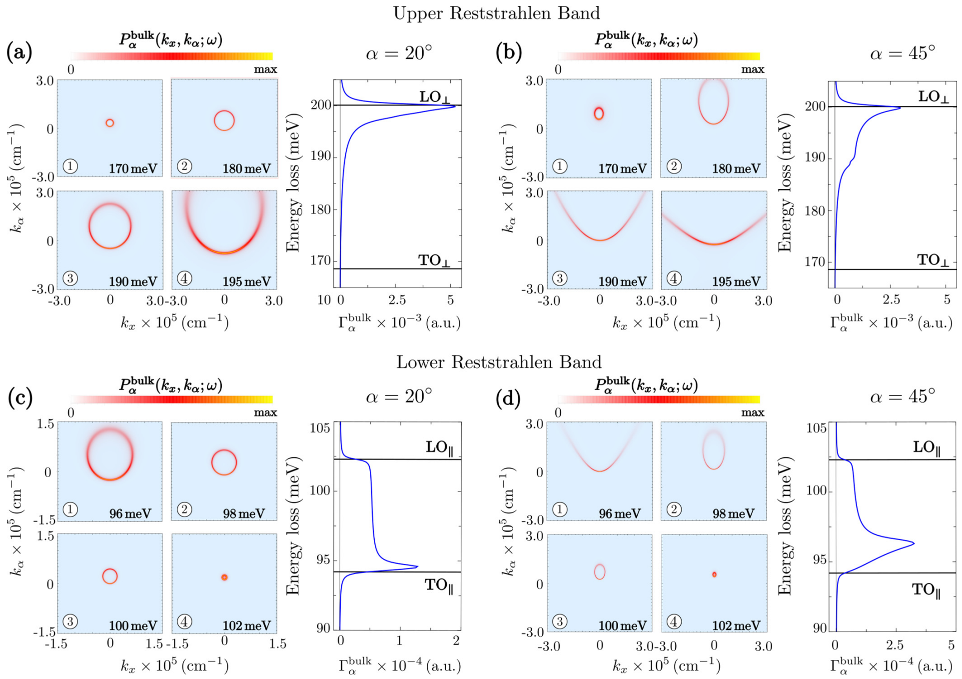

FIG. 13. The color plots in (a) and (b) show the momentum-resolved loss probabilities $P_\alpha^{\rm bulk}(k_x, k_\alpha; \omega)$ for representative energies within the upper reststrahlen band (170, 180, 190, and 195 meV) when the angle α of the electron beam trajectory is equal to (a) 20° and (b) 45° with $v = 0.1c$. The right panels in (a) and (b) show $\Gamma_\alpha^{\rm bulk}(\omega)$ obtained by integrating $P_\alpha^{\rm bulk}(\mathbf{q}; \omega)$ over the reciprocal coordinates (q, ϕ) up to the cutoff value $q^c = 0.05$ Å^{-1}. (c), (d) Analogous to (a) and (b) but for representative energies within the lower reststrahlen band (96, 98, 100, and 102 meV). The color plots are normalized with respect to the maximum value in each case: (a.1) 500 a.u., (a.2) 1500 a.u., (a.3) > 1500 a.u., (a.4) 1250 a.u.; (b.1) >300 a.u., (b.2) 2000 a.u., (b.3) >2500 a.u., (b.4) >2500 a.u.; (c.1) 1250 a.u., (c.2) 4000 a.u., (c.3) >6000 a.u., (c.4) >10 000 a.u.; (d.1) >2000 a.u., (d.2) >5000 a.u., (d.3) >8000 a.u., (d.4) >8000 a.u.

we obtain the following solutions for the components of the total electric field:

$$E_x^{(\mathrm{I})}(x, k_y, k_z; \omega) = B_{\mathrm{I}}\, e^{-\kappa_{\mathrm{I}} x} - \frac{\pi e}{\varepsilon_0}\mathrm{sign}(x - x_0)\delta(\omega - k_z v) \times e^{-\kappa_{\mathrm{I}}|x - x_0|}, \tag{F2a}$$

$$E_y^{(\mathrm{I})}(x, k_y, k_z; \omega) = D_{\mathrm{I}}\, e^{-\kappa_{\mathrm{I}} x} - i\frac{\pi e}{\varepsilon_0}\frac{k_y - \frac{\omega}{c^2}v_y}{\kappa_{\mathrm{I}}}\delta(\omega - k_z v) \times e^{-\kappa_{\mathrm{I}}|x - x_0|}, \tag{F2b}$$

$$E_z^{(\mathrm{I})}(x, k_y, k_z; \omega) = G_{\mathrm{I}}\, e^{-\kappa_{\mathrm{I}} x} - i\frac{\pi e}{\varepsilon_0}\frac{k_z - \frac{\omega}{c^2}v_z}{\kappa_{\mathrm{I}}}\delta(\omega - k_z v) \times e^{-\kappa_{\mathrm{I}}|x - x_0|}, \tag{F2c}$$

$$E_x^{(\mathrm{II})}(x, k_y, k_z; \omega) = A_{\mathrm{II}} e^{\kappa_{\mathrm{II}}^o x} - iF_{\mathrm{II}}\frac{k_z \kappa_{\mathrm{II}}^e}{\left(\kappa_{\mathrm{II}}^o\right)^2 - k_y^2}e^{\kappa_{\mathrm{II}}^e x}, \tag{F2d}$$

$$E_y^{(\mathrm{II})}(x, k_y, k_z; \omega) = C_{\mathrm{II}} e^{\kappa_{\mathrm{II}}^o x} + F_{\mathrm{II}}\frac{k_y k_z}{\left(\kappa_{\mathrm{II}}^o\right)^2 - k_y^2}e^{\kappa_{\mathrm{II}}^e x}, \tag{F2e}$$

$$E_z^{(\mathrm{II})}(x, k_y, k_z; \omega) = F_{\mathrm{II}} e^{\kappa_{\mathrm{II}}^e x}, \tag{F2f}$$

where

$$\kappa_{\mathrm{I}}^2 = k_y^2 + k_z^2 - \frac{\omega^2}{c^2}, \quad \left(\kappa_{\mathrm{II}}^e\right)^2 = k_y^2 + \frac{\varepsilon_\parallel}{\varepsilon_\perp}\left(k_z^2 - \frac{\omega^2}{c^2}\varepsilon_\perp\right)$$

and

$$\left(\kappa_{\mathrm{II}}^o\right)^2 = k_y^2 + k_z^2 - \varepsilon_\perp\frac{\omega^2}{c^2}. \tag{F3}$$

The coefficients A_{II}, B_{I}, C_{II}, D_{I}, F_{II}, and G_{I} can be found from the application of the standard boundary conditions for the electric field at the interface ($x = 0$) between both media, that is,

$$E_y^{(\mathrm{II})}|_{x=0} = E_y^{(\mathrm{I})}|_{x=0}, \quad E_z^{(\mathrm{II})}|_{x=0} = E_z^{(\mathrm{I})}|_{x=0},$$
$$\varepsilon_\perp E_x^{(\mathrm{II})}|_{x=0} = E_x^{(\mathrm{I})}|_{x=0}, \tag{F4}$$

together with the Gauss law and the boundary conditions for the magnetic field.

APPENDIX G: MOMENTUM-RESOLVED LOSS AND EEL PROBABILITIES FOR ELECTRON TRAJECTORIES ABOVE THE SURFACE OF h-BN PARALLEL TO THE OPTICAL AXIS

By solving the linear system of equations set by the boundary conditions [Eq. (F4)], one finds that each coefficient in Eqs. (F2a)–(F2f) can be expressed as

$$A_{\rm II} = \tilde{\rho}\, a_{\rm II}, \quad B_{\rm I} = \tilde{\rho}\, b_{\rm I}, \quad C_{\rm II} = \tilde{\rho}\, c_{\rm II},$$
$$D_{\rm I} = \tilde{\rho}\, d_{\rm I}, \quad F_{\rm II} = \tilde{\rho} f_{\rm II}, \quad G_{\rm I} = \tilde{\rho} g_{\rm I},$$

with $\tilde{\rho} = -2\pi e\delta(\omega - k_z v)e^{-\kappa_{\rm I} x_0}/\varepsilon_0$. Thus, we obtain that the induced electric fields in vacuum (labeled as I) and h-BN (labeled as II) are given by [Eqs. (F2a)–(F2f)]

$$\mathbf{E}^{\rm ind}_{\rm I}(x, k_y, k_z; \omega) = (b_{\rm I}, d_{\rm I}, g_{\rm I})\, \tilde{\rho}\, e^{-\kappa_{\rm I} x}, \tag{G1a}$$

$$\mathbf{E}^{\rm ind}_{\rm II}(x, k_y, k_z; \omega) = (a_{\rm II}, c_{\rm II}, 0)\, \tilde{\rho}\, e^{\kappa^o_{\rm II} x} + \left(-i\frac{k_z \kappa^e_{\rm II}}{\left(\kappa^o_{\rm II}\right)^2 - k_y^2}, \frac{k_z k_y}{\left(\kappa^o_{\rm II}\right)^2 - k_y^2}, 1\right) \times \tilde{\rho}\, f_{\rm II}\, e^{\kappa^e_{\rm II} x}. \tag{G1b}$$

Substituting Eq. (G1a) into Eq. (6), one obtains that the EEL probability $\Gamma^{\rm surf}(\omega)$ can be written as

$$\Gamma^{\rm surf}(\omega) = \frac{e}{\pi\hbar\omega}{\rm Re}\left[\mathbf{E}^{\rm ind}_{\rm I}(\mathbf{r}_e;\omega)\cdot\hat{\mathbf{z}}\, e^{-i\omega t_e}\right] = \int_0^{k_y^c} dk_y\, P^{\rm surf}(k_y;\omega), \tag{G2}$$

with $\hbar k_y^c$ the maximum momentum of the electrons that can pass through the collection aperture of the detector in the y direction, and

$$P^{\rm surf}(k_y;\omega) = -\frac{e^2}{\pi^2\varepsilon_0\hbar\omega v}{\rm Re}\left[g_{\rm I} e^{-2\kappa_{\rm I} x_0}\right]\big|_{k_z=\omega/v}, \tag{G3}$$

Lower Reststrahlen Band

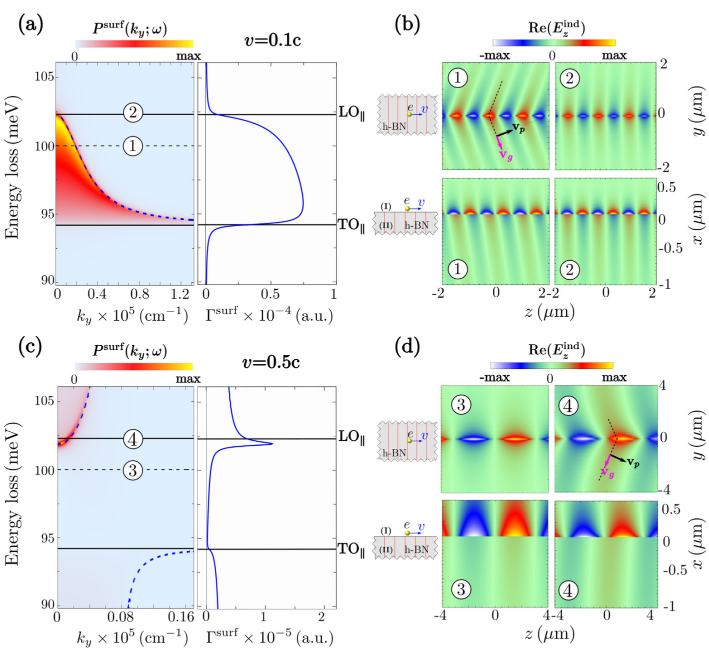

FIG. 14. The left panel in (a) displays the momentum-resolved loss probability $P^{\rm surf}(k_y;\omega)$ normalized to the maximum value (>0.6 a.u.) in the vicinity of the lower reststrahlen band for $x_0 = 10$ nm and $v = 0.1c$. The right panel in (a) shows the EEL probability $\Gamma^{\rm surf}(\omega)$ obtained by integrating $P^{\rm surf}(k_y;\omega)$ over k_y up to $k_y^c = 0.09$ Å^{-1}. (c) Same as in (a) but considering $v = 0.5c$. For this case the maximum value of the momentum-resolved loss probability is 2 a.u. The color maps in (b) and (d) show the real part of the z component of the induced electric field for the energies: 100 (marked 1, 3) and LO$_\parallel$ (marked 2, 4). The top panels in (b) and (d) correspond to the in-plane views (yz plane) of the induced field, while the bottom panels correspond to the out-of-plane views (xz plane). The field plots are normalized with respect to the maximum value in each case. For the top panels: (b) 7.5×10^{-6} a.u., (d.3) 4×10^{-7} a.u., and (d.4) 3×10^{-7} a.u. For the bottom panels: (b) 5×10^{-6} a.u., (d.3) 3×10^{-7} a.u., and (d.4) 4×10^{-7} a.u.

where $\hbar k_z = \hbar\omega/v$ is the momentum transferred by the electron to the polaritons along the beam trajectory.

APPENDIX H: ELECTRON ENERGY-LOSS PROBABILITY FOR ENERGIES AROUND THE LOWER RESTSTRAHLEN BAND FOR ELECTRON TRAJECTORIES ABOVE THE SURFACE OF h-BN

In the left panel of Fig. 14(a) we show the momentum-resolved loss probability $P^{\rm surf}(k_y;\omega)$ for an electron traveling above an h-BN surface for energies around the lower reststrahlen band. The probing electron travels above the surface at an impact parameter of 10 nm and $v = 0.1c$. The blue dashed line corresponds to the bulk phonon polariton dispersion [Eq. (3)]. We can recognize some similarities between $P^{\rm surf}(k_y;\omega)$ and $P^{\rm bulk}(k_\perp;\omega)$ [compare the left panels of Figs. 4(b) and 14(a)]. For instance, the maximum values of $P^{\rm surf}(k_y;\omega)$ are close to the bulk dispersion (blue dashed line). Interestingly, this bulk dispersion corresponds to the envelope curve of $P^{\rm surf}(k_y;\omega)$ implying that electron energy losses in the lower band are mainly due to bulk hyperbolic phonon polariton excitations. To obtain spectroscopic information on the excitations in the lower band, we calculate the EEL probability $\Gamma^{\rm surf}(\omega)$ by integrating $P^{\rm surf}(k_y;\omega)$ over k_y up to a cutoff k_y^c [right panel in Fig. 14(a)]. Similarly to $\Gamma^{\rm bulk}(\omega)$ [Fig. 4(b), right panel], $\Gamma^{\rm surf}(\omega)$ [right panel in Fig. 14(a)] exhibits a uniform loss probability between $\mathrm{TO}_\parallel$ and $\mathrm{LO}_\parallel$ which depends on the selected cutoff momenta $\hbar k_y^c$.

In Fig. 14(b) we show the real part of the z component of the induced electric field for the same electron velocity and impact parameter as in Fig. 14(a), for two different energies marked as 1 and 2 in Fig. 14(a). We can recognize the excitation of the wake fields in the h-BN surface for those energy losses [compare the top panels labeled as 1 and 2 in Fig. 14(b)]. The bulk nature of the excited modes is revealed in the bottom panels of Fig. 14(b), where we show the z component of the real part of the induced electric field $\mathrm{Re}[E_z^{\rm ind}(\mathbf{r};\omega)]$ in the xz plane. In this lateral view of the field distribution one notices the excitation and propagation of the field into the bulk from the h-BN surface.

Figures 14(c) and 14(d) show $P^{\rm surf}(k_y;\omega)$, $\Gamma^{\rm surf}(\omega)$ and the induced field distribution when the electron velocity is $v = 0.5c$. It is worth noting that the blue dashed line superimposed on $P^{\rm surf}(k_y;\omega)$ [Fig. 14(c), left panel] corresponds to another branch of Dyakonov's dispersion relation given by Eqs. (19a)–(19c) and (20).

[1] L. Venema, B. Verberck, I. Georgescu, G. Prando, E. Couderc, S. Milana, M. Maragkou, L. Persechini, G. Pacchioni, and L. Fleet, Nat. Phys. **12**, 1085 (2016).
[2] D. L. Mills and E. Burstein, Rep. Prog. Phys. **37**, 817 (1974).
[3] R. Hillenbrand, T. Taubner, and F. Keilmann, Nature (London) **418**, 159 (2002).
[4] D. N. Basov, M. M. Fogler, and F. J. García de Abajo, Science **354**, aag1992 (2016).
[5] T. G. Folland, L. Nordin, D. Wasserman, and J. D. Caldwell, J. Appl. Phys. **125**, 191102 (2019).
[6] J. M. Pitarke, V. M. Silkin, E. V. Chulkov, and P. M. Echenique, Rep. Prog. Phys. **70**, 1 (2007).
[7] Z. Jacob, Nat. Mater. **13**, 1081 (2014).
[8] J. D. Caldwell, L. Lindsay, V. Giannini, I. Vurgaftman, T. L. Reinecke, S. A. Maier, and O. J. Glembocki, Nanophotonics **4**, 44 (2015).
[9] T. Low, A. Chaves, J. D. Caldwell, A. Kumar, N. X. Fang, P. Avouris, T. F. Heinz, F. Guinea, L. Martin-Moreno, and F. Koppens, Nat. Mater. **16**, 182 (2017).
[10] J. D. Caldwell, I. Aharonovich, G. Cassabois, J. H. Edgar, B. Gil, and D. N. Basov, Nat. Rev. Mater. **4**, 552 (2019).
[11] S. Dai, Z. Fei, Q. Ma, A. S. Rodin, M. Wagner, A. S. McLeod, M. K. Liu, W. Gannett, W. Regan, K. Watanabe, T. Taniguchi, M. Thiemens, G. Dominguez, A. H. Castro Neto, A. Zettl, F. Keilmann, P. Jarillo-Herrero, M. M. Fogler, and D. N. Basov, Science **343**, 1125 (2014).
[12] J. D. Caldwell, A. V. Kretinin, Y. Chen, V. Giannini, M. M. Fogler, Y. Francescato, C. T. Ellis, J. G. Tischler, C. R. Woods, A. J. Giles, M. Hong, K. Watanabe, T. Taniguchi, S. A. Maier, and K. S. Novoselov, Nat. Commun. **5**, 5221 (2014).
[13] Z. Shi, H. A. Bechtel, S. Berweger, Y. Sun, B. Zeng, C. Jin, H. Chang, M. C. Martin, M. B. Raschke, and F. Wang, ACS Photonics **2**, 790 (2015).
[14] F. J. Alfaro-Mozaz, P. Alonso-González, S. Vélez, I. Dolado, M. Autore, S. Mastel, F. Casanova, L. E. Hueso, P. Li, A. Y. Nikitin, and R. Hillenbrand, Nat. Commun. **8**, 15624 (2017).
[15] L. Gilburd, K. S. Kim, K. Ho, D. Trajanoski, A. Maiti, D. Halverson, S. de Beer, and G. C. Walker, J. Phys. Chem. Lett. **8**, 2158 (2017).
[16] A. Ambrosio, M. Tamagnone, K. Chaudhary, L. A. Jauregui, P. Kim, W. L. Wilson, and F. Capasso, Light-Sci. Appl. **7**, 27 (2018).
[17] J. D. Caldwell and K. S. Novoselov, Nat. Mater. **14**, 364 (2015).
[18] A. Poddubny, I. Iorsh, P. Belov, and Y. Kivshar, Nat. Photonics **7**, 948 (2013).
[19] O. L. Krivanek, T. C. Lovejoy, N. Dellby, T. Aoki, R. W. Carpenter, P. Rez, E. Soignard, J. Zhu, P. E. Batson, M. J. Lagos, R. F. Egerton, and P. A. Crozier, Nature (London) **514**, 209 (2014).
[20] A. A. Govyadinov, A. Konečná, A. Chuvilin, S. Vélez, I. Dolado, A. Y. Nikitin, S. Lopatin, F. Casanova, L. E. Hueso, J. Aizpurua, and R. Hillenbrand, Nat. Commun. **8**, 95 (2017).
[21] F. S. Hage, R. J. Nicholls, J. R. Yates, D. G. McCulloch, T. C. Lovejoy, N. Dellby, O. L. Krivanek, K. Refson, and Q. M. Ramasse, Sci. Adv. **4**, eaar7495 (2018).
[22] A. Eroglu, *Wave Propagation and Radiation in Gyrotropic and Anisotropic Media* (Springer, New York, 2010).
[23] A. S. Potemkin, A. N. Poddubny, P. A. Belov, and Y. S. Kivshar, Phys. Rev. A **86**, 023848 (2012).
[24] R. H. Ritchie, Phys. Rev. **106**, 874 (1957).
[25] R. García-Molina, A. Gras-Marti, A. Howie, and R. H. Ritchie, J. Phys. C: Solid State Phys. **18**, 5335 (1985).
[26] F. J. García de Abajo, Rev. Mod. Phys. **82**, 209 (2010).
[27] A. Polman, M. Kociak, and F. J. García de Abajo, Nat. Mater. **18**, 1158 (2019).

[28] U. Hohenester, *Nano and Quantum Optics. An Introduction to Basic Principles and Theory* (Springer, Switzerland, 2020).
[29] R. H. Ritchie, Philos. Mag. A **44**, 931 (1981).
[30] R. H. Ritchie and A. Howie, Philos. Mag. A **58**, 753 (1988).
[31] A. Rivacoba and N. Zabala, New J. Phys. **16**, 073048 (2014).
[32] L. B. Felsen and N. Marcuvitz, *Radiation and Scattering of Waves* (Wiley, Hoboken, NJ, 2003).
[33] S. N. Galyamin and A. V. Tyukhtin, Phys. Rev. E **84**, 056608 (2011).
[34] E. Yoxall, M. Schnell, A. Y. Nikitin, O. Txoperena, A. Woessner, M. B. Lundeberg, F. Casanova, L. E. Hueso, F. H. L. Koppens, and R. Hillenbrand, Nat. Photonics **9**, 674 (2015).
[35] L. D. Landau and E. M. Lifshitz, *Electrodynamics of Continuous Media* (Pergamon, New York, 1984).
[36] A. Yariv and P. Yeh, *Optical Waves in Crystals* (Wiley, New York, 1983).
[37] J. Tao, Q. J. Wang, J. Zhang, and Y. Luo, Sci. Rep. **6**, 30704 (2016).
[38] J. Tao, L. Wu, G. Zheng, and S. Yu, Carbon **150**, 136 (2019).
[39] V. N. Neelavathi, R. H. Ritchie, and W. Brandt, Phys. Rev. Lett. **33**, 302 (1974).
[40] P. M. Echenique, R. H. Ritchie, and W. Brandt, Phys. Rev. B **20**, 2567 (1979).
[41] R. H. Ritchie, P. M. Echenique, W. Brandt, and G. Basbas, IEEE Trans. Nucl. Sci. **26**, 1001 (1979).
[42] F. J. García de Abajo and P. M. Echenique, Phys. Rev. B **46**, 2663 (1992).
[43] F. Liu, L. Xiao, Y. Ye, M. Wang, K. Cui, X. Feng, W. Zhang, and Y. Huang, Nat. Photonics **11**, 289 (2017).
[44] P. A. Cherenkov, C. R. (Dokl.) Acad. Sci. URSS **2**, 451 (1934).
[45] P. A. Cherenkov, Phys. Rev. **52**, 378 (1937).
[46] I. Frank and I. Tamm, C. R. (Dokl.) Acad. Sci. URSS **14**, 109 (1937).
[47] I. Tamm, J. Phys. (USSR) **1**, 439 (1939).
[48] A. A. Lucas and E. Kartheuser, Phys. Rev. B **1**, 3588 (1970).
[49] C. H. Chen and J. Silcox, Phys. Rev. B **20**, 3605 (1979).
[50] V. L. Ginzburg, Phys. Usp. **39**, 973 (1996).
[51] N. Talebi, *Near-Field-Mediated Photon-Electron Interactions* (Springer, Switzerland, 2019).
[52] D. E. Fernandes, S. I. Maslovski, and M. G. Silveirinha, Phys. Rev. B **85**, 155107 (2012).
[53] P. R. Ribič and R. Podgornik, Europhys. Lett. **102**, 24001 (2013).
[54] M. I. D'yakonov, Zh. Eksp. Teor. Fiz. **94**, 119 (1988) [Sov. Phys.–JETP **67**, 4 (1988)].
[55] O. Takayama, L. C. Crasovan, S. K. Johansen, D. Mihalache, D. Artigas, and L. Torner, Electromagnetics **28**, 126 (2008).
[56] N. Talebi, *Topological Hyperbolic and Dirac Plasmons. In Reviews in Plasmonics 2017* (Springer, Switzerland, 2019).
[57] P. Li, I. Dolado, F. J. Alfaro-Mozaz, A. Yu. Nikitin, F. Casanova, L. E. Hueso, S. Vélez, and R. Hillenbrand, Nano Lett. **17**, 1 (2017).
[58] N. Talebi, C. Ozsoy-Keskinbora, H. M. Benia, K. Kern, C. T. Koch, and P. A. van Aken, ACS Nano **10**, 6988 (2016).
[59] E. Cojocaru, J. Opt. Soc. Am. B **31**, 2558 (2014).
[60] G. Álvarez-Pérez, K. V. Voronin, V. S. Volkov, P. Alonso-González, and A. Y. Nikitin, Phys. Rev. B **100**, 235408 (2019).
[61] B. Zhu, G. Ren, Y. Gao, Q. Wang, C. Wan, J. Wang, and S. Jian, J. Opt. **18**, 125006 (2016).
[62] W. C. Chew, *Waves and Fields in Inhomogeneous Media* (IEEE Press, Piscataway, NJ, 1995).
[63] F. J. García de Abajo and M. Kociak, Phys. Rev. Lett. **100**, 106804 (2008).
[64] R. E. Collin, *Field Theory of Guided Waves*, 2nd ed. (IEEE Press, Piscataway, NJ, 1991).
[65] L. Novotny and B. Hecht, *Principles of Nano-Optics*, 3rd ed. (Cambridge University Press, New York, 2006).
[66] F. Fossard, L. Sponza, L. Schué, C. Attaccalite, F. Ducastelle, J. Barjon, and A. Loiseau, Phys. Rev. B **96**, 115304 (2017).
[67] J. D. Jackson, *Classical Electrodynamics*, 3rd ed. (Wiley, New York, 1998).

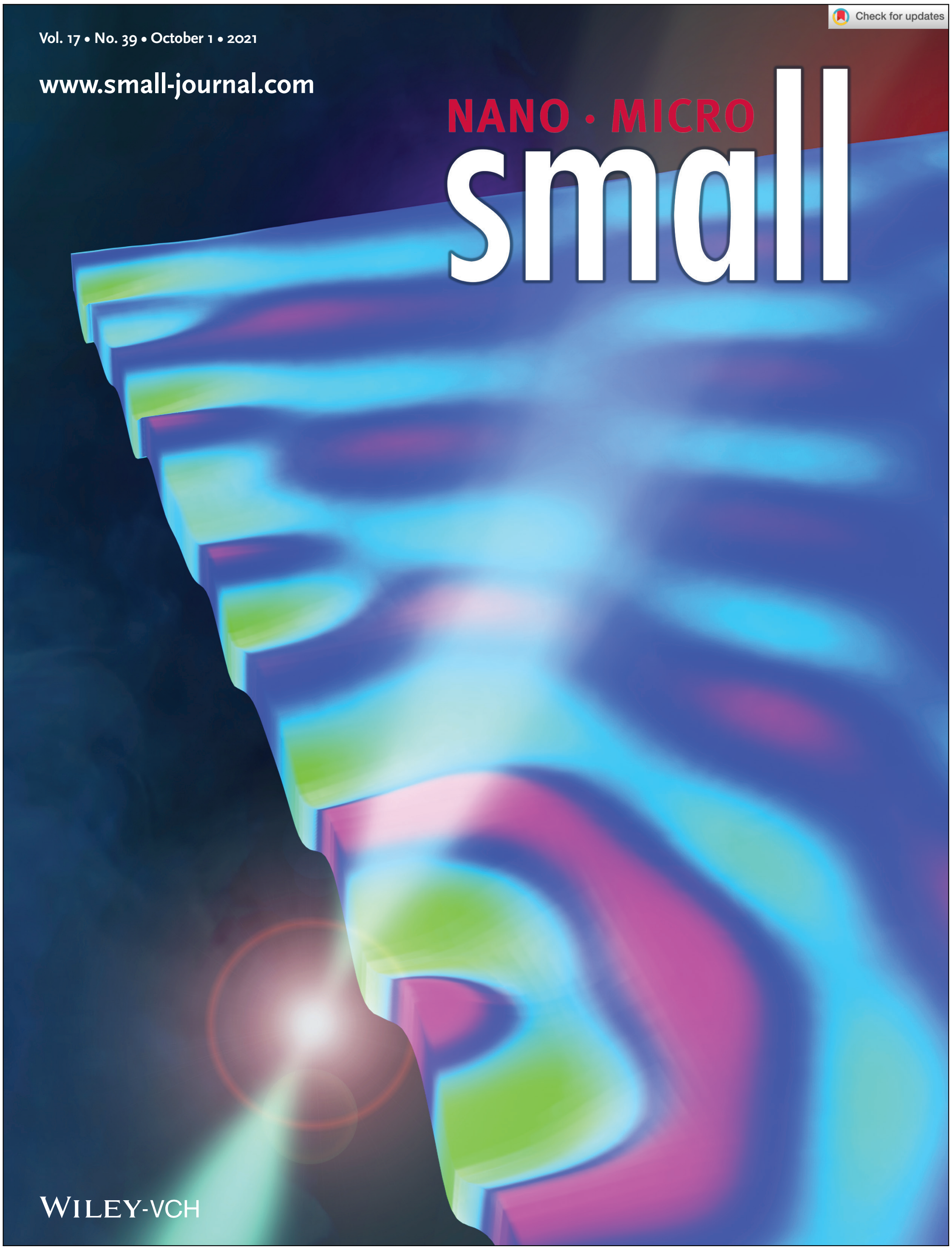
Check for updates
Vol. 17 • No. 39 • October 1 • 2021
www.small-journal.com
NANO · MICRO
small
WILEY-VCH

RESEARCH ARTICLE

NANO · MICRO small

www.small-journal.com

Revealing Nanoscale Confinement Effects on Hyperbolic Phonon Polaritons with an Electron Beam

Andrea Konečná, Jiahan Li, James H. Edgar, F. Javier García de Abajo, and Jordan A. Hachtel**

Hyperbolic phonon polaritons (HPhPs) in hexagonal boron nitride (hBN) enable the direct manipulation of mid-infrared light at nanometer scales, many orders of magnitude below the free-space light wavelength. High-resolution monochromated electron energy-loss spectroscopy (EELS) facilitates measurement of excitations with energies extending into the mid-infrared while maintaining nanoscale spatial resolution, making it ideal for detecting HPhPs. The electron beam is a precise source and probe of HPhPs, which allows the observation of nanoscale confinement in HPhP structures and directly extract hBN polariton dispersions for both modes in the bulk of the flake and modes along the edge. The measurements reveal technologically important nontrivial phenomena, such as localized polaritons induced by environmental heterogeneity, enhanced and suppressed excitation due to 2D interference, and strong modification of high-momenta excitations such as edge-confined polaritons by nanoscale heterogeneity on edge boundaries. The work opens exciting prospects for the design of real-world optical mid-infrared devices based on hyperbolic polaritons.

1. Introduction

Localized plasmon and phonon polaritons can be used to confine and manipulate light in the visible and near-infrared spectral regimes at the nanoscale.[1–3] The less developed mid-infrared (mid-IR) range holds great potential for new applications,[4–6] but is still limited by the lack of suitable material systems for controlling low-energy excitations. Hexagonal boron nitride (hBN) is one such material, which, due to its dielectric anisotropy, possesses two Reststrahlen bands that support hyperbolic phonon polaritons (HPhPs) that confine mid-IR light to nanometer scales and allow it to propagate over micrometer scales.[7,8] As a result, hBN can be combined with engineered nanopatterning as well as hybridization with other materials to enable a wide range of powerful nanophotonic devices.[9–15]

Only recently have optical analysis techniques achieved the spatial-resolution necessary to access HPhPs directly at the nanoscale. Scanning near-field optical microscopy (SNOM) is extensively used to probe the localization and dispersions of HPhPs at nanolength scales,[16] and for studying other types of mid-IR light/matter interactions[17,18] in polaritonic nanostructures, heterostructures, and metamaterials.[19–22] However, the spatial resolution of SNOM is typically limited to a few tens of nanometers due to the size of the probe tip. Recently, electron energy-loss spectroscopy (EELS) in the scanning transmission electron microscope (STEM) has emerged as an alternative, more precise technique, as it can access the mid-IR excitations with sub-Ångstrom spatial resolution and as low as 3 meV (24 cm^{-1}) spectral resolution.[23–25] The electron beam can access a number of low-energy excitations including localized phonon modes,[26–29] molecular vibrations,[30–33] and the HPhPs.[34–36] Moreover, the precise control of the probe enables on-demand excitation of polarization-dependent modes,[37] directly induced localized quasiparticle coupling,[38–40] and measurements of polariton dispersions.[36,41–43] Consequently, while EELS lacks the spectral resolution of SNOM, it possesses a key advantage in terms of spatial resolution, since the geometry of the tip and the sample fundamentally limit the maximum achievable resolution in SNOM. Beyond spatial resolution, monochromated EELS has several other benefits. For instance, in EELS, the spectral axis is recorded in parallel (as opposed to serially) enabling fast acquisition of hyperspectral datasets at a far denser sampling of vibrational frequencies to more comprehensively characterize the polaritonic response.[44] Moreover, while high harmonics

A. Konečná, F. J. García de Abajo
ICFO-Institut de Ciencies Fotoniques
The Barcelona Institute of Science and Technology
Castelldefels, Barcelona 08860, Spain

A. Konečná
Central European Institute of Technology
Brno University of Technology
Brno 612 00, Czech Republic
E-mail: andrea.konecna@vutbr.cz

J. Li, J. H. Edgar
Tim Taylor Department of Chemical Engineering
Kansas State University
Manhattan, KS 66506, USA

F. J. García de Abajo
ICREA-Institució Catalana de Recerca i Estudis Avançats
Passeig Lluís Campanys 23, Barcelona 08010, Spain

J. A. Hachtel
Center for Nanophase Materials Sciences
Oak Ridge National Laboratory
Oak Ridge, TN 37831, USA
E-mail: hachtelja@ornl.gov

The ORCID identification number(s) for the author(s) of this article can be found under https://doi.org/10.1002/smll.202103404.

DOI: 10.1002/smll.202103404

Small **2021**, 2103404 **2103404 (1 of 9)**

ADVANCED SCIENCE NEWS
www.advancedsciencenews.com

NANO · MICRO small
www.small-journal.com

can push the maximum potential spatial resolution of SNOM to <10 nm values,[45] the measurement and its interpretation are made more complex by the interaction of the tip and the sample. The converged electron probe is far-less sensitive to surface topographies/defects and sample geometries, and its sub-Ångstrom spatial-resolution is not sample-dependent. These factors combine to make monochromated EELS a powerful complement to SNOM, one that is extremely versatile and capable of expanding on relevant types of accessible samples for comprehensive nanoscale-resolved IR nanospectroscopy characterization.

Here, we discover several unique aspects of the nanoscale polaritonic response in hBN nanostructures by spectrally imaging HPhPs using monochromated STEM-EELS. A key property of HPhPs is geometrical confinement, and therefore, we examine the distinction between 1) HPhPs confined to the bulk of an exfoliated hBN flake and 2) HPhPs confined to the edge. Edge polaritons have been identified using EELS[36] and their dispersion measured by SNOM,[46] but here, we additionally provide EELS dispersion measurements of the edge polariton. The use of EELS is critical, as the high-spatial-resolution of the STEM accesses the high-wave-vector range of the edge polariton dispersion, revealing an extreme sensitivity to morphology of the flake wall. In addition, we find localization of polariton modes induced by either material contacting the surface of the hBN flake and the flake geometry itself. For all of our measurements, we carefully model the behavior of the polaritons using idealized systems and demonstrate that nanoscale heterogeneity in the sample is responsible for the formation of the localized polariton modes.

2. Results and Discussion

A key aspect of the EELS analysis is that the beam is both the source and the probe, enabling control of excitations through beam positioning. **Figure 1** illustrates how the probe position on and around an ≈18 nm thick hBN flake changes the excitation of HPhPs and the EEL spectra. Panels in Figure 1a–i show simulations of the electrostatic potential associated with the polariton excitation at 180, 185, and 190 meV (corresponding to 1451, 1492, and 1532 cm^{-1}, respectively) for probe positions 100 nm outside the flake, at the flake edge, and 100 nm inside the flake at each of these three mode energies. For all probe positions and energies the beam excites polaritons that propagate into the flake in all directions, as well as along the edge, even when the beam does not directly intersect the flake due to the "aloof" effect.[47] The primary difference between probe positions is the relative intensity of the bulk versus edge excitation, and the primary difference between energies are the

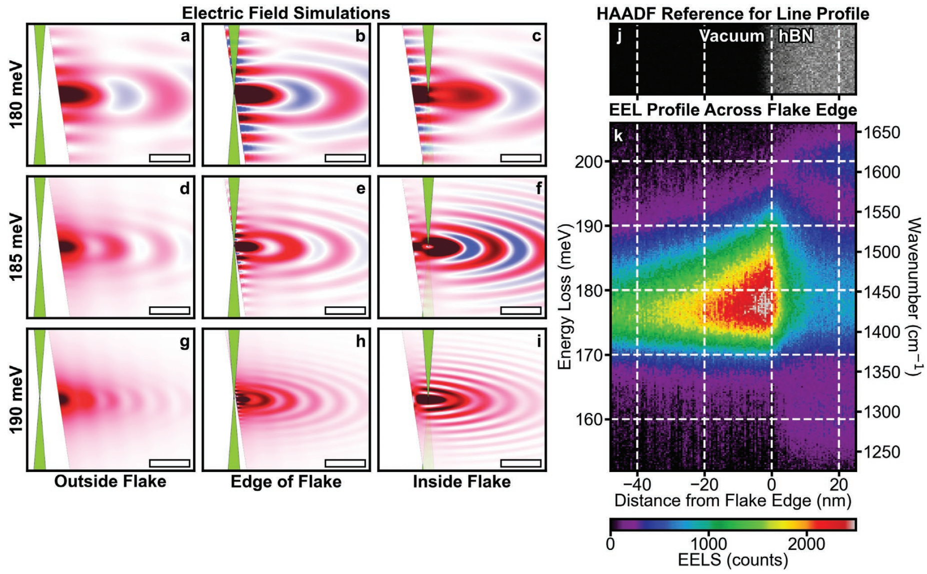

Figure 1. EELS excitation of hyperbolic phonon polaritons (HPhPs) at the edge of an hBN flake. a–i) Electric field simulations of the polaritonic response in an hBN flake for different probe positions: a,d,g) 100 nm outside the flake, b,e,h) at the flake edge, and c,f,i) 100 nm inside the flake at energy losses of a–c) 180 meV (1451 cm^{-1}), d–f) 185 meV (1492 cm^{-1}), and g–i) 190 meV (1532 cm^{-1}). Scale bars = 200 nm. j) HAADF reference image for line profile across hBN flake edge. k) Measured EELS line profile across the edge of an 18 nm thick flake demonstrating highly localized excitation of the edge-confined polaritons.

ADVANCED SCIENCE NEWS
www.advancedsciencenews.com

NANO · MICRO small
www.small-journal.com

wavelengths of the excitations in the flake. Note that at all energies, the wavelength of the edge excitation is visibly shorter than that of the bulk excitation.

These effects manifest in the EELS line profile of an hBN flake edge. A high-angle annular-dark-field (HAADF) image of a flake edge is shown in Figure 1j, with the EEL line profile in Figure 1k (flake thickness ≈12 nm). The EELS has a peak at ≈176 meV (1419 cm^{-1}) that is excited everywhere, corresponding to the bulk polariton, but when the probe is close to the edge, excitations at even higher energy losses are observed, corresponding to the edge polariton. Only when the probe is within ≈10 nm of the edge of the flake, is there a sufficiently strong excitation of the edge polariton to resolve it over the bulk-polariton signal, but, as illustrated in the simulations, it is still being excited at all probe positions. The high degree of localization of the edge polariton is surprising given that the aloof excitations are normally delocalized on the scale of hundreds of nm for comparable energies.[48] However, the result follows naturally from the high degree of confinement of the edge polariton to the flake edge, and the geometrical constraints on momentum transfer from the beam. When the beam is at the edge of the sample, it can transfer a large amount of momentum along the flake edge, enabling efficient excitation of the high-momentum (and hence high-energy-loss) branch of the polariton dispersions. Then, as the beam moves further away, only lower-momentum (lower-energy-loss) excitations are detected. The effect is most visible for the edge polariton, but it is also present in the aloof excitation of the bulk polariton, which continually redshifts as the probe moves further away from the sample (see Figure S1 in the Supporting Information).

Note that peaks at 160 and 200 meV (1290 and 1613 cm^{-1}) are observed when the beam does intersect the flake, corresponding to the transverse optical (TO) and longitudinal optical (LO) phonons, respectively. These excitations are only accessed through impact scattering, and are not part of the polaritonic response, but they still play an important role, as they define the limits of the Reststrahlen band in which the HPhPs are active.

The momentum selectivity afforded through careful probe positioning can go a step further to directly acquire HPhP dispersions with polariton interferometry.[34,36,41–43] This is exemplified for the bulk polariton dispersion in **Figure 2**. The experiment is shown schematically in Figure 2a: a line profile is acquired normal to the flake edge, in which polaritons that propagate directly toward the edge of the flake can reflect back resulting in interference. This is directly analogous to SNOM interferometry experiments, where the cantilevered tip is positioned at different distances away from the sample edge to isolate different polariton wavelengths and extract the dispersion.[16,18,19]

Such a line profile is plotted in Figure 2b, which shows that as the probe moves from deep (≈200 nm) into the flake toward the edge, a dispersive peak corresponding to constructive interference with reflected polaritons emerges. As a result, each probe position approximately corresponds to a specific wavelength for which interference is maximized. Thus, by fitting the peak energy as a function of distance from the edge, the entire dispersion is measured (see details of the fitting process expanded in Discussion S1 in the Supporting Information).

The interference peaks also emerge in our numerical modeling. Figure 2c,d shows the simulated EELS line profile, both broadened to match our experimental EELS energy resolution of 6 meV (Figure 2c) and as directly obtained from the simulation (Figure 2d). The broadened profile qualitatively and quantitatively matches with the EELS experiment, demonstrating that EELS accurately measures the bulk polariton interference. Note that both in the EELS experiment (Figure 2b) and in the simulation at EELS resolution (Figure 2c) the intensity on the high-energy side of the dispersive peak does not return to zero. The signal here corresponds to higher-order interference fringes, where instead of only completing one full period during propagation to the flake-edge and back, the polariton completes multiple periods. The full simulation (Figure 2d) clearly resolves many orders of these interference maxima, but only the first order peak can be individually identified at 6 meV energy resolution.

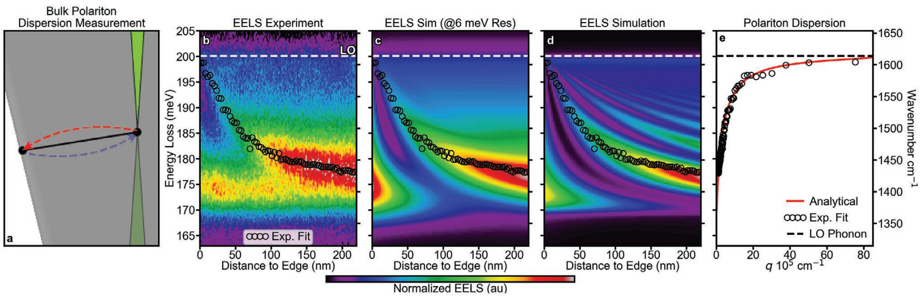

Figure 2. Hyperbolic polariton dispersion measurement in hBN flakes. a) Schematic of polariton interferometry for a bulk HPhP dispersion measurement. Polaritons reflected from the edge create constructive interference at different wave vectors of the HPhP dispersion. b) Experimental EELS line profile and fit of first-order interference peak (black circles). Simulated EELS line profiles c) broadened to match the 6 meV experimental energy resolution and d) at the native resolution of the calculation. e) The dispersion is achieved by transforming the distance to the edge in the EELS measurement considering an edge-reflection phase $\phi_R = \pi/2$. We compare the experimental dispersion to our analytical expression, showing good agreement out to high q values (flake thickness = 12 nm).

ADVANCED SCIENCE NEWS
www.advancedsciencenews.com

NANO · MICRO small
www.small-journal.com

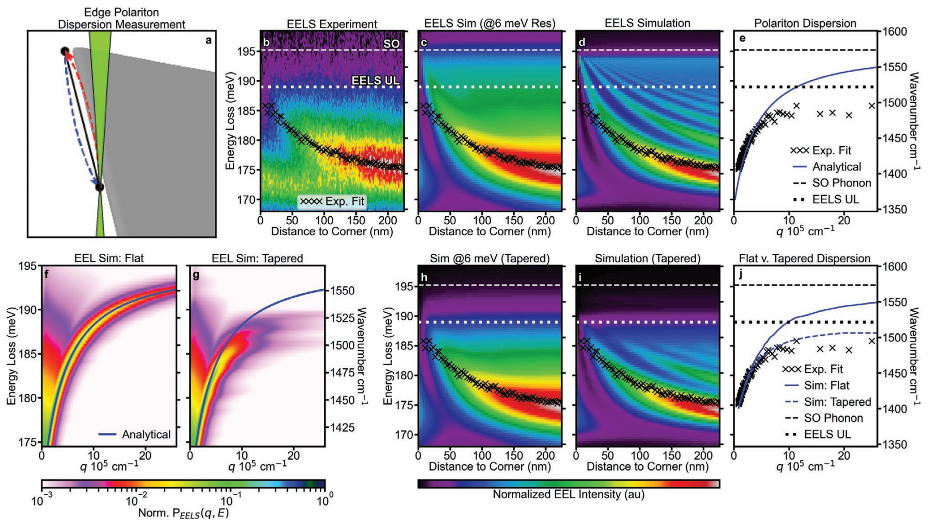

Figure 3. Polariton dispersion measurement at heterogeneous edges in hBN flakes. a) Schematic of polariton interferometry for an edge HPhP dispersion measurement. Here, edge-confined polaritons propagating along the flake wall can reflect off the corner to produce interference patterns and access the edge HPhP dispersion. Experimental and simulated EELS line profiles: b) experiment, c) spectrally broadened simulation to match EELS energy resolution, and d) the actual simulation. In panels (b)–(d), the upper limit of the measured EELS (at 189 meV, 1524 cm^{-1}) is marked with a dotted line and the theoretical upper limit (the SO phonon at 195.2 meV, 1574 cm^{-1}) is marked with a dashed line, demonstrating that measured and simulated EELS line scans have significantly different upper limits. e) EELS dispersion transformed with a reflection phase $\phi_R = \frac{3\pi}{4}$, compared to the analytical expression for the edge polariton, exhibiting significant discrepancies. Momentum-resolved EELS simulations for a f) 90° flat and g) 45° tapered edge, illustrating that high-q excitations are suppressed in the tapered edge (more closely resembling the excitations measured in the experimental line profile). h) Broadened and i) actual line profiles simulated for a tapered edge flake, producing a much better match to the experimental upper limit. j) Comparison of the experimental and simulated (for both flat and tapered edges) edge HPhP dispersions. The flake thickness is 12 nm.

We now transform the distances on the x-axis of the interference peak to dispersion values, using the transformation $q = \frac{2\pi - \phi_R}{2x}$, where q is the polariton wave vector and ϕ_R is a reflection phase that is acquired by the polariton upon reflection. Here, we use $\phi_R = \frac{\pi}{2}$, which presents the best match between theory and experiment (Figure S2 and Discussion S2, Supporting Information). The transformed experimental dispersion is directly compared the analytical expression (Equation (S1), Supporting Information) in Figure 2e, achieving excellent agreement almost all the way out to 10^7 cm^{-1}.

We can also apply the same interferometry technique to measure the dispersion of edge-confined polaritons, as shown in **Figure 3**. Here, an aloof line profile is acquired moving along the edge of the flake (the same flake as from Figure 2) toward a sharp corner, enabling excited edge polaritons to propagate to the corner, reflect, and interfere with one another (see schematic in Figure 3a). The experimental and simulated (with and without broadening) EELS line profiles for the edge polariton are shown in Figure 3b–d, respectively, with the experimental fitted peak values plotted as black crosses in all three panels. While a dispersive peak is observed in both experiment and simulation, the agreement with theory here is far worse than it is for the bulk polariton in Figure 2.

Perhaps most importantly, the upper limit of the spectral intensity from the polariton excitation appears to be ≈189 meV (1524 cm^{-1}), while it is at 195.2 meV (1574 cm^{-1}) in the simulations, corresponding to the energy of the high-q surface optical (SO) phonon.[34] Additionally, the EELS fits deviate from the simulated first-order peaks as the probe gets closer to the corner. The experimental dispersion is plotted in Figure 3e (using $\phi_R = \frac{3\pi}{4}$ for the transformation; see Figure S3 and Discussion S2 in the Supporting Information for more details), and when compared to the analytical expression (Equation (S4), Supporting Information), a significant deviation is observed. We attribute the effect to the nanoscale morphology of the edge wall. The above calculations treat the edge as a perfectly flat face, while real hBN flakes typically have significant heterogeneity and thickness variation along the edge. Figure S4 in the Supporting Information shows several hBN flakes and demonstrates how the edge-wall morphology takes on a highly variable and heterogeneous character during the exfoliation process. The bulk HPhPs in the interior of the flake exist in a nominally uniform environment, but the edge HPhPs are confined

ADVANCED SCIENCE NEWS
www.advancedsciencenews.com
NANO · MICRO small
www.small-journal.com

directly to this heterogeneous region. Edge heterogeneity can be partly included in the simulations by changing the model system from a flat 90° wall to a tapered 45° wall to account for the step-like thickness gradient normally found in exfoliated flakes. Simulations of the q-resolved EELS probability of an excitation at a flat and tapered hBN flake edge are shown in Figure 3f,g, respectively. The flat edge probability exhibits high intensity directly along the analytical dispersion, but the tapered edge probability is both suppressed and redshifted from the analytical dispersion, especially at high-q, similar to the experiment.

The simulated (with and without broadening) EELS line profiles for the tapered edge are shown in Figure 3h,i. Here, the simulated and the experimental upper limit are in good agreement, and the fitted experimental peaks match the simulated first-order peak much more closely. The dispersions at the flat and tapered edge are determined by fitting the dispersive peaks in Figure 3c,h, respectively, and are compared to the experimental dispersion in Figure 3j. The flat-edge simulation replicates the analytical dispersion in Figure 3e, while the tapered-edge simulation is in excellent agreement with the experimentally retrieved dispersion. The comparison emphasizes the power of EELS as a complementary technique to SNOM. While the spatial variation of the dispersive peak is not significant and can be straightforwardly detected at the resolution of SNOM, it is the measurements within only a few nanometers of the flake edge where the real dispersion varies significantly from the analytical form. The spatial resolution of the STEM readily measures polaritons at this length scale, allowing us to reach far higher q values in a polariton interferometry measurement. Conversely, SNOM typically can only probe smaller q values $<10^6$ cm^{-1},[16,36,46] which is not sufficient to see the limiting behavior induced by the edge heterogeneity. However, as revealed by Figure 3e, the deviations between the analytical and experimental edge polariton expressions only become significant above 10^6 cm^{-1}, necessitating the high-q interferometry in EELS with a well-defined focused probe.

The bulk polaritons can also be modified by subtle nanoscale environmental and geometric heterogeneity. In **Figure 4**, we consider the effect of materials contacting the surface of the hBN flakes. All our samples are supported on lacey carbon TEM grids, nominally thought to only support the flake and not influence the optical response substantially. However, hyperbolic polaritons are extremely sensitive to the surrounding environment,[41] and they can scatter and interact with the bordering region in a predictable manner.[49,50] Thus, the lacey carbon that supports the flake also directly induces localized polariton

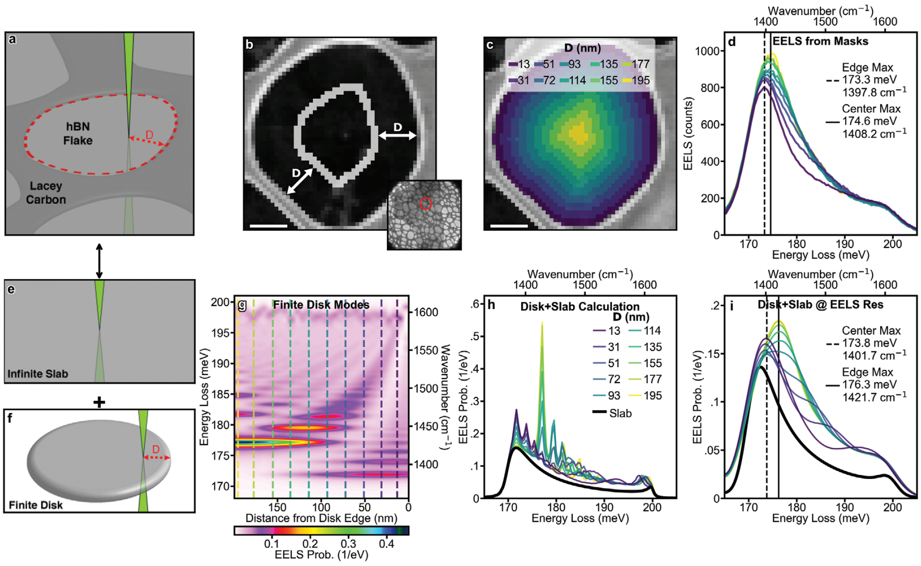

Figure 4. Localized polariton modes induced by environmental heterogeneity. a) Schematic of experiment to probe polariton interaction with supporting lacey carbon. b) HAADF reference image of the region of interest. Inset: Low-magnification STEM image of the entire hBN flake of thickness 8 nm with the hole marked in red. c) Different regions of the selected hole in lacey carbon classified by the average distance D from carbon edge. d) Spectra acquired from regions highlighted in panel (c). Scale bars = 100 nm. Spectra in panel (d) can be described as a combination of the e) infinite slab response expected in the center of a large flake with f) finite-disk-like modes induced by the lacey carbon. g) Calculated modes for a finite hBN disk with 200 nm radius. D values from panels (c) and (d) are indicated through color-coordinated contours and lines. h) Simulated EELS spectra for the same D values as in panels (c) and (d), obtained by combining the spectrum of an infinite slab signal (black) with the D-dependent disk modes (color). i) Spectra in panel (h) broadened to match the EELS energy resolution, showing qualitative agreement with experiment in panel (d).

ADVANCED SCIENCE NEWS
www.advancedsciencenews.com
NANO · MICRO small
www.small-journal.com

modes in the flake. A schematic of our experiment is shown in Figure 4a. We find a hole in the lacey carbon underneath a large flake (far from the edges) and probe the hole region as a function of distance from the carbon edge (flake thickness ≈8 nm). Figure 4b shows a HAADF image of the region used for the hyperspectral acquisition, centered around an ≈400 nm diameter hole in the lacey carbon. For reference, the inset contains a low-magnification STEM image of the flake with the selected hole highlighted.

The hyperspectral dataset is partitioned into regions at different average distances D away from the carbon (i.e., the white ring in Figure 4b). We use ten different distances (highlighted by different colors in Figure 4c) and plot the average EELS signal from each of them in Figure 4d. With no carbon/hBN interaction, the EELS signal would be uniform in all ten regions, which is clearly not the case. The intensity of the bulk polariton peak increases by ≈20% compared to the edge and it blueshifts slightly (173.3to 174.6 meV or 1398 to 1408 cm^{-1}). In addition, at the outmost region (D = 13 nm), there is a shoulder at about 190 meV (1532 cm^{-1}), which redshifts to 185 meV (1492 cm^{-1}) for the D = 51 nm region, and then further up toward the edge of the dominant peak as the probe gets closer to the center of the hole. The effect can be understood by considering different pathways for polaritons excited by the beam: they can propagate past the carbon, or they can be reflected off it in analogy to the reflection observed at the edge of a disk. Thus, we describe the EELS signal as a combination of the two effects: infinite slab excitations (Figure 4e) and finite disk excitations (Figure 4f).

The calculated EEL spectra, showing the localized phonon polariton modes of a 400 nm diameter finite hBN disk, are plotted in Figure 4g. We identify multipole modes excited at the edge of the disk, breathing modes excited at the center, and hybrid modes emerging as combination of those two (analogous to localized surface plasmon modes[51,52]). We select finite-disk spectra to match the average D from the regions in Figure 4c, and then add them to the infinite slab spectrum, and finally plot the combination in Figure 4h. The results after broadening with the 6 meV resolution of our microscope are plotted in Figure 4i.

The superposition of slab and disk excitations reproduces the major effects observed in the experiment, exhibiting enhanced intensity and a small blueshift of the peak energy at the center of the flake, which can now be attributed to the different localizations of the multipole and breathing modes. Moreover, Figure 4g shows that the hybrid modes have a dispersive change in energy as the probe gets closer to the edge, explaining the secondary position-dependent peak in the EELS data, which is also reproduced in the calculations. The localized disk modes can be further visualized using linear unmixing techniques as shown in Figure S5 in the Supporting Information.

The geometry of the flake boundaries also has a dominant effect on the bulk polariton response. Here, we return to the flake used in Figures 2 and 3, which possessed a sharp corner, and acquire a hyperspectral image from the entire region (**Figure 5**). The probe interacts with both linear edges of the flake simultaneously, as shown schematically in Figure 5a. In Figure 5b–e, we show experimental energy-filtered EELS images for 0.5 meV wide windows centered at 180, 185, 190, and 195 meV (1452, 1492, 1532, and 1573 cm^{-1}), respectively, capturing the 2D interference pattern at the hBN corner. The corresponding EELS simulations are shown in Figure 5f–i. The latter shows a much larger degree of interference detail (especially at higher energies) compared to the experimental EELS with limited energy resolution. However, several key aspects of the interference patterns are still clearly discernable in the EELS experiment. Notably, interference minima forming dark fringes along the flake edges are observed in experiment and to exhibit similar width and energy dependence as the dark fringes in the simulations. The simulations also show higher-order interference minima and maxima deeper into the flake, increasing in number at the higher energies, although such interference is mostly blurred out at the 6 meV energy resolution of our EELS

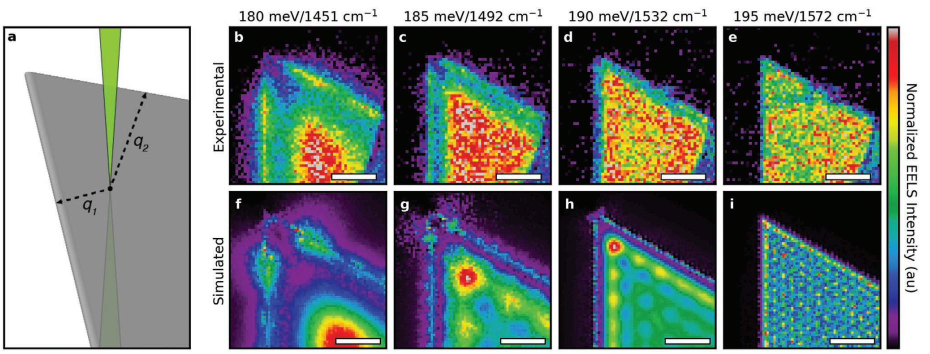

Figure 5. Phonon polariton mapping in the corner of an hBN flake. a) Schematic of the experiment geometry. b–e) Experimental measurements. f–i) Simulations. The maps show the simultaneous existence of both bulk and edge HPhPs, producing both positive and negative interference along the surface and at the edges, respectively, and accompanied by a localized mode emerging close to the corner tip. Scale bars = 100 nm; flake thickness = 12 nm.

instrument. However, even these higher-order fringes are present in experiment under some circumstances: note that in both the 185 and 190 meV experimental images, bright spots/fringes emerge from the positive interference. Additionally, the triangle-like geometry generates a localized-edge-polariton corner mode that is most pronounced in the 180 and 185 meV simulations as a bright spot on the edge of the flake (see further details in Figure S6 and Discussion S3 in the Supporting Information), while faint, comparable bright spots are present at the same position in the EELS image at 180 meV (see detectable features highlighted directly in Figure S7 in the Supporting Information).

Last, note that far away from the corner the signal is dominated by the interaction with the nearest edge. In contrast, close to the tip (within 100 nm), the polaritonic response is strongly influenced by both edges simultaneously and the full 2D geometry is needed to understand the response. This 2D interference is observed in the experiment almost as clearly as in the theory, demonstrating the ability of STEM-EELS to map constructive and destructive interference in nanostructured polaritonic materials.

3. Conclusion

We have revealed important characteristics of hyperbolic phonon polaritons in hBN flakes by controllably exciting and detecting these modes using a nanoscale electron probe. The polaritons are extremely sensitive to the surrounding environment and geometry, which enable us to probe a wide range of polariton properties including the dispersions of edge and bulk HPhPs, the emergence of localized modes induced by the surrounding environment and the flake geometry, and the presence of 2D interference patterns in nanostructured flakes. Our interferometry measurements show that, at high wave vector, nanoscale heterogeneity at the flake edge significantly modifies the real dispersion of the edge-confined polaritons, in a way that cannot be resolved by traditional infrared optical experiments. The bulk-confined polaritons are also highly sensitive to local nanoscale heterogeneity and can create 2D interference that suppresses or enhances the excitation of HPhPs at nanolength scales. Interaction of such heterogeneities within the material gives rise to localized modes determined by morphology. The combined use of aberration-correction and monochromation reduces the length scales that can be effectively characterized with interferometry, while it provides access to the high-q branch of polariton dispersions and further allows us to rigorously characterize heterogeneity in the sample to reveal its influence on the polaritonic response. Furthermore, by using EELS, we can directly correlate signals across multiple energy regimes to compare the vibrational response (ultralow-loss regime), the electronic structure (low-loss regime), and the chemical composition (core-loss regime). Monochromated EELS elevates the potential design and understanding of nanophotonics in structured hBN flakes by providing precision control over both measurement and excitation of the nanoscale optical response to illuminate the innerworkings of complex photonics devices operating in the mid-infrared.

4. Experimental Section

Sample Growth: hBN crystals were grown at atmospheric pressure from a molten iron-chromium solution using a ^{10}B isotopically enriched boron source.[53] Flakes were then chemically exfoliated and transferred onto lacey carbon TEM grids, where the flakes were only supported by the thin carbon web. The sizes of the flakes varied from tens of micrometers to tens of nanometers in diameter and a few layers to a few hundred nanometers in thickness. The flakes used in experiment were chosen as the ones with the most uniform thickness and cleanest edges, as determined from low magnification STEM imaging for monochromated EELS analysis.

STEM-EELS Experiment: All EELS spectra were acquired on a Nion aberration-corrected high-energy-resolution monochromated EELS-STEM (HERMES) equipped with the Nion Iris Spectrometer,[54] operated at 30 kV with a convergence angle of 27 mrad and a collection angle of 25 mrad. All spectra were measured to have an energy resolution between 5.5 and 6.5 meV, as measured by the elastic scattering/zero loss peak (ZLP) full-width at half-maximum. In all acquisitions, a power law background was used to fit the spectral regions directly before (120–140 meV) and after (220–250 meV) the Rehstrahlen band, and then subtracted to remove contributions from the ZLP tail.

Acquisition details were as follows: The line profile in Figure 1 consisted of 150 spectra, with a calibration of 0.5 nm per pixel, a dispersion of 0.22 meV per spectrometer channel, and an acquisition time of 3 s per spectrum. The line profiles in Figures 2 and 3 were both 2D spectrum images binned in the axis normal to the dispersive direction to create line profiles. For the bulk polariton measurement, a 9×192 pixel spectrum image was acquired and subsequently vertically binned across all nine pixels, with a calibration of 1.5625 nm per pixel, a dispersion of 0.40 meV per spectrometer channel, and an acquisition time of 128 ms per pixel. For the edge polariton measurement, a 163×20 pixel spectrum image was acquired and binned across only the two pixels closest to the edge extending into the flake (region for binning shown in Figure S3 in the Supporting Information). Including pixels in the edge of the flake for horizontal binning did not vary the measured dispersion significantly, and only had the effect of including small contributions from the LO phonon, which made the upper limit of the measured dispersion more difficult to quantify. The spectrum image had a calibration of 1.5703 nm per pixel, a dispersion of 0.40 meV per spectrometer channel, and an acquisition time of 500 ms per pixel. For Figure 3, a 50×50 pixels spectrum image was acquired with a calibration of 10 nm per pixel, a dispersion of 0.40 meV per spectrometer channel, and an acquisition time of 400 ms per pixel. For Figure 4, a 64×64 pixel spectrum image was acquired, with a calibration of 4 nm per pixel, a dispersion of 0.40 meV per spectrometer channel, and an acquisition time of 400 ms per pixels.

Videos of the spectrum images for the bulk polariton, edge polariton, finite disk, and corner analyses were also included, where a normalized 2D intensity is shown at frame-by-frame for all the energies in the Reststrahlen band (see the Supporting Information).

The thickness of the flakes (18 nm in Figure 1, 12 nm in Figures 2, 3, and 5, and 8 nm in Figure 4) were determined by comparing the experimental energy of the nondispersive polariton peak to simulations, as is shown in depth in Figure S12 in the Supporting Information.

Calibration and Validation of Datasets: Many factors can strongly influence the measured polariton dispesrsion, which need to be properly accounted for. In this analysis, the specific pixel was included in the dataset deemed as the edge of the flake (a nontrivial assignment), the calibration of the spectrometer, which is difficult to carry out more accurately than around 1% at the high dispersions used in monochromated EELS, and the reflection phase. The measurements were calibrated to the LO phonon at 200.1 meV in the BN flakes, the energy of which was not dependent on flake thickness or geometry. For the dataset in Figure 1, it was found that a dispersion correction of 0.5% was needed. The datasets in Figures 2–5, which were all performed on the same day at the same dispersion, needed a dispersion correction of 1%. For the reflection phases and the edge pixel determination, which only applied to

ADVANCED SCIENCE NEWS
www.advancedsciencenews.com
NANO · MICRO small
www.small-journal.com

Figures 2 and 3, the simulated line profiles were compared to determine the correct values. This calibration and selection process is shown in detail in Discussion S2 in the Supporting Information.

Simulations: All calculations were performed within the framework of classical macroscopic electrodynamics, which is known to reproduce very well the interaction of focused electron probes with optical excitations[55] in nanostructures such as those considered in this work. Analytical expressions were used to calculate EELS spectra when dealing with an electron beam interacting with an infinite hBN slab. For more complex geometries (linear edge, corners, and disks), numerical solvers of the Poisson and Maxwell equations implemented in the commercial software Comsol Multiphysics were used. Further details on the formalism, analytical expressions, and models, as well as setting parameters for the numerical solvers, are described in Discussion S3 in the Supporting Information.

Supporting Information

Supporting Information is available from the Wiley Online Library or from the author.

Acknowledgements

Microscopy experiments were conducted at the Center for Nanophase Materials Sciences, which is a DOE Office of Science User Facility using instrumentation within ORNL's Materials Characterization Core provided by UT-Battelle, LLC, under Contract No. DE-AC05- 00OR22725 with the DOE and sponsored by the Laboratory Directed Research and Development Program of Oak Ridge National Laboratory, managed by UT-Battelle, LLC, for the U.S. Department of Energy (JAH). A.K. and F.J.G.d.A. acknowledge support from the European Research Council (Advanced Grant No. 789104eNANO), the European Commission (Horizon 2020 Grants No. FET-Proactive 101017720-EBEAM and No. FET-Open 964591-SMART-electron), and the Spanish MINECO (SEV2015-0522). Support for hBN crystal growth from the Office of Naval Research (Award No. N00014-20-1-2474) is appreciated (J.L. and J.H.E.).

Conflict of Interest

The authors declare no conflict of interest.

Data Availability Statement

The data that support the findings of this study are available from the corresponding author upon reasonable request.

Keywords

2D materials, hexagonal boron nitride, hyperbolic phonon polaritons, infrared spectroscopy, monochromated electron energy-loss spectroscopy, nanophotonics, optoelectronics

Received: June 10, 2021
Revised: July 29, 2021
Published online:

[1] H. A. Atwater, A. Polman, *Nat. Mater.* **2010**, *9*, 205.
[2] F. Xia, H. Wang, D. Xiao, M. Dubey, A. Ramasubramaniam, *Nat. Photonics* **2014**, *8*, 899.
[3] F. Hu, Y. Luan, M. E. Scott, J. Yan, D. G. Mandrus, X. Xu, Z. Fei, *Nat. Photonics* **2017**, *11*, 356.
[4] F. Lu, M. Jin, M. A. Belkin, *Nat. Photonics* **2014**, *8*, 307.
[5] Z. Han, P. Lin, V. Singh, L. Kimerling, J. Hu, K. Richardson, A. Agarwal, D. T. H. Tan, *Appl. Phys. Lett.* **2016**, *108*, 141106.
[6] Y. Wu, Z. Hu, X.-T. Kong, J. C. Idrobo, A. G. Nixon, P. D. Rack, D. J. Masiello, J. P. Camden, *Phys. Rev. B* **2020**, *101*, 085409.
[7] A. Poddubny, I. Iorsh, P. Belov, Y. Kivshar, *Nat. Photonics* **2013**, *7*, 948.
[8] A. Nemilentsau, T. Low, G. Hanson, *Phys. Rev. Lett.* **2016**, *116*, 066804.
[9] S. Dai, Q. Ma, T. Andersen, A. S. Mcleod, Z. Fei, M. K. Liu, M. Wagner, K. Watanabe, T. Taniguchi, M. Thiemens, F. Keilmann, P. Jarillo-Herrero, M. M. Fogler, D. N. Basov, *Nat. Commun.* **2015**, *6*, 6963.
[10] E. Yoxall, M. Schnell, A. Y. Nikitin, O. Txoperena, A. Woessner, M. B. Lundeberg, F. Casanova, L. E. Hueso, F. H. L. Koppens, R. Hillenbrand, *Nat. Photonics* **2015**, *9*, 674.
[11] D. N. Basov, M. M. Fogler, F. J. García de Abajo, *Science* **2016**, *354*, aag1992.
[12] M. Autore, P. Li, I. Dolado, F. J. Alfaro-Mozaz, R. Esteban, A. Atxabal, F. Casanova, L. E. Hueso, P. Alonso-González, J. Aizpurua, A. Y. Nikitin, S. Vélez, R. Hillenbrand, *Light: Sci. Appl.* **2018**, *7*, 17172.
[13] A. J. Giles, S. Dai, I. Vurgaftman, T. Hoffman, S. Liu, L. Lindsay, C. T. Ellis, N. Assefa, I. Chatzakis, T. L. Reinecke, J. G. Tischler, M. M. Fogler, J. H. Edgar, D. N. Basov, J. D. Caldwell, *Nat. Mater.* **2018**, *17*, 134.
[14] J. D. Caldwell, I. Aharonovich, G. Cassabois, J. H. Edgar, B. Gil, D. N. Basov, *Nat. Rev. Mater.* **2019**, *4*, 552.
[15] S. Dai, W. Fang, N. Rivera, Y. Stehle, B.-Y. Jiang, J. Shen, R. Y. Tay, C. J. Ciccarino, Q. Ma, D. Rodan-Legrain, P. Jarillo-Herrero, E. H. T. Teo, M. M. Fogler, P. Narang, J. Kong, D. N. Basov, *Adv. Mater.* **2019**, *31*, 1806603.
[16] S. Dai, Z. Fei, Q. Ma, A. S. Rodin, M. Wagner, A. S. McLeod, M. K. Liu, W. Gannett, W. Regan, K. Watanabe, T. Taniguchi, M. Thiemens, G. Dominguez, A. H. C. Neto, A. Zettl, F. Keilmann, P. Jarillo-Herrero, M. M. Fogler, D. N. Basov, *Science* **2014**, *343*, 1125.
[17] J. D. Caldwell, L. Lindsay, V. Giannini, I. Vurgaftman, T. L. Reinecke, S. A. Maier, O. J. Glembocki, *Nanophotonics* **2015**, *4*, 44.
[18] Z. Yuan, R. Chen, P. Li, A. Y. Nikitin, R. Hillenbrand, X. Zhang, *ACS Photonics* **2020**, *7*, 2610.
[19] S. Dai, Q. Ma, M. K. Liu, T. Andersen, Z. Fei, M. D. Goldflam, M. Wagner, K. Watanabe, T. Taniguchi, M. Thiemens, F. Keilmann, G. C. A. M. Janssen, S.-E. Zhu, P. Jarillo-Herrero, M. M. Fogler, D. N. Basov, *Nat. Nanotechnol.* **2015**, *10*, 682.
[20] L. V. Brown, M. Davanco, Z. Sun, A. Kretinin, Y. Chen, J. R. Matson, I. Vurgaftman, N. Sharac, A. J. Giles, M. M. Fogler, T. Taniguchi, K. Watanabe, K. S. Novoselov, S. A. Maier, A. Centrone, J. D. Caldwell, *Nano Lett.* **2018**, *18*, 1628.
[21] P. Li, I. Dolado, F. J. Alfaro-Mozaz, F. Casanova, L. E. Hueso, S. Liu, J. H. Edgar, A. Y. Nikitin, S. Vélez, R. Hillenbrand, *Science* **2018**, *359*, 892.
[22] S. Dai, J. Zhang, Q. Ma, S. Kittiwatanakul, A. McLeod, X. Chen, S. G. Corder, K. Watanabe, T. Taniguchi, J. Lu, Q. Dai, P. Jarillo-Herrero, M. Liu, D. N. Basov, *Adv. Mater.* **2019**, *31*, 1900251.
[23] O. L. Krivanek, T. C. Lovejoy, N. Dellby, T. Aoki, R. W. Carpenter, P. Rez, E. Soignard, J. Zhu, P. E. Batson, M. J. Lagos, R. F. Egerton, P. A. Crozier, *Nature* **2014**, *514*, 209.
[24] J. A. Hachtel, A. R. Lupini, J. C. Idrobo, *Sci. Rep.* **2018**, *8*, 5637.
[25] N. Dellby, T. Lovejoy, G. Corbin, N. Johnson, R. Hayner, M. Hoffman, P. Hrncrik, B. Plotkin-Swing, D. Taylor, O. Krivanek, *Microsc. Microanal.* **2020**, *26*, 1804.
[26] M. J. Lagos, A. Trügler, U. Hohenester, P. E. Batson, *Nature* **2017**, *543*, 529.

[27] H. Lourenço-Martins, M. Kociak, *Phys. Rev. X* **2017**, *7*, 041059.
[28] F. S. Hage, G. Radtke, D. M. Kepaptsoglou, M. Lazzeri, Q. M. Ramasse, *Science* **2020**, *367*, 1124.
[29] X. Li, G. Haberfehlner, U. Hohenester, O. Stéphan, G. Kothleitner, M. Kociak, *Science* **2021**, *371*, 1364.
[30] P. Rez, T. Aoki, K. March, D. Gur, O. L. Krivanek, N. Dellby, T. C. Lovejoy, S. G. Wolf, H. Cohen, *Nat. Commun.* **2016**, *7*, 10945.
[31] J. A. Hachtel, J. Huang, I. Popovs, S. Jansone-Popova, J. K. Keum, J. Jakowski, T. C. Lovejoy, N. Dellby, O. L. Krivanek, J. C. Idrobo, *Science* **2019**, *363*, 525.
[32] S. M. Collins, D. M. Kepaptsoglou, J. Hou, C. W. Ashling, G. Radtke, T. D. Bennett, P. A. Midgley, Q. M. Ramasse, *Nano Lett.* **2020**, *20*, 1272.
[33] K. March, K. Venkatraman, C. D. Truong, D. Williams, P.-L. Chiu, P. Rez, *J. Microsc.* **2021**, *282*, 215.
[34] A. A. Govyadinov, A. Konečná, A. Chuvilin, S. Vélez, I. Dolado, A. Y. Nikitin, S. Lopatin, F. Casanova, L. E. Hueso, J. Aizpurua, R. Hillenbrand, *Nat. Commun.* **2017**, *8*, 95.
[35] W. Dong, R. Qi, T. Liu, Y. Li, N. Li, Z. Hua, Z. Gao, S. Zhang, K. Liu, J. Guo, P. Gao, *Adv. Mater.* **2020**, *32*, 2002014.
[36] N. Li, X. Guo, X. Yang, R. Qi, T. Qiao, Y. Li, R. Shi, Y. Li, K. Liu, Z. Xu, L. Liu, F. J. García de Abajo, Q. Dai, E.-G. Wang, P. Gao, *Nat. Mater.* **2021**, *20*, 43.
[37] G. Radtke, D. Taverna, N. Menguy, S. Pandolfi, A. Courac, Y. Le Godec, O. L. Krivanek, T. C. Lovejoy, *Phys. Rev. Lett.* **2019**, *123*, 256001.
[38] A. Konečná, T. Neuman, J. Aizpurua, R. Hillenbrand, *ACS Nano* **2018**, *12*, 4775.
[39] A. B. Yankovich, B. Munkhbat, D. G. Baranov, J. Cuadra, E. Olsén, H. Lourenço-Martins, L. H. G. Tizei, M. Kociak, E. Olsson, T. Shegai, *Nano Lett.* **2019**, *19*, 8171.
[40] L. H. G. Tizei, V. Mkhitaryan, H. Lourenço-Martins, L. Scarabelli, K. Watanabe, T. Taniguchi, M. Tencé, J.-D. Blazit, X. Li, A. Gloter, A. Zobelli, F.-P. Schmidt, L. M. Liz-Marzán, F. J. García de Abajo, O. Stéphan, M. Kociak, *Nano Lett.* **2020**, *20*, 2973.
[41] D. T. Schoen, A. C. Atre, A. García-Etxarri, J. A. Dionne, M. L. Brongersma, *Nano Lett.* **2015**, *15*, 120.
[42] Y. Li, R. Qi, R. Shi, N. Li, P. Gao, *Sci. Bull.* **2020**, *65*, 820.
[43] M. Taleb, F. Davoodi, F. Diekmann, K. Rossnagel, N. Talebi, *arXiv preprint arXiv:2101.01465* **2021**.
[44] Y. Kurman, R. Dahan, H. H. Sheinfux, K. Wang, M. Yannai, Y. Adiv, O. Reinhardt, L. H. G. Tizei, S. Y. Woo, J. Li, J. H. Edgar, M. Kociak, F. H. L. Koppens, I. Kaminer, *Science* **2021**, *372*, 1181.
[45] S. Mastel, A. A. Govyadinov, C. Maissen, A. Chuvilin, A. Berger, R. Hillenbrand, *ACS Photonics* **2018**, *5*, 3372.
[46] P. Li, I. Dolado, F. J. Alfaro-Mozaz, A. Y. Nikitin, F. Casanova, L. E. Hueso, S. Vélez, R. Hillenbrand, *Nano Lett.* **2017**, *17*, 228.
[47] P. A. Crozier, *Ultramicroscopy* **2017**, *180*, 104.
[48] J. A. Hachtel, J. R. Jokisaari, O. L. Krivanek, J. C. Idrobo, R. F. Klie, *Microsc. Today* **2021**, *29*, 36.
[49] T. G. Folland, A. Fali, S. T. White, J. R. Matson, S. Liu, N. A. Aghamiri, J. H. Edgar, R. F. Haglund, Y. Abate, J. D. Caldwell, *Nat. Commun.* **2018**, *9*, 4371.
[50] A. Fali, S. T. White, T. G. Folland, M. He, N. A. Aghamiri, S. Liu, J. H. Edgar, J. D. Caldwell, R. F. Haglund, Y. Abate, *Nano Lett.* **2019**, *19*, 7725.
[51] F.-P. Schmidt, H. Ditlbacher, U. Hohenester, A. Hohenau, F. Hofer, J. R. Krenn, *Nano Lett.* **2012**, *12*, 5780.
[52] F. P. Schmidt, H. Ditlbacher, F. Hofer, J. R. Krenn, U. Hohenester, *Nano Lett.* **2014**, *14*, 4810.
[53] J. Li, C. Elias, G. Ye, D. Evans, S. Liu, R. He, G. Cassabois, B. Gil, P. Valvin, B. Liu, J. H. Edgar, *J. Mater. Chem. C* **2020**, *8*, 9931.
[54] O. L. Krivanek, T. C. Lovejoy, N. Dellby, R. W. Carpenter, *Microscopy* **2013**, *62*, 3.
[55] F. J. García de Abajo, *Rev. Mod. Phys.* **2010**, *82*, 209.

Check for updates

RESEARCH ARTICLE

NANO · MICRO small
www.small-journal.com

Low-Loss Tunable Infrared Plasmons in the High-Mobility Perovskite (Ba,La)SnO_3

Hongbin Yang, Andrea Konečná, Xianghan Xu, Sang-Wook Cheong, Eric Garfunkel, F. Javier García de Abajo, and Philip E. Batson*

$BaSnO_3$ exhibits the highest carrier mobility among perovskite oxides, making it ideal for oxide electronics. Collective charge carrier oscillations known as plasmons are expected to arise in this material, thus providing a tool to control the nanoscale optical field for optoelectronics applications. Here, the existence of relatively long-lived plasmons supported by high-mobility charge carriers in La-doped $BaSnO_3$ (BLSO) is demonstrated. By exploiting the high spatial and energy resolution of electron energy-loss spectroscopy with a focused beam in a scanning transmission electron microscope, the dispersion, confinement ratio, and damping of infrared localized surface plasmons (LSPs) in BLSO nanoparticles are systematically investigated. It is found that LSPs in BLSO exhibit a high degree of spatial confinement compared to those sustained by noble metals and have relatively low losses and high quality factors with respect to other doped oxides. Further analysis clarifies the relation between plasmon damping and carrier mobility in BLSO. The results support the use of nanostructured degenerate semiconductors for plasmonic applications in the infrared region and establish a solid alternative to more traditional plasmonic materials.

1. Introduction

Noble metals are the go-to choices for applications in plasmonics because of their relatively low optical losses and robustness,[1–5] with intrinsic bulk plasmons emerging in the visible regime. Although surface plasmons in these materials can be pushed down to the near infrared (IR) by shaping the materials into structures of high aspect ratio, this solution is not ideal, and alternative materials with their bulk plasmon frequency already in that spectral range would be useful. Additionally, traditional plasmonic metals do not allow for active tuning or ultrafast optical switching because of their high electron density, to which added doping charges can only contribute negligibly. Alkali metals present lower electron densities that place their plasmons in the near-IR-visible region with extremely low losses,[6] but these materials are unstable under ambient conditions and thus challenging to integrate in actual devices with long-term stability. The appeal of tunable carrier density, high carrier mobility, and good chemical stability has motivated the search for alternative plasmonic materials,[7] including transparent conducting oxides (TCO),[8,9] transition metal nitrides,[8,10] chalcogenides,[11] and alloys,[12] as well as two-dimensional materials,[13] especially graphene[14–16] and black phorphous.[17,18] Among these, doped binary oxides, such as In_2O_3, SnO_2, ZnO, and CdO, have been intensively studied in various geometries for their IR plasmonic properties.[19–22] More recently, semi-metallic perovskite oxides $SrBO_3$ (with B = Ge, V, or Nb)[23–26] have also been identified as alternative IR plasmonic materials.

H. Yang, E. Garfunkel
Department of Chemistry and Chemical Biology
Rutgers University
Piscataway, NJ, USA
E-mail: hongbin.yang@rutgers.edu

A. Konečná, F. J. García de Abajo
ICFO-Institut de Ciencies Fotoniques
The Barcelona Institute of Science and Technology
Castelldefels, Barcelona 08860, Spain

The ORCID identification number(s) for the author(s) of this article can be found under https://doi.org/10.1002/smll.202106897.

DOI: 10.1002/smll.202106897

A. Konečná
Central European Institute of Technology
Brno University of Technology
Brno 61200, Czech Republic

X. Xu, S.-W. Cheong, E. Garfunkel, P. E. Batson
Department of Physics and Astronomy
Rutgers University
Piscataway, NJ, USA

X. Xu, S.-W. Cheong
Rutgers Center for Emergent Materials
Rutgers University
Piscataway, NJ, USA

F. J. García de Abajo
ICREA-Institució Catalana de Recerca i Estudis Avançats
Passeig Lluís Companys 23, Barcelona 08010, Spain

ADVANCED SCIENCE NEWS
www.advancedsciencenews.com
NANO · MICRO small
www.small-journal.com

The combination of appealing plasmonic and electronic properties in a single material adds extra versatility in the design of actual devices. In search of such materials, we consider $BaSnO_3$ (BSO), which is a wide band gap (2.9 to 3.2 eV)[27] perovskite oxide that holds great promises for applications in oxide electronics.[28] This material has a room-temperature carrier mobility >300 cm^2 V^{-1} s^{-1} in single crystals,[29,30] which is the highest among all transparent conductors and perovskite oxides, exceeding III–V semiconductors at high carrier densities.[31] This indium-free TCO also has exceptional stability of oxygen vacancies even under extreme biasing conditions[32] or at elevated temperatures.[29] Although several experimental works have studied the IR optical properties of bulk crystals,[33] thin films,[34] and ensembles of nanocrystals,[35] individual La-doped BSO (BLSO) nanoparticles with well-defined doping and shape have not been characterized yet. To that end, we exploit electron energy-loss spectroscopy (EELS) in a monochromated scanning transmission electron microscope (STEM), which allows for the spatial and spectral characterization of low-energy excitations at the single-particle level.[36,37]

In this work, we systematically study plasmons emerging in BLSO nanocrystals with well-defined shapes by measuring their spectral and spatial characteristics using state-of-the-art STEM-EELS.[37,38] We observe IR plasmons in the 50–800 meV energy range, and image their spatial distribution and localization in BLSO nanorods. We further explore the doping limit of La in BSO and the associated plasmon energies, which allow covering a wide range of IR frequencies reaching up to the telecom wavelength at 1.55 µm. In addition, we characterize the surface plasmon dispersion, confinement ratio, lifetime, and quality factor in individual nanoparticles with varying sizes. By comparing our results with recent studies of plasmons in conventional plasmonic metals (Au, Ag, Cu), we establish BLSO as an appealing plasmonic material more suitable to the infrared range, with some degree of tunability, and a low level of losses that correlates well with the carrier mobility.

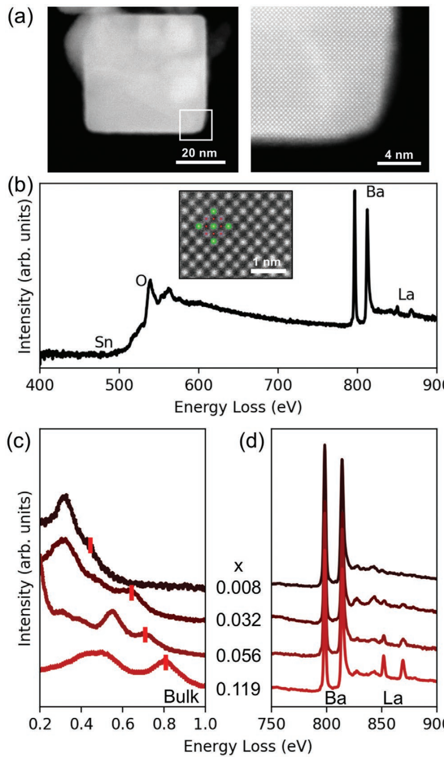

Figure 1. a) Low magnification (left) and atomic resolution (right) HAADF-STEM images of a typical BLSO nanocrystal with rectangular cross section, taken along the [100] zone axis. b) Core-loss EELS with edges indicating the presence of different elements. The inset shows a zoom-in view of the HAADF image in (a) with a structural model of $BaSnO_3$ superimposed. c,d) Evolution with doping level of the plasmon energy in the low-loss spectra and the intensity of the La $M_{4,5}$ edge in the core-loss spectra, respectively. Dopant percentages, x, determined from core-loss EELS, are shown as labels. Red markers in (c) denote bulk plasmon energies.

2. Results and Discussion

We synthetized nanocrystals of BLSO with varying sizes and geometries by a sol–gel method modified from ref. [35] (Experimental Section). Through atomic resolution high-angle annular dark-field (HAADF) imaging in **Figure 1**a,b, and X-ray diffraction (Figure S1, Supporting Information), we confirmed the expected cubic perovskite structure. For the BLSO rods and cubes, we also observed that the BLSO particles have {100} terminated surfaces. Core-loss EELS in Figure 1b shows the presence of Ba, Sn, O, and La in the doped samples. Here, La acts as n-type dopant that replaces a portion of the A-site Ba, which introduces free electrons that occupy the bottom of the conduction band. With sufficient La doping, the Fermi level is located above the conduction band minimum (by typically less than 1 eV), making BLSO a degenerate semiconductor.[39] The collective oscillations of these conduction band electrons form IR plasmons that we study in this paper. We also investigate the doping limit of La in BSO and the maximum plasmon energy in this material with STEM-EELS. The bulk plasmon energy and the corresponding La percentage are extracted from low-loss and core-loss EELS, respectively. As shown in Figure 1c,d, both the bulk carrier plasmon energy and La $M_{4,5}$ edge intensity increase with nominal doping level. The low-loss and core-loss EELS signals are obtained from the same region, which allows correlating composition and plasmonic properties at the nanoscale. We find that highly doped BLSO can support plasmons up to an energy of 0.8 eV (corresponding to a wavelength of 1.55 µm), supporting BLSO as a promising candidate for plasmonics applications (such as epsilon-near-zero-based devices[40]) at the telecom wavelength with better optical properties than traditional TCOs because of the high carrier mobility of BLSO.[34] However, we find that doping inhomogeneity can play a role at high doping

ADVANCED SCIENCE NEWS
www.advancedsciencenews.com
NANO · MICRO small
www.small-journal.com

levels. Therefore, we limit our investigation to moderately (5%) La-doped BSO in the rest of this paper.

Besides the peaks assigned to bulk plasmon excitations denoted by red markers in Figure 1c, additional peaks appear at lower energies. These can also be observed in the aloof EELS spectra shown in **Figure 2**b, where surface plasmon resonances of free charge carriers in BLSO are probed when the electron beam is placed just outside a BLSO nanorod displayed in Figure 2a. We attribute these resonances to different localized surface plasmon (LSP) modes, which are spatially imaged in the energy-filtered maps shown in Figure 2c. Regions of high intensity in the maps are associated with an accumulation of induced electric field that is characteristic of LSP excitations, as inferred from theoretical simulations (Figure S2, Supporting Information). The distribution of these hotspots strongly depends on geometry. In particular, in the rectangular BLSO nanorod shown in Figure 2a [length L = 427 nm, aspect ratio (AR) ≈ 7], we observe multiple LSPs oscillating along the long axis, starting with a dipolar mode of wavelength $\lambda_{n=1} \approx 2L$, and two higher-order modes ($\lambda_{n=2} \approx L$ and $\lambda_{n=3} \approx 2L/3$). A transverse LSP mode is also observed at energies above 400 meV. In the BLSO cube shown in Figure 2d (L = 50 nm, AR ≈ 1), we observe plasmon resonances of shorter wavelengths characterized by field and charge accumulation at the corners, edges, and faces of the cube (Figure 2e).[41–44]

One distinct difference between degenerate semiconductors and metals refers to the spatial confinement of LSPs with sub-eV energies. Noble metals present large ratios of the real and imaginary parts of the dielectric function in the IR, which guarantees high quality factors of their LSP resonances. However, the corresponding plasmon wavelengths are very close to those of free-space photons in the IR because they host large densities of conduction electrons, so their bulk plasmons appear in the visible part of the spectrum, therefore demanding high ARs to move surface plasmons to the IR, where the dielectric function takes larger absolute values. In contrast to noble metals, LSPs in degenerate semiconductors can produce a large confinement ratio in IR plasmons because of their lower carrier densities, which lead to bulk plasmon energies already placed in the IR, so smaller ARs and lower values of the dielectric function already provide strongly confined plasmons in that region. With the plasmon energy and wavelength from the measured EELS energy-filtered maps in Figure 2c, we can readily obtain the plasmon confinement ratio in BLSO nanoparticles, as shown in Figure 2d, which turns out to be about one order of magnitude larger than for noble metals. In Figure 2f, we demonstrate that LSPs in BLSO nanoparticles have wavelengths ≈6 to 12 times shorter than the photon wavelength at the same energy (but we note that a factor of 20 can be reached with the corner modes in nanocubes). The large spatial confinement is equally evident from the plasmon dispersions of BLSO

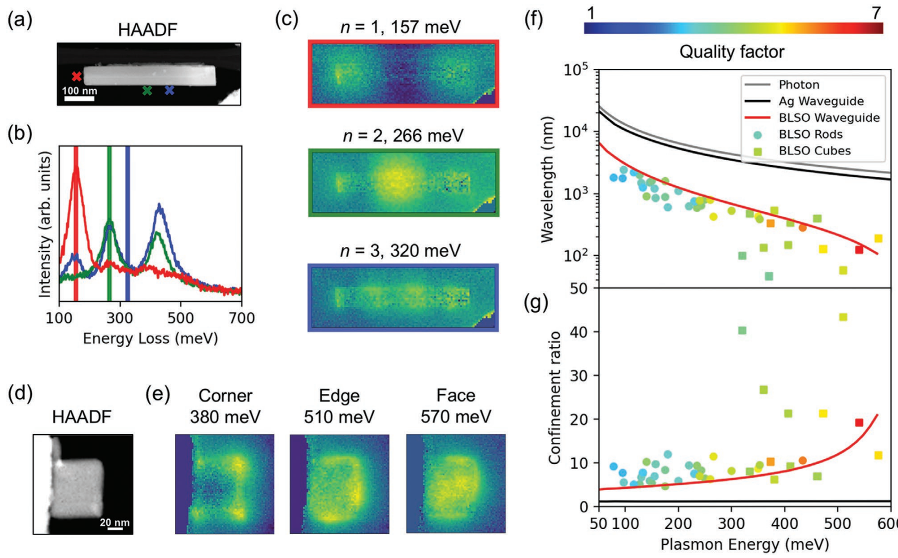

Figure 2. a) HAADF image of a BLSO nanorod. High intensity in the lower right corner is due to a neighboring BLSO particle. b) Aloof EELS spectra taken near the nanorod. Electron beam positions are indicated by the color-matching crosses in the HAADF image. c) Measured energy-filtered EELS maps for the infrared localized surface plasmon modes in the nanorod. EELS maps are integrated over 10 meV wide windows marked in (b). d) HAADF image of a BLSO nanocube attached to a larger BLSO particle on its left. e) EELS energy-filtered maps of LSPs in the BLSO nanocube for the labeled resonance energies. f) Measured IR plasmon wavelengths in BLSO nanoparticles (symbols) compared with calculated values obtained for BLSO (red curve) and Ag (black curve) waveguides with a cross section of 50 × 50 nm^2. We also show the free-space photon dispersion (gray curve) for reference. g) Confinement ratio obtained from (f) as the ratio of the plasmon excitation wavelength to the free-space photon wavelength.

ADVANCED SCIENCE NEWS
www.advancedsciencenews.com
NANO · MICRO small
www.small-journal.com

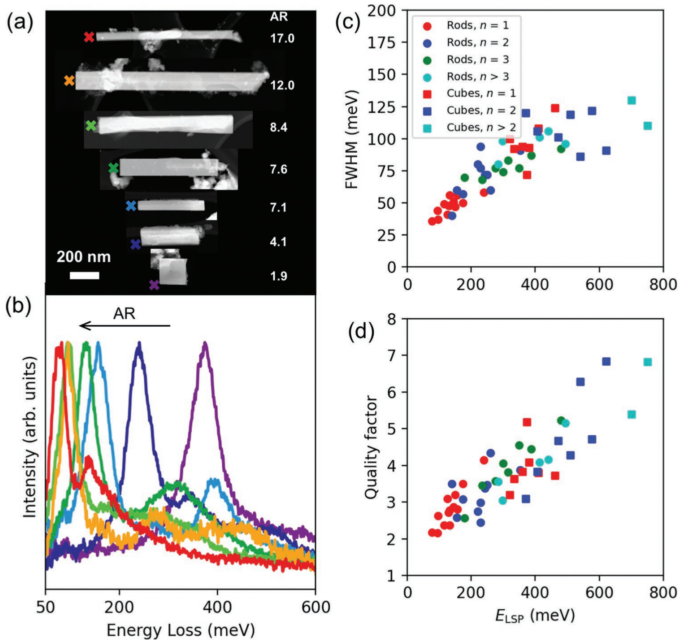

Figure 3. a) HAADF-STEM images of BLSO rod-like particles with varying length and aspect ratio (AR, see labels). b) Aloof EELS spectra acquired for beam positions as indicated by the color-matching crosses in (a), near the tip of the BLSO nanorods. c) LSP FWHM and d) quality factor as a function of LSP energy.

calculated for an infinite waveguide with a square cross section (see also Figure S3, Supporting Information for calculations with different cross sections), which deviates away from the light line much more than the dispersion calculated for Ag waveguides of similar characteristics.

Next, we study plasmon spectra for the series of BLSO nanorods shown in **Figure 3**a, which have a similar cross section but varying length and aspect ratio. These rod-like particles have rectangular cross sections and lengths of ≈ 200–1200 nm, with AR ranging from 4 to 12. They are supported in part by lacey carbon TEM grids, while mostly suspended in vacuum. The EEL spectra shown in Figure 3b were acquired with the beam placed just outside the nanorod tip or cube corner, as indicated by the colored markers in Figure 3a. With the help of the spatial mapping demonstrated in Figure 2, we attribute the sharpest and most intense resonance peaks present in all spectra to the dipolar modes (n = 1). While the dipolar LSPs decrease in energy with increasing AR, their spectral width also decreases substantially. For a quantitative assessment of this trend, we performed Lorentzian fitting to extract the full width at half maximum (FWHM) of all peaks corresponding to the observed LSPs, including the higher-order LSPs. As shown in Figure 3c, the FWHM can be as small as 35 meV for the nanorod with the largest AR and increases to about 120 meV for higher-energy LSPs. The quality factors Q (defined as the ratio of the plasmon-energy to the FHWM) obtained for these plasmons are shown in Figure 3d. The dipolar modes are found to have Q factors in the 2–5 range, while higher-energy LSPs show Q up to 8. Compared with other doped semiconductor nanocrystals,[45–47] the LSPs observed in this study exhibit the largest Q factors in the mid-IR.

While plasmon damping is often associated with carrier mobility of the material, such correlation is generally not direct, as several factors other than carrier mobility (i.e., nonlocal effects, surface quality, and radiative coupling) can play an essential role in determining the plasmon lifetime. We notice such variation of LSP FWHM with particle size and geometry in Figure 3c and further study the plasmon FWHM as a function of nanoparticle AR and particle length L in **Figure 4** and Figure S6 (Supporting Information), respectively. We notice a substantial increase of LSP damping for BLSO particles with decreasing AR. To understand the possible origin of this trend, we calculate aloof EEL spectra for varying nanoparticle dimensions and extract the FWHM of the theoretically predicted peaks. We model the optical properties of BLSO using a Drude dielectric function, which we find is sufficient for describing the charge carriers in doped BSO (Figure S4, Supporting Information), and perform numerical modeling as described in Methods. Also shown in Figure 4 , we find that the calculated FWHM of the dipolar plasmons increases only slightly above the bulk damping value $\hbar\gamma_{bulk}$ = 35 meV here considered for the model, and in particular, the increase is only about 5 meV

ADVANCED SCIENCE NEWS
www.advancedsciencenews.com
NANO · MICRO small
www.small-journal.com

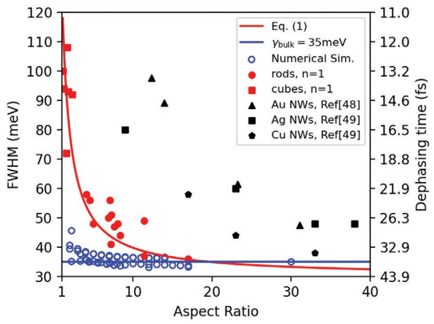

Figure 4. Plasmon FWHM and the corresponding dephasing time as a function of aspect ratio. Experimental data from dipolar LSPs in BLSO nanorods and cubes (filled red circles and squares) are compared with numerical simulations for particles with similar lateral dimensions but varying cross sections (blue open circles). Results from literature for noble metal nanorods[48,49] (black) are shown for comparison. The horizontal blue line indicates the fitted Drude damping of our LBSO samples, $\hbar\gamma$= 35 meV.

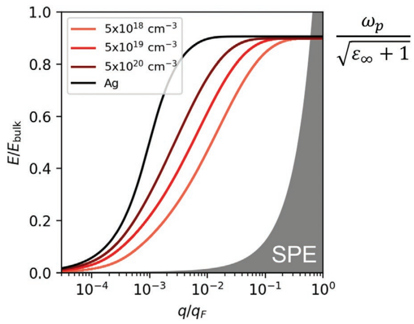

Figure 5. Normalized surface-plasmon dispersions of BLSO with carrier densities $N_{BLSO} = 5 \times 10^{18}$, 5×10^{19}, and 5×10^{20} cm^{-3} (colored curves) and Ag (conduction electron density $N_{Ag} = 6 \times 10^{22}$ cm^{-3}, black curve), as calculated for an infinite interface geometry. The vertical and horizontal axes are the normalized energy and the wave vector, where E_{bulk} and q_F are the bulk plasmon energy and Fermi wave vector, respectively. The single-particle excitation regime is indicated in gray.

for small AR or L. In the opposite limit, for very large AR or L, the FWHM of the dipolar plasmons only moves by 2–3 meV below the bulk Drude damping. However, we stress that the calculated results deviate substantially from the experimental observations, especially when the particle sizes (and so the AR too) are small.

To further understand this discrepancy in the spectral widths, we calculate the optical scattering and absorption spectra near BLSO nanorods (SI) to analyze the origin of the plasmon damping. These quantities are roughly proportional to the cathodoluminescence (CL) and EELS probabilities, respectively, so we show in Figure S7a,b (Supporting Information) the intensity ratio between these two probabilities (EELS/CL), which takes large values for the range of AR and L studied here, suggesting a dominantly nonradiative character of the plasmonic excitations. We therefore conclude that damping in these excitations is mainly contributed by material properties (i.e., intrinsic effects of the material and its modification due to the specific geometry of the particles), while radiative damping plays a negligible role.

To compare plasmon damping in BLSO with other plasmonic materials, it is also illuminating to look at their respective normalized plasmon dispersions (**Figure 5**). The surface plasmon dispersion relations are evaluated for infinite slabs with thickness of 50 nm.[50] We adopt the Drude model permittivity $\varepsilon(\omega) = \varepsilon_\infty - \omega_p^2/\omega(\omega + i\gamma_p)$ with parameters $\varepsilon_\infty = 4.0$ and $E_{bulk} \equiv \hbar\omega_p/\sqrt{\varepsilon_\infty} = 4.6$ eV for silver, and $\varepsilon_\infty = 4.5$ and $\omega_p^2 = e^2 N/\varepsilon_0 m^*$ for BLSO, where N is the carrier density (see legend in Figure 5) and $m^*/m_e = 0.2$ is the carrier effective mass.[51] We plot the plasmon energy as a function of wave vector q, normalized to E_{bulk} and the Fermi wave vector q_F, respectively. For the same ratio E/E_{bulk} of the plasmon energy E to the bulk plasmon energy E_{bulk}, plasmons sustained by free carriers with lower density possess a higher ratio of the wave vector $q = 2\pi/\lambda$ to the Fermi wave vector q_F compared to Ag, and this behavior extends up to the large-wave-vector limit, where the plasmon frequency converges to the non-retarded limit $\omega_p/\sqrt{\varepsilon_\infty + 1}$. In addition to their high spatial confinement, this indicates that BLSO plasmons are closer to the single-particle excitation (SPE) regime. It has been observed that surface plasmons exhibit a damping that increases with q, even before reaching the onset of SPEs at $q = q_F$.[52] This might happen because for increasing wave vectors, shorter-wavelength plasmons are more likely to be scattered by doping inhomogeneities, neighboring nanoparticles, and shape irregularities. The differences in LSP energy between our simulations and experiments (Figure S5, Supporting Information) are likely related to these extra scattering mechanisms, which are not contemplated in the theory. Furthermore, we investigate LSPs up to the high E/E_{bulk} regime, where size effects are known to affect both the energy and width of LSPs.[53] A phenomenological model has often been used to take into account the size effects via the expression[54]

$$\gamma = \gamma_{bulk} + \frac{A v_F}{L} \quad (1)$$

where v_F is the carrier Fermi velocity, A is a phenomenological parameter that depends on particle morphology, surface details, and the surrounding medium, and L is the particle size. We find that $\hbar\gamma_{bulk}$ = 30 meV and A in the range of 2 to 3 provides a reasonable agreement of γ as a function of L in comparison with experiment, as shown in Figure 4. Although such size dependence has been observed for small metal particles,[55] the physical explanation of the phenomenon is somewhat controversial,[56] with two possible explanations for the increase in damping with decreasing particle size associated with either additional surface scattering determined by a size-independent electron mean free path[54] or the increasing role of the inhomogeneous electron density profile at the surface.[57] The range of particle size in which we observe an increase in plasmon FWHM is relatively large compared to that of metal particles (≈10 nm or less), an effect that can be possibly related to the lower density of free carriers in BLSO.

ADVANCED SCIENCE NEWS
www.advancedsciencenews.com
NANO · MICRO small
www.small-journal.com

It is also worth noting that the Debye temperature for $BaSnO_3$ is around 500 K,[58] above the temperature at which we perform our experiments. High-frequency phonons could contribute to carrier scattering[59] when higher-energy mid-IR LSPs are excited. However, electron–phonon interaction was only found to limit the plasmon lifetime within a small energy region around the optical phonon frequency.[60,61] Thus, the contribution from this scattering mechanism to the damping of high-energy plasmons may require further investigation.

Nevertheless, the dipolar plasmons in BLSO discussed in Figures 3 and 4 are systematically displaying smaller values of the FWHM than those in noble metals of the same size.[48,49] The reported BLSO plasmons reach their FWHM limit at an AR between 10 and 20, which is 2 to 3 times smaller than that for Ag, Au, or Cu. The BLSO particles required to support IR LSPs are much smaller than those made of noble metals, which makes radiative damping negligible in the former. In addition, both the intrinsic carrier mobility and the particle size affect the damping of plasmons in degenerate semiconductors, including BLSO. At large sizes, the FWHM of LSPs are primarily limited by the carrier mobility. In contrast, in smaller particles, additional contributions to plasmon damping are observed. The narrowest LSP that we found in BLSO has a FWHM of 35 meV (i.e., a dephasing time of 38 fs). This amounts to a lower limit of carrier mobility $\mu \approx 160$ cm^2 V^{-1} s^{-1}, which falls within the range of carrier mobilities previously determined for this material.[62,63] Given that the carrier mobility in $BaSnO_3$ can be as high as 300 cm^2 V^{-1} s^{-1}, it is likely that better synthetic approaches and fabrication processes will lead to even better IR plasmons in doped BSO with more compact dimensions compared to noble metals.

3. Conclusions

In summary, we systematically identified and characterized infrared localized surface plasmons in individual nanocrystals of La-doped $BaSnO_3$ by STEM-EELS. Our results show that infrared plasmons sustained by BLSO are superior in spatial confinement ratio compared to those in noble metals. We also demonstrate that, with high enough La doping, BLSO can have a sufficiently large density of free carriers for its bulk plasma frequency to reach the telecommunication wavelength at 1.55 µm/0.8 eV. Our analysis of LSPs in BLSO nanorods with varying length and aspect ratio shows that the low-loss IR plasmons are primarily limited by non-radiative damping, which is closely related to the carrier mobility. Our results emphasize the strong potential of this high-mobility perovskite oxide for application in infrared plasmonic devices.

4. Experimental Section

BLSO Synthesis: A recipe for $BaSnO_3$ nanoparticle synthesis via a sol–gel approach modified from ref. [35] was followed. Chlorine salts of Ba, La, and Sn were weighted in desired molar ratio and added in a mixture of deionized water and ethanol. Citric acid was then added into the solution. The solution was then kept at 80 °C under stirring for 30 min to aid complete dissolution. Overdosed ethylene glycol was then added, and the solution was heated to 100 °C for 2 h until the gel was formed. Annealing at 600 °C followed by annealing at 1000 °C in atmosphere resulted in phase pure cubic BLSO. Nanorod-like and cubic-shaped BLSO particles can often be found in the product. When doping was successful and relatively uniform, the powder had a greenish and blue appearance, for small and large particle size, respectively.

Another synthetic route involved the formation of $BaSn(OH)_6$ as the middle product[64,65] via participation at room temperature, followed by high-temperature annealing to form perovskite $BaSnO_3$. For this route, the solution containing salts of Ba, La, and Sn was kept at 80 °C under vigorous stirring, while a NaOH solution was added dropwise until reaching a pH > 7. During this process, Argon purging was also required to prevent the formation of oxides. At this point, white participation should already form, which is $BaSn(OH)_6$. Subsequent annealing above 600 °C in Argon allowed BSO nanorods to be formed with large length and aspect ratio. However, we find that it is difficult to incorporate La dopant into the A-site via this approach. Thus, this method is not suitable for producing plasmonic BLSO.

STEM-EELS: A Nion UltraSTEM 100 scanning transmission electron microscope was used in this work. The microscope features a HERMES electron monochromator to improve the energy resolution. Energy loss spectra and energy-filtered maps were taken with energy resolution in the 10–12 meV range. The EELS detector dispersions were 0.9 and 1.3 meV pixel^{-1} for point of EELS spectra acquisition and EELS mapping, respectively. Aloof energy loss spectra were recorded with a detector dwell time of 256 ms. EELS spectra taken in vacuum far away from any specimen or grid were used to obtain the elastic background, which was then removed from the spectra containing the inelastic signal.[66,67]

Numerical Simulations: The theoretical calculations were performed using the software Comsol Multiphysics (RF module),[68,69] where a line current representing the electron beam was implemented as a field source. The induced electric field $\mathbf{E}^{\text{ind}}$ was then used to evaluate the frequency and spatially dependent loss probability $\Gamma(\omega)$ as[70]

$$\Gamma(\mathbf{R}_b,\omega) = \frac{e}{\pi\hbar\omega}\int dz \ \mathrm{Re}\left\{E_z^{\text{ind}}(\mathbf{R}_b, z,\omega)e^{\frac{-i\omega z}{v}}\right\} \tag{2}$$

Here, electrons moving with constant velocity v parallel to the z axis and intersecting the xy plane at $\mathbf{R}_b$ were assumed.

Supporting Information

Supporting Information is available from the Wiley Online Library or from the author.

Acknowledgements

H.Y. and P.E.B. acknowledge the financial support of the US Department of Energy, Office of Science, Basic Energy Sciences under award number DE-SC0005132. X.X. and S.W.C. were supported by the center for Quantum Materials Synthesis (cQMS), funded by the Gordon and Betty Moore Foundation's EPiQS initiative through grant GBMF10104, and by Rutgers University. F.J.G.A. acknowledges support from the European Research Council (789104-eNANO) and the Spanish MINECO (PID2020-112625GB-I00 and CEX2019-000910-S).

Conflict of Interest

The authors declare no conflict of interest.

Data Availability Statement

The data that support the findings of this study are available from the corresponding author upon reasonable request.

ADVANCED SCIENCE NEWS
www.advancedsciencenews.com

NANO · MICRO small
www.small-journal.com

Keywords

monochromated electron energy-loss spectroscopy (EELS), perovskite oxide, STEM-electron energy-loss spectroscopy (EELS), surface plasmons, transparent conducting oxides

Received: November 9, 2021
Revised: February 6, 2022
Published online: March 13, 2022

[1] A. Boltasseva, H. A. Atwater, *Science* **2011**, *331*, 290.
[2] S.-Y. Ding, J. Yi, J.-F. Li, B. Ren, D.-Y. Wu, R. Panneerselvam, Z.-Q. Tian, *Nat. Rev. Mater.* **2016**, *1*, 16021.
[3] M. Ha, J.-H. Kim, M. You, Q. Li, C. Fan, J.-M. Nam, *Chem. Rev.* **2019**, *119*, 12208.
[4] S. C. Warren, E. Thimsen, *Energy Environ. Sci.* **2012**, *5*, 5133.
[5] P. Huo, Si Zhang, Y. Liang, Y. Lu, T. Xu, *Adv. Opt. Mater.* **2019**, *7*, 1801616.
[6] Y. Wang, J. Yu, Y.-F. Mao, J. Chen, S. Wang, H.-Z. Chen, Y. Zhang, S.-Y. Wang, X. Chen, T. Li, L. Zhou, R.-M. Ma, S. Zhu, W. Cai, J. Zhu, *Nature* **2020**, *581*, 401.
[7] P. R. West, S. Ishii, G. V. Naik, N. K. Emani, V. M. Shalaev, A. Boltasseva, *Laser Photonics Rev.* **2010**, *4*, 795.
[8] G. V. Naik, J. Kim, A. Boltasseva, *Opt. Mater. Express* **2011**, *1*, 1090.
[9] S. H. Brewer, S. Franzen, *J. Phys. Chem. B* **2002**, *106*, 12986.
[10] U. Guler, V. M. Shalaev, A. Boltasseva, *Mater. Today* **2015**, *18*, 227.
[11] T. M. Mattox, X. Ye, K. Manthiram, P. J Schuck, A P Alivisatos, J. J. Urban, *Adv. Mater.* **2015**, *27*, 5830.
[12] D. A. Bobb, G. Zhu, M. Mayy, A. V. Gavrilenko, P. Mead, V. I. Gavrilenko, M. A. Noginov, *Appl. Phys. Lett.* **2009**, *95*, 151102.
[13] A. Agarwal, M. S. Vitiello, L. Viti, A. Cupolillo, A. Politano, *Nanoscale* **2018**, *10*, 8938.
[14] A. N. Grigorenko, M. Polini, K. S. Novoselov, *Nat. Photonics* **2012**, *6*, 749.
[15] F. J. García de Abajo, *ACS Photonics* **2014**, *1*, 135.
[16] G. X. Ni, A. S. Mcleod, Z. Sun, L. Wang, L. Xiong, K. W. Post, S. S. Sunku, B.-Y. Jiang, J. Hone, C. R. Dean, M. M. Fogler, D. N. Basov, *Nature* **2018**, *557*, 530.
[17] Z. Liu, K. Aydin, *Nano Lett.* **2016**, *16*, 3457.
[18] T. Low, R. Roldán, H. Wang, F. Xia, P. Avouris, L. M. Moreno, F. Guinea, *Phys. Rev. Lett.* **2014**, *113*, 106802.
[19] M. A. Noginov, L. Gu, J. Livenere, G. Zhu, A. K. Pradhan, R. Mundle, M. Bahoura, Yu. A. Barnakov, V. A. Podolskiy, *Appl. Phys. Lett.* **2011**, *99*, 021101.
[20] G. V. Naik, V. M. Shalaev, A. Boltasseva, *Adv. Mater.* **2013**, *25*, 3264.
[21] E. Sachet, C. T. Shelton, J. S. Harris, B. E. Gaddy, D. L. Irving, S. Curtarolo, B. F. Donovan, P. E. Hopkins, P. A. Sharma, A. L. Sharma, J. Ihlefeld, S. Franzen, J.-P. Maria, *Nat. Mater.* **2015**, *14*, 414.
[22] A. Agrawal, S. H. Cho, O. Zandi, S. Ghosh, R. W. Johns, D. J. Milliron, *Chem. Rev.* **2018**, *118*, 3121.
[23] T. C. Asmara, D. Wan, Y. Zhao, M. A. Majidi, C. T. Nelson, M. C. Scott, Y. Cai, B. Yan, D. Schmidt, M. Yang, T. Zhu, P. E. Trevisanutto, M. R. Motapothula, Y. P. Feng, M. B. H. Breese, M. Sherburne, M. Asta, A. Minor, T. Venkatesan, A. Rusydi, *Nat. Commun.* **2017**, *8*, 15271.
[24] C. A. Niedermeier, Y. Kumagai, K. Ide, T. Katase, F. Oba, H. Hosono, T. Kamiya, *Phys. Rev. B* **2020**, *101*, 125206.
[25] M. Mirjolet, M. Kataja, T. K. Hakala, P. Komissinskiy, L. Alff, G. Herranz, J. Fontcuberta, *Adv. Opt. Mater.* **2021**, *9*, 2100520.
[26] L. Zhang, Y. Zhou, L. Guo, W. Zhao, A. Barnes, H.- T. Zhang, C. Eaton, Y. Zheng, M. Brahlek, H. F. Haneef, N. J. Podraza, M. H. W. Chan, V. Gopalan, K. M. Rabe, R. Engel-Herbert, *Nat. Mater.* **2016**, *15*, 204.
[27] B. Monserrat, C. E. Dreyer, K. M. Rabe, *Phys. Rev. B* **2018**, *97*, 104310.
[28] S. Ismail-Beigi, F. J. Walker, S.-W. Cheong, K. M. Rabe, C. H. Ahn, *APL Mater.* **2015**, *3*, 062510.
[29] H. J. Kim, U. Kim, H. M. Kim, T. H. Kim, H. S. Mun, B.-G. Jeon, K. T. Hong, W.-J. Lee, C. Ju, K. H. Kim, K. Char, *Appl. Phys. Express* **2012**, *5*, 061102.
[30] R. J. Terry, N. Combs, C. D. Mcmillen, S. Stemmer, J. W. Kolis, *J. Cryst. Growth* **2020**, *536*, 125529.
[31] W.-J. Lee, H. J. Kim, J. Kang, D. H. Jang, T. H. Kim, J. H. Lee, K. H. Kim, *Annu. Rev. Mater. Res.* **2017**, *47*, 391.
[32] H. Wang, J. Walter, K. Ganguly, B. Yu, G. Yu, Z. Zhang, H. Zhou, H. Fu, M. Greven, C. Leighton, *Phys. Rev. Mater.* **2019**, *3*, 075001.
[33] T. N. Stanislavchuk, A. A. Sirenko, A. P. Litvinchuk, X. Luo, S.-W. Cheong, *J. Appl. Phys.* **2012**, *112*, 044108.
[34] Y. Smirnov, J. Holovsky, G. Rijnders, M. Morales-Masis, *APL Mater.* **2020**, *8*, 061108.
[35] W. Shepherd, M. Wilms, J. Van Embden, E. Della Gaspera, *Chem. Commun.* **2019**, *55*, 11880.
[36] A. Polman, M. Kociak, F. J. García De Abajo, *Nat. Mater.* **2019**, *18*, 1158.
[37] O. L. Krivanek, T. C. Lovejoy, N. Dellby, T. Aoki, R. W. Carpenter, P. Rez, E. Soignard, J. Zhu, P. E. Batson, M. J. Lagos, R. F. Egerton, P. A. Crozier, *Nature* **2014**, *514*, 209.
[38] O. L. Krivanek, N. Dellby, J. A. Hachtel, J.-C. Idrobo, M. T. Hotz, B. Plotkin-Swing, N. J. Bacon, A. L. Bleloch, G. J. Corbin, M. V. Hoffman, C. E. Meyer, T. C. Lovejoy, *Ultramicroscopy* **2019**, *203*, 60.
[39] S. Sallis, D. O. Scanlon, S. C. Chae, N. F. Quackenbush, D. A. Fischer, J. C. Woicik, J.-H. Guo, S. W. Cheong, L. F. J. Piper, *Appl. Phys. Lett.* **2013**, *103*, 042105.
[40] M. Silveirinha, N. Engheta, *Phys. Rev. Lett.* **2006**, *97*, 157403.
[41] O. Nicoletti, F. De La Peña, R. K. Leary, D. J. Holland, C. Ducati, P. A. Midgley, *Nature* **2013**, *502*, 80.
[42] M. J. Lagos, A. Trügler, U. Hohenester, P. E. Batson, *Nature* **2017**, *543*, 529.
[43] L. J. Sherry, S.-H. Chang, G. C. Schatz, R. P. Van Duyne, B. J. Wiley, Y. Xia, *Nano Lett.* **2005**, *5*, 2034.
[44] S. H. Cho, S. Ghosh, Z. J. Berkson, J. A. Hachtel, J. Shi, X. Zhao, L. C. Reimnitz, C. J. Dahlman, Y. Ho, A. Yang, Y. Liu, J.-C. Idrobo, B. F. Chmelka, D. J. Milliron, *Chem. Mater.* **2019**, *31*, 2661.
[45] Z. Liu, Y. Zhong, I. Shafei, S. Jeong, L. Wang, H. T. Nguyen, C.-J. Sun, T. Li, J. Chen, L. Chen, Y. Losovyj, X. Gao, W. Ma, X. Ye, *Nano Lett.* **2020**, *20*, 2821.
[46] G. Liu, S. Qi, J. Chen, Y. Lou, Y. Zhao, C. Burda, *Nano Lett.* **2021**, *21*, 2610.
[47] S. Askari, D. Mariotti, J. E. Stehr, J. Benedikt, J. Keraudy, U. Helmersson, *Nano Lett.* **2018**, *18*, 5681.
[48] Y. Wu, Z. Hu, X.-T. Kong, J. C. Idrobo, A. G. Nixon, P. D. Rack, D. J. Masiello, J. P. Camden, *Phys. Rev. B* **2020**, *101*.
[49] V. Mkhitaryan, K. March, E. N. Tseng, X. Li, L. Scarabelli, L. M. Liz-Marzán, S.-Y. Chen, L. H. G. Tizei, O. Stéphan, J.-M. Song, M. Kociak, F. J. García de Abajo, Al. Gloter, *Nano Lett.* **2021**, *21*, 2444.
[50] C. H. Chen, J. Silcox, *Phys. Rev. B* **1979**, *20*, 3605.
[51] S. James Allen, S. Raghavan, T. Schumann, K.-M. Law, S. Stemmer, *Appl. Phys. Lett.* **2016**, *108*, 252107.
[52] Y. Liu, R. F. Willis, K. V. Emtsev, Th. Seyller, *Phys. Rev. B* **2008**, *78*, 201403.
[53] J. A. Scholl, A. L. Koh, J. A. Dionne, *Nature* **2012**, *483*, 421.
[54] U. Kreibig, *J. Phys. F: Met. Phys.* **1974**, *4*, 999.
[55] P. E. Batson, *Solid State Commun.* **1980**, *34*, 477.
[56] U. Kreibig, L. Genzel, *Surf. Sci.* **1985**, *156*, 678.
[57] P. Apell, D. R. Penn, *Phys. Rev. Lett.* **1983**, *50*, 1316.

ADVANCED SCIENCE NEWS
www.advancedsciencenews.com
NANO · MICRO small
www.small-journal.com

[58] E. Mccalla, D. Phelan, M. J. Krogstad, B. Dabrowski, C. Leighton, *Phys. Rev. Mater.* **2018**, *2*, 084601.
[59] A. Prakash, P. Xu, A. Faghaninia, S. Shukla, J. W. Ager, C. S. Lo, B. Jalan, *Nat. Commun.* **2017**, *8*, 15167.
[60] H. Yan, T. Low, W. Zhu, Y. Wu, M. Freitag, X. Li, F. Guinea, P. Avouris, F. Xia, *Nat. Photonics* **2013**, *7*, 394.
[61] F. J. Bezares, A. De Sanctis, J. R. M. Saavedra, A. Woessner, P. Alonso-González, I. Amenabar, J. Chen, T. H. Bointon, S. Dai, M. M. Fogler, D. N. Basov, R. Hillenbrand, M. F. Craciun, F. J García De Abajo, S. Russo, F. H. L. Koppens, *Nano Lett.* **2017**, *17*, 5908.
[62] S. Raghavan, T. Schumann, H. Kim, J. Y. Zhang, T. A. Cain, S. Stemmer, *APL Mater.* **2016**, *4*, 016106.
[63] H. Paik, Z. Chen, E. Lochocki, H. A. Seidner, A. Verma, N. Tanen, J. Park, M. Uchida, S. Shang, B.-C. Zhou, M. Brützam, R. Uecker, Z.-K. Liu, D. Jena, K. M. Shen, D. A. Muller, D. G. Schlom, *APL Mater.* **2017**, *5*, 116107.
[64] W. Lu, H. Schmidt, *Ceram. Int.* **2008**, *34*, 645.
[65] H. Mizoguchi, N. S. P. Bhuvanesh, Y.-I. Kim, S. Ohara, P. M. Woodward, *Inorg. Chem.* **2014**, *53*, 10570.
[66] H. Yang, E. L. Garfunkel, P. E. Batson, *Phys. Rev. B* **2020**, *102*, 205427.
[67] M. J. Lagos, P. E. Batson, *Nano Lett.* **2018**, *18*, 4556.
[68] A. Wiener, H. Duan, M. Bosman, A. P. Horsfield, J. B. Pendry, J. K. W. Yang, S. A. Maier, A. I. Fernández-Domínguez, *ACS Nano* **2013**, *7*, 6287.
[69] S. Raza, N. Stenger, A. Pors, T. Holmgaard, S. Kadkhodazadeh, J. B. Wagner, K. Pedersen, M. Wubs, S. I. Bozhevolnyi, N. A. Mortensen, *Nat. Commun.* **2014**, *5*, 4125.
[70] F. J. García De Abajo, *Rev. Mod. Phys.* **2010**, *82*, 209.

ACS NANO

www.acsnano.org

ARTICLE

Simultaneous Imaging of Dopants and Free Charge Carriers by Monochromated EELS

Hongbin Yang,* Andrea Konečná, Xianghan Xu, Sang-Wook Cheong, Philip E. Batson,* F. Javier García de Abajo,* and Eric Garfunkel

Cite This: *ACS Nano* 2022, 16, 18795−18805

Read Online

ACCESS | Metrics & More | Article Recommendations | Supporting Information

ABSTRACT: **Doping inhomogeneities in solids are not uncommon, but their microscopic observation and understanding are limited due to the lack of bulk-sensitive experimental techniques with high enough spatial and spectral resolution. Here, we demonstrate nanoscale imaging of both dopants and free charge carriers in La-doped $BaSnO_3$ (BLSO) using high-resolution electron energy-loss spectroscopy (EELS). By analyzing high- and low-energy excitations in EELS, we reveal chemical and electronic inhomogeneities within a single BLSO nanocrystal. The inhomogeneous doping leads to distinctive localized infrared surface plasmons, including a previously unobserved plasmon mode that is highly confined between high- and low-doping regions. We further quantify the carrier density, effective mass, and dopant activation percentage by EELS and transport measurements on the bulk single crystals of BLSO. These results not only represent a practical approach for studying heterogeneities in solids and understanding structure−property relationships at the nanoscale, but also demonstrate the possibility of infrared plasmon tuning by leveraging nanoscale doping texture.**

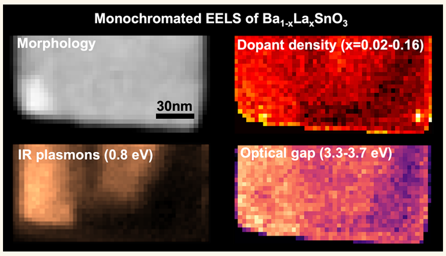

KEYWORDS: *doped semiconductor, high-mobility oxide, infrared plasmonics, band gap, carrier effective mass, monochromated electron energy-loss spectroscopy, inhomogeneity*

The electrical and optical properties of materials are strongly influenced by their free charge carriers.[1] Consequently, tuning the carrier density has been of critical importance for the design and fabrication of semiconductor devices, as well as for exploring exotic electronic states in complex oxides such as superconductivity[2−4] and topological effects.[5] Chemical doping is often exploited to tune the carrier density in solids, although it may introduce chemical and electronic inhomogeneities at the nanoscale.[6−8] These inhomogeneities are often detrimental to carrier mobility and device performance.[9−11] However, in some material systems, the inevitable heterogeneities exhibit a close correlation with the emergence of ferroelectricity,[12−14] high-temperature superconductivity,[15−17] and unconventional magnetism.[18−21]

The relationship between these exotic properties and nanoscale heterogeneities has been challenging to study because of the high demand on both spatial and spectral resolution of the required experimental techniques. Scanning probe microscopy has been useful to cover this gap because it offers the possibility to investigate a wide range of local phenomena, including surface structures and local density of electronic states by scanning tunneling microscopy,[22] nanoscale electrical properties by electrostatic force microscopy,[23,24] and optical excitation strengths by scanning near-field optical microscopy.[25−29] However, the scanning probe techniques are primarily sensitive to surface properties and only offer access to a limited spectral range. Thus, it remains difficult to directly relate the local structure and chemical composition to the electrical or optical properties in materials of interest.[9,30] In this regard, scanning transmission electron microscopy (STEM) combined with electron energy-loss spectroscopy (EELS) represents a powerful alternative, as it allows imaging of atomic structures with the simultaneous measurement of local elemental composition, chemical bonding, and electronic excitations down to the single-atom level.[31]

Received: July 28, 2022
Accepted: October 26, 2022
Published: November 1, 2022

https://doi.org/10.1021/acsnano.2c07540
ACS Nano 2022, 16, 18795−18805

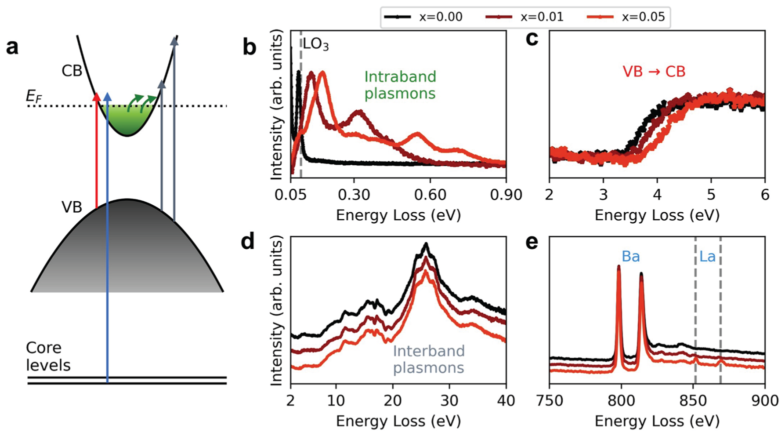

Figure 1. Electronic excitations in EELS. (a) Schematic diagram of electronic excitations, including collective modes (intraband plasmons of free carriers indicated by the green arrows, and interband plasmons indicated by the gray arrows) and single-particle transitions from core levels (blue) or the valence band (VB, red) to the conduction band (CB) states above E_F. (b−e) Doping dependence of low-loss and core-loss EELS in $Ba_{1-x}La_xSnO_3$ single crystals with x = 0, 0.01, and 0.05. (b) Electron energy losses associated with the excitation of phonons and carrier plasmons. The vertical dashed line indicates the highest longitudinal optical phonon energy near 100 meV. (c) Valence to conduction-band-edge transitions. (d) Valence plasmons and higher-energy interband transitions. (e) Core-loss EELS of transitions from Ba and La core levels to unoccupied states. EEL spectra in (d) and (e) are offset for clarity.

Thanks to a series of recent advances in energy resolution,[32,33] state-of-the-art monochromated STEM-EELS provides access into excitations over a broad energy range (from meVs to keVs[34]), thus emerging as the technique of choice to simultaneously probe high-energy core-level transitions and low-energy excitations, such as phonons,[35−43] infrared plasmons,[44−47] and valence electronic excitations.[48,49] Importantly, EELS can be combined with high-resolution imaging[50,51] to reveal local structure−property relationships.

Here, we report a method for characterizing both chemical and electronic inhomogeneities at the nanoscale, demonstrated by a simultaneous imaging of dopants and free charge carriers in La-doped $BaSnO_3$ (BLSO), a high-mobility perovskite oxide.[52−54] Through monochromated STEM-EELS, we measure electronic excitations associated with free carriers and dopants in the low-loss and core-loss regions of EELS, respectively. These measurements and analyses allow for direct imaging of chemical and electronic inhomogeneities, as well as local doping characteristics, even within a single nanocrystal of BLSO. Our results unambiguously show the strong influence of inhomogeneous doping on the plasmonic response. Specifically, we experimentally observe and numerically corroborate an interfacial plasmon mode localized between high- and low-doping regions. We demonstrate inhomogeneous doping as a tool for plasmon customization on the few-nanometer scale, with potential application in the design of advanced devices necessitating a high surface and bulk hybrid confinement of optical fields.

RESULTS AND DISCUSSION

Doping Dependence of Low-Loss and Core-Loss EELS. In EELS, energy-loss events can occur due to different mechanisms, including individual and collective electronic excitations that span a wide energy range, as schematically shown in Figure 1a. The spatial distribution of these excitations can be revealed thanks to the sub-nanometer size of the electron beam traversing the specimen. At relatively high energies, valence plasmons (i.e., collective electronic modes analogous to interband plasmons, but occurring at energies largely exceeding the electronic band gap) and core-losses (single-particle interband transitions involving core electrons to unoccupied states above E_F) are routinely observed in EELS experiments, even at a relatively low energy resolution.[48] Lower-energy excitations in solids, such as phonons and plasmons, as well as interband transitions in the UV−visible spectral range, can be better resolved with the aid of an electron monochromator capable of providing few-meV energy resolution.[32,55]

Here, we observe all of these types of excitations in the bulk single crystals of $Ba_{1-x}La_xSnO_3$ as a function of nominal doping, x, as shown in Figure 1b−e. The crystals were grown by a floating-zone method with homogeneous doping (see Methods). We acquire the EEL spectra in Figure 1 from 5 × 5 nm^2 regions of the TEM specimens. Starting from a wide-band-gap insulator without doping (x = 0), $Ba_{1-x}La_xSnO_3$ becomes a degenerate semiconductor as the level of La doping increases (see x = 0.01, 0.05 curves in Figure 1b,c). The metallic transport properties are manifested in the infrared dielectric response, as revealed in the low-loss region of monochromated EELS in Figure 1b. In the 50−900 meV spectral window, the main processes contributing to electron energy losses are phonons and excitations associated with the doping charge carriers. For undoped crystals, we observe only narrow resonances below ~90 meV, corresponding to the phonon polaritons in $BaSnO_3$.[56] With increasing n-type doping, the carrier electrons have higher Fermi velocities and

https://doi.org/10.1021/acsnano.2c07540
ACS Nano 2022, 16, 18795−18805

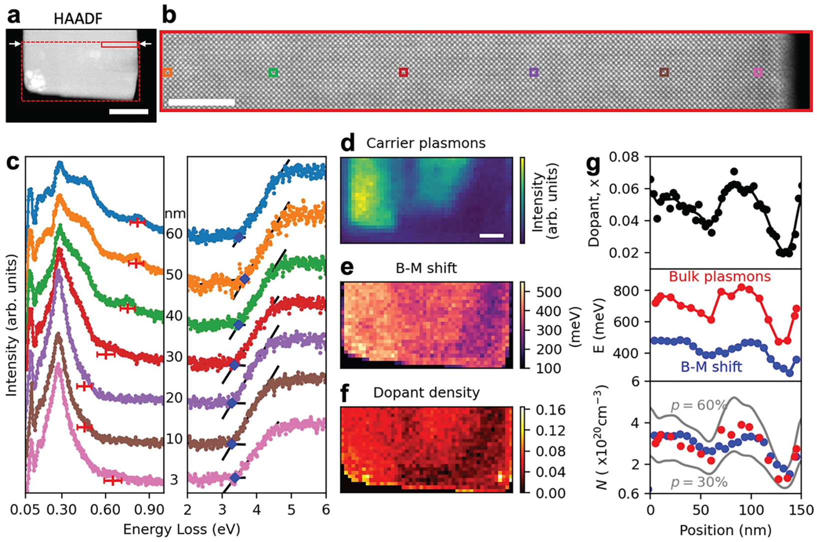

Figure 2. Mapping chemical and electronic inhomogeneities in a BLSO nanocrystal. (a) STEM-HAADF image of a square-shaped BLSO nanocrystal. (b) Atomic-resolution HAADF image near the edge of the crystal, within the rectangular region marked by solid red lines in (a). (c) Low-loss EELS signal acquired at electron beam positions indicated by color-matching squares in the HAADF image in (b). The corresponding distances to the crystal edge are labeled between the two sets of spectra. Spectra at consecutive distances are offset for clarity. The spectrum at 60 nm (blue) is taken outside the region shown in (b). Red and blue markers indicate energies of bulk carrier plasmons and band gaps, respectively. (d) Energy-filtered maps of bulk plasmons integrated from 780 to 830 meV. (e) Burstein−Moss shift map and (f) dopant percentage map for the nanocrystal in (a) over the region indicated by the red dashed rectangle. (g) Dopant percentage (top), bulk carrier plasmon energy and B-M shift (middle), and carrier density (bottom) as a function of electron beam position along a horizontal line between the two white arrows in (a). Gray curves in the bottom panel of (g) indicate doping activation percentages of 30% and 60%. The scale bars in (a), (b), and (d) indicate 50, 5, and 20 nm, respectively.

respond more quickly to the external field than the ions; the phonons are thus screened in doped $BaSnO_3$. The Coulomb interaction between fast electrons and free carriers gives rise to the plasmons that we observe in doped $BaSnO_3$.[57] We refer to these low-energy excitations as carrier plasmons in what follows. As elaborated in later sections, the spectral range of carrier plasmons is primarily set by the carrier density. For the doping level studied here, we observe surface and bulk carrier plasmons below about 1 eV.[58]

Doping-induced changes in the optical band gap, the Burstein−Moss (B-M) shift,[59,60] is also prominent in our EELS measurements over the 2−6 eV energy range shown in Figure 1c. $BaSnO_3$ has a wide band gap of >3 eV[61] and a sufficiently small high-frequency dielectric constant ε_∞ for it to make Cherenkov losses negligible in our EELS experiments with a 60 keV electron beam.[62,63] Although $BaSnO_3$ has a smaller indirect band gap, the associated transition probability is orders of magnitude lower than the direct transitions.[61] Thus, the energy loss intensities we observe here primarily stem from direct interband transitions near the Γ points.[64] The loss signal from indirect transitions likely overlaps with that from defect states from the top and bottom surfaces of the TEM specimen,[65] thus appearing as a nonzero background below the absorption onset dictated by the direct band gap energy. With increasing doping, a blue shift of the optical gap is clearly observed, as shown in Figure 1c.

It should be noted that the carrier plasmons with a strong doping dependence in Figure 1b are intraband in nature. They are accompanied by other more lossy interband plasmons at relatively high energies, whose energy is in fact proportional to the square root of the valence electron density. In view of their origin, we denote these modes as valence plasmons, in contrast to the aforementioned sub-eV carrier plasmons. In the case of undoped $BaSnO_3$, the valence plasmon is around ∼26 eV.[66] In our results, valence plasmons and high-energy interband transitions both show no measurable dependence on doping—we observe nearly identical spectra in undoped and doped crystals (see Figure 1d). This is not unexpected because the lattice constant and valence electronic band structure remain largely unaffected when substituting La for Ba. The introduced carrier density is typically below 1×10^{21} cm^{-3},[67] which is orders of magnitude smaller than the valence electron density and should accordingly cause only marginal variations in the valence plasmons at about 26 eV. Therefore, changes due to carrier doping can be measured exclusively in the low-loss EELS region shown in Figure 1b,c.

We also analyzed core-loss EELS associated with the A-site chemical composition of $BaSnO_3$ (Figure 1e). As expected, the La-$M_{4,5}$ edge intensity increases with nominal doping. For this

https://doi.org/10.1021/acsnano.2c07540
ACS Nano 2022, 16, 18795−18805

ACS Nano www.acsnano.org Article

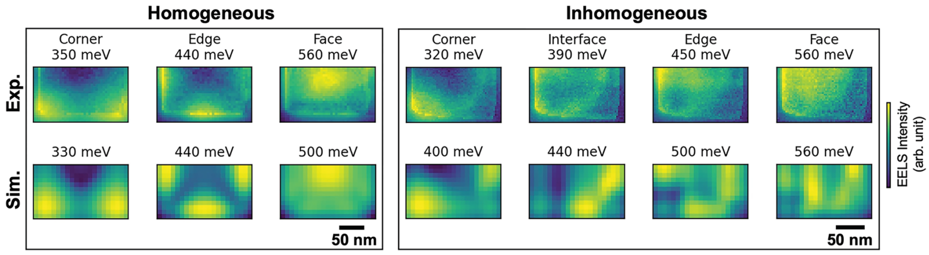

Figure 3. Localized surface plasmons in BLSO nanocrystals. Experimental (top) and simulated (bottom) localized surface plasmons in square-shaped BLSO nanocrystals with homogeneous (left) and inhomogeneous (right) carrier density distributions.

material system and many others, where the dopant and host lattice differ in atomic number by only 1, core-loss EELS is more useful than high-angle annular dark field (HAADF) imaging for identifying dopant locations.

Real-Space Mapping of Dopants and Charge Carrier Excitations. From the knowledge of the excitation energies shown above, dopants and free carriers can be visualized in real space by monochromated EELS mapping. This is demonstrated for a single BLSO nanocrystal, as shown in Figure 2a. This square-shaped BLSO nanoflake is about 20 nm thick as measured by EELS (Section S3, Supporting Information). Although atomic-resolution HAADF imaging of the crystal in Figure 2b shows no substantial contrast variation, low-loss EEL spectra shown in Figure 2c reveal significant changes due to electronic inhomogeneities. From the spectra in the 50−1000 meV energy range, we see how the bulk carrier plasmons are shifting from 830 meV (at a distance of 50 nm from the flake edge) to about 500 meV (20 nm away from the edge). Bulk plasmon energies are signaled by the zero crossing of the frequency-dependent BLSO dielectric function $\varepsilon(\omega)$ (i.e., a pole in the loss function $\mathrm{Im}\{-1/\varepsilon(\omega)\}$). These modes show up as isolated peak maxima in the loss spectra for an electron beam placed at 60, 50, 40, and 3 nm from the flake edge, while they emerge as shoulders of the more intense surface plasmons in the spectra acquired at distances of 30, 20, and 10 nm. This is because, with decreasing energy, the bulk plasmon peaks not only red-shift in energy but also decrease in intensity[68] (Section S1, Supporting Information). In the 200−600 meV spectral range, we observe surface carrier plasmons whose energies are influenced by both the local plasma frequency and the specimen shape, as we show in Figure 3. In addition, we observe phonon polaritons between 80 and 100 meV, whose intensities are inversely proportional to the bulk plasmon energy. We believe the phonon polaritons stem from regions where lattice vibrations are not completely screened by free charge carriers, such as in surface depletion layers.[69,70]

Local optical gaps measured by EELS also show spatial variations, as shown the in 2−6 eV spectra in Figure 2c. We extract the optical gap by modeling the absorption onset (Section S2, Supporting Information) and find that the local optical gap changes between 3.28 and 3.66 eV within the region shown in Figure 2b, depending on the electron beam positions.

Spatial variations of carrier plasmons and optical gap are visualized in the EELS maps in Figure 2d,e for the whole nanocrystal. Figure 2d shows an energy-filtered map of the bulk carrier plasmons in the vicinity of 800 meV. The resonances are observed only in part of the flake (left and center-top), because the rest of the flake shows an $\hbar\omega_p$ value that is considerably lower (Figure 2c and Section S1, Supporting Information). The B-M shift (evaluated with respect to the value obtained for $x = 0$) also shows significant spatial variation, in the range of 200−550 meV. The maps of these two quantities exhibit close correlations, suggesting that the electronic inhomogeneity is a common origin of these variations.

Moreover, we also measure the dopant percentage of this inhomogeneously doped crystal by core-loss EELS mapping, as shown in Figure 2f. The dopant percentage x is defined as $N_{La}/(N_{Ba} + N_{La})$, where N_{Ba} and N_{La} are the numbers of atoms per unit area for Ba and La, respectively. We quantify the dopant percentage from core-loss EELS via the k-factor method, which only requires knowing the ratio of Ba- and La-$M_{4,5}$-edge cross sections, rather than their absolute values.[71] Specifically, we approximate the $M_{4,5}$-edge intensity for Ba and La as N_{Ba} and N_{La}, respectively, and calculate x for each pixel (3.2×3.2 nm^2) of the core-loss EELS map. The result is shown in Figure 2f, where we see that the spatial regions with larger x coincide with regions exhibiting a large B-M shift, as shown in Figure 2e. These regions also feature the high-energy bulk carrier plasmons. Thus, the chemical and electronic heterogeneties are closely related in real space. These spatial variations are also compared more quantitatively as line profiles in Figure 2g, where we plot dopant percentage, the bulk plasmon energy, and the B-M shift as a function of beam position.

Influence of Doping Inhomogeneity on Localized Surface Plasmons. The doping inhomogeneity determined above has a strong influence on the global plasmonic response of the BLSO nanocrystal. This can be seen in a comparison between BLSO nanocrystals with homogeneous and inhomogeneous carrier density distributions, as illustrated in Figure 3. In the left panel of Figure 3, a square-shaped BLSO nanoflake with a relatively homogeneous carrier density distribution shows localized surface plasmon resonances near the corners, edges, and faces at around 350, 440, and 560 meV, respectively. The energy and spatial distribution of these surface plasmons are well reproduced by numerical calculations. Similar geometrically controlled modes are characteristic in cubic-shaped particles, as previously observed in both plasmonic[72−74] and phononic[35,75] materials.

In contrast to homogeneous particles, the BLSO nanocrystals under study, featuring inhomogeneous doping, exhibit substantially different surface plasmon resonances. In the right panel of Figure 3, we visualize the localized surface plasmons of

18798 https://doi.org/10.1021/acsnano.2c07540 ACS Nano 2022, 16, 18795−18805

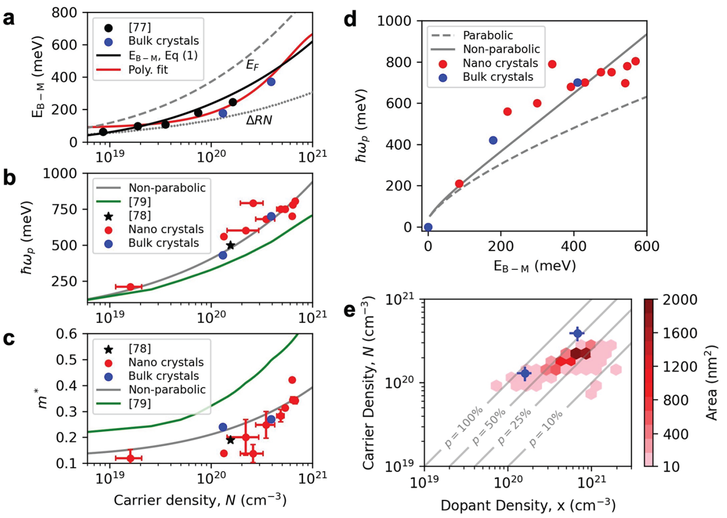

Figure 4. Free carrier characteristics and doping efficiency. Dependence of (a) Burstein−Moss (B-M) shift, (b) bulk plasma frequency, and (c) carrier effective mass on carrier density. Results from refs 77−79 are shown for comparison. (d) Bulk plasmon energy as a function of B-M shift for bulk and nanocrystals as extracted from experiments (symbols), compared with modeled results (gray curves). The red and blue dots represent nano crystals and bulk crystals of BLSO, respectively. (e) Carrier density as a function of dopant density in BLSO. The carrier densities of bulk single crystals are obtained from Hall measurements at room temperature. Carrier and dopant densities of the nanocrystals are extracted from EELS maps in Figure 2. Data points from each pixel (3.2 × 3.2 nm^2) in the EELS maps are represented by hexagons, colored according to the total area for a given N and x.

the BLSO nanoparticle studied in Figure 2. Instead of the existence of corner mode plasmons that brighten all corners at one resonance energy, we observe resonances localized near the left and right corner at different energies. The corner mode at 320 meV only appears near the left corner. The right corner also shows a localized plasmon, but at a much lower energy of ∼180 meV (Section S1, Supporting Information). Although this particle has a size and shape almost identical with that in the left panel of Figure 3, the inhomogeneity in local dopant percentage leads to a different spatially varying carrier density and thus bulk plasma frequency. We corroborate these experimental results through numerical simulations, where we use locally varying bulk plasmon frequencies extracted from experiments. The simulated results also reveal corner modes occurring at different energies as well as similar patterns in energy-filtered maps corresponding to the edge- and face-like plasmons around 450 and 560 meV, respectively. The relatively minor differences between experimental and theoretical results, particularly visible at higher energies, can stem from additional inhomogeneities in plasmon damping, not incorporated in the numerical models. The lower left corner of the flake has a larger thickness (Section S3, Supporting Information), which is the reason plasmon intensities near this location in experiments are higher than the simulated values.

Furthermore, we observe an interesting interfacial plasmon mode in the inhomogeneous nanocrystal. As shown in Figure 3 (right panel), this mode starts to appear near 320 meV, which becomes more pronounced with increasing energy and finally peaks at about 390 meV, before merging with the face-like mode resonance near the high-doping side (above 450 meV in experiments). This interfacial mode forms a circular pattern that is highly confined between the low- and high-doping regions across the whole particle. An interfacial plasmon generally occurs at a boundary that separates two metal-like regions $j = 1, 2$ that are characterized by different bulk plasma frequencies $\omega_{p,j} \propto \sqrt{N_j/m_j^*}$, dictated in turn by their respective carrier densities N_j and effective masses m_j^*. For a planar interface, the mismatch between the corresponding Drude-like permittivities ($\varepsilon_j(\omega)$; similar to eq S2 in Section S1, Supporting Information) gives rise to a mode signaled by a pole in the Fresnel reflection coefficient. Neglecting retardation, this implies $\varepsilon_1 + \varepsilon_2 = 0$, which leads to the mode frequency $\omega_{12} = \sqrt{(\omega_{p,1}^2 + \omega_{p,2}^2)/(\varepsilon_{\infty,1} + \varepsilon_{\infty,2})}$, where $\varepsilon_{\infty,j}$ are high-frequency dielectric constants. The mode confinement is directly revealed by the EELS probability, which is symmetrically decaying with the distance b to the interface as described by the modified Bessel function $\propto K_0(2\omega_{12}b/v)$, where v is the electron velocity.[48] Although the dopant positions here are random, this phenomenon points to the possibility of infrared plasmon engineering by tuning chemical doping at the atomic scale. For instance, an electromagnetic wave could be guided[76] along an arbitrary path in a low-doping channel with extremely confined size that is determined by the placement of dopants.

Quantifying Free Carrier Characteristics and Doping Efficiency. Next, we quantify the carrier density from the

https://doi.org/10.1021/acsnano.2c07540
ACS Nano 2022, 16, 18795−18805

experimentally measured bulk plasma frequency and optical band gap without making assumptions on the carrier effective mass. The bulk plasma frequency takes the form $\omega_p = \sqrt{Ne^2/\varepsilon_0 m^*}$, where N is the carrier density and m^* the effective mass, e and ε_0 stand for the elementary charge and the vacuum permittivity, respectively. Although the bulk plasma frequency is informative about the infrared and optical properties of materials, it only reveals the ratio between carrier density and effective mass.[80] The carrier effective mass is often highly dependent on doping level because of the band nonparabolicity. Thus, in order to unambiguously determine the carrier density and effective mass from a measurement of $\hbar\omega_p$, knowledge of another doping-dependent quantity is required. In this work, we find that the simultaneous measurement of bulk plasmon loss and the Burstein−Moss shift by EELS makes it possible to quantify both the local carrier density and the effective mass.

In order to corroborate the free carrier density and effective mass quantified from EELS, we have also performed Hall measurements on the bulk single crystals, whose bulk plasmon energy and B-M shift were studied by EELS as shown in Figure 1. The BLSO bulk crystals with $x = 0.01$, 0.05 have carrier densities $N = 1.3 \times 10^{20}$ and 3.9×10^{20} cm^{-3}, respectively. The results are shown in Figure 4a, together with data from a previous study of BLSO thin films by optical and Hall experiments.[77] We see that the B-M shift increases with carrier density, following a similar trend, although the data are measured with different techniques. The dependence of the B-M shift on carrier density is determined directly from the electronic band structure of $BaSnO_3$. Specifically, the B-M shift can be modeled based on the conduction band structure and doping level as[81]

$$E_{\text{B-M}} = E_F - \Delta_{RN} \tag{1}$$

where E_F is the Fermi energy relative to the conduction band minimum and Δ_{RN} is the gap renormalization due to electron−electron and electron−impurity interactions. More precisely, $\Delta_{RN} = \Delta E_g^{ee} + \Delta E_g^{ei}$, where

$$\Delta E_g^{ee} = \frac{e^2 k_F}{2\pi^2 \varepsilon_s \varepsilon_0} + \frac{e^2 k_{TF}}{8\pi \varepsilon_s \epsilon_0}\left[1 - \frac{4}{\pi}\tan^{-1}\left(\frac{k_F}{k_{TF}}\right)\right] \tag{2}$$

and

$$\Delta E_g^{ei} = \frac{Ne^2}{\varepsilon_s \varepsilon_0 a_B^* k_{TF}^3} \tag{3}$$

Here, ε_s is the static relative dielectric permittivity, $a_B^* = \frac{\varepsilon_s}{m^*} a_0$ is the effective Bohr radius, a_0 is the Bohr radius, $k_{TF} = \sqrt{\frac{4k_F}{\pi a_B^*}}$ is the Thomas−Fermi screening wave vector, and $k_F = (3\pi N)^{1/3}$ is the Fermi wave vector. Considering a first-order nonparabolic model, the effective mass follows

$$m^* = m^*_{E_F=0}\sqrt{1 + 2\beta\frac{\hbar^2 k^2}{m^*_{E_F=0}}} \tag{4}$$

where $m^*_{E_F=0}$ is the carrier effective mass at the conduction band bottom and β is a parameter describing the band curvature (the increase in m^* with electron wave vector k).

We model the conduction band of $BaSnO_3$ by varying the carrier effective mass, so that the $E_{\text{B-M}}$ values measured at different doping levels can be reproduced by eq 1. Additional material-dependent quantities are the static- and high-frequency dielectric constants, ε_s and ε_∞, which do not change significantly with doping. The results are compared with the experimentally measured $E_{\text{B-M}}$ and N as shown in Figure 4a. Alternatively, a polynomial fit of $E_{\text{B-M}}(N)$ (red curve in Figure 4a) can also provide information on the conduction band curvature. The mean value of the nonparabolic conduction band model and the polynomial fit are shown in Figure 4b,c (solid gray curves). Our best fit to experimental results were found with $m^*_{E_F=0} = 0.12 \pm 0.2$ and $\beta = 1.4$ for the conduction band of $BaSnO_3$.

The electron effective mass in $BaSnO_3$ was found in a wide range in earlier studies, with the smallest value being $^*_{E_F=0}$ = 0.06[82] and most experimental results indicating m^* close to 0.2[78,83,84] for doped $BaSnO_3$. Our results suggest a relatively small m^* at the conduction band bottom and a large nonparabolicity. For N above 1×10^{20} cm^{-3}, our results are in good agreement with the value reported in ref 78, which is obtained from Hall and infrared reflectivity measurements and is widely accepted for $BaSnO_3$. The quick increase of m^* with N we find here is also in line with a recent theoretical study[79] (green curve in Figure 4b,c), where a conduction band inflection point is predicted to exist in $BaSnO_3$ at large Fermi energies.

Given that the B-M shift and the bulk carrier plasmon energy are both dependent on the band curvature, a comparison between the experimental $E_{\text{B-M}}$ and $\hbar\omega_p$ with the modeled values based on the conduction band extracted above serves as a further verification. As shown in Figure 4d, the relation between the B-M shift and the bulk plasma frequency can be described reasonably well with the nonparabolic conduction band model and parameters given above. We note that it should be also possible to extract the conduction band curvature by fitting the relation between the bulk plasmon energy and the B-M shift.

Furthermore, combining the above analysis with core-loss excitations allows us to extract the doping activation percentage p, another important parameter for many material systems,[85−89] which is defined by the ratio between carrier density and dopant concentrations ($p = NV/x$, where V is the unit cell volume). In practice, p is usually evaluated from the ratio between the Hall carrier density and nominal dopant concentration, which is difficult to measure and not well understood at the microscopic level. In BLSO thin films studied earlier, p was found to vary over a wide range, from <10% to ∼70%.[83,90−92]

In our study, the Hall carrier densities for the bulk single crystals with $x = 0.01$, 0.05 correspond to p = 80%, 50%, respectively, as shown in Figure 4e. With the band curvature extracted above, the local carrier density can be calculated from either the B-M shift or the bulk plasma frequency. We use the former in our calculation, as the overlap between bulk and surface carrier plasmons renders the extraction of ω_p less straightforward for low-doping regions. We note that the carrier densities calculated from the B-M shift and the bulk plasma frequency are in good agreement with each other, as shown in the bottom panel of Figure 2g.

Combining the local carrier density with the La percentage shown in Figure 2, we show the activation percentage for the inhomogeneous nanocrystals in Figure 4e, separately measured in 3.2×3.2 nm^2 regions. We observe that the dopant densities

https://doi.org/10.1021/acsnano.2c07540
ACS Nano 2022, 16, 18795−18805

in this nanocrystal vary over a broad range, between 6×10^{19} and 2×10^{21} cm^{-3}, while the carrier densities are centered around 2×10^{20} cm^{-3}. As a result, p for the majority of the regions lies in the range between 25% and 50%. Overall, the dopant activation percentage decreases with doping level for both bulk crystals and nanocrystals of BLSO. The primary source of electron donors are La dopants, as oxygen vacancies are not likely to form in $BaSnO_3$.[93] Thus, the percentage of La dopants that does not contribute to free carriers is rather high, at least 50% for most of the regions. Possible reasons for the incomplete doping activation include charge compensation at surfaces and by defects.[94]

CONCLUSIONS

This study demonstrates the usefulness of low-energy excitations in EELS for understanding the electrical and optical properties at a length scale of a few nanometers. We have shown that the doping-induced changes in the electronic structure can be measured with high spectral and spatial resolution. Changes in the conduction band occupancy should, in principle, also be reflected in near-edge fine structures of core-loss EELS. However, it is impractical to measure such small changes with high accuracy by core-loss EELS (i.e., due to the core−hole lifetime broadening and the small energy loss cross section at high energies). In comparison, low-energy excitations are more sensitive to electronic states near the Fermi level and can be probed with better accuracy. The good agreement between EELS and other experimental methods (Hall measurement, infrared spectroscopy) also supports the validity of the bulk plasma frequency and optical gap measured from monochromated EELS. With a combined analysis of EELS and transport data, it is possible to quantify the local carrier densities and the conduction band curvature. Moreover, combining low-loss and core-loss EELS even allows for a quantification of the doping activation percentage, which otherwise can only be acquired from multiple measurements averaged over large areas. By exploiting the advanced STEM imaging together with monochromated EELS, it should be possible to study local changes in electronic structure down to the individual dopant level.

Our results also suggest that imaging with electronic excitations is not severely limited by inelastic delocalization. It is well-known that higher energy core-loss EELS provides information down to the Ångstrom scale,[95−97] while low-loss EELS often suffers from a poorer spatial localization.[98] Here, we show that both carrier plasmons and band-gap transitions contain information that is sufficiently well localized as to yield useful insight into local optical properties and electronic structure with a resolution of a few nanometers. For example, from the bottom panel of Figure 2g, we see that the carrier density (red and blue dots, obtained via the plasmon energy and B-M shift, respectively) closely tracks the dopant profile (from core loss). This clearly indicates that low-energy excitations are not necessarily more delocalized than high-energy excitations. In our case, carrier electrons in BLSO have an effective Bohr radius of 5−8 nm, which should be the ultimate limit for the attainable spatial resolution.

Quite surprisingly, we have also revealed the existence of a previously unobserved plasmon mode that is highly confined between regions with different doping levels. This finding points to the possibility of engineering a doping profile at the few-nanometer level to guide electromagnetic waves along an arbitrary path, complementary to the geometric control of metallic nanostructures.[99,100] While this approach can be followed over a wide range of length scales depending on the light wavelength and degree of confinement (i.e., in metamaterials operating from the microwave to the visible region), the present analysis relying on BLSO demonstrates a specific example operating in the mid-infrared regime with a high degree of spatial confinement by 2−3 orders of magnitude relative to the light wavelength.

In brief, our work unlocks the full potential of monochromated EELS in providing microscopic insights into the local electronic structure and optical properties, demonstrated here by revealing the electron effective mass, dopant activation percentage, and a heterogeneous-doping-induced interfacial plasmon. These capabilities may lead to exciting discoveries in a wide range of other material systems, where structure−property relationships are of interest.

METHODS

BLSO Crystal Growth and Hall Measurement. The $Ba_{1-x}La_xSnO_3$ nanocrystals were synthesized by the sol−gel method described in ref 58. The nanocrystals studied here have been synthesized with a nominal doping of x = 0.05. The bulk $Ba_{1-x}La_xSnO_3$ crystals were grown by a laser floating-zone technique, for x = 0, 0.01, 0.05. High-purity powders of La_2O_3, $BaCO_3$, and SnO_2 were mixed in the molar ratio x/2:1 − x:1.5. La_2O_3 was baked at 900 °C overnight before weighing. The mixed powder was calcined at 1000 °C for 10 h. The product was reground and sintered at 1400 °C for 20 h with one intermediate grinding. The product was reground, filled into a rubber tube, and pressed under 8000 psi hydrostatic pressure. The rod was sintered at 1400 °C for 10 h. The crystals were grown at a rate of 50 mm/h under 8 bar O_2 pressure. The as-grown crystals were annealed at 1400 °C for 20 h in an oxygen flow before measurements.

For Hall measurements, the crystal was oriented, cut, and polished into a (100) plate. The electrodes were made by gold sputtering. The Hall measurements were performed with a Quantum Design PPMS-9 instrument by sweeping the magnetic field at room temperature.

STEM-EELS Experiments. STEM-EELS data were acquired using a Nion Ultra STEM 100 instrument equipped with an electron monochromator. The microscope was operated at 60 kV with a convergence collection half angle of 30 mrad. We set the EELS collection half-angle to 16 mrad when the monochromator was used. In our EELS experiments, the energy resolution and beam current were balanced for each energy range of interest. For phonons and plasmons in the infrared region, a spectrometer dispersion of 1.2 meV/pixel was used to provide the highest possible energy resolution, which is around 10 meV. For band-gap measurements, the spectrometer dispersion was set to 30 meV/pixel to improve the signal-to-noise ratio. This gave a full width at half-maximum of the zero-loss peak (ZLP) of 33 meV. For infrared plasmon and band-gap mapping, the EELS dwell time was set such that the ZLP was just below saturation. This gives 500−800 ms/frame for phonon and plasmon spectra acquisition. For core-loss EELS in the 400−900 eV region, we set the spectrometer dispersion to 300 meV/pixel and did not introduce the monochromator in order to maximize the beam current and thus the signal-to-noise ratio. The EELS dwell time for core-loss spectra acquisition and mapping was set to 2 s/pixel. The point spectra shown in Figures 1 and 2 are integrated over 80−100 frames, with the dwell time mentioned above. Details of EELS data processing are provided in the Supporting Information.

EELS Simulations. We use a finite-element method (as implemented in COMSOL Multiphysics) to calculate the EELS probability for BLSO flakes, with the dielectric function made position-dependent through the spatial distribution of the doping density, as specified in the Supporting Information.

https://doi.org/10.1021/acsnano.2c07540
ACS Nano 2022, 16, 18795−18805

ASSOCIATED CONTENT

Supporting Information

The Supporting Information is available free of charge at https://pubs.acs.org/doi/10.1021/acsnano.2c07540.

EELS data and simulation for phonons and infrared plasmons, band gap analysis from EELS, and low-magnification image and thickness map of the inhomogeneous crystal (PDF)

AUTHOR INFORMATION

Corresponding Authors

Hongbin Yang − *Department of Chemistry and Chemical Biology, Rutgers University, Piscataway, New Jersey 08854, United States;* orcid.org/0000-0002-0098-6944; Email: hongbin.yang@rutgers.edu

Philip E. Batson − *Department of Physics and Astronomy, Rutgers University, Piscataway, New Jersey 08854, United States*; Email: batson@physics.rutgers.edu

F. Javier García de Abajo − *ICFO-Institut de Ciencies Fotoniques, The Barcelona Institute of Science and Technology, 08860 Castelldefels, Barcelona, Spain; ICREA-Institució Catalana de Recerca i Estudis Avançats, 08010 Barcelona, Spain;* orcid.org/0000-0002-4970-4565; Email: javier.garciadeabajo@nanophotonics.es

Authors

Andrea Konečná − *ICFO-Institut de Ciencies Fotoniques, The Barcelona Institute of Science and Technology, 08860 Castelldefels, Barcelona, Spain; Central European Institute of Technology, Brno University of Technology, 61200 Brno, Czech Republic;* orcid.org/0000-0002-7423-5481

Xianghan Xu − *Department of Physics and Astronomy, Rutgers University, Piscataway, New Jersey 08854, United States*

Sang-Wook Cheong − *Department of Physics and Astronomy, Rutgers University, Piscataway, New Jersey 08854, United States*

Eric Garfunkel − *Department of Chemistry and Chemical Biology, Rutgers University, Piscataway, New Jersey 08854, United States; Department of Physics and Astronomy, Rutgers University, Piscataway, New Jersey 08854, United States*

Complete contact information is available at: https://pubs.acs.org/10.1021/acsnano.2c07540

Notes

The authors declare no competing financial interest.

ACKNOWLEDGMENTS

H.Y. and P.E.B. acknowledge financial support of the U.S. Department of Energy, Office of Science, Basic Energy Sciences, under Award No. DESC0005132. X.X. and S.-W.C. were supported by the center for Quantum Materials Synthesis (cQMS), funded by the Gordon and Betty Moore Foundations EPiQS initiative through grant GBMF10104, and by Rutgers University. F.J.G.d.A. acknowledges support by the European Research Council (Advanced Grant 789104-eNANO), the Spanish MICINN (PID2020-112625GB-I00 and Severo Ochoa CEX2019-000910-S), and Fundaciós Cellex and Mir-Puig.

REFERENCES

(1) Zunger, A.; Malyi, O. I. Understanding doping of quantum materials. *Chem. Rev.* **2021**, *121*, 3031−3060.

(2) Ye, J. T.; Zhang, Y. J.; Akashi, R.; Bahramy, M. S.; Arita, R.; Iwasa, Y. Superconducting dome in a gate-tuned band insulator. *Science* **2012**, *338* (6111), 1193.

(3) Edge, J. M.; Kedem, Y.; Aschauer, U.; Spaldin, N. A.; Balatsky, A. V. Quantum critical origin of the superconducting dome in $SrTiO_3$. *Phys. Rev. Lett.* **2015**, *115* (24), 247002.

(4) Li, D.; Wang, B. Y.; Lee, K.; Harvey, S. P.; Osada, M.; Goodge, B. H.; Kourkoutis, L.; Hwang, H. Superconducting dome in $Nd_{1-x}Sr_xNiO_2$ infinite layer films. *Phys. Rev. Lett.* **2020**, *125* (2), 027001.

(5) Hong, S. S.; Cha, J. J.; Kong, D.; Cui, Y. Ultra-low carrier concentration and surface-dominant transport in antimony-doped bi2se3 topological insulator nanoribbons. *Nat. Commun.* **2012**, *3*, 757.

(6) Perea, D. E.; Hemesath, E. R.; Schwalbach, E. J.; Lensch-Falk, J. L.; Voorhees, P. W.; Lauhon, L. J. Direct measurement of dopant distribution in an individual vapour-liquid-solid nanowire. *Nat. Nanotechnol.* **2009**, *4* (5), 315−319.

(7) Koren, E.; Berkovitch, N.; Rosenwaks, Y. Measurement of active dopant distribution and diffusion in individual silicon nanowires. *Nano Lett.* **2010**, *10* (4), 1163−1167.

(8) Ko, W.; Gai, Z.; Puretzky, A. A.; Liang, L.; Berlijn, T.; Hachtel, J. A.; Xiao, K.; Ganesh, P.; Yoon, M.; Li, A.-P. Understanding heterogeneities in quantum materials. *Adv. Mater.* **2022**, 2106909.

(9) Weber, B.; Mahapatra, S.; Ryu, H.; Lee, S.; Fuhrer, A.; Reusch, T. C. G.; Thompson, D. L.; Lee, W. C. T.; Klimeck, G.; Hollenberg, L. C. L.; Simmons, M. Y. Ohmas law survives to the atomic scale. *Science* **2012**, *335* (6064), 64−67.

(10) Jariwala, D.; Krayev, A.; Wong, J.; Robinson, A. E.; Sherrott, M. C.; Wang, S.; Liu, G.-Y.; Terrones, M.; Atwater, H. A. Nanoscale doping heterogeneity in few-layer WSe_2 exfoliated onto noble metals revealed by correlated spm and ters imaging,. *2D Materials* **2018**, *5*, 035003.

(11) Jagadamma, L. K.; Edwards, P. R.; Martin, R. W.; Ruseckas, A.; Samuel, I. D. W. Nanoscale heterogeneity in cspbbr3 and cspbbr3:ki perovskite films revealed by cathodoluminescence hyperspectral imaging. *ACS Applied Energy Materials* **2021**, *4* (3), 2707−2715.

(12) Manley, M. E.; Lynn, J. W.; Abernathy, D. L.; Specht, E. D.; Delaire, O.; Bishop, A. R.; Sahul, R.; Budai, J. D. Phonon localization drives polar nanoregions in a relaxor ferroelectric. *Nat. Commun.* **2014**, *5*, 3683.

(13) Li, F.; Zhang, S.; Yang, T.; Xu, Z.; Zhang, N.; Liu, G.; Wang, J.; Wang, J.; Cheng, Z.; Ye, Z.-G.; Luo, J.; Shrout, T. R.; Chen, L.-Q. The origin of ultrahigh piezoelectricity in relaxor-ferroelectric solid solution crystals,. *Nat. Commun.* **2016**, *7*, 13807.

(14) Kumar, A.; Baker, J. N.; Bowes, P. C.; Cabral, M. J.; Zhang, S.; Dickey, E. C.; Irving, D. L.; LeBeau, J. M. Atomic-resolution electron microscopy of nanoscale local structure in lead-based relaxor ferroelectrics. *Nat. Mater.* **2021**, *20*, 62−67.

(15) Pan, S. H.; O'Neal, J. P.; Badzey, R. L.; Chamon, C.; Ding, H.; Engelbrecht, J. R.; Wang, Z.; Eisaki, H.; Uchida, S.; Gupta, A. K.; Ng, K. W.; Hudson, E. W.; Lang, K. M.; Davis, J. C. Microscopic electronic inhomogeneity in the high-t_c superconductor $Bi_2Sr_2CaCu_2O_{8+x}$. *Nature* **2001**, *413* (6853), 282−285.

(16) Hanaguri, T.; Lupien, C.; Kohsaka, Y.; Lee, D. H.; Azuma, M.; Takano, M.; Takagi, H.; Davis, J. C. A checkerboard electronic crystal state in lightly hole-doped $Ca_{2-x}Na_xCuO_2Cl_2$. *Nature* **2004**, *430* (7003), 1001−1005.

(17) Vershinin, M.; Misra, S.; Ono, S.; Abe, Y.; Ando, Y.; Yazdani, A. Local ordering in the pseudogap state of the high-t_c superconductor $Bi_2Sr_2CaCu_2O_{8+\delta}$. *Science* **2004**, *303* (5666), 1995−1998.

(18) Uehara, M.; Mori, S.; Chen, C. H.; Cheong, S.-W. Percolative phase separation underlies colossal magnetoresistance in mixed-valent manganites. *Nature* **1999**, *399*, 560−563.

(19) Burgy, J.; Mayr, M.; Martin-Mayor, V.; Moreo, A.; Dagotto, E. Colossal effects in transition metal oxides caused by intrinsic inhomogeneities. *Phys. Rev. Lett.* **2001**, *87*, 277202.

https://doi.org/10.1021/acsnano.2c07540
ACS Nano 2022, 16, 18795−18805

(20) Akahoshi, D.; Uchida, M.; Tomioka, Y.; Arima, T.; Matsui, Y.; Tokura, Y. Random potential effect near the bicritical region in perovskite manganites as revealed by comparison with the ordered perovskite analogs. *Phys. Rev. Lett.* **2003**, *90*, 177203.
(21) Dagotto, E. Complexity in strongly correlated electronic systems. *Science* **2005**, *309* (5732), 257−262.
(22) Yin, J.-X.; Pan, S. H.; Zahid Hasan, M. Probing topological quantum matter with scanning tunnelling microscopy. *Nat. Rev. Phys.* **2021**, *3*, 249−263.
(23) Girard, P. Electrostatic force microscopy: principles and some applications to semiconductors. *Nanotechnology* **2001**, *12*, 485−490.
(24) Gramse, G.; Kölker, A.; Škereň, T.; Stock, T. J. Z.; Aeppli, G.; Kienberger, F.; Fuhrer, A.; Curson, N. J. Nanoscale imaging of mobile carriers and trapped charges in delta doped silicon p−n junctions. *Nature Electronics* **2020**, *3*, 531−538.
(25) Johns, R. W.; Bechtel, H. A.; Runnerstrom, E. L.; Agrawal, A.; Lounis, S. D.; Milliron, D. J. Direct observation of narrow mid-infrared plasmon linewidths of single metal oxide nanocrystals. *Nat. Commun.* **2016**, *7*, 11583.
(26) Mooshammer, F.; Sandner, F.; Huber, M. A.; Zizlsperger, M.; Weigand, H.; Plankl, M.; Weyrich, C.; Lanius, M.; Kampmeier, J.; Mussler, G.; Gr-tzmacher, D.; Boland, J. L.; Cocker, T. L.; Huber, R. Nanoscale near-field tomography of surface states on $(Bi_{0.5}Sb_{0.5})_2Te_3$. *Nano Lett.* **2018**, *18* (12), 7515−7523.
(27) Lu, X.; Khatib, O.; Du, X.; Duan, J.; Wei, W.; Liu, X.; Bechtel, H. A.; D'Apuzzo, F.; Yan, M.; Buyanin, A.; Fu, Q.; Chen, J.; Salmeron, M.; Zeng, J.; Raschke, M. B.; Jiang, P.; Bao, X. Nanoimaging of electronic heterogeneity in bi2se3 and sb2te3 nanocrystals. *Advanced Electronic Materials* **2018**, *4* (1), 1700377.
(28) Chen, X.; Hu, D.; Mescall, R.; You, G.; Basov, D. N.; Dai, Q.; Liu, M. Modern scattering-type scanning near-field optical microscopy for advanced material research. *Adv. Mater.* **2019**, *31* (24), 1804774.
(29) Chu, Z.; Zheng, L.; Lai, K. Microwave microscopy and its applications. *Annu. Rev. Mater. Res.* **2020**, *50* (1), 105−130.
(30) Cojocaru, B.; Avram, D.; Kessler, V.; Parvulescu, V.; Seisenbaeva, G.; Tiseanu, C. Nanoscale insights into doping behavior, particle size and surface effects in trivalent metal doped sno2. *Sci. Rep.* **2017**, *7*, 9598.
(31) Zhou, W.; Lee, J.; Nanda, J.; Pantelides, S. T.; Pennycook, S. J.; Idrobo, J. C. Atomically localized plasmon enhancement in monolayer graphene. *Nat. Nanotech* **2012**, *7*, 161−165.
(32) Krivanek, O. L.; Lovejoy, T. C.; Dellby, N.; Aoki, T.; Carpenter, R. W.; Rez, P.; Soignard, E.; Zhu, J.; Batson, P. E.; Lagos, M. J.; Egerton, R. F.; Crozier, P. A. Vibrational spectroscopy in the electron microscope. *Nature* **2014**, *514* (7521), 209−12.
(33) Dellby, N.; Lovejoy, T.; Corbin, G.; Johnson, N.; Hayner, R.; Hoffman, M.; Hrncrik, P.; Plotkin-Swing, B.; Taylor, D.; Krivanek, O.; et al. Ultra-high energy resolution eels,. *Microscopy and Microanalysis* **2020**, *26* (S2), 1804−1805.
(34) Krivanek, O. L.; Dellby, N.; Hachtel, J. A.; Idrobo, J. C.; Hotz, M. T.; Plotkin-Swing, B.; Bacon, N. J.; Bleloch, A. L.; Corbin, G. J.; Hoffman, M. V.; Meyer, C. E.; Lovejoy, T. C. Progress in ultrahigh energy resolution eels. *Ultramicroscopy* **2019**, *203*, 60−67.
(35) Lagos, M. J.; Trugler, A.; Hohenester, U.; Batson, P. E. Mapping vibrational surface and bulk modes in a single nanocube. *Nature* **2017**, *543* (7646), 529−532.
(36) Govyadinov, A. A.; Konečná, A.; Chuvilin, A.; Velez, S.; Dolado, I.; Nikitin, A. Y.; Lopatin, S.; Casanova, F.; Hueso, L. E.; Aizpurua, J.; Hillenbrand, R. Probing low-energy hyperbolic polaritons in van der waals crystals with an electron microscope. *Nat. Commun.* **2017**, *8* (1), 95.
(37) Hage, F. S.; Nicholls, R. J.; Yates, J. R.; McCulloch, D. G.; Lovejoy, T. C.; Dellby, N.; Krivanek, O. L.; Refson, K.; Ramasse, Q. M. Nanoscale momentum-resolved vibrational spectroscopy. *Science Advances* **2018**, *4* (6), eaar7495.
(38) Senga, R.; Suenaga, K.; Barone, P.; Morishita, S.; Mauri, F.; Pichler, T. Position and momentum mapping of vibrations in graphene nanostructures. *Nature* **2019**, *573*, 247−250.
(39) Venkatraman, K.; Levin, B. D. A.; March, K.; Rez, P.; Crozier, P. A. Vibrational spectroscopy at atomic resolution with electron impact scattering. *Nat. Phys.* **2019**, *15*, 1237−1241.
(40) Hage, F. S.; Radtke, G.; Kepaptsoglou, D. M.; Lazzeri, M.; Ramasse, Q. M. Single-atom vibrational spectroscopy in the scanning transmission electron microscope. *Science* **2020**, *367*, 1124−1127.
(41) Yan, X.; Liu, C.; Gadre, C. A.; Gu, L.; Aoki, T.; Lovejoy, T. C.; Dellby, N.; Krivanek, O. L.; Schlom, D. G.; Wu, R.; Pan, X. Single-defect phonons imaged by electron microscopy. *Nature* **2021**, *589* (7840), 65−69.
(42) Konečná, A.; Li, J.; Edgar, J. H.; García de Abajo, F. J.; Hachtel, J. A. Revealing nanoscale confinement effects on hyperbolic phonon polaritons with an electron beam. *Small* **2021**, *17* (39), 2103404.
(43) Li, Y.-H.; Qi, R.-S.; Shi, R.-C.; Hu, J.-N.; Liu, Z.-T.; Sun, Y.-W.; Li, M.-Q.; Li, N.; Song, C.-L.; Wang, L.; Hao, Z.-B.; Luo, Y.; Xue, Q.-K.; Ma, X.-C.; Gao, P. Atomic-scale probing of heterointerface phonon bridges in nitride semiconductor. *Proc. Natl. Acad. Sci. U. S. A.* **2022**, *119* (8), e2117027119.
(44) Granerød, C. S.; Bilden, S. R.; Aarholt, T.; Yao, Y.-F.; Yang, C. C.; Look, D. C.; Vines, L.; Johansen, K. M.; Prytz, O. Direct observation of conduction band plasmons and the related burstein-moss shift in highly doped semiconductors: A STEM-EELS study of Ga−doped ZnO. *Phys. Rev. B* **2018**, *98*, 115301.
(45) Yang, H.; Garfunkel, E. L.; Batson, P. E. Probing free carrier plasmons in doped semiconductors using spatially resolved electron energy loss spectroscopy. *Phys. Rev. B* **2020**, *102* (20), 205427.
(46) Olafsson, A.; Busche, J. A.; Araujo, J. J.; Maiti, A.; Idrobo, J. C.; Gamelin, D. R.; Masiello, D. J.; Camden, J. P. Electron beam infrared nano-ellipsometry of individual indium tin oxide nanocrystals. *Nano Lett.* **2020**, *20* (11), 7987−7994.
(47) Mkhitaryan, V.; March, K.; Tseng, E. N.; Li, X.; Scarabelli, L.; Liz-Marzan, L. M.; Chen, S.-Y.; Tizei, L. H. G.; Stephan, O.; Song, J.-M.; Kociak, M.; García de Abajo, F. J.; Gloter, A. Can copper nanostructures sustain high-quality plasmons? *Nano Lett.* **2021**, *21* (6), 2444−2452.
(48) García de Abajo, F. J. Optical excitations in electron microscopy. *Rev. Mod. Phys.* **2010**, *82*, 209−275.
(49) Tizei, L. H. G.; Lin, Y.-C.; Mukai, M.; Sawada, H.; Lu, A.-Y.; Li, L.-J.; Kimoto, K.; Suenaga, K. Exciton mapping at subwavelength scales in two-dimensional materials. *Phys. Rev. Lett.* **2015**, *114*, 107601.
(50) Voyles, P. M.; Muller, D. A.; Grazul, J. L.; Citrin, P. H.; Gossmann, H. J. L. Atomic-scale imaging of individual dopant atoms and clusters in highly n-type bulk Si. *Nature* **2002**, *416* (6883), 826−829.
(51) Varela, M.; Findlay, S. D.; Lupini, A. R.; Christen, H. M.; Borisevich, A. Y.; Dellby, N.; Krivanek, O. L.; Nellist, P. D.; Oxley, M. P.; Allen, L. J.; Pennycook, S. J. Spectroscopic imaging of single atoms within a bulk solid. *Phys. Rev. Lett.* **2004**, *92* (9), 095502.
(52) Kim, H. J.; Kim, U.; Kim, H. M.; Kim, T. H.; Mun, H. S.; Jeon, B.-G.; Hong, K. T.; Lee, W.-J.; Ju, C.; Kim, K. H.; Char, K. High mobility in a stable transparent perovskite oxide. *Applied Physics Express* **2012**, *5*, 061102.
(53) Raghavan, S.; Schumann, T.; Kim, H.; Zhang, J. Y.; Cain, T. A.; Stemmer, S. High-mobility $BaSnO_3$ grown by oxide molecular beam epitaxy. *APL Materials* **2016**, *4* (1), 016106.
(54) Paik, H.; Chen, Z.; Lochocki, E.; Seidner H, A.; Verma, A.; Tanen, N.; Park, J.; Uchida, M.; Shang, S.; Zhou, B.-C.; Brtzam, M.; Uecker, R.; Liu, Z.-K.; Jena, D.; Shen, K. M.; Muller, D. A.; Schlom, D. G. Adsorption-controlled growth of La-doped $BaSnO_3$ by molecular-beam epitaxy. *APL Materials* **2017**, *5* (11), 116107.
(55) García de Abajo, F. J.; Di Giulio, V. Optical excitations with electron beams: Challenges and opportunities. *ACS Photonics* **2021**, *8* (4), 945−974.
(56) Stanislavchuk, T. N.; Sirenko, A. A.; Litvinchuk, A. P.; Luo, X.; Cheong, S. W. Electronic band structure and optical phonons of $BaSnO_3$ and $Ba_{0.97}Sn_{0.03}O_3$ single crystals: Theory and experiment. *J. Appl. Phys.* **2012**, *112* (4), 044108.

(57) Pines, D.; Bohm, D. A collective description of electron interactions: Ii. collective vs individual particle aspects of the interactions. *Phys. Rev.* **1952**, *85*, 338−353.
(58) Yang, H.; Konečná, A.; Xu, X.; Cheong, S.-W.; Garfunkel, E.; García de Abajo, F. J.; Batson, P. E. Low-loss tunable infrared plasmons in the high-mobility perovskite (Ba,La)SnO_3. *Small* **2022**, *18* (16), 2106897.
(59) Burstein, E. Anomalous optical absorption limit in InSb. *Phys. Rev.* **1954**, *93* (3), 632−633.
(60) Moss, T. S. The interpretation of the properties of indium antimonide. *Proc. Phys. Soc. Sect. B* **1954**, *67* (10), 775−782.
(61) Monserrat, B.; Dreyer, C. E.; Rabe, K. M. Phonon-assisted optical absorption in $BaSnO_3$ from first principles. *Phys. Rev. B* **2018**, *97* (10), 104310.
(62) Chen, C. H.; Silcox, J.; Vincent, R. Electron-energy losses in silicon: Bulk and surface plasmons and Čerenkov radiation. *Phys. Rev. B* **1975**, *12* (1), 64−71.
(63) Stoger-Pollach, M.; Franco, H.; Schattschneider, P.; Lazar, S.; Schaffer, B.; Grogger, W.; Zandbergen, H.W. Cerenkov losses: A limit for bandgap determination and Kramers-Kronig analysis. *Micron* **2006**, *37* (5), 396−402.
(64) Aggoune, W.; Eljarrat, A.; Nabok, D.; Irmscher, K.; Zupancic, M.; Galazka, Z.; Albrecht, M.; Koch, C.; Draxl, C. A consistent picture of excitations in cubic $BaSnO_3$ revealed by combining theory and experiment. *Commun. Mater.* **2022**, *3*, 12.
(65) Rafferty, B.; Brown, L. M. Direct and indirect transitions in the region of the band gap using electron-energy-loss spectroscopy. *Phys. Rev. B* **1998**, *58* (16), 10326−10337.
(66) Yun, H.; Topsakal, M.; Prakash, A.; Ganguly, K.; Leighton, C.; Jalan, B.; Wentzcovitch, R. M.; Mkhoyan, K. A.; Jeong, J. S. Electronic structure of $BaSnO_3$ investigated by high-energy-resolution electron energy-loss spectroscopy and ab initio calculations. *Journal of Vacuum Science and Technology A* **2018**, *36* (3), 031503.
(67) Prakash, A.; Xu, P.; Faghaninia, A.; Shukla, S.; Ager, J. W.; Lo, C. S.; Jalan, B. Wide bandgap $BaSnO_3$ films with room temperature conductivity exceeding 104 S cm^{-1}. *Nat. Commun.* **2017**, *8*, 15167.
(68) Caruso, F.; Verdi, C.; Poncé, S.; Giustino, F. Electron-plasmon and electron-phonon satellites in the angle-resolved photoelectron spectra of n-doped anatase TiO_2. *Phys. Rev. B* **2018**, *97*, 165113.
(69) Chen, Y.; Nannarone, S.; Schaefer, J.; Hermanson, J. C.; Lapeyre, G. J. Coupled plasmon and phonon excitations in the space-charge layer on GaAs (110) surfaces. *Phys. Rev. B* **1989**, *39*, 7653−7658.
(70) Chen, Y.; Hermanson, J. C.; Lapeyre, G. J. Coupled plasmon and phonon in the accumulation layer of InAs (110) cleaved surfaces. *Phys. Rev. B* **1989**, *39*, 12682−12687.
(71) Hofer, F.; Golob, P.; Brunegger, A. EELS quantification of the elements Sr to W by means of $M_{4,5}$ edges. *Ultramicroscopy* **1988**, *25* (1), 81−84.
(72) Sherry, L. J.; Chang, S.-H.; Schatz, G. C.; Van Duyne, R. P.; Wiley, B. J.; Xia, Y. Localized surface plasmon resonance spectroscopy of single silver nanocubes. *Nano Lett.* **2005**, *5* (10), 2034−2038.
(73) Nicoletti, O.; de la Peña, F.; Leary, R. K.; Holland, D. J.; Ducati, C.; Midgley, P. A. Three-dimensional imaging of localized surface plasmon resonances of metal nanoparticles. *Nature* **2013**, *502* (7469), 80−84.
(74) Zhang, S.; Bao, K.; Halas, N. J.; Xu, H.; Nordlander, P. Substrate-induced fano resonances of a plasmonic nanocube: A route to increased-sensitivity localized surface plasmon resonance sensors revealed. *Nano Lett.* **2011**, *11* (4), 1657−1663.
(75) Li, X.; Haberfehlner, G.; Hohenester, U.; Stephan, O.; Kothleitner, G.; Kociak, M. Three-dimensional vectorial imaging of surface phonon polaritons. *Science* **2021**, *371* (6536), 1364.
(76) Law, S.; Roberts, C.; Kilpatrick, T.; Yu, L.; Ribaudo, T.; Shaner, E. A.; Podolskiy, V.; Wasserman, D. All-semiconductor negative-index plasmonic absorbers. *Phys. Rev. Lett.* **2014**, *112*, 017401.
(77) Lebens-Higgins, Z.; Scanlon, D. O.; Paik, H.; Sallis, S.; Nie, Y.; Uchida, M.; Quackenbush, N. F.; Wahila, M. J.; Sterbinsky, G. E.; Arena, D. A.; Woicik, J. C.; Schlom, D. G.; Piper, L. F. Direct observation of electrostatically driven band gap renormalization in a degenerate perovskite transparent conducting oxide. *Phys. Rev. Lett.* **2016**, *116* (2), 027602.
(78) James Allen, S.; Raghavan, S.; Schumann, T.; Law, K.-M.; Stemmer, S. Conduction band edge effective mass of La-doped $BaSnO_3$. *Appl. Phys. Lett.* **2016**, *108* (25), 252107.
(79) Rowberg, A. J. E.; Krishnaswamy, K.; Van de Walle, C. G. Inflection points in the conduction-band structure of $BaSnO_3$. *Phys. Rev. B* **2020**, *102*, 115201.
(80) Franzen, S. Surface plasmon polaritons and screened plasma absorption in indium tin oxide compared to silver and gold. *J. Phys. Chem. C* **2008**, *112* (15), 6027−6032.
(81) Berggren, K. F.; Sernelius, B. E. Band-gap narrowing in heavily doped many-valley semiconductors. *Phys. Rev. B* **1981**, *24*, 1971−1986.
(82) Moreira, E.; Henriques, J.; Azevedo, D.; Caetano, E.; Freire, V.; Albuquerque, E. Structural and electronic properties of $Sr^xBa^{1-x}SnO_3$ from first principles calculations. *J. Solid State Chem.* **2012**, *187*, 186−194.
(83) Kim, H. J.; Kim, U.; Kim, T. H.; Kim, J.; Kim, H. M.; Jeon, B.-G.; Lee, W.-J.; Mun, H. S.; Hong, K. T.; Yu, J.; Char, K.; Kim, K. H. Physical properties of transparent perovskite oxides (Ba,La)SnO_3 with high electrical mobility at room temperature. *Phys. Rev. B* **2012**, *86* (16), 165205.
(84) Niedermeier, C. A.; Rhode, S.; Ide, K.; Hiramatsu, H.; Hosono, H.; Kamiya, T.; Moram, M. A. Electron effective mass and mobility limits in degenerate perovskite stannate $BaSnO_3$. *Phys. Rev. B* **2017**, *95*, 161202.
(85) Capano, M. A.; Ryu, S.; Melloch, M. R.; Cooper, J. A.; Buss, M. R. Dopant activation and surface morphology of ion implanted 4h- and 6h-silicon carbide. *J. Electron. Mater.* **1998**, *27*, 370−376.
(86) Tandon, B.; Ghosh, S.; Milliron, D. J. Dopant selection strategy for high-quality factor localized surface plasmon resonance from doped metal oxide nanocrystals. *Chem. Mater.* **2019**, *31* (18), 7752−7760.
(87) Son, J.; Moetakef, P.; Jalan, B.; Bierwagen, O.; Wright, N. J.; Engel-Herbert, R.; Stemmer, S. Epitaxial srtio3 films with electron mobilities exceeding 30,000 $cm^2V^{-1}s^{-1}$. *Nat. Mater.* **2010**, *9*, 482−484.
(88) Mairoser, T.; Schmehl, A.; Melville, A.; Heeg, T.; Canella, L.; Böni, P.; Zander, W.; Schubert, J.; Shai, D. E.; Monkman, E. J.; Shen, K. M.; Schlom, D. G.; Mannhart, J. Is there an intrinsic limit to the charge-carrier-induced increase of the curie temperature of euo? *Phys. Rev. Lett.* **2010**, *105*, 257206.
(89) Held, R.; Mairoser, T.; Melville, A.; Mundy, J. A.; Holtz, M. E.; Hodash, D.; Wang, Z.; Heron, J. T.; Dacek, S. T.; Holländer, B.; Muller, D. A.; Schlom, D. G. Exploring the intrinsic limit of the charge-carrier-induced increase of the curie temperature of lu- and la-doped euo thin films. *Phys. Rev. Mater.* **2020**, *4*, 104412.
(90) Niedermeier, C. A.; Rhode, S.; Fearn, S.; Ide, K.; Moram, M. A.; Hiramatsu, H.; Hosono, H.; Kamiya, T. Solid phase epitaxial growth of high mobility La:$BaSnO_3$ thin films co-doped with interstitial hydrogen. *Appl. Phys. Lett.* **2016**, *108* (17), 172101.
(91) Singh, P.; Swartz, A.; Lu, D.; Hong, S. S.; Lee, K.; Marshall, A. F.; Nishio, K.; Hikita, Y.; Hwang, H. Y. Large-area crystalline $BaSnO_3$ membranes with high electron mobilities,. *ACS Appl. Electr. Mater.* **2019**, *1* (7), 1269−1274.
(92) Wang, Z.; Paik, H.; Chen, Z.; Muller, D. A.; Schlom, D. G. Epitaxial integration of high-mobility La-doped $BaSnO_3$ thin films with silicon,. *APL Mater.* **2019**, *7* (2), 022520.
(93) Wang, H.; Walter, J.; Ganguly, K.; Yu, B.; Yu, G.; Zhang, Z.; Zhou, H.; Fu, H.; Greven, M.; Leighton, C. Wide-voltage-window reversible control of electronic transport in electrolyte-gated epitaxial $basno_3$. *Phys. Rev. Mater.* **2019**, *3*, 075001.
(94) Scanlon, D. O. Defect engineering of $basno_3$ for high-performance transparent conducting oxide applications. *Phys. Rev. B* **2013**, *87*, 161201.

(95) Batson, P. E. Simultaneous stem imaging and electron energy-loss spectroscopy with atomic-column sensitivity. *Nature* **1993**, *366*, 727–728.
(96) Muller, D. A. Structure and bonding at the atomic scale by scanning transmission electron microscopy. *Nat. Mater.* **2009**, *8*, 263–270.
(97) Botton, G. A.; Lazar, S.; Dwyer, C. Elemental mapping at the atomic scale using low accelerating voltages. *Ultramicroscopy* **2010**, *110* (8), 926–934.
(98) Egerton, R. Scattering delocalization and radiation damage in stem-eels. *Ultramicroscopy* **2017**, *180*, 115–124.
(99) Rossouw, D.; Botton, G. A. Plasmonic response of bent silver nanowires for nanophotonic subwavelength waveguiding. *Phys. Rev. Lett.* **2013**, *110*, 066801.
(100) Raza, S.; Esfandyarpour, M.; Koh, A. L.; Mortensen, N. A.; Brongersma, M. L.; Bozhevolnyi, S. I. Electron energy-loss spectroscopy of branched gap plasmon resonators. *Nat. Commun.* **2016**, *7*, 13790.

https://doi.org/10.1021/acsnano.2c07540
ACS Nano 2022, 16, 18795–18805

PHYSICAL REVIEW APPLIED **19,** 024042 (2023)

Strongly Coupled Plasmon and Phonon Polaritons as Seen by Photon and Electron Probes

Pavel Gallina,[1,2] Andrea Konečná,[1,*] Jiří Liška,[1] Juan Carlos Idrobo,[3] and Tomáš Šikola[1,2]

[1] *Central European Institute of Technology, Brno University of Technology, Brno 612 00, Czech Republic*
[2] *Institute of Physical Engineering, Brno University of Technology, Brno 616 69, Czech Republic*
[3] *Materials Science and Engineering Department, University of Washington, Seattle, Washington 98195, USA*

(Received 12 November 2022; revised 22 December 2022; accepted 23 December 2022; published 15 February 2023)

The ability to control and modify infrared excitations in condensed matter is of both fundamental and applied interest. Here we explore a system supporting low-energy excitations, in particular, mid-infrared localized plasmon modes and phonon polaritons that are tuned to be strongly coupled. We study the coupled modes by using far-field infrared spectroscopy, state-of-the-art monochromated electron energy-loss spectroscopy, numerical simulations, and analytical modeling. We demonstrate that the electron probe facilitates a precise characterization of polaritons constituting the coupled system, and enables an active control over the coupling and the resulting sample response both in frequency and space. Although far-field optical spectra can be substantially different from near-field electron energy-loss spectra, we show that a direct comparison is possible via postprocessing and right positioning of the electron beam. The resulting spectra allow us to evaluate the key parameters of the coupled system, such as the coupling strength, which we demonstrate to be probe independent. Our work establishes a rigorous description of the spectral features observed in light- and localized electron-based spectroscopies, which can be extended to the analysis of analogous optical systems with applications in heat management and electromagnetic field concentration or nanofocusing.

DOI: 10.1103/PhysRevApplied.19.024042

I. INTRODUCTION

Polaritons are quasiparticles emerging due to strong coupling between photons and excitations in condensed matter, such as plasmons in metals and semiconductors or optical phonons in ionic crystals [1]. The resulting plasmon polaritons (PPs) and phonon polaritons (PhPs) are known to facilitate the confinement of light at the nanoscale, often deeply below the diffraction limit, which finds applications in nanoscale focusing [2–5], extreme waveguiding [6], the design of optical elements [7], or enhanced molecular detection [8]. Spatial confinement and energies of the polaritonic excitations can be typically tuned by nanostructuring, e.g., in a form of gratings or the so-called optical nanoantennas [9], but also by coupling between polaritons themselves. Such coupling results in hybridized modes [10–15] and introduces more degrees of freedom to engineer system functionalities and on-demand optical response [16,17],

Both uncoupled and coupled polaritons in the mid-infrared (MIR) energy range have been experimentally explored by far-field IR spectroscopy [18–21]. IR spectroscopy provides very high spectral resolution; however, its spatial resolution is restricted by the diffraction limit. Accessing both spectral and spatial information on the coupled polaritonic modes is only possible by utilizing near-field probes. Besides scanning near-field optical microscopy [22], which relies on light localized at sharp tips, we can nowadays employ focused fast electron beams. Only very recently, due to instrumental improvements [23], electron energy-loss spectroscopy (EELS) [24] in a scanning transmission electron microscope (STEM) has become another suitable technique for mapping MIR polaritons with (sub)nanometric spatial and few-millielectronvolt spectral resolution [25–32].

Coupled polaritonic systems have so far been analyzed by one of the aforementioned experimental techniques; however, a correlative study that would bring detailed understanding of common aspects and differences between spectral features measured by light- or electron-based spectroscopic techniques in the same sample is, to the best of our knowledge, missing. In this work, we present such a correlative study and explore nanostructured systems, where both infrared PhPs and PPs can exist. We probe the electromagnetic coupling between MIR surface PhPs (SPhPs) in a thin silicon dioxide film and low-energy localized surface plasmon (LSP) modes formed by the

*andrea.konecna@vutbr.cz

2331-7019/23/19(2)/024042(11)

confinement of PPs in micrometer-long gold antennas. We find that far-field IR spectra of the coupled LSPs-SPhPs can be substantially different from EEL spectra, which we confirm by experiments supported by numerical simulations and analytical modeling. We show that, by precisely positioning the electron beam, the coupling between the polaritonic excitations can selectively trigger either SPhPs only or coupled LSPs-SPhPs. We also present a postprocessing analysis in the EEL spectra that facilitates identification of the hybrid modes, allowing an easier comparison to far-field optical spectroscopy.

II. METHODS

A. Numerical simulations

Finite-difference time-domain simulations of far-field optical spectra are obtained using the Ansys Lumerical software [33]. A single rectangular antenna placed on a semi-infinite membrane is illuminated by a linearly polarized plane wave impinging at normal incidence with respect to the substrate provided by a total-field–scattered-field (TFSF) source. The scattering (absorption) spectra are calculated from the scattered (total) power flux monitors placed outside (inside) the TFSF source. The whole simulation domain with dimensions of 10 µm × 10 µm × 6 µm is enclosed in a perfectly matched layer.

EEL spectra and field plots are obtained using the finite-element method implemented within the COMSOL Multiphysics® software [34], where we calculate the induced electromagnetic field emerging in the interaction of the nanostructure with a line current representing the focused electron probe. The EEL probability is then evaluated as [35]

$$\Gamma(\mathbf{R}_b,\omega) = \frac{e}{\pi\hbar\omega}\int_{-\infty}^{\infty} dz\,\mathrm{Re}\{E_z^{\mathrm{ind}}(\mathbf{R}_b,z,\omega)\,e^{-i\omega z/v}\}, \quad (1)$$

where e is the elementary charge, $\hbar\omega$ energy, and v the electron velocity; z denotes the optical axis along which the fast electron propagates, $\mathbf{R}_b = (x_b, y_b)$ is the impact parameter (i.e., position in the transverse plane with respect to the optical axis that the electron trajectory intersects), and we integrate the z component of the induced electric field along the beam trajectory.

B. Experimental methods

Electron-beam lithography on SiO_2 TEM membranes (thickness 40 nm) is performed using a scanning electron microscope Mira3 (Tescan) with a laser interferometry stage (Raith). Subsequent gold deposition is done using an electron-beam evaporator (Bestec).

Fourier-transform infrared spectroscopy (FTIR) is performed with an IR microscope [Vertex 70v and an IR microscope Hyperion 3000 (Bruker)] with an aperture allowing signal collection from an area of 50 µm × 50 µm in a spectral range of 600 – 6000 cm^{-1} and resolution of 2 cm^{-1}. Convergence (illumination) and collection semiangles are between 15° and 30°.

Electron energy-loss spectra are acquired using a Nion monochromated aberration-corrected scanning transmission electron microscope operated at 60 kV accelerating voltage [23,36]. The measurements are performed with a convergence semiangle of 30 mrad, a collection semiangle of 20 mrad, a beam current of about 20 pA, using a Nion Iris spectrometer with a dispersion of 0.4 meV/channel [37], and an energy resolution [defined as the full width at half maximum (FWHM) of the zero loss peak] between 10 and 14 meV.

III. RESULTS AND DISCUSSION

A. Response of uncoupled system constituents

To understand the spectral response of the studied nanostructured system, we first theoretically analyze the response of its individual constituents, i.e., a SiO_2 film and a long Au antenna, when they are excited by light and by a focused electron probe in Fig. 1. The optical response of SiO_2 in the spectral region of interest is governed by a phononic mode corresponding to the Si-O-Si symmetric stretching vibration around 100 meV and a mode stemming from the Si-O-Si antisymmetric stretch around 130 meV [38]. The latter mode is associated with strong polarization, yielding the transverse optical–longitudinal optical (TO-LO) splitting associated with the energy region, known as the Reststrahlen band (RB), where $\mathrm{Re}[\epsilon_{\mathrm{SiO}_2}] < 0$, which forbids propagation of light within the bulk. However, in the presence of boundaries, such as those imposed in the thin-film geometry, interface SPhPs emerge inside the RB [40].

Because of the energy-momentum mismatch, infrared photons cannot excite SPhPs in a thin film, as demonstrated in Fig. 1(a). The most intense spectral feature corresponds to the excitation of the TO phonons that yields a strong absorption (red line) and featureless field profile (not shown). The absorption spectrum is nearly equal to extinction (scattering is negligible) and thus proportional to $\mathrm{Im}[\epsilon_{\mathrm{SiO}_2}]$.

Focused fast electrons, on the other hand, can provide sufficient momentum and naturally excite the SPhPs inside the RB, as shown by the green spectrum in Fig. 1(a), consistent with recent experiments [27,41,42]. More precisely, fast electrons interacting with a thin film supporting polaritons can excite either charge-symmetric or charge-antisymmetric SPhP modes [9,43] [see the inset in (a)]. SPhPs in SiO_2 are rather damped compared especially to those in ionic crystals [22,25], resulting in the two SPhP modes being spectrally indistinguishable. However, due to the symmetry of the probing field, the main peak close to 140 meV is dominated by charge-symmetric SPhPs, as shown schematically in the inset and further confirmed in

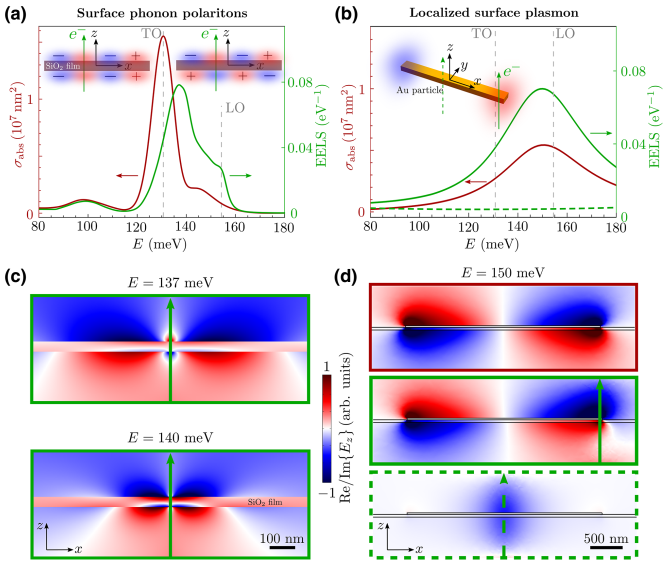

FIG. 1. (a) Numerically calculated EEL (green) and optical absorption (red) spectra of an infinitely extended SiO_2 thin film with a thickness of $t = 40$ nm. The dielectric response of SiO_2 is modeled using the complex dielectric response obtained from experimental measurements in Ref. [38]. All the spectra are probe-position invariant. Vertical dashed lines denote energies of the TO and LO phonons in SiO_2. The inset shows charge-symmetric (left) and charge-antisymmetric (right) SPhP modes. (b) Spectral response of a gold (dielectric response taken from Ref. [39]) rectangular plasmonic antenna with length $L = 3$ µm, width $w = 400$ nm, and height $h = 25$ nm on top of a substrate of thickness $t = 40$ nm with a constant dielectric response (characterized by a relative dielectric constant $\epsilon_{\mathrm{sub}} = 1.8$). Absorption (red line) cross section is calculated for excitation by a plane wave impinging at normal incidence along the z axis with a linear polarization aligned along the long antenna's axis (x axis). EEL spectra are obtained for an electron beam placed 10 nm outside the antenna's corner (solid green line) and at the antenna's center (dashed green line), as shown in the schematics. The electron-beam energy is 60 keV in both (a) and (b). (c) The z component of the total electric field emerging in the excitation of the SiO_2 film by focused electrons (trajectories shown by green arrows) at two energies around the peak in the EEL spectrum in (a). (d) The z component of the electric field confirming the excitation of the dipolar plasmon by the plane wave (top red framed plot) and the electron beam placed close to the antenna side (middle green solid framed plot). When the electron beam passes close to the antenna center, it can only weakly excite a higher-order plasmon mode (bottom dashed green framed plot). All plots are obtained at energy 150 meV, approximately corresponding to the peaks in (b), and are extracted at the central plane $y = 0$ while the electron beam is passing in the plane $y_b = d/2 + 10$ nm (10 nm from the antenna's shorter edge). In (c), (d), we show total field in the electron-beam excitation (green frames) and induced field for the plane-wave excitation (red frame). Real part of the field is shown in panels (c) while imaginary part is plotted in (d).

the field plots in (c). The field plots demonstrate that the electron beam couples (with different probability) to SPhPs with varying wavelengths and energies within the entire RB. The fast electrons can also excite the bulk LO phonon, which requires high momentum to be activated, corresponding to the polarization along the electron trajectory. The LO phonon excitation appears as a small "shoulder" close to 155 meV.

To enable an efficient coupling between the different types of polaritons, a spatial overlap of their electromagnetic fields as well as an overlap of their energies needs to be simultaneously targeted. As the SPhPs in SiO_2 emerge in the RB between about 130 and 155 meV, we tune the LSP resonances accordingly by a careful choice of the metal used and dimensions of the plasmonic antenna. We consider gold particles of a rectangular shape and numerically simulate their spectral response as if the antenna is probed by a plane wave polarized along its long axis or by a perfectly focused electron beam placed close to the antenna's corner [see the inset in Fig. 1(b)].

For antennas with dimensions $L \times w \times h = 3000 \times 400 \times 25$ nm^3 placed on a 40-nm-thick dielectric substrate (mimicking a constant dielectric offset imposed by the SiO_2 film), we obtain the theoretical lowest-energy dipolar LSP resonance centered around 150 meV, as shown in Fig. 1(b). The light excitation leads to relatively strong absorption (red line) associated with a dipolar mode that enhances the electric field close to the antenna's tips. The electron beam is also capable of excitation of the same dipolar mode, which is demonstrated in the numerically calculated EEL probability (solid green line). Alternatively, focusing the electrons close to the antenna center results in a near zero signal (dashed green line) in the energy region of interest, since only higher-order modes at larger energies can be excited in this case [44,45]. We confirm these observations in Fig. 1(d), where we plot the electric field in the vicinity of the antenna. For the plane-wave excitation (red-framed plot) and for the electron beam placed close to the antenna side (green framed plot), the field clearly corresponds to the opposite charges accumulated at the left and right sides of the antenna, and thus the dipolar plasmon. The electron beam placed at the antenna center is capable of exciting only a higher-order plasmon and therefore the corresponding plot [dashed green framed plot in Fig. 1(d)] is dominated by the field produced by the electron beam.

B. Coupled system

From the analysis of the system constituents, we can see that in an uncoupled scenario, the setup consisting of a gold antenna on top of a thin SiO_2 film can sustain three dominant polaritonic modes in the energy region of interest: a single LSP mode, and symmetric and antisymmetric thin-film SPhP modes (in formulas abbreviated as SPhP_1 and SPhP_2, respectively). The electromagnetic interaction between these polaritonic modes can be described by a model of three coupled oscillators captured within the matrix

$$\mathbf{M} = \begin{bmatrix} 1/(\alpha_{\mathrm{LSP}} f_{\mathrm{LSP}}) & -K_1 & -K_2 \\ -K_1 & 1/(\alpha_{\mathrm{SPhP}_1} f_1) & 0 \\ -K_2 & 0 & 1/(\alpha_{\mathrm{SPhP}_2} f_2) \end{bmatrix}, \quad (2)$$

where $\alpha_n = 1/[\omega_n^2 - \omega(\omega + i\gamma_n)]$ (here $n = \{\mathrm{LSP}, \mathrm{SPhP}_1, \mathrm{SPhP}_2\}$) determines the spectral response of a mode with a resonant energy $\hbar\omega_n$, damping $\hbar\gamma_n$, and effective strength f_n. In the following, we assume that the phononic modes are nonradiative, while the damping of the LSP involves radiative losses, i.e., $\gamma_{\mathrm{LSP}} \to \gamma_{\mathrm{LSP}} + \omega^2/(6\pi\epsilon_0 c^3)$ [15,46,47]. The coupling will introduce three new hybrid modes whose eigenfrequencies and dampings are obtained from $|\mathbf{M}| = 0$. However, the coupling is efficient only if both spectral and spatial overlaps of the modes' electromagnetic fields are achieved, which is described by the coupling parameters K_1 and K_2. We also assumed that SPhPs do not couple to each other.

Now we consider the same antenna and thin-film dimensions as in Fig. 1 and analyze optical absorption and scattering spectra of the coupled system [red and blue lines in Fig. 2(a), respectively], which exhibit several spectral features. The absorption is again dominated by the excitation of the TO phonon mode and with a similar spectral behavior as that of pure SiO_2 [as shown in Fig. 1(a)], which is due to the large extent of the thin film and the presence of absorption unrelated to the coupling. The scattering, on the other hand, clearly shows excitations beyond the RB as well as an additional weaker peak within the RB. All three peaks are associated with the new hybrid modes emerging due to the coupling. We also empirically find that the experimental measurement of $(1 - T_{\mathrm{rel}})$, where T_{rel} is the relative transmission obtained from FTIR (orange line), strongly resembles the theoretically predicted scattering spectra with only a slight discrepancy in the positions of the new peaks [see also Fig. 3(b) below and Appendix A].

As previously mentioned, an electron beam allows us to control the strength of the plasmonic excitation by simply positioning the beam at different relative positions from the antenna's center (or tip), as shown in the inset of Fig. 2(b). The corresponding simulated spectra (shown in the figure as thin lines) then capture either only nearly noninteracting SPhPs and bulk LO phonons excited in the SiO_2 (black), or a mixture of noninteracting SPhPs and coupled LSP-SPhPs (red to violet). The coupling is clearly manifested by a dip around the TO phonon position and emergence of new peaks beyond the RB. The weaker excitation inside the RB is here indistinguishable due to the presence of the uncoupled SPhP and bulk signal.

Note that the spectrum calculated at the antenna's center is slightly different from that of a plain SiO_2 film shown in Fig. 1(a). This happens because the antenna represents an obstacle for the SPhPs and thus favors excitation of SPhPs with slightly different momenta. As faintly observed in the corresponding field plot in Fig. 2(d) at 137 meV, the SPhPs interact with the edges of the antenna.

The experimental EEL spectra plotted in Fig. 2(b) (shown as thick lines) obtained for similar beam positions as in the simulations show less features due to limited energy resolution (between 10 and 14 meV). However, a clear broadening and emergence of "shoulders" of the main peak associated with the polaritonic coupling when the beam approaches the tip of the antenna can still be resolved. Similar behavior of the simulated spectra is obtained when the finite experimental resolution is introduced in the simulations (see Fig. 6 in Appendix B).

In general, the far-field optical spectra of the coupled system are very different to EELS due to the absence of the spectral features corresponding to the nearly uncoupled SPhPs that are not directly excitable by plane waves, but launchable by fast electrons. Interestingly, we can

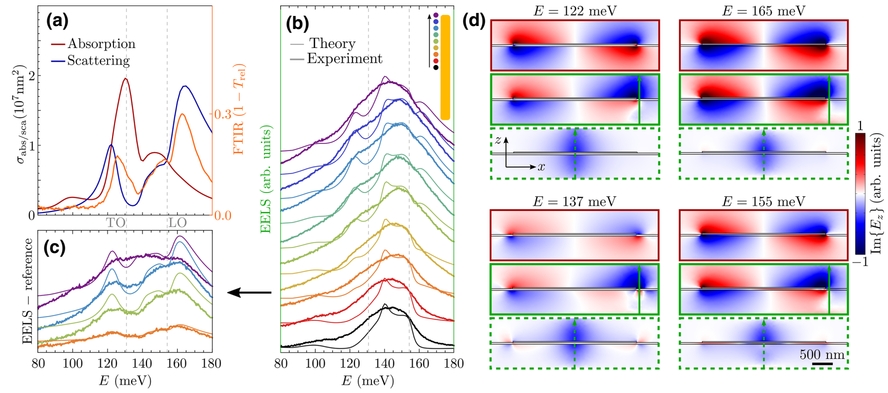

FIG. 2. Comparison of electron and light spectra for an approximately optimally coupled antenna-substrate system (individual system components have the same geometry and dimensions as in Fig. 1). (a) Experimentally measured FTIR spectrum corresponding to $(1 - T_{\mathrm{rel}})$, where T_{rel} is the transmission (orange line) for light polarized along the long antenna axis, divided by a reference transmission spectrum on a plain SiO_2 layer. Numerically calculated absorption (red) and scattering (blue) cross-section spectra for an entire system are shown for comparison. (b) Experimental versus calculated electron spectra (thick versus thin lines) obtained for the 60-keV beam, which is placed just next to the antenna and scanned along the antenna's long axis. Colors approximately correspond to the electron positions as marked schematically in the inset. (c) Selected EEL spectra from (b) after subtraction of the (reference) spectrum recorded at the center of the antenna, which is dominated by uncoupled SPhPs and LO phonon excitation in SiO_2 [black lines in (b)]. For clarity, subsequent spectra in (b) and (c) are vertically shifted by a constant offset. The vertical dashed lines denote energies of TO and LO phonon modes in SiO_2. (d) The z component of the electric field for plane-wave and electron excitation (red and blue framed plots, respectively) at different energies as denoted above. The electron beam is placed at the side of the antenna or close to its center (solid versus dashed framed plots; electron trajectories are represented by green lines). All plots are extracted at the central plane $y = 0$ while the electron beam is passing in the plane $y_b = w/2 + 10$ nm (10 nm from the antenna's shorter edge). We show total field in the electron-beam excitation (green frame) and induced field for the plane-wave excitation (red frames).

achieve resemblance between the light and EEL spectral signals by postprocessing of EEL spectra. As only bulk LO phonon and nearly uncoupled SPhPs are excited by the beam at the center of the antenna, we take the black spectrum in Fig. 2(b) as a reference and subtract it from the spectra obtained with the beam positioned at different distances from the antenna tip. Although the directly launched SPhPs for varying beam positions acquire slightly different momenta because of varying distance between the beam and antenna edges at which the polaritons scatter, such subtraction makes the EEL spectra better comparable with optical scattering spectra. See, for instance, the selected spectra in Fig. 2(c). The resulting peak intensities, relative strength, and contrast however change with the beam position, which controls the plasmon mode excitation efficiency. We emphasize that the subtraction also allows clear distinction of the coupling-related spectral signatures for the measured data, which before the subtraction in (b) showed only one broad spectral feature.

Electric field profiles shown in Fig. 2(d) for the plane-wave (red frames) and electron-beam (green frames) excitations are dominated by the presence of the dipolar plasmonic field, except for the cases when the electron beam is passing close the antenna center (dashed green framed plots). Hence, they strongly resemble the field plots in Fig. 1(d) with slight, yet important differences due to the presence of the SiO_2 film: (1) depletion versus enhancement of the field inside the SiO_2 film beneath the antenna (energies outside the RB; 122 versus 165 meV), and (2) emergence of uncoupled SPhPs freely propagating from the antenna at 137 meV within the RB. Unfortunately, due to the strong damping of the SPhPs, we can only observe one field oscillation [similarly as in Fig. 1(c)] near the antenna boundaries and close to the electron beam. We also note that the directly launched SPhPs strongly contribute to EEL spectra [black line in Fig. 2(b)] as they couple to the electron beam, while for plane-wave excitation, we only observe a small contribution from the SPhPs launched secondarily by the antenna (faint features close to the antenna sides appearing in the plot at 137 meV).

IV. CONTROLLING THE COUPLING

The coupling can be adjusted by tuning the LSP energies, as shown in many preceding studies [8,14,28,45].

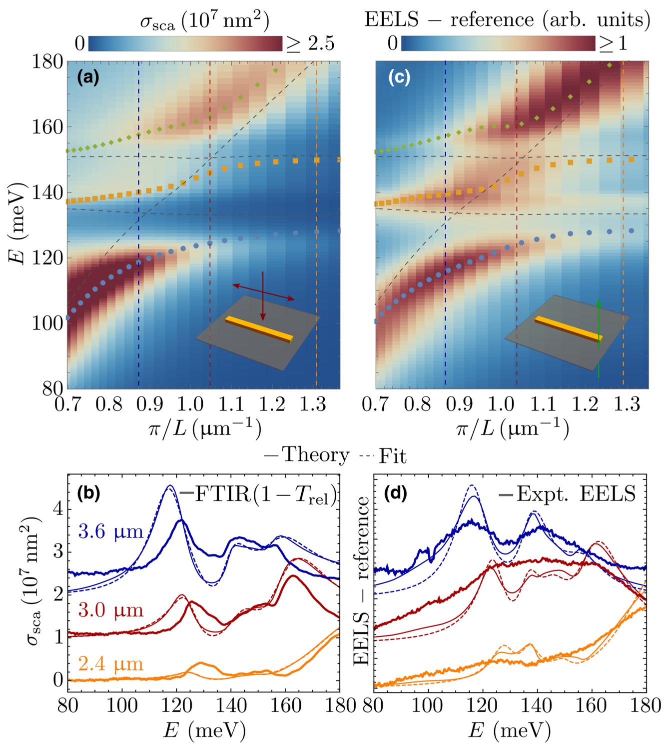

FIG. 3. Coupled system response as a function of the plasmonic antenna length. (a),(b) Optical scattering and (c),(d) reference-subtracted EEL spectra (see Fig. 2 for details). Simulated pseudodispersions in (a) and (c) are obtained via the transformation $k_{\mathrm{LSP}} = \pi/L$, where L is the antenna length and k_{LSP} is the effective wave vector of the dipolar LSP. Gray dashed lines trace energies of the uncoupled LSPs and PhPs, whereas the colored symbols denote energies of the new hybrid modes characterized by eigenvalues obtained from fitting of spectra and solution of $|\mathbf{M}| = 0$. Examples of numerically calculated, fitted, and experimental spectra (thin, dashed, and thick curves, respectively) for three selected lengths (2.4, 3.0, 3.6 μm) are shown in (b) and (d) [denoted by vertical colored dashed lines in (a) and (c)]. All EEL spectra are obtained for a 60-keV electron beam placed close to the corner of the antenna [violet line in Fig. 2(c)]. Experimental measurements of EELS and FTIR are performed on the same sample.

Figure 3 shows the dependence of the coupled system response on the parameter controlling the energy of the LSP, which is simply given by the length of the antenna's long axis L. Changing the antenna's dimension enables us to analyze the length-dependent coupling strengths $g_i = K_i\sqrt{f_i f_{\mathrm{LSP}}}/\sqrt{\omega_{\mathrm{SPhP}_i}\omega_{\mathrm{LSP}}}$, where $i = \{1, 2\}$ [48], which can be obtained from fitting the optical scattering cross section and reference-subtracted EEL spectra to analytical models. We find that the overall system spectral response is approximately governed by an effective polarizability

$$\alpha \propto [\mathbf{M}^{-1}]_{11} = \frac{\alpha_{\mathrm{LSP}} f}{1 - \sum_{i=1,2} g_i^2 \omega_{\mathrm{SPhP}_i}\omega_{\mathrm{LSP}}\alpha_{\mathrm{SPhP}_i}\alpha_{\mathrm{LSP}}}, \quad (3)$$

where f is an effective response strength, and which indicates that the LSP primarily couples and decouples to the propagating IR photons as well as to the evanescent electromagnetic field supplied by the electron beam. The $[\mathbf{M}^{-1}]_{11}$ term also suggests that the SPhPs are launched secondarily by the antenna.

The scattering cross-section spectra in Figs. 3(a) and 3(b) can then be modeled by [46,47]

$$\sigma_{\mathrm{sca}} \approx \frac{k^4}{6\pi\epsilon_0^2}|\alpha|^2, \quad (4)$$

where ϵ_0 is the permittivity of vacuum and $k = \omega/c$ is the free-space wave vector of light with photon energy $\hbar\omega$ moving at the speed of light c. To model the reference-subtracted EEL probabilities in Figs. 3(c) and 3(d), we use [15]

$$\text{EELS} - \text{reference} \approx \mathcal{F}_1(\omega)\text{Im}\{\alpha\} + \mathcal{F}_2(\omega)\text{Im}\{\alpha_{\text{SPhP}_1}\}, \tag{5}$$

where $\mathcal{F}_{1/2}(\omega) = A_{1/2}\omega^{j_{1/2}}$ with A_x and j_x being unknown real fitting parameters representing scaling factors and powers. These spectral functions incorporate an overlap of the plasmonic field with the field of the electron beam. The second term in Eq. (5) captures a residual spectral contribution of the noninteracting SPhPs, which remains even after the reference subtraction. A residual spectral contribution remains because a slightly larger portion of SPhPs (or SPhPs with different momenta) can be excited when the beam is placed close to the antenna's corner. This residue can be clearly seen within the RB in Fig. 3(c) when compared to Fig. 3(a).

Fitting the simulated scattering and the reference-subtracted EEL spectra with models in Eqs. (4) and (5), respectively, allows us to obtain the parameters characterizing the uncoupled system constituents, i.e., the excitations' energies and dampings. The theoretically obtained LSP and SPhP energies are interpolated by the gray dashed lines in Figs. 3(a) and 3(c). We can observe the plasmon energy linearly increasing with the inverse antenna length, which is typical for MIR plasmonic antennas on transparent substrates [49]. Note, however, that energies of both SPhPs remain nearly constant, as expected. The equation $|\mathbf{M}| = 0$ together with the parameters obtained from the model fitting provides the energies of the new hybrid modes, shown as colored symbols. These energies should be close to the actual peak positions, but typically do not coincide perfectly. However, we observe a close correspondence of the coupled system energies obtained for both types of probes.

The simulated spectra are compared with the experimental results for three fabricated antenna lengths in Figs. 3(b) and 3(d). The $(1 - T_{\text{rel}})$ FTIR spectra exhibit decent agreement with the calculated scattering with only slight discrepancies in the observed peak energies and relative strengths. However, it is important to keep in mind that the correspondence of the $(1 - T_{\text{rel}})$ with the scattering cross section is established only empirically; an exact illumination and light collection geometry can play a role (see Appendix A for further discussion). Maybe more importantly, the optical spectra are recorded for an antenna array and thus involve many antennas with various imperfections and divergences with respect to nominal dimensions. On the other hand, each reference-subtracted experimental EEL spectrum in Fig. 3(d) is recorded for an individual antenna within the array and thus does not involve any size averaging, which represents a great advantage of using focused electron probes. However, some of the fine details are hidden due to the current instrumental resolution (see Fig. 6 in Appendix B).

V. QUANTIFICATION OF THE COUPLING

The fitting enables us to extract the values of the coupling strengths g_i that are key for the classification of the coupling in the system. We theoretically predict and experimentally confirm that a rectangular Au nanoantenna on a SiO_2 substrate can be in a strong coupling regime, supported by the fulfillment of the criterion [50] $2g_i > \gamma_{\text{LSP}} + \gamma_{\text{SPhP}_i}$ for coupling of the LSP with both SPhPs, as documented in Fig. 4, where we find optimal coupling conditions for $L \sim 3.4$ μm. The fits of the optical spectra and reference-subtracted EELS (the latter not shown) provide similar coupling strengths with differences within uncertainties due to fitting errors, which demonstrates that the coupling is determined by the system itself, and is not probe dependent. Moving the electron beam towards the antenna center substantially lowers the overall efficiency of the LSP excitation, and thus the contrast of the spectral features. However, the coupling strengths stay nearly the same except for the beam positioned at the center of the antenna, where we observe a dramatic change of the coupling strengths towards zero as the dipolar LSP cannot be excited anymore.

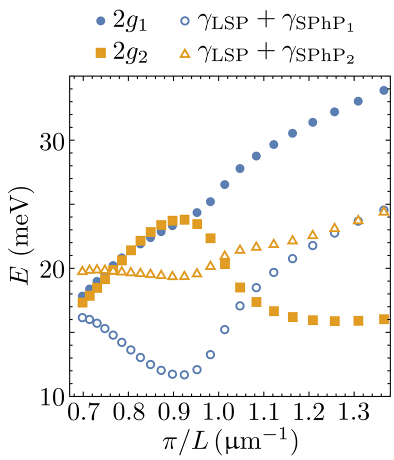

FIG. 4. Coupling parameters compared to their damping extracted from the fitted optical spectra in Fig. 3 (fitting reference-subtracted EEL spectra provides values with a difference within about 1 meV). The criterion $2g_i > \gamma_{\text{LSP}} + \gamma_{\text{SPhP}_i}$ establishes the strong coupling.

VI. CONCLUSIONS

In conclusion, here we have performed a comparative experimental study of spectra of the coupled antenna-substrate system obtained with far-field light and near-field electron spectroscopy. The study reveals fundamental differences when probing a complex polaritonic system with light and focused electron probes. We show that a precise positioning of the electron beam offers the possibility to probe coupled or uncoupled excitations at will, thus offering complementary information to that obtained from far-field optical spectroscopy.

We also present a postprocessing analysis in the EEL spectra that consists of subtracting a reference from spectra acquired for different beam positions with respect to the nanostructure system to reveal the strength of coupling between phonon and plasmon polariton excitations. The postprocessing facilitates comparison of EEL with far-field optical spectra, from which we find that both techniques can yield nearly identical coupled-system parameters. Such comparison confirms that the coupling is eventually determined by the optical properties and geometry of the system constituents, and should be independent of probing technique. The workflow presented here can be generalized for the study of excitations arising when geometry, topology, and different materials are used to generate hybrid optical systems.

ACKNOWLEDGMENTS

We acknowledge support from the Czech Science Foundation (Grant No. 20-28573S), European Commission (H2020-Twinning Project No. 810626 - SINNCE, M-ERA NET HYSUCAP/TACR-TH71020004), BUT - specific research No. FSI-S-20-6485, and the Ministry of Education, Youth and Sports of the Czech Republic (CzechNanoLab Research Infrastructure - LM2018110). EELS measurements were supported by the Center for Nanophase Materials Sciences (CNMS), which is a U.S. Department of Energy, Office of Science User Facility. EELS experimental work at ORNL was conducted, in part, using instrumentation within ORNL's Materials Characterization Core provided by UT-Batelle, LLC, under Contract No. DE-AC05-00OR22725 with the U.S. Department of Energy, and sponsored by the Laboratory Directed Research and Development Program of Oak Ridge National Laboratory, managed by UT-Battelle, LLC, for the U.S. Department of Energy. We thank our colleagues Michal Horák, Marek Vaňatka and Vojtěch Švarc for their advice on lithography on TEM membranes.

APPENDIX A: CORRESPONDENCE BETWEEN EXPERIMENTAL FTIR AND NUMERICALLY CALCULATED SPECTRA

It is well known that experimentally measured optical spectra strongly depend on exact illumination and collection geometry [51]. In our case, the illumination and collection angles are between 15° and 30°; however, we do not know an exact instrument point spread function, which prevents us from perfectly mimicking the experimental setup in the simulations.

Moreover, the collected signal comes from an array of antennas where fabrication imperfections cause averaging over the signal from slightly different antenna sizes (estimated size deviation of about 10 nm) and, maybe more importantly, the antenna edges and surfaces are not perfectly smooth. Our approach thus relies on evaluation of all relevant optical quantities in a standard bright-field illumination geometry, which we then compare with experimentally measured spectra and establish the best correspondence.

Figure 5(a) shows the calculated reflection, absorption, and transmission (or, more precisely, $1 - T$) spectra, whose spectral shapes strongly resemble scattering, absorption, and extinction cross sections, respectively. The experimentally measured spectra on the antenna-SiO_2 layer system are, however, normalized with respect to

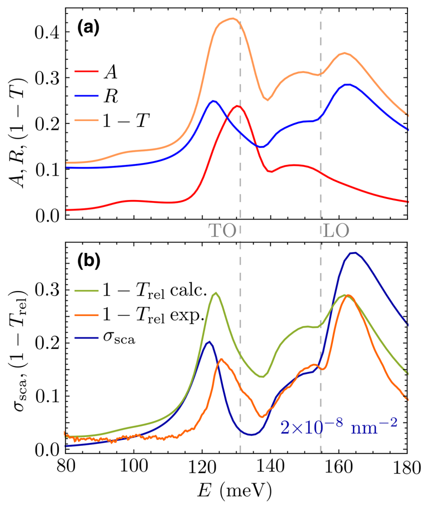

FIG. 5. (a) Comparison of theoretically calculated absorption (A, red line), reflection (R, blue line), and 1− transmission ($1 - T$, orange line) spectra for the plane-wave excitation and the geometry considered in Fig. 2. (b) Comparison of "relative" transmission spectra ($1 - T_{rel}$) obtained by dividing the total transmission spectra by a reference on a plain SiO_2 layer. We show calculated and experimentally measured FTIR spectra (green versus orange lines) together with the calculated scattering cross section (dark blue line).

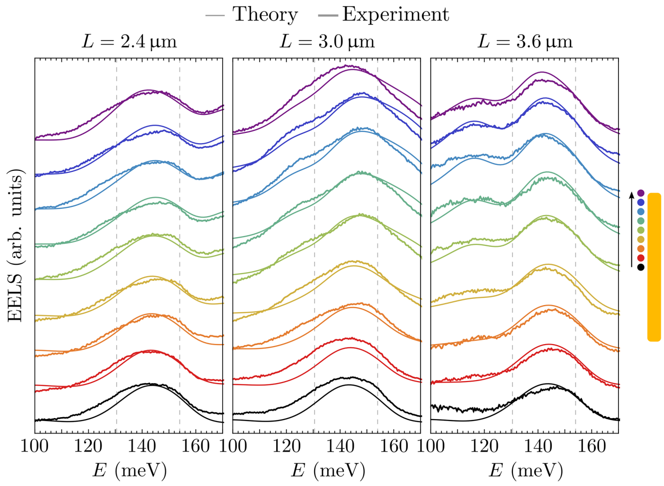

FIG. 6. Comparison of theoretically calculated EEL spectra after convolution with a Gaussian function of 14 meV FWHM (thin lines) with experimentally measured spectra (thick lines) for the varying beam position as shown in the inset and three antenna's lengths.

spectra measured on plain SiO_2 membranes. This "relative" experimental transmission spectrum [orange line in Fig. 5(b) and also in Fig. 2(a)] then exhibits a slightly better correspondence with the calculated scattering cross section [blue line in Fig. 5(b)] compared to the calculated relative transmission (green line). Such empirical observation leads us to considering calculated scattering cross sections for the comparison with relative transmission obtained from FTIR measurements.

APPENDIX B: FINITE SPECTRAL RESOLUTION IN EELS

Figure 6 shows a comparison of the theoretical EEL spectra when convoluted with a Gaussian function of 14 meV FWHM to mimic the energy resolution of the involved STEM-EELS setup.

TABLE I. Bounds for fitting of model parameters.

Parameter	Lower bound	Upper bound
ω_{SPhP_1} (meV)	131.9	135.6
γ_{SPhP_1} (meV)	1	10
ω_{SPhP_2} (meV)	148	154.6
γ_{SPhP_2} (meV)	2	20
ω_{LSP} (meV)	80	200
γ_{LSP} (meV)	1	50
f	1	10
g_1 (meV)	1	50
g_2 (meV)	1	50
j_1	−2	3
j_2	−1	1.5

APPENDIX C: DETAILS ON FITTING

We use the least-square method and fix parameters within the restricted ranges specified in Table I.

[1] J. D. Caldwell, L. Lindsay, V. Giannini, I. Vurgaftman, T. L. Reinecke, S. A. Maier, and O. J. Glembocki, Low-loss, infrared and terahertz nanophotonics using surface phonon polaritons, Nanophotonics **4**, 44 (2015).

[2] M. I. Stockman, Nanofocusing of Optical Energy in Tapered Plasmonic Waveguides, Phys. Rev. Lett. **93**, 137404 (2004).

[3] A. J. Huber, B. Deutsch, L. Novotny, and R. Hillenbrand, Focusing of surface phonon polaritons, Appl. Phys. Lett. **92**, 203104 (2008).

[4] E. Moreno, S. G. Rodrigo, S. I. Bozhevolnyi, L. Martín-Moreno, and F. J. García-Vidal, Guiding and Focusing of Electromagnetic Fields with Wedge Plasmon Polaritons, Phys. Rev. Lett. **100**, 023901 (2008).

[5] P. Li, M. Lewin, A. V. Kretinin, J. D. Caldwell, K. S. Novoselov, T. Taniguchi, K. Watanabe, F. Gaussmann, and T. Taubner, Hyperbolic phonon-polaritons in boron nitride for near-field optical imaging and focusing, Nat. Commun. **6**, 1 (2015).

[6] S. Dai, Z. Fei, Q. Ma, A. S. Rodin, M. Wagner, A. S. McLeod, M. K. Liu, W. Gannett, W. Regan, K. Watanabe, T. Taniguchi, M. Thiemens, G. Dominguez, A. H. C. Neto, A. Zettl, F. Keilmann, P. Jarillo-Herrero, M. M. Fogler, and D. N. Basov, Tunable phonon polaritons in atomically thin van der Waals crystals of boron nitride, Science **343**, 1125 (2014).

[7] G. Spektor, A. David, B. Gjonaj, G. Bartal, and M. Orenstein, Metafocusing by a metaspiral plasmonic lens, Nano Lett. **15**, 5739 (2015).

[8] M. Autore, P. Li, I. Dolado, F. J. Alfaro-Mozaz, R. Esteban, A. Atxabal, F. Casanova, L. E. Hueso, P. Alonso-González, J. Aizpurua, A. Y. Nikitin, S. Vélez, and R. Hillenbrand, Boron nitride nanoresonators for phonon-enhanced molecular vibrational spectroscopy at the strong coupling limit, Light Sci. Appl. **7**, 17172 (2018).

[9] U. Hohenester, *Nano and Quantum Optics* (Springer Nature Switzerland, Cham, 2020).

[10] E. Prodan, C. Radloff, N. J. Halas, and P. Nordlander, Hybridization model for the plasmon response of complex nanostructures, Science **302**, 419 (2003).

[11] P. Nordlander, C. Oubre, E. Prodan, K. Li, and M. I. Stockman, Plasmon hybridizaton in nanoparticle dimers, Nano Lett. **4**, 899 (2004).

[12] C. Cherqui, Y. Wu, G. Li, S. C. Quillin, J. A. Busche, N. Thakkar, C. A. West, N. P. Montoni, D. Rack, J. P. Camden, and D. J. Masiello, STEM/EELS imaging of magnetic hybridization in symmetric and symmetry-broken plasmon oligomer dimers and all-magnetic Fano interference, Nano Lett. **16**, 6668 (2016).

[13] S. C. Quillin, C. Cherqui, N. P. Montoni, G. Li, J. P. Camden, and D. J. Masiello, Imaging plasmon hybridization in metal nanoparticle aggregates with electron energy-loss spectroscopy, J. Phys. Chem. C **120**, 20852 (2016).

[14] A. B. Yankovich, B. Munkhbat, D. G. Baranov, J. Cuadra, E. Olsén, H. Lourenço-Martins, L. H. G. Tizei, M. Kociak, E. Olsson, and T. Shegai, Visualizing spatial variations of plasmon–exciton polaritons at the nanoscale using electron microscopy, Nano Lett. **19**, 8171 (2019).

[15] K. C. Smith, A. Olafsson, X. Hu, S. C. Quillin, J. C. Idrobo, R. Collette, P. D. Rack, J. P. Camden, and D. J. Masiello, Direct Observation of Infrared Plasmonic Fano Antiresonances by a Nanoscale Electron Probe, Phys. Rev. Lett. **123**, 177401 (2019).

[16] V. Křápek, A. Konečná, M. Horák, F. Ligmajer, M. Stöger-Pollach, M. Hrtoň, J. Babocký, and T. Šikola, Independent engineering of individual plasmon modes in plasmonic dimers with conductive and capacitive coupling, Nanophotonics **9**, 623 (2020).

[17] G. Lu, C. R. Gubbin, J. R. Nolen, T. Folland, M. J. Tadjer, S. De Liberato, and J. D. Caldwell, Engineering the spectral and spatial dispersion of thermal emission via polariton–phonon strong coupling, Nano Lett. **21**, 1831 (2021).

[18] T. Šikola, R. D. Kekatpure, E. S. Barnard, J. S. White, P. Van Dorpe, L. Břínek, O. Tomanec, J. Zlámal, D. Y. Lei, Y. Sonnefraud, S. A. Maier, J. Humlíček, and M. L. Brongersma, Mid-IR plasmonic antennas on silicon-rich oxinitride absorbing substrates: Nonlinear scaling of resonance wavelengths with antenna length, Appl. Phys. Lett. **95**, 253109 (2009).

[19] C. Huck, J. Vogt, T. Neuman, T. Nagao, R. Hillenbrand, J. Aizpurua, A. Pucci, and F. Neubrech, Strong coupling between phonon-polaritons and plasmonic nanorods, Opt. Express **24**, 25528 (2016).

[20] P. Pons-Valencia, F. J. Alfaro-Mozaz, M. M. Wiecha, V. Biolek, I. Dolado, S. Vélez, P. Li, P. Alonso-González, F. Casanova, L. E. Hueso, L. Martín-Moreno, R. Hillenbrand, and A. Y. Nikitin, Launching of hyperbolic phonon-polaritons in h-BN slabs by resonant metal plasmonic antennas, Nat. Commun. **10**, 1 (2019).

[21] L. Břínek, M. Kvapil, T. Šamořil, M. Hrtoň, R. Kalousek, V. Křápek, J. Spousta, P. Dub, P. Varga, and T. Šikola, Plasmon resonances of mid-IR antennas on absorbing substrate: Optimization of localized plasmon-enhanced absorption upon strong coupling effect, ACS Photonics **5**, 4378 (2018).

[22] R. Hillenbrand, T. Taubner, and F. Keilmann, Phonon-enhanced light-matter interaction at the nanometer scale, Nature **418**, 159 (2002).

[23] O. L. Krivanek, T. C. Lovejoy, N. Dellby, T. Aoki, R. W. Carpenter, P. Rez, E. Soignard, J. Zhu, P. E. Batson, M. J. Lagos, R. F. Egerton, and P. A. Crozier, Vibrational spectroscopy in the electron microscope, Nature **514**, 209 (2014).

[24] R. F. Egerton, *Electron Energy-Loss Spectroscopy in the Electron Microscope* (Plenum Press, New York, 1996).

[25] M. J. Lagos, A. Trügler, U. Hohenester, and P. E. Batson, Mapping vibrational surface and bulk modes in a single nanocube, Nature **543**, 529 (2017).

[26] A. A. Govyadinov, A. Konečná, A. Chuvilin, S. Vélez, I. Dolado, A. Y. Nikitin, S. Lopatin, F. Casanova, L. E. Hueso, J. Aizpurua, and R. Hillenbrand, Probing low-energy hyperbolic polaritons in van der Waals crystals with an electron microscope, Nat. Commun. **8**, 1 (2017).

[27] A. Konečná, K. Venkatraman, K. March, P. A. Crozier, R. Hillenbrand, P. Rez, and J. Aizpurua, Vibrational electron energy loss spectroscopy in truncated dielectric slabs, Phys. Rev. B **98**, 205409 (2018).

[28] L. H. G. Tizei, V. Mkhitaryan, H. Lourenço-Martins, L. Scarabelli, K. Watanabe, T. Taniguchi, M. Tencé, J. D. Blazit, X. Li, A. Gloter, A. Zobelli, F. P. Schmidt, L. M. Liz-Marzán, F. J. García de Abajo, O. Stéphan, and M. Kociak, Tailored nanoscale plasmon-enhanced vibrational electron spectroscopy, Nano Lett. **20**, 2973 (2020).

[29] H. Yang, E. L. Garfunkel, and P. E. Batson, Probing free carrier plasmons in doped semiconductors using spatially resolved electron energy loss spectroscopy, Phys. Rev. B **102**, 205427 (2020).

[30] N. Li, X. Guo, X. Yang, R. Qi, T. Qiao, Y. Li, R. Shi, Y. Li, K. Liu, Z. Xu, L. Liu, F. J. García de Abajo, Q. Dai, E.-G. Wang, and P. Gao, Direct observation of highly confined phonon polaritons in suspended monolayer hexagonal boron nitride, Nat. Mater. **20**, 43 (2020).

[31] A. Konečná, J. Li, J. H. Edgar, F. J. García de Abajo, and J. A. Hachtel, Revealing nanoscale confinement effects on hyperbolic phonon polaritons with an electron beam, Small **17**, 2103404 (2021).

[32] M. J. Lagos, P. E. Batson, Z. Lyu, and U. Hohenester, Imaging strongly coupled plasmon–phonon modes in mid-infrared double antennas, ACS Photonics **8**, 1293 (2021).

[33] Ansys Lumerical inc. www.lumerical.com.

[34] Comsol Multiphysics, www.comsol.com.

[35] F. J. García de Abajo, Optical excitations in electron microscopy, Rev. Mod. Phys. **82**, 209 (2010).

[36] J. A Hachtel, A. R. Lupini, and J. C. Idrobo, Exploring the capabilities of monochromated electron energy loss spectroscopy in the infrared regime, Sci. Rep. **8**, 5637 (2018).

[37] T. Lovejoy, G. Corbin, N. Dellby, M. Hoffman, and O. L. Krivanek, Advances in ultra-high energy resolution STEM-EELS., Microsc. Microanal. **24**, 446 (2018).

[38] J. Kischkat, S. Peters, B. Gruska, M. Semtsiv, M. Chashnikova, M. Klinkmüller, O. Fedosenko, S. Machulik, A. Aleksandrova, G. Monastyrskyi, Y. Flores, and W. T. Masselink, Mid-infrared optical properties of thin films of aluminum oxide, titanium dioxide, silicon dioxide, aluminum nitride, and silicon nitride, Appl. Opt. **51**, 6789 (2012).

[39] E. D. Palik, *Handbook of Optical Constants of Solids* (Academic Press, San Diego, 1985).

[40] R. Fuchs and K. L. Kliewer, Optical modes of vibration in an ionic crystal slab, Phys. Rev. **140**, A2076 (1965).

[41] K. Venkatraman, P. Rez, K. March, and P. A Crozier, The influence of surfaces and interfaces on high spatial resolution vibrational EELS from SiO_2, Microscopy **67**, i14 (2018).

[42] Y.-H. Li, M. Wu, R.-S. Qi, N. Li, Y.-W. Sun, C.-L. Shi, X.-T. Zhu, J.-D. Guo, D.-P. Yu, and P. Gao, Probing lattice vibrations at SiO_2/Si surface and interface with nanometer resolution, Chin. Phys. Lett. **36**, 026801 (2019).

[43] A. A. Lucas and E. Kartheuser, Energy-loss spectrum of fast electrons in a dielectric slab. I. Nonretarded losses and Cherenkov bulk loss, Phys. Rev. B **1**, 3588 (1970).

[44] D. Rossouw, M. Couillard, J. Vickery, E. Kumacheva, and G. A. Botton, Multipolar plasmonic resonances in silver nanowire antennas imaged with a subnanometer electron probe, Nano Lett. **11**, 1499 (2011).

[45] A. Konečná, T. Neuman, J. Aizpurua, and R. Hillenbrand, Surface-enhanced molecular electron energy loss spectroscopy, ACS Nano **12**, 4775 (2018).

[46] S. Albaladejo, R. Gómez-Medina, L. S. Froufe-Pérez, H. Marinchio, R. Carminati, J. F. Torrado, G. Armelles, A. García-Martín, and J. J. Sáenz, Radiative corrections to the polarizability tensor of an electrically small anisotropic dielectric particle, Opt. Express **18**, 3556 (2010).

[47] E. Castanié, R. Vincent, R. Pierrat, and R. Carminati, Absorption by an optical dipole antenna in a structured environment, Int. J. Opt. **2012**, 452047 (2012).

[48] L. Novotny, Strong coupling, energy splitting, and level crossings: A classical perspective, Am. J. Phys. **78**, 1199 (2010).

[49] Y. Wu, Z. Hu, X.-T. Kong, J. C. Idrobo, A. G. Nixon, P. D. Rack, D. J. Masiello, and J. P. Camden, Infrared plasmonics: STEM-EELS characterization of Fabry-Pérot resonance damping in gold nanowires, Phys. Rev. B **101**, 085409 (2020).

[50] P. Törmä and W. L. Barnes, Strong coupling between surface plasmon polaritons and emitters: A review, Rep. Prog. Phys. **78**, 013901 (2014).

[51] M. W. Knight, J. Fan, F. Capasso, and N. J. Halas, Influence of excitation and collection geometry on the dark field spectra of individual plasmonic nanostructures, Opt. Express **18**, 2579 (2010).

3 Electron-based spectroscopy of optical excitations

STEM-EELS in the infrared range is undoubtedly one of the exciting directions among electron-based spectroscopic techniques. Here we first discuss another STEM-EELS work, but compared to the results in the previous chapter applied solely in the visible spectral range. We also extend the scope to an alternative interferometric technique based on the collection of CL signal, and PINEM as applied in the detection of the nonlinear optical response of gold nanoparticles.

Excitons probed by STEM-EELS

Reidy, K., Majchrzak, P. E., Haas, B., Thomsen, J. D., Konečná, A., Park, E., Klein, J., Jones, A. J. H., Volckaert, K., Biswas, D., Watson, M. D., Cacho, C., Narang, P., Koch, C. T., Ulstrup, S., Ross, F. M. & Idrobo, J. C. Direct Visualization of Subnanometer Variations in the Excitonic Spectra of 2D/3D Semiconductor/Metal Heterostructures. *Nano Lett.* **23,** 1068–1076 (2023).

Besides plasmons, excitons are other electronic excitations of high interest in nanophotonics. They emerge due to the formation of an electron-hole pair, typically in semiconductors. Similarly to plasmons, excitons can be largely influenced by nanoconfinement, with an extreme case represented by the so-called quantum dots. Our ability to control the excitonic states offers applications in generating single- (or few-) photon sources for quantum communication, in photovoltaics or sensing.

STEM-EELS has recently emerged as a possible technique to study the excitonic properties at the nanoscale. In our work, we studied the difference in the excitonic structure in a plain few-layer transition metal dichalcogenide (TMD) MoS_2 with respect to areas with epitaxially grown gold nanoparticles on top of MoS_2. We reveal that the gold contact is responsible for the dielectric screening of the exciton and the emergence of a new peak in the EEL spectra. Such an arrangement of metal-TMD contacts can be found in TMD-based nanodevices and understanding the changes in the excitonic properties induced by the metal contacts is even technologically important.

Coherent cathodoluminescence

Sannomiya, T., Konečná, A., Matsukata, T., Thollar, Z., Okamoto, T., García de Abajo, F. J. & Yamamoto, N. Cathodoluminescence Phase Extraction of the Coupling between Nanoparticles and Surface Plasmon Polaritons. *Nano Lett.* **20,** 592–598 (2020).

When a focused electron beam impinges on a metallic film, it produces the so-called transition radiation (TR) due to the annihilation of a mirror charge. Simultaneously, the beam launches a surface PP (SPP) propagating along the boundary. The polaritonic wave propagates until it gets damped due to the absorption of the metal or adsorbate layers, but it can also reach a grating or a scatterer through which the energy can be radiated to the far field.

In our work, the scatterers are represented by silver nanospheres separated by a thin dielectric spacer from a thick metallic film. This geometry leads to the hybridization of localized plasmon modes of a free-standing particle with the corresponding mirror charges in the metal film underneath[61]. By placing the electron beam close to the particle, we can directly excite the hybridized modes and detect them through radiation in the far field in the CL setup. We identify bonding and anti-bonding dipolar modes with polarization parallel to the metal-dielectric interface, as well as an out-of-plane (perpendicular to the interface) bonding dipolar mode and higher-order quadrupolar modes.

If the electron beam is focused at larger distances from the particles, it excites the TR and simultaneously the SPP, which in turn excites in-plane hybridized plasmonic modes of the nanosphere-on-mirror system. The plasmons radiate to the far field and interfere with the TR. By scanning the electron beam with respect to the nanoparticle, we can retrieve the relative phase shifts between the events. By applying a conformal mapping scheme, it is then possible to visualize the phase flip between the SPP excitation and the scattered field around the resonance energy of the localized mode.

Nonlinear optical response probed by photon-induced near-field electron microscopy

Konečná, A., Di Giulio, V., Mkhitaryan, V., Ropers, C. & García de Abajo, F. J. Nanoscale Nonlinear Spectroscopy with Electron Beams. *ACS Photonics* **7,** 1290–1296 (2020).

A non-linear optical response can be observed in a broad range of nanophotonic systems, including metallic nanoparticles and interfaces when stimulated by an intense excitation field. As PINEM often relies on intense laser fields, it could naturally become a technique suitable for probing the non-linear optical response at the nanoscale.

The PINEM spectrum is symmetric for electrons interacting with the field at a single frequency (*i.e.*, only the linear field) – the probability that an electron gains a quantum of photon energy $l\hbar\omega$, P_l, is equal to the probability of losing a quantum of photon energy $-l\hbar\omega$, P_{-l}. However, we theoretically find that this is not true anymore when the nonlinear field components emerge, *i.e.*, $P_l \neq P_{-l}$. We further present two particular cases of electrons interacting with metallic nanoparticles in the form of a sphere or a nanorod excited by strong laser fields inducing the second-harmonic (SH) response. We confirm that the asymmetries in the PINEM spectra, from which we could deduce the strength of the SH field, are achievable for realistic laser powers.

NANO LETTERS

pubs.acs.org/NanoLett Letter

Direct Visualization of Subnanometer Variations in the Excitonic Spectra of 2D/3D Semiconductor/Metal Heterostructures

Kate Reidy,* Paulina Ewa Majchrzak, Benedikt Haas, Joachim Dahl Thomsen, Andrea Konečná, Eugene Park, Julian Klein, Alfred J. H. Jones, Klara Volckaert, Deepnarayan Biswas, Matthew D. Watson, Cephise Cacho, Prineha Narang, Christoph T. Koch, Søren Ulstrup, Frances M. Ross, and Juan Carlos Idrobo*

Cite This: *Nano Lett.* 2023, 23, 1068−1076 Read Online

ACCESS | Metrics & More | Article Recommendations | Supporting Information

ABSTRACT: The integration of metallic contacts with two-dimensional (2D) semiconductors is routinely required for the fabrication of nanoscale devices. However, nanometer-scale variations in the 2D/metal interface can drastically alter the local optoelectronic properties. Here, we map local excitonic changes of the 2D semiconductor MoS_2 in contact with Au. We utilize a suspended and epitaxially grown 2D/metal platform that allows correlated electron energy-loss spectroscopy (EELS) and angle resolved photoelectron spectroscopy (nanoARPES) mapping. Spatial localization of MoS_2 excitons uncovers an additional EELS peak related to the MoS_2/Au interface. NanoARPES measurements indicate that Au−S hybridization decreases substantially with distance from the 2D/metal interface, suggesting that the observed EELS peak arises due to dielectric screening of the excitonic Coulomb interaction. Our results suggest that increasing the van der Waals distance could optimize excitonic spectra of mixed-dimensional 2D/3D interfaces and highlight opportunities for Coulomb engineering of exciton energies by the local dielectric environment or moiré engineering.

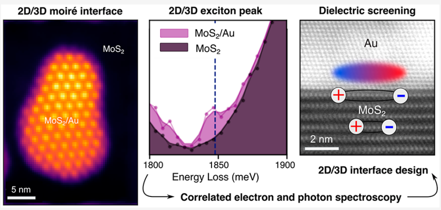

KEYWORDS: *excitons, electron energy-loss spectroscopy (EELS), angle resolved photoemission spectroscopy (nanoARPES), dielectric screening, moiré, 2D/3D interface*

Metallic contacts are often crucial for the fabrication of two-dimensional (2D) devices: for example, in electronic gating, control, and readout, optical signal processing, and spin injection.[1−4] Metallic nanoisland integration with 2D materials, such as MoS_2 or other transition-metal dichalcogenides (TMDs), can also enable exotic light−matter interactions such as exciton−plasmonic coupling,[5−8] Purcell enhancement of single-photon emission,[9,10] integration in spintronic circuits,[11] and other quantum technologies such as tunnel barriers in Josephson junctions.[12] Such mixed-dimensional 2D/metal heterostructures can exhibit unique physics that is not present in either of the materials alone, often due to interfacial hybridization, which results in a band structure with mixed 2D/3D character.[13] In all of these cases, the atomic structure at the interface between the metal and the 2D material (2D/metal or other 2D/3D interface) directly affects the device performance.[14−18] For example, the presence of a 2D/metal interface changes fundamental physical properties such as dielectric screening, electronic charge transfer, and doping, which in turn affect the optoelectronic properties (exciton binding energies, band structure, and contact resistance) of the resulting heterostructure.[16,19,20]

It is known that 2D materials in contact with metals or other substrates display variations of optoelectronic properties on the nanometer length scale.[7,21−23] It is therefore critical to probe these position-dependent properties with nanoscale spatial resolution. Until recently, information on the effect of metal integration on the system's spectral response has generally been obtained using optical spectroscopy.[24] Optical spectroscopy exhibits high energy resolution; however, it is diffraction limited by the relatively long wavelengths of light. This makes it ideal for bulk systems but less well suited for measuring nanoscale spectral response. More recently, angle-resolved photoemission spectroscopy with sub-micrometer spatial resolution (termed nanoARPES)[25] has been used to complement optical spectroscopy and applied to 2D van der Waals heterostructures to monitor local changes in electrical

Received: December 3, 2022
Revised: January 4, 2023
Published: January 13, 2023

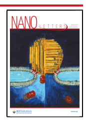

https://doi.org/10.1021/acs.nanolett.2c04749
Nano Lett. 2023, 23, 1068−1076

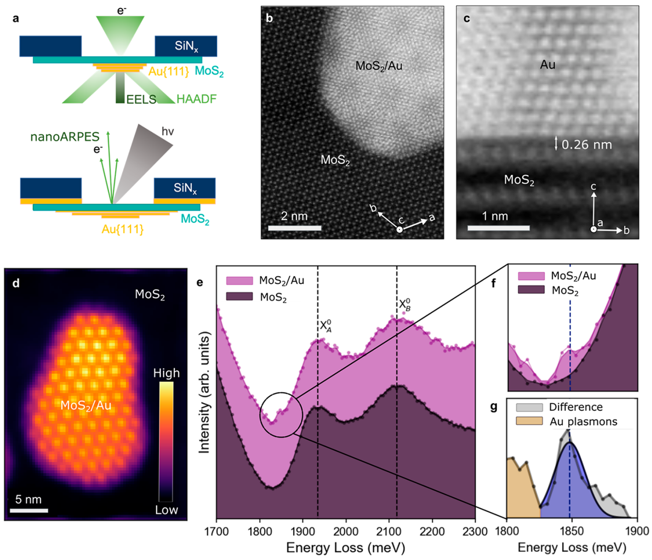

Figure 1. EELS analysis of MoS_2 excitonic spectra on freestanding 6L MoS_2 vs MoS_2/Au. (a) Schematic of suspended MoS_2/Au{111} structure with (upper diagram) electron beam excitation from the back (MoS_2) side for EELS detection and (lower diagram) nanoscale photoemission probe from the back (MoS_2) side through holes in the supporting SiN_x TEM grid for nanoARPES measurement. (b) HAADF image showing an Au nanoisland on suspended MoS_2 at atomic resolution. Epitaxially aligned Au and MoS_2 lattices are evident through the well-defined moiré pattern. (c) Cross-sectional HAADF image of the 6L MoS_2/Au{111} interface, showing a 0.26 nm distance between Au and S. (d) HAADF image of island. The image is shown in false colors in a perceptually uniform sequential color map, where a brighter color means higher intensity (arbitrary units, see inset), which is the same color scale used in other figures. (e) EEL spectra of average of pristine, suspended 6L MoS_2 areas (purple) vs MoS_2/Au areas (pink). Neutral A and B excitons (X_A^0 and X_B^0) are labeled. Dots are raw data, and lines represent the same data convolved with a Gaussian of 5 meV full width at half-maximum. (f) Enlargement of energy range from 1800 to 1900 meV. Note that the MoS_2/Au spectrum is shifted down by a constant intensity to align with the pristine MoS_2. (g) Difference between the MoS_2/Au spectrum and pristine MoS_2 spectrum. Gray dots represent the raw data, the yellow shading represents the Au plasmons, and the blue curve shows the best fit to the Gaussian peak.

potential, Fermi level, and band structure during the application of a gate voltage.[19] At an even smaller length scale, emerging advances in scanning transmission electron microscopy (STEM), including cathodoluminescence (CL) and monochromated electron energy-loss spectroscopy (EELS), have also allowed studies of the optoelectronic properties of 2D materials on a sub-nanometer scale, when the substrates are suspended on TEM grids.[7,21,23] CL and EELS can obtain spectral information similar to that obtained with optical photoluminescence and absorption measurements, respectively, but with the added opportunity for nanometer spatial resolution. This spatial resolution is particularly important for 2D/metal heterostructure systems, where the local environment greatly affects the resulting properties.

In this Letter, we study the effect of Au contacts on the local excitonic response of MoS_2 using a thin suspended sample which removes substrate effects and allows correlation of mapping measurements by EELS with sub-nanometer spatial resolution and angle resolved photoemission spectroscopy (nanoARPES). Figure 1a shows a schematic of our suspended 2D/metal MoS_2/Au geometry, where the sample is probed in transmission from the back side through the SiN_x holes during the EELS analysis (upper diagram) and also during nano-ARPES measurements (lower diagram) with an extra Au contact layer. Figure 1b shows an example of a high-angle annular dark field (HAADF) image of an epitaxially grown Au island on six layer (6L) MoS_2. The Au islands are deposited on pristine, suspended MoS_2 under ultrahigh vacuum (UHV), as discussed in Methods.[22,26] We use a UHV precleaning technique to minimize trapped impurities at the 2D/metal interface followed by UHV deposition at a low rate (0.05 nm/min) to create a quasi-van der Waals MoS_2/Au interface with low defect density (Figure 1c).[27] The Au{111} nanoislands are epitaxially aligned on the MoS_2{0001} basal plane, as showcased by the uniform moiré periodicities across the sample.[22] The Au grows in an epitaxial Volmer−Weber growth mode on suspended MoS_2, with the Au [220] direction parallel to MoS_2 $[1\bar{1}20]$. A variety of MoS_2 thicknesses can be transferred on the same sample (Supplementary Figure 1), and the Au nanoislands are consistent across all thicknesses of MoS_2.

Figure 1e shows a direct comparison of pristine 6L MoS_2 and MoS_2/Au{111} EEL spectra, as averaged over the separate MoS_2 and MoS_2/Au areas in Figure 1d. All EEL spectra were acquired on a Nion aberration-corrected high energy resolution monochromated EELS-STEM instrument (HERMES) operated at 60 kV (Methods). Due to the semiconducting nature of MoS_2, long EELS acquisitions

https://doi.org/10.1021/acs.nanolett.2c04749
Nano Lett. 2023, 23, 1068−1076

caused substantial charging of our sample. Therefore, we obtained 2D EELS maps with a high signal-to-noise ratio by acquiring multiple spectral maps at short dwell times and subsequently aligning the spectra using non-rigid registration to create a single summed spectrum.[28] Image intensity filtering was used to determine the area boundaries and allowed us to discard the island edges (Methods). Our EELS mapping allows spatial variations to be revealed between MoS_2/Au and freestanding MoS_2 regions with ~1 nm precision.

The energy positions of peak maxima corresponding to the neutral A (X_A^0) and B (X_B^0) excitons in MoS_2 are marked in Figure 1e. Since this sample consists of six layers of MoS_2, the bottom few layers of the MoS_2 sample are not in direct contact with Au; thus, it is unsurprising that their neutral excitons do not exhibit an observable shift from their original positions. However, we observe a spectral feature that is ~80 meV red-shifted with respect to the A exciton in the MoS_2/Au system compared to pristine MoS_2. This spectral feature is related to the structure close to the MoS_2/Au interface and can be further explored by subtracting the pristine MoS_2 spectrum from that of MoS_2/Au, as shown in Figure 1f, and performing a Gaussian fitting (Methods and Figure 1g). Repeating our analysis on another MoS_2/Au area of the same sample, we find this additional spectral feature is also present, as shown in Supplementary Figure 2.

Several explanations for this red-shifted excitonic feature identified in EEL spectra (referred to hereafter as the 1850 meV peak) are possible, and these are summarized in Table 1.

Table 1. Several Mechanisms That Can Account for Additional Features in the MoS_2 Exciton Spectra When in Contact with Au[a]

peak identification	red shift with respect to the neutral A exciton (X_A^0)
(1) a trion (X_A^-)	ΔA = 30−50 meV[31,34]
(2) dielectric screening (X_A^0 shift)	ΔA = 30−70 meV[31]
(3) plasmon−exciton coupling	ΔA = 10−100 meV, depending on island shape[7]
(4) defect-related resonance	$\Delta A \approx$ 100 meV[32,33]

[a]The table shows the proposed physical explanation and the measured red shift in energy of the feature (ΔA) with respect to the neutral A exciton (X_A^0) energy. Since exact energy positions of X_A^0 vary between samples and measurement methods, we cite the energy difference between the pre-peak and X_A^0 for more accurate comparison.

It has been suggested that MoS_2 interfaced with metallic Au{111} gives rise to an n-type electrical contact with the Fermi level pinned near the conduction band of MoS_2.[29,30] This n-type doping agrees with the theoretically calculated excitation spectra of MoS_2 on Au{111}, which postulates the existence of negative A (X_A^-) and B (X_B^-) trions at low temperature (mechanism 1 in Table 1), although screening may affect this.[31] Separately, dielectric screening has been predicted to red-shift the A exciton depending on the distance to Au{111} contacts (mechanism 2).[31] Third, plasmon−exciton coupling can cause splitting and shifting of the excitonic peak in accordance with the metal nanoisland shape and size (mechanism 3).[7] Finally, defect-related resonances in MoS_2 have been shown to produce additional peaks in the excitonic spectra (mechanism 4).[32,33]

We can initially rule out trion emission (mechanism 1) being responsible for the 1850 meV peak, as the trion binding energy is on the order of 30−50 meV, far from the observed peak shift. Further evidence for the absence of trion formation in our samples is reported in Supplementary Note 1. We also rule out defect-related resonance (mechanism 4), since our experiments are carried out at room temperature, and such resonances are strongly quenched above 120 K.[33] Moreover, no detectable defect formation in the MoS_2 after Au deposition is found via atomic resolution STEM (Figure 1b,c) or Raman spectroscopy,[27] and no electron-beam-induced spectral variations were observed for the duration of the measurement which would indicate defect introduction.

In order to determine whether plasmon exciton coupling (mechanism 3) is responsible for the 1850 meV peak, we first study the spatial localization of spectral features. Here, the EEL spectra at each beam position are integrated over specific energy ranges to obtain a 2D intensity map that can be compared with theoretical calculations. It is worthwhile to note that the variation in intensity of the Au interband transition (Au_{IB}) between experiment and theory in Figure 2b is attributed to the fact that the dielectric response in the theoretical calculations is extracted from ellipsometry of large polycrystalline samples. This can introduce changes in damping, screening, or plasma frequency compared to the single-crystalline samples studied here. Modeling nanoscale islands using a macroscopic dielectric function introduces some level of uncertainty in the spectral intensity. Moreover, theoretical calculations also assumed that the nanostructures exhibit sharp edges and flat tops. In reality, these nanostructures exhibit surface steps, rounded edges, and atomic terraces that affect the Au interband transitions and result in the edge enhancement observed in Figure 2f,h. Aside from these enhancements noted above, all experimental spectra and intensity maps are reproduced by theory.

In Figure 2a we show the results of integrating the spectrum over a range (1820−1880 meV) that is centered on the spectral feature of interest (E_{IP}). The 1850 meV peak appears strongest in the center of the island. We can compare this to the localized surface plasmon resonance locations for the long axis dipolar plasmon between ~1100 and 1400 meV (Figure 2c) and a short axis dipolar plasmon between ~1500 and 1700 meV (Figure 2e). In accordance with theoretical EELS simulations (Methods and Figure 2b,d,f), these appear with different energies and at different positions. A characteristic Au interband transition is also present (Figure 2g,h). The spatial localization of the 1850 meV peak in Figure 2a in the center of the island, as opposed to at either of the plasmon resonance locations, suggests that the peak does not arise due to plasmon−exciton coupling but instead from the direct contact of MoS_2 with the Au metal. This rules out mechanism 3 from Table 1, leaving mechanism 2 as the potential solution. These results are consistent for another Au particle on MoS_2, as shown in Supplementary Figure 3.

To explore the validity of mechanism 2 from Table 1, we measured the quasi-particle valence band (VB) dispersion of suspended MoS_2/Au using nanoARPES. Due to the surface sensitivity of ARPES, the electronic structure of MoS_2 cannot be resolved through the 5−8 nm thick Au{111} islands. Instead, our sample geometry allows us to focus the photon beam down to ~900 nm diameter and illuminate the sample from the MoS_2 side through the 3 μm holes in the SiN_x TEM membrane, as sketched in Figure 1a. We then scan the photon beam across the sample (Figure 3a) such that the $E(k)$

https://doi.org/10.1021/acs.nanolett.2c04749
Nano Lett. 2023, 23, 1068−1076

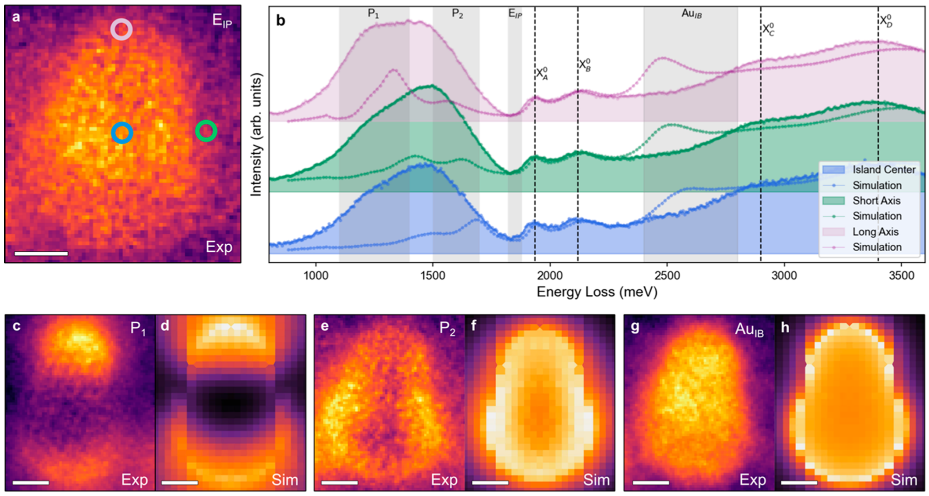

Figure 2. Spatial localization of MoS_2/Au localized surface plasmons and excitonic spectral features. (a) 2D map of integrated EELS intensity over the energy range 1820−1880 meV for the excitonic interfacial peak (E_{IP}) at 1850 meV. For all maps a brighter color means higher intensity (scale bars 5 nm). (b) EEL spectra averaged for beam positions around regions of the high EEL intensity associated with the long axis plasmon (pink), short axis plasmon (green), and island center (blue). Comparisons with simulation are shown as dotted lines of the same color. Neutral A and B excitons (X_A^0 and X_B^0) are labeled and regions corresponding to P_1, P_2, E_{IP}, and Au_{IB} are shaded in gray. Raw data sets are Gaussian smoothed by 5 meV. (c−h) 2D maps of integrated EELS intensity: (c) over the energy range 1100−1400 meV and (d) corresponding EELS simulations for the long axis dipolar plasmon (P_1) at 1250 meV; (e) over the energy range 1500−1700 meV and (f) corresponding EELS simulations for the short axis dipolar plasmon (P_2) at 1550 meV; (g) over the energy range 2400−2600 meV and (h) corresponding EELS simulations for the Au interband transitions (Au_{IB}) at 2550 meV.

dispersion is collected at each position, leading to a four-dimensional data set.

Projecting the measured (E,k) intensity onto the (x,y) coordinates of the scan allows us to obtain a photoemission intensity map of the entire sample from the MoS_2 side, as seen in Figure 3b. We then average the dispersion from specific areas demarcated by the circles in Figure 3b. This allows us to measure the dispersion for a known MoS_2 thickness. Figure 3c shows the dispersion, at different thicknesses, of the isotropic part of the MoS_2 VB located around the Γ point. These states are mainly composed of out-of-plane sulfur p_z orbitals and are therefore expected to be sensitive to interactions with the Au{111} islands and adjacent MoS_2 layers.[29] The number of energy-separated bands around Γ confirms the assignment of layer number by optical contrast: suspended monolayer (1L), bilayer (2L), and four layer (4L) MoS_2 areas produce distinct signals, in correspondence with known MoS_2 thicknesses. The binding energy of the local VB maximum (VBM) changes dramatically from 1.66 eV in the 1L area to 1.02 and 1.05 eV in the 2L and 4L areas, respectively.

Our nanoARPES measurements suggest that Au−S hybridization is stronger in the first MoS_2 layer and decreases substantially in the second and subsequent layers. In 2L and 4L MoS_2, the additional bands around Γ display a narrower line width than the single band around Γ in 1L MoS_2 (Figure 3c). The 1L band has a line width of 425 meV, and the line widths of the highest binding energy bands in the 2L and 4L are also higher than 400 meV. In contrast, the other bands have line widths of 295 and 160−180 meV for 2L and 4L, respectively (Figure 3c). This indicates that Au mainly affects the MoS_2 layer directly adjacent, exhibiting a small effect on the second layer and a negligible effect on subsequent layers. This steep drop-off in the influence of Au contacts on the electronic properties of MoS_2 has also been reported in the literature, where monolayer Au vacancies result in a quasi-freestanding band structure of MoS_2 that is decoupled from the Au.[35] Moreover, modeling with Rytova−Keldysh potentials shows that screening from chalcogen atoms, charge neutrality of the 1s excitons, and small Bohr radius all contribute to the substantial drop in interaction of MoS_2 excitons as the distance from the interface increases.[36]

We can zoom in on a detailed view of the dispersion of suspended 1L MoS_2/Au along the high symmetry Γ−K direction, shown in Figure 3d, to confirm this stronger influence on the topmost MoS_2 layer. An energy distribution curve (EDC) analysis of the states at K and Γ, shown in Figures 3e,f, reveals a global VBM at K (labeled VB_A due to the relation with the A exciton observed in photoluminescence). Furthermore, a local maximum is determined 0.14 eV below VB_A, which is denoted as VB_B. At Γ, the local VBM, denoted VB_Γ, is characterized by a peak with an asymmetric intensity distribution and a flattening of the dispersion. This is caused by MoS_2/Au hybridization, and the characteristic kink feature sketched in Figure 3f has been described previously in 1L MoS_2 epitaxially grown on Au{111}.[29,37] We can extract a binding energy of 1.39 eV of VB_A and a VB_A−VB_B splitting of 0.14 eV, which corresponds to the spin-splitting of these states. These values are fully consistent with ARPES measurements of

https://doi.org/10.1021/acs.nanolett.2c04749
Nano Lett. 2023, 23, 1068−1076

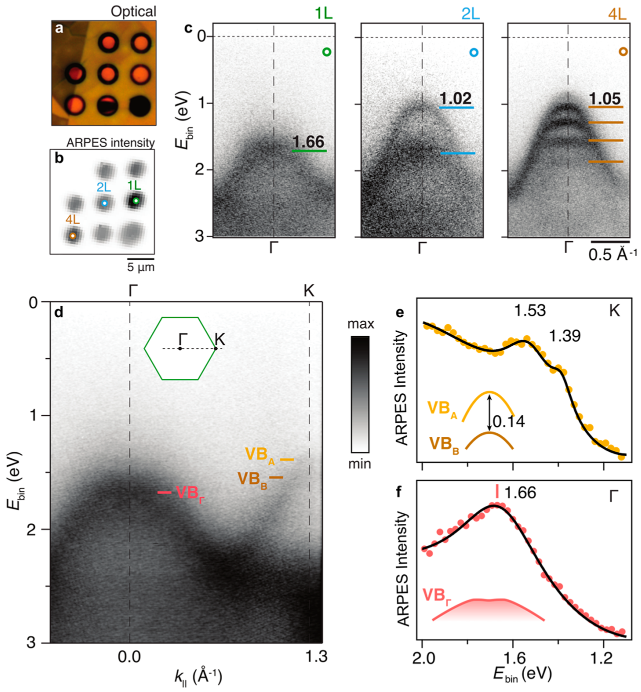

Figure 3. Thickness-dependent band structure of suspended MoS_2/Au measured by nanoARPES. (a) Optical micrograph of the SiN_x TEM grid with eight 3 μm holes. The contrast is caused by MoS_2 flakes with different thicknesses across the holes, monolayer (1L), bilayer (2L), and four layer (4L). 2D layer transfer further described in Methods and Supplementary Figure 1. (b) Spatially resolved ARPES intensity from the area of the SiN_x membrane shown in (a). (c) Electronic structure around Γ from the areas demarcated by correspondingly colored circles in (b). Distinct MoS_2 bands are marked by colored ticks. The binding energy of the local VBM is stated in units of eV. (d) ARPES intensity collected along the Γ−K direction, indicated by a dotted line in the sketch of the 1L MoS_2 Brillouin zone. Ticks indicate the VB maxima at K and Γ. (e, f) Energy distribution curves (markers) at (e) K and (f) Γ. Curves represent fits to Lorentzian peaks on a polynomial background. Fitted peak positions are indicated by ticks and stated in units of eV. The inset in (e) indicates the extracted spin-splitting of the MoS_2 bands at K. The sketch in (f) highlights the flattening of the MoS_2 VB at Γ and the asymmetric intensity distribution caused by MoS_2−Au hybridization. The kink in the center of the VB is previously predicted from calculations in ref 29.

large-area epitaxial 1L MoS_2 on Au{111} which affects the electronic structure of MoS_2.[37]

Based on all the data presented above, we hypothesize that the experimentally observed interfacial EEL spectral feature arises from dielectric screening of the excitonic Coulomb interaction (mechanism 2 in Table 1).[31,38−40] Previous theoretical calculations for 1L MoS_2 have predicted an ∼30−70 meV red shift of the A exciton on contact with Au{111}, dependent on the Au−S distance (Figure 4a; data reproduced from ref 31). This is due to a contribution of dielectric polarizability in the Au contact which creates an image charge effect. This image charge effect is illustrated schematically in Figure 4b. Here, the Au interacts most strongly with the excitons in the topmost MoS_2 layer, screening the Coulomb interaction and resulting in a more weakly bound electron−hole pair (illustrated by a larger distance between the electron and hole in this schematic). This results in a red shift of the exciton in this layer. Such red shifts due to image charges have been reported in other material systems, such as nanotube interfaces, metal−molecule heterostructures, and inorganic−organic quantum well crystals.[41−43] Our experimentally measured Au−S distance (0.26 nm) from Figure 4b should theoretically correspond to an ∼50−60 meV exciton shift (Figure 4a, dashed line). Although theoretical shifts cannot be quantitatively compared with experiment due to variation in dielectric environment, we note this value is in close correspondence to the shift observed in our EEL spectra.

The fact that we see a small 1850 meV peak alongside a larger A exciton peak in Figure 1e−g in the 6L MoS_2 spectrum suggests that excitons in the topmost MoS_2 layer in contact with Au are mostly shifted. Excitons in the second MoS_2 layer may also be affected by the Au screening, although their distance from the Au is on the order of ∼3.5 nm which, according to Figure 4a, would correspond to only a 30−40 meV shift in the exciton energy. In our system, this is observed as a broadening of the peak. Subsequent MoS_2 layers are much

https://doi.org/10.1021/acs.nanolett.2c04749
Nano Lett. 2023, 23, 1068−1076

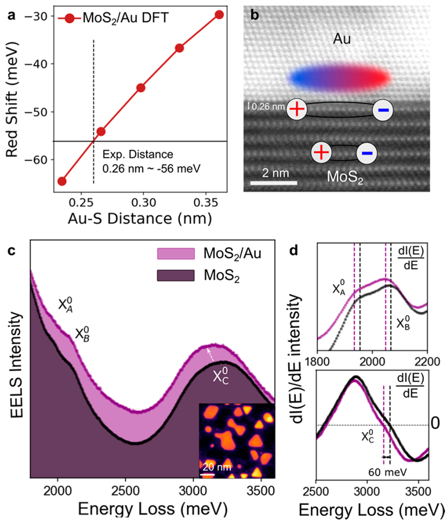

Figure 4. Further discussion of dielectric screening. (a) Red shift of the A exciton energy as a function of the distance between the topmost S atom in MoS_2 and the Au contact. Red data points are *ab initio* many-body calculations, where data points are obtained from ref 31 (under open access Creative Commons CC BY License). Lines mark our experimentally calculated Au−S distance from a HAADF cross-section on our suspended MoS_2/Au heterostructure. (b) Schematic showing polarization of the metallic Au contact, which screens the exciton Coulomb interaction in MoS_2. (c) Spatially averaged EEL spectra of pristine, suspended 1L MoS_2 areas (purple) vs MoS_2/Au areas (pink). Neutral A, B, and C excitons (X_A^0, X_B^0, X_C^0) are labeled. The inset shows a HAADF image of the suspended 1L MoS_2/Au{111} area, where the Au islands are the brighter regions and the suspended 1L MoS_2 is dark. The image has been averaged over multiple frames to increase the signal-to-noise ratio. (d) First derivative of signal shows X_A^0 and X_B^0 excitons as peaks (top) and quantitatively shows an ~60 meV red shift of C exciton energy on contact with Au by observing the zero axis crossing (bottom).

less screened by the Au and are therefore only slightly red-shifted in energy (illustrated by a closer distance between the electron and hole in this schematic), resulting in a small 1850 meV peak (from the topmost 1L) alongside a broadened A exciton peak (from 2L to 6L).

Finally, we corroborate the role of dielectric screening with EEL spectra of 1L MoS_2/Au. The exciton signals are weaker here, due to the smaller interaction volume of monolayer MoS_2. Despite this, we can still deduce the red shift in exciton energies, particularly observable in the C exciton (Figure 4c). The peak positions of the X_A^0 and X_B^0 excitons can be approximately determined by finding the local maxima of the first derivative of the signal (since they are related to the inflection points in the original spectrum), as in Figure 4d, top. As expected for a monolayer sample, the excitons are red-shifted from their expected position on contact with Au. A value of 60 meV can also be determined for the X_C^0 exciton red shift on contact with Au by obtaining the derivative of the signal and finding the zero cross point (Figure 4d, bottom) since this is a clear peak maximum. This 60 meV value is in close correspondence to that predicted by DFT (Figure 4a) and further confirms the dielectric screening mechanism.

In summary, we have used correlative EELS and nano-ARPES measurements to identify and explain the emergence of an excitonic peak related to the MoS_2/Au interface. The use of a suspended MoS_2/Au sample with epitaxially grown Au provides an ideal platform for EELS mapping with subnanometer resolution. We observe local variations in the exciton spectrum due to the dielectric screening effect of the Au contact, which reduces the Coulomb interaction of the exciton in MoS_2. The MoS_2/Au interaction is found to be strongest in the topmost MoS_2 layer, with a substantial falloff in the second and subsequent layers, as measured by nanoARPES. These results suggest that methods to increase the van der Waals distance between the topmost TMD layer and a metallic contact, such as intercalation[44] or insertion of a graphene layer,[45] will result in a more consistent optical and electronic response when interfacing TMDs with metallic contacts; the results also highlight opportunities to utilize metallic contacts to tune monolayer TMD excitonic energies. Moreover, we showcase an exciting advantage of our suspended sample geometry, in which correlative experiments with both photons and electrons as excitation sources can be performed.

In the future, this correlative mapping in a suspended 2D/metal platform could be extended to other materials, as a variety of metals exhibit epitaxial growth on suspended 2D materials.[27] Opportunities include plasmon−exciton coupling of TMD/metal systems and metal growth on magnetic 2D materials to alter spin−orbit coupling. Moreover, coupling to metallic films has been shown to enable the detection of dark excitons in 2D TMDs[46] and moiré excitons can be observed at low temperature.[47] Experiments carried out at cryogenic temperatures or with sample encapsulation could improve the signal-to-noise ratio of measurements and decrease exciton absorption line width,[23,48,49] opening opportunities to measure the influence of moiré potential and many-body phenomena in such heterostructures.[50] Recent advances in cryo-STEM, in situ biasing, strain, and heating make such studies at the 2D/metal interface an exciting future avenue of research.

■ ASSOCIATED CONTENT

Supporting Information

The Supporting Information is available free of charge at https://pubs.acs.org/doi/10.1021/acs.nanolett.2c04749.

Detailed methods, Supplementary Note 1 on n-doping and trions in the MoS_2/Au heterostructure, and Supplementary Figures 1−3 including 2D transfer, EELS analysis of another Au island, and EELS mapping of plasmon modes (PDF)

■ AUTHOR INFORMATION

Corresponding Authors

Kate Reidy − *Department of Materials Science and Engineering, Massachusetts Institute of Technology, Cambridge, Massachusetts 02139, United States;* orcid.org/0000-0003-1178-0009; Email: kareidy@mit.edu

Juan Carlos Idrobo − *Materials Science and Engineering Department, University of Washington, Seattle, Washington*

https://doi.org/10.1021/acs.nanolett.2c04749
Nano Lett. 2023, 23, 1068−1076

98195, United States; orcid.org/0000-0001-7483-9034; Email: jidrobo@uw.edu

Authors

Paulina Ewa Majchrzak − *Department of Physics and Astronomy, Aarhus University, 8000 Aarhus C, Denmark;* orcid.org/0000-0002-5200-3866

Benedikt Haas − *Department of Physics & IRIS Adlershof, Humboldt-Universität zu Berlin, 12489 Berlin, Germany*

Joachim Dahl Thomsen − *Department of Materials Science and Engineering, Massachusetts Institute of Technology, Cambridge, Massachusetts 02139, United States;* Present Address: College of Letters and Science, Physical Sciences, UCLA, Los Angeles, CA 90095, USA

Andrea Konečná − *Central European Institute of Technology, Brno University of Technology, 61200 Brno, Czech Republic;* orcid.org/0000-0002-7423-5481

Eugene Park − *Department of Materials Science and Engineering, Massachusetts Institute of Technology, Cambridge, Massachusetts 02139, United States*

Julian Klein − *Department of Materials Science and Engineering, Massachusetts Institute of Technology, Cambridge, Massachusetts 02139, United States;* orcid.org/0000-0002-0873-8224

Alfred J. H. Jones − *Department of Physics and Astronomy, Aarhus University, 8000 Aarhus C, Denmark*

Klara Volckaert − *Department of Physics and Astronomy, Aarhus University, 8000 Aarhus C, Denmark*

Deepnarayan Biswas − *Department of Physics and Astronomy, Aarhus University, 8000 Aarhus C, Denmark*

Matthew D. Watson − *Diamond Light Source, Didcot OX11 0DE, United Kingdom*

Cephise Cacho − *Diamond Light Source, Didcot OX11 0DE, United Kingdom*

Prineha Narang − *College of Letters and Science, Physical Sciences, UCLA, Los Angeles, California 90095, United States;* orcid.org/0000-0003-3956-4594

Christoph T. Koch − *Department of Physics & IRIS Adlershof, Humboldt-Universität zu Berlin, 12489 Berlin, Germany;* orcid.org/0000-0002-3984-1523

Søren Ulstrup − *Department of Physics and Astronomy, Aarhus University, 8000 Aarhus C, Denmark;* orcid.org/0000-0001-5922-4488

Frances M. Ross − *Department of Materials Science and Engineering, Massachusetts Institute of Technology, Cambridge, Massachusetts 02139, United States;* orcid.org/0000-0003-0838-9770

Complete contact information is available at: https://pubs.acs.org/10.1021/acs.nanolett.2c04749

Author Contributions

J.C.I. and K.R. conceived the idea and directed the project with input from F.M.R. S.U., P.E.M. and J.D.T. initiated and directed the nanoARPES part of the project. B.H., J.C.I., and K.R. performed EELS experiments. K.R. and J.D.T. fabricated samples. B.H. performed EELS data postprocessing and control experiments. A.K. performed EELS simulations and analysis. K.R., J.C.I., and E.P. performed EELS data analysis, and A.K., B.H., F.M.R., J.K., P.N., and C.T.K. provided scientific input. P.E.M., A.J.H.J., K.V., D.B., M.D.W., C.C., and S.U. performed nanoARPES measurements and data analysis. K.R. and J.C.I. wrote the initial manuscript, P.E.M. and S.U. contributed nanoARPES figures and description to the manuscript, and all authors contributed to writing and editing. All authors have given approval to the final version of the manuscript.

Notes

The authors declare no competing financial interest.

■ ACKNOWLEDGMENTS

This work was carried out with the use of facilities and instrumentation supported by NSF through the Massachusetts Institute of Technology Materials Research Science and Engineering Center DMR-1419807. The authors thank Diamond Light Source for access to Beamline I05 (Proposal Nos. SI25368 and SI29607) that contributed to the results presented here. This work was carried out in part through the use of MIT.nano's facilities. K.R. acknowledges funding and support from a MIT MathWorks Engineering Fellowship and ExxonMobil Research and Engineering Company through the MIT Energy Initiative. J.D.T. and P.N. acknowledge support from the Office of Naval Research (ONR) MURI Program under grant number ONR N00014-21-1-2537 as well as the by the U.S. Department of Energy, Office of Science, Basic Energy Sciences (BES), Materials Sciences and Engineering Division, under FWP ERKCK47. J.D.T. acknowledges support from Independent Research Fund Denmark though Grant 9035-00006B. J.K. acknowledges support by the Alexander von Humboldt foundation. S.U. acknowledges financial support from VILLUM FONDEN under the Young Investigator Program (Grant No. 15375) and from Independent Research Fund Denmark under the Sapere Aude program (Grant No. 9064-00057B). The EELS data included in the manuscript were taken at Humboldt-Universität zu Berlin. Initial EELS and STEM experiments were conducted at the Center for Nanophase Materials Sciences, which is a DOE Office of Science User Facility. This research was conducted, in part, using instrumentation within ORNL's Materials Characterization Core provided by UT-Battelle, LLC, under contract no. DE-AC05-00OR22725 with the DOE, and sponsored by the Laboratory Directed Research and Development Program of Oak Ridge National Laboratory, managed by UT-Battelle, LLC, for the U.S. Department of Energy. The EELS data analysis workflow development of this work was funded in part by the US Department of Energy in the program "4D Camera Distillery: From Massive Electron Microscopy Scattering Data to Useful Information with AI/ML". B.H. and C.T.K. acknowledge support by the German Research Foundation, project numbers 182087777 (CRC 951), INST 276/721-1 FUGB, and INST 276/829-1. The authors acknowledge Dr. Rami Dana for help with UHV equipment, Dr. Georgios Varnavides and Dr. HaeYeon Lee for useful discussions, Dr. Baoming Wang for help with FIB sample prep, and Dr. Lewys Jones for advice on how to improve image registration.

■ REFERENCES

(1) Allain, A.; Kang, J.; Banerjee, K.; Kis, A. Electrical contacts to two-dimensional semiconductors. *Nat. Mater.* **2015**, *14*, 1195−1205.

(2) Bae, S.-H.; Kum, H.; Kong, W.; Kim, Y.; Choi, C.; Lee, B.; Lin, P.; Park, Y.; Kim, J. Integration of bulk materials with two-dimensional materials for physical coupling and applications. *Nat. Mater.* **2019**, *18*, 550−560.

(3) Miao, J.; Liu, X.; Jo, K.; He, K.; Saxena, R.; Song, B.; Zhang, H.; He, J.; Han, M. G.; Hu, W.; Jariwala, D. Gate-Tunable Semiconductor Heterojunctions from 2D/3D van der Waals Interfaces. *Nano Lett.* **2020**, *20*, 2907−2915.

(4) Ahn, E. C. 2D materials for spintronic devices. *npj 2D Mater. Appl.* **2020**, *4*, 1−14.
(5) Lee, B.; Liu, W.; Naylor, C. H.; Park, J.; Malek, S. C.; Berger, J. S.; Johnson, A. T. C.; Agarwal, R. Electrical Tuning of Exciton-Plasmon Polariton Coupling in Monolayer MoS_2 Integrated with Plasmonic Nanoantenna Lattice. *Nano Lett.* **2017**, *17*, 4541−4547.
(6) Liu, W.; Lee, B.; Naylor, C. H.; Ee, H.-S.; Park, J.; Johnson, A. T. C.; Agarwal, R. Strong Exciton−Plasmon Coupling in MoS_2 Coupled with Plasmonic Lattice. *Nano Lett.* **2016**, *16*, 1262.
(7) Yankovich, A. B.; Munkhbat, B.; Baranov, D. G.; Cuadra, J.; Olsén, E.; Lourenço-Martins, H.; Tizei, L. H. G.; Kociak, M.; Olsson, E.; Shegai, T. Visualizing Spatial Variations of Plasmon-Exciton Polaritons at the Nanoscale Using Electron Microscopy. *Nano Lett.* **2019**, *19*, 8171−8181.
(8) Kleemann, M. E.; Chikkaraddy, R.; Alexeev, E. M.; Kos, D.; Carnegie, C.; Deacon, W.; De Pury, A. C.; Große, C.; De Nijs, B.; Mertens, J.; Tartakovskii, A. I.; Baumberg, J. J. Strong-coupling of WSe_2 in ultra-compact plasmonic nanocavities at room temperature. *Nat. Commun.* **2017**, *8*, 1−7.
(9) Tran, T. T.; Xu, Z.-Q.; Odom, T. W.; Wang, D.; Aharonovich, I.; Toth, M.; Yang, A. Deterministic Coupling of Quantum Emitters in 2D Materials to Plasmonic Nanocavity Arrays. *Nano Lett.* **2017**, *17*, 2634−2639.
(10) Nguyen, M.; Kim, S.; Tran, T. T.; Xu, Z. Q.; Kianinia, M.; Toth, M.; Aharonovich, I. Nanoassembly of quantum emitters in hexagonal boron nitride and gold nanospheres. *Nanoscale* **2018**, *10*, 2267−2274.
(11) Avsar, A.; Unuchek, D.; Liu, J.; Sanchez, O. L.; Watanabe, K.; Taniguchi, T.; Özyilmaz, B.; Kis, A. Optospintronics in Graphene via Proximity Coupling. *ACS Nano* **2017**, *11*, 11678−11686.
(12) Lee, K. H.; Chakram, S.; Kim, S. E.; Mujid, F.; Ray, A.; Gao, H.; Park, C.; Zhong, Y.; Muller, D. A.; Schuster, D. I.; Park, J. Two-Dimensional Material Tunnel Barrier for Josephson Junctions and Superconducting Qubits. *Nano Lett.* **2019**, *19*, 8287−8293.
(13) Jariwala, D.; Marks, T. J.; Hersam, M. C. Mixed-dimensional van der Waals heterostructures. *Nat. Mater.* **2017**, *16*, 170−181.
(14) Liu, Y.; Huang, Y.; Duan, X. Van der Waals integration before and beyond two-dimensional materials. *Nature* **2019**, *567*, 323.
(15) Schauble, K.; Zakhidov, D.; Yalon, E.; Deshmukh, S.; Grady, R. W.; Cooley, K. A.; McClellan, C. J.; Vaziri, S.; Passarello, D.; Mohney, S. E.; Toney, M. F.; Sood, A. K.; Salleo, A.; Pop, E. Uncovering the Effects of Metal Contacts on Monolayer MoS_2. *ACS Nano* **2020**, *14*, 14798−14808.
(16) English, C. D.; Shine, G.; Dorgan, V. E.; Saraswat, K. C.; Pop, E. Improved Contacts to MoS_2 Transistors by Ultra High Vacuum Deposition. *Nano Lett.* **2016**, *16*, 3824−3830.
(17) Rahaman, M.; Marino, E.; Joly, A. G.; Song, S.; Jiang, Z.; O'Callahan, B. T.; Rosen, D. J.; Jo, K.; Kim, G.; El-Khoury, P. Z.; Murray, C. B.; Jariwala, D. Tunable Localized Charge Transfer Excitons in a Mixed Dimensional van der Waals Heterostructure. *2022 ArXiv* arxiv.org/abs/2210.12608 (Accessed 22 Dec 2022).
(18) Miao, J.; Leblanc, C.; Wang, J.; Gu, Y.; Liu, X.; Song, B.; Zhang, H.; Krylyuk, S.; Hu, W.; Davydov, A. V.; Back, T.; Glavin, N.; Jariwala, D. Heterojunction tunnel triodes based on two-dimensional metal selenide and three-dimensional silicon. *Nat. Electron.* **2022**, *5*, 744−751.
(19) Nguyen, P. V.; Teutsch, N. C.; Wilson, N. P.; Kahn, J.; Xia, X.; Graham, A. J.; Kandyba, V.; Giampietri, A.; Barinov, A.; Constantinescu, G. C.; Yeung, N.; Hine, N. D. M.; Xu, X.; Cobden, D. H.; Wilson, N. R. Visualizing electrostatic gating effects in two-dimensional heterostructures. *Nature* **2019**, *572*, 220−223.
(20) Chernikov, A.; Berkelbach, T. C.; Hill, H. M.; Rigosi, A.; Li, Y.; Aslan, O. B.; Reichman, D. R.; Hybertsen, M. S.; Heinz, T. F. Exciton Binding Energy and Nonhydrogenic Rydberg Series in Monolayer WS_2. *Phys. Rev. Lett.* **2014**, *113*, 076802.
(21) Tizei, L. H. G.; Lin, Y.-C.; Mukai, M.; Sawada, H.; Lu, A.-Y.; Li, L.-J.; Kimoto, K.; Suenaga, K. Exciton Mapping at Subwavelength Scales in Two-Dimensional Materials. *Phys. Rev. Lett.* **2015**, *114*, 107601.
(22) Reidy, K.; Varnavides, G.; Dahl Thomsen, J.; Kumar, A.; Pham, T.; Blackburn, A. M.; Anikeeva, P.; Narang, P.; Lebeau, J. M.; Ross, F. M. Direct imaging and electronic structure modulation of moiré superlattices at the 2D/3D interface. *Nat. Commun.* **2021**, *12*, 1290.
(23) Bonnet, N.; Lee, H. Y.; Shao, F.; Woo, S. Y.; Blazit, J.-D.; Watanabe, K.; Taniguchi, T.; Zobelli, A.; Stéphan, O.; Kociak, M.; Gradecak-Garaj, S.; Tizei, L. H. G. Nanoscale modification of WS_2 trion emission by its local electromagnetic environment. *Nano Lett.* **2021**, *21*, 10178−10185.
(24) Najmaei, S.; Mlayah, A.; Arbouet, A.; Girard, C.; Léotin, J.; Lou, J. Plasmonic pumping of excitonic photoluminescence in hybrid MoS_2-Au nanostructures. *ACS Nano* **2014**, *8*, 12682−12689.
(25) Rotenberg, E.; Bostwick, A. microARPES and nanoARPES at diffraction-limited light sources: opportunities and performance gains. *J. Synchrotron Radiat.* **2014**, *21*, 1048−1056.
(26) Periwal, P.; Thomsen, J. D.; Reidy, K.; Varnavides, G.; Zakharov, D. N.; Gignac, L.; Reuter, M. C.; Booth, T. J.; Hofmann, S.; Ross, F. M. Catalytically mediated epitaxy of 3D semiconductors on van der Waals substrates. *Appl. Phys. Rev.* **2020**, *7*, 031402.
(27) Reidy, K.; Thomsen, J. D.; Lee, H. Y.; Zarubin, V.; Yu, Y.; Wang, B.; Pham, T.; Periwal, P.; Ross, F. M. Mechanisms of Quasi van der Waals Epitaxy of Three-Dimensional Metallic Nanoislands on Suspended Two-Dimensional Materials. *Nano Lett.* **2022**, *22*, 5849−5858.
(28) Jones, L.; Yang, H.; Pennycook, T. J.; Marshall, M. S. J.; Van Aert, S.; Browning, N. D.; Castell, M. R.; Nellist, P. D. Smart Align-a new tool for robust non-rigid registration of scanning microscope data. *Adv. Struct. Chem. Imaging* **2015**, *1*, 8.
(29) Bruix, A.; Miwa, J. A.; Hauptmann, N.; Wegner, D.; Ulstrup, S.; Grønborg, S. S.; Sanders, C. E.; Dendzik, M.; Grubišic, A.; Cabo, G.; Bianchi, M.; Lauritsen, J. V.; Khajetoorians, A. A.; Hammer, B.; Hofmann, P. Single-layer MoS_2 on Au(111): Band gap renormalization and substrate interaction. *Phys. Rev. B* **2016**, *93*, 165422.
(30) Kang, J.; Liu, W.; Sarkar, D.; Jena, D.; Banerjee, K. Computational Study of Metal Contacts to Monolayer Transition-Metal Dichalcogenide Semiconductors. *Phys. Rev. X* **2014**, *4*, 031005.
(31) Drüppel, M.; Deilmann, T.; Krüger, P.; Rohlfing, M. Diversity of trion states and substrate effects in the optical properties of an MoS_2 monolayer. *Nat. Commun.* **2017**, *8*, 2117.
(32) Wierzbowski, J.; Klein, J.; Sigger, F.; Straubinger, C.; Kremser, M.; Taniguchi, T.; Watanabe, K.; Wurstbauer, U.; Holleitner, A. W.; Kaniber, M.; Müller, K.; Finley, J. J. Direct exciton emission from atomically thin transition metal dichalcogenide heterostructures near the lifetime limit. *Sci. Rep.* **2017**, *7*, 7−12.
(33) Korn, T.; Heydrich, S.; Hirmer, M.; Schmutzler, J.; Schller, C. Low-temperature photocarrier dynamics in monolayer MoS_2. *Appl. Phys. Lett.* **2011**, *99*, 102109.
(34) Florian, M.; Hartmann, M.; Steinhoff, A.; Klein, J.; Holleitner, A. W.; Finley, J. J.; Wehling, T. O.; Kaniber, M.; Gies, C. The Dielectric Impact of Layer Distances on Exciton and Trion Binding Energies in van der Waals Heterostructures. *Nano Lett.* **2018**, *18*, 2725−2732.
(35) Krane, N.; Lotze, C.; Läger, J. M.; Reecht, G.; Franke, K. J. Electronic Structure and Luminescence of Quasi-Freestanding MoS_2 Nanopatches on Au(111). *Nano Lett.* **2016**, *16*, 5163−5168.
(36) Van Tuan, D.; Yang, M.; Dery, H. Coulomb interaction in monolayer transition-metal dichalcogenides. *Phys. Rev. B* **2018**, *98*, 125308.
(37) Miwa, J. A.; Ulstrup, S.; Sørensen, S. G.; Dendzik, M.; Čabo, A. G.; Bianchi, M.; Lauritsen, J. V.; Hofmann, P. Electronic structure of epitaxial single-layer MoS_2. *Phys. Rev. Lett.* **2015**, *114*, 046802.
(38) Raja, A.; Chaves, A.; Yu, J.; Arefe, G.; Hill, H. M.; Rigosi, A. F.; Berkelbach, T. C.; Nagler, P.; Schüller, C.; Korn, T.; Nuckolls, C.; Hone, J.; Brus, L. E.; Heinz, T. F.; Reichman, D. R.; Chernikov, A. Coulomb engineering of the bandgap and excitons in two-dimensional materials. *Nat. Commun.* **2017**, *8*, 1−7.
(39) Rösner, M.; Steinke, C.; Lorke, M.; Gies, C.; Jahnke, F.; Wehling, T. O. Two-Dimensional Heterojunctions from Nonlocal Manipulations of the Interactions. *Nano Lett.* **2016**, *16*, 2322−2327.

https://doi.org/10.1021/acs.nanolett.2c04749
Nano Lett. 2023, 23, 1068−1076

(40) Ugeda, M. M.; Bradley, A. J.; Shi, S. F.; Da Jornada, F. H.; Zhang, Y.; Qiu, D. Y.; Ruan, W.; Mo, S. K.; Hussain, Z.; Shen, Z. X.; Wang, F.; Louie, S. G.; Crommie, M. F. Giant bandgap renormalization and excitonic effects in a monolayer transition metal dichalcogenide semiconductor. *Nat. Mater.* **2014**, *13*, 1091−1095.

(41) Rohlfing, M. Redshift of excitons in carbon nanotubes caused by the environment polarizability. *Phys. Rev. Lett.* **2012**, *108*, 087402.

(42) Neaton, J. B.; Hybertsen, M. S.; Louie, S. G. Renormalization of molecular electronic levels at metal-molecule interfaces. *Phys. Rev. Lett.* **2006**, *97*, 216405.

(43) Tanaka, K.; Takahashi, T.; Kondo, T.; Umebayashi, T.; Asai, K.; Ema, K. Image charge effect on two-dimensional excitons in an inorganic-organic quantum-well crystal. *Phys. Rev. B - Condens. Matter Mater. Phys.* **2005**, *71*, 045312.

(44) Wu, Q.; Bagheri Tagani, M.; Zhang, L.; Wang, J.; Xia, Y.; Zhang, L.; Xie, S.-Y.; Tian, Y.; Yin, L.-J.; Zhang, W.; Rudenko, A. N.; Wee, A. T. S.; Wong, P. K. J.; Qin, Z. Electronic Tuning in WSe_2/Au via van der Waals Interface Twisting and Intercalation. *ACS Nano* **2022**, *16*, 6541−6551.

(45) Qi, D.; Li, P.; Ou, H.; Shenzhen, D. W.; Lian, W.; Wang, Z.; Ouyang, F.; Chai, Y.; Zhang, W. Graphene-enhanced van der Waals contacts between three-dimensional metals and two-dimensional semiconductors. *Res. Sq.* **2022** DOI: 10.21203/RS.3.RS-1854850/V1 (Accessed 22 Dec 2022).

(46) Zhou, Y.; Scuri, G.; Wild, D. S.; High, A. A.; Dibos, A.; Jauregui, L. A.; Shu, C.; De Greve, K.; Pistunova, K.; Joe, A. Y.; Taniguchi, T.; Watanabe, K.; Kim, P.; Lukin, M. D.; Park, H. Probing dark excitons in atomically thin semiconductors via near-field coupling to surface plasmon polaritons. *Nat. Nanotechnol.* **2017**, *12*, 856−860.

(47) Susarla, S.; M. Sassi, L.; Zobelli, A.; Woo, S. Y.; Tizei, L. H. G.; Stéphan, O.; Ajayan, P. M. Mapping Modified Electronic Levels in the Moiré Patterns in MoS_2/WSe_2 Using Low-Loss EELS. *Nano Lett.* **2021**, *21*, 4071−4077.

(48) Shao, F.; Woo, S. Y.; Wu, N.; Schneider, R.; Mayne, A. J.; De Vasconcellos, S. M.; Arora, A.; Carey, B. J.; Preuß, J. A.; Bonnet, N.; Och, M.; Mattevi, C.; Watanabe, K.; Taniguchi, T.; Niu, Z.; Bratschitsch, R.; Tizei, L. H. G. Substrate influence on transition metal dichalcogenide monolayer exciton absorption linewidth broadening. *Phys. Rev. Mater.* **2022**, *6*, 074005.

(49) Cadiz, F.; Courtade, E.; Robert, C.; Wang, G.; Shen, Y.; Cai, H.; Taniguchi, T.; Watanabe, K.; Carrere, H.; Lagarde, D.; Manca, M.; Amand, T.; Renucci, P.; Tongay, S.; Marie, X.; Urbaszek, B. Excitonic linewidth approaching the homogeneous limit in MoS_2-Based van der Waals Heterostructures. *Phys. Rev. X* **2017**, *7*, 1−12.

(50) Susarla, S.; Naik, M. H.; Blach, D. D.; Zipfel, J.; Taniguchi, T.; Watanabe, K.; Huang, L.; Ramesh, R.; Jornada, F. H. da; Louie, S. G.; Ercius, P.; Raja, A. Hyperspectral imaging of exciton confinement within a moiré unit cell with a subnanometer electron probe. *Science* **2022**, *378*, 1235−1239.

https://doi.org/10.1021/acs.nanolett.2c04749
Nano Lett. 2023, 23, 1068−1076

NANO LETTERS
Letter
Cite This: *Nano Lett.* 2020, 20, 592−598
pubs.acs.org/NanoLett

Cathodoluminescence Phase Extraction of the Coupling between Nanoparticles and Surface Plasmon Polaritons

Takumi Sannomiya,[*,†,‡] Andrea Konečná,[§] Taeko Matsukata,[†] Zac Thollar,[†] Takayuki Okamoto,[∥] F. Javier García de Abajo,[§,⊥] and Naoki Yamamoto[†]

[†]Department of Materials Science and Technology, Tokyo Institute of Technology, 4259 Nagatsuta, Midoriku, Yokohama 226-8503, Japan

[‡]PRESTO, 4259 Nagatsuta, Midoriku, Yokohama 226-8503, Japan

[§]ICFO-Institut de Ciencies Fotoniques, The Barcelona Institute of Science and Technology, 08860 Castelldefels, Barcelona, Spain

[∥]Advanced Device Laboratory, RIKEN, Wako, Saitama 351-0198, Japan

[⊥]ICREA-Institució Catalana de Recerca i Estudis Avançats, Passeig Lluís Companys, 23, 08010 Barcelona, Spain

Supporting Information

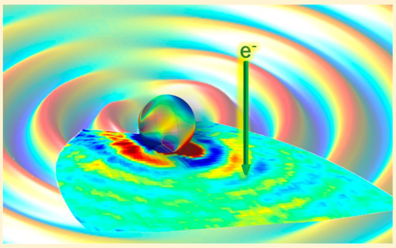

ABSTRACT: Nanoscale gaps between metals can strongly confine electromagnetic fields that enable efficient electromagnetic energy conversion and coupling to nanophotonic structures. In particular, the gap formed by depositing a metallic particle on a metallic substrate produces coupling of localized particle plasmons to propagating surface plasmon polaritons (SPPs). Understanding and controlling the phase of such coupling is essential for the design of devices relying on nanoparticles coupled through SPPs. Here we demonstrate the experimental visualization of the phase associated with the plasmonic field of metallic particle−surface composites through nanoscopically and spectroscopically resolved cathodoluminescence using a scanning transmission electron microscope. Specifically, we study the interference between the substrate transition radiation and the field resulting from out-coupling of SPP excitation, therefore giving rise to angle-, polarization-, and energy-dependent photon emission fringe patterns from which we extract phase information. Our methods should be readily applicable to more complex nanostructures, thus providing direct experimental insight into nanoplasmonic near-fields with potential applications in improving plasmon-based devices.

KEYWORDS: *Surface plasmons, plasmon gap mode, cathodoluminescence, scanning transmission electron microscopy, transition radiation*

The spatial confinement of optical fields plays an essential role in improving photonic energy conversion,[1] enhancing nonlinear effects,[2] assisting optical sensing,[3] producing nanoscale lasing,[4] processing information through optical signals,[5] and mediating photocatalysis,[6] among other feats. Plasmons—the collective electron oscillations in conducting materials—provide the means to materialize these important applications, and in particular, they can produce extremely focused electromagnetic fields on the nanoscale, which are well known to pile up in nanogaps between two metallic structures.[6] Although the proper control of such nanogaps is generally not trivial because of their strong dependence on the detailed surface morphology, a simple and relatively controllable system consists of an individual metallic nanoparticle separated from a metallic planar substrate by a nanoscale gap of a precisely determined distance. Using such particle-on-plane configuration with resonances at optical frequencies, strongly enhanced Raman scattering,[7] large coupling to molecules showing Rabi splitting,[8] intense Purcell enhancement,[9] strong nonlinear response,[10] efficient nanolasing,[11] and functional metasurface applications[12] have been demonstrated, reaching the quantum limit for field confinement. Besides producing strongly enhanced local fields, the particle-on-plane configuration also operates as an efficient antenna that can mediate the coupling between the fields of photons propagating in free space and those of surface plasmon polaritons (SPPs) evolving on the metallic substrate. Such coupling to propagating waves is needed to enable surface-based on-chip devices accessing the nanogap cavity through SPPs as well as sensing platforms based on far-field excitation and detection. In the design of applications of such nanogap antennas, knowledge of near- and far-field distributions including the field phase is essential to engineer an efficient coupling between SPPs and propagating waves.

Received: October 21, 2019
Revised: December 18, 2019
Published: December 19, 2019

DOI: 10.1021/acs.nanolett.9b04335
Nano Lett. 2020, 20, 592−598

We propose a general methodology to access the phase associated with the interaction of SPPs with a nanostructure placed on a SPP-supporting metal surface. Our method is based on the interference between light that is directly emitted from the planar surface upon electron impact and light resulting from SPPs also generated by the electron and subsequently out-coupled by the nanostructure; such interference is determined by measuring the resulting cathodoluminescence (CL) signal. (See Figure 1a.) In other currently

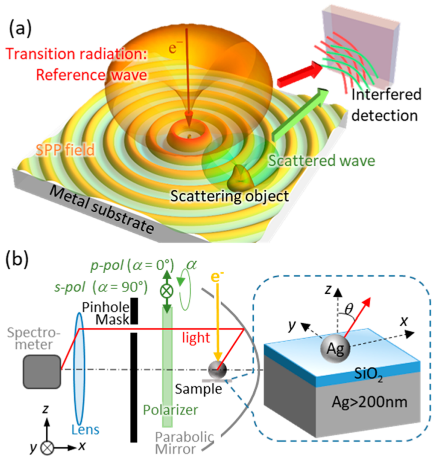

Figure 1. (a) Illustration of our method for the extraction of the SPP scattering phase through CL. Transition radiation (TR) from the metallic substrate is used as a reference wave, interfering in the far field (at the detector) with out-coupled light resulting from the SPP interaction with the sampled object. (b) Illustration of the measurement setup, the sample, and the coordinate system. The light emitted from the specimen is collimated by a parabolic mirror placed around the specimen and transferred to the spectrometer through a polarizer and an angle-selection mask. We define p polarization parallel to the plane formed by the electron beam and the light optical axis (i.e., polarization vector in the x−z plane). Accordingly, the polarization angle is defined as α, with $\alpha = 0°$ denoting p polarization.

available techniques, truly nanoscopic and spectroscopic imaging of the SPP scattering phase is far from trivial. Visualization of propagating SPPs has been performed using scanning near-field optical microscopy (SNOM)[13] as well as dark-field optical microscopy. However, these techniques have worse spatial resolution compared with CL.[14−17] Electron energy-loss spectroscopy (EELS) provides subnanometer resolution but cannot retrieve the phase, although some progress has been made through plasmon holography and pulsed beam methods.[18,19] Now, because of its high combined spatial and spectral resolution, angle-resolved CL appears as an ideal tool that can potentially access the phase of photonic fields through interference.[20] In fact, angle-resolved CL measurements have already been proved useful to describe the multipolar character of the emission and even to investigate time-resolved photon-emission correlation from quantum emitters,[21−23] but phase visualization such as we report here has so far not been described.

Here we visualize both near- and far-field distributions through CL performed on a scanning transmission electron microscope, allowing us to obtain the scattering phase associated with the interaction of SPPs with individual metallic nanoparticles. Specifically, we retrieve phase information by analyzing the interference between simultaneously emitted transition radiation (TR) and light resulting from the interaction between SPPs and the particle (Figure 1a). Leveraging the spectral and spatial resolution of CL, we visualize the retrieved phase as a function of the light frequency and the electron-beam excitation position. We first identify the hybridized modes of the metal nanoparticle−surface system by collecting CL light emission with nanometer spatial resolution, in excellent agreement with numerical simulations. We then spatially and spectrally visualize the TR−SPP interference patterns, which map the propagating SPPs exciting the particle, and further use an analytical model to extract the associated scattering phase. This method can be readily generalized to extract phase information from arbitrary nanoscale systems.

CL measurements were performed at 80 kV electron acceleration voltage using a STEM instrument (JEOL 2100F, Japan) with a custom-built optical detection system, as shown in Figure 1b. In brief, the CL signal was collimated by a parabolic mirror and detected after passing through a polarizer and an angle-selection mask. (More details can be found elsewhere.[24,25]) A substrate silver layer of >200 nm in thickness was deposited on an InP substrate by thermal evaporation in a vacuum, and a thin SiO_2 spacer layer was deposited by radio frequency (RF) sputtering. The silver spheres were deposited by thermal evaporation in an argon atmosphere. (See fabrication details in the SI.) The coordinate system used throughout this work is defined in Figure 1b.

We first determine the optical modes of individual metallic spheres coupled to a metallic substrate. Figure 2 shows line profiles of the CL signal acquired for different emitted-light polarizations and collected over the entire range of emission directions provided by the parabolic mirror (i.e., roughly half of the upper hemisphere). With the electron beam positioned close to the nanoparticle, interference effects are then smeared out by angular integration, and the mode energy can be safely determined. Figure 2a shows the results with a substrate containing a 10 nm SiO_2 spacer layer, and Figure 2b shows the corresponding secondary electron (SE) images of spheres with different diameters. With p polarization (polarization angle α = 0°), the bonding perpendicular dipole mode (the so-called gap mode with strong field concentration in the metal sphere−surface gap) that shows up around 2.0 eV for small particles (50−80 nm) produces a highest CL signal intensity when the beam is aimed at the center of the sphere.[17] As the diameter increases, the resonance shifts to lower energy, and the CL intensity associated with this mode becomes stronger. The size dependence of the resonance energy is summarized in Figure 2e. The energy of this perpendicular dipole, emerging due to the presence of the metallic substrate, is much lower than the energy of the conventional dipolar mode of spheres placed on a thin elastic carbon membrane with the same size, as shown in Figure 2c. (See also the Supporting Information (SI) for line profiles.) Similar tendencies are found for different spacer thicknesses, as summarized in Figure 2d (5 nm SiO_2 spacer) and Figure 2f (15 nm SiO_2 spacer). When s polarization is selected, in-plane coupled dipoles are preferentially detected,

DOI: 10.1021/acs.nanolett.9b04335
Nano Lett. 2020, 20, 592−598

Nano Letters Letter

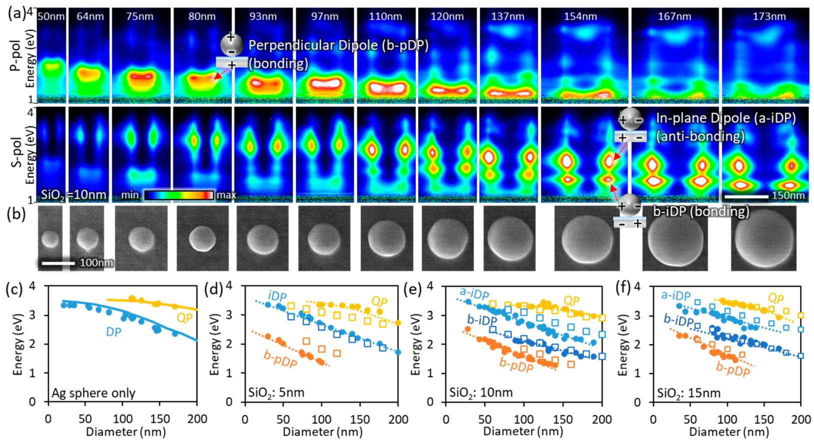

Figure 2. Identification of resonance of silver spheres coupled to a silver substrate. (a) CL line profiles along the y direction at the center of individual spheres of different diameters (see labels) deposited on a SiO_2-coated (10 nm) silver substrate. The emission is resolved in p- (top panels) and s- (bottom panels) polarization components. (b) Corresponding backscattered electron images. (c−f) Measured particle-size dependence of the plasmon resonance energies (symbols) extracted from spectral maps similar to those shown in panels a and b when the particle is deposited on (c) an elastic carbon membrane (i.e., without metal substrate) and a metal substrate coated with a SiO_2 layer of (d) 5, (e) 10, and (f) 15 nm thickness. Solid lines in panel c correspond to Mie scattering calculations. Dotted lines in panels d−f are guides for the eye. Empty square symbols show finite-element method simulations. We label the modes as dipole plasmon (DP), quadrupole (QP), in-plane dipole (iDP), bonding perpendicular dipole (b-pDP), bonding in-plane dipole (b-iDP), and antibonding in-plane dipole (a-iDP), respectively.

showing high CL intensities at the edge of the spheres (Figure 2a, lower row). Then, the in-plane dipole splits into two modes for larger spheres: the bonding and antibonding modes resulting from coupling to the metallic substrate.[14,26]

Closer inspection of the line profiles for s-polarized light emission (Figure 2a, lower row) reveals that the low-energy bonding dipolar mode shows its hotspots more inside the sphere compared with the antibonding mode. This is due to the more confined field distribution produced when induced charges of opposite signs are arranged in a quadrupole-like configuration. (See the schematic illustration in the insets of Figure 2a.) This is clearly confirmed by the photon maps with mode selection, displaying a *smaller* (i.e., more compact) dipole pattern for the bonding mode (Figure S6).

Interestingly, the antibonding mode at higher energies appears to be stronger for smaller particles, whereas the bonding mode becomes stronger for larger ones (s-pol result in Figure 2a). For the 15 nm silica spacer, the antibonding mode is not efficiently excited for larger sizes (Figure 2f and Figure S4). We interpret this result to be related to the excitation phase mismatch by the swift electron moving with finite velocity (∼50% of the light speed): The shorter the distance between the sphere center and the substrate (i.e., smaller particles), the smaller the time difference taken by the swift electron to induce separated charges of the same sign required to excite the antibonding mode. In contrast, for a larger distance between the sphere and the substrate (i.e., larger particles), the excitation of charges with opposite signs becomes comparatively more efficient with a larger time difference; for example, 80 kV electrons travel across a 156 nm sphere in half a cycle of 2 eV light. (See also the line profiles observed for the 15 nm silica spacer in Figure S4.) We also note that the splitting of the in-plane dipole is not clearly observed for the 5 nm silica spacer, presumably because of finer surface roughness, which we later explore by means of numerical simulations. (See Figure S5.)

We performed finite-element-method (FEM) simulations of Maxwell's equations with electron beam excitation using COMSOL Multiphysics to confirm the symmetry assignment of the observed modes and their dependence on sphere size. We truncated the sphere bottom to mimic a more realistic situation of non-point-like contact between the sphere and the substrate. A truncation length of 10 nm was used for 10 and 15 nm SiO_2 layer thickness results. This is an effective way to account for the presence of finite-size facets in the particle; additionally, the actual substrates used in the experiment have finite grain-like roughness mainly due to the deposited silver films underneath, which can produce a large departure from point-like sphere-substrate contact. (See Section S3 of the SI.) In fact, this sphere truncation was essential to theoretically reproduce the experimental results with well-separated bonding and antibonding in-plane dipole modes. For 5 nm SiO_2 spacing, we found that no truncation was needed to reproduce the experimental results, which indicates that the truncation length should be adapted for smaller gap sizes. Additionally, the film roughness could slightly shift the dispersion of SPPs to higher wavenumbers and introduce losses due to scattering.[27,28] Figure 3a,b shows the simulated line profiles for p- and s-polarized CL emission from a 160 nm silver particle on a 10 nm SiO_2/Ag substrate. The radiation signal was integrated over the upper hemisphere. The calculated line profiles satisfactorily reproduce the experimen-

DOI: 10.1021/acs.nanolett.9b04335
Nano Lett. 2020, 20, 592−598

Nano Letters Letter

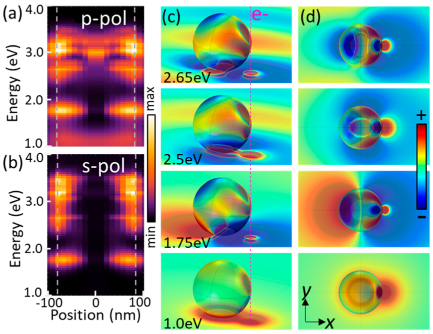

Figure 3. Finite-element-method simulations with electron beam excitation for a 160 nm sphere on a 10 nm SiO_2/Ag substrate. (a,b) Simulated CL line-scan profiles. The intensity is resolved in (a) p- and (b) s-polarization components. The emission signal is integrated over the upper hemisphere. The sphere edges are indicated by vertical dashed lines. (c,d) Out-of-plane z-component of the spectrally resolved total electric field amplitude produced by the electron in its interaction with the particle-on-plane system plotted for different photon energies with fixed electron beam position and orientation relative to the sphere, indicated by a purple line in panel c. The field distributions are shown in (c) side and (d) top views of the structure.

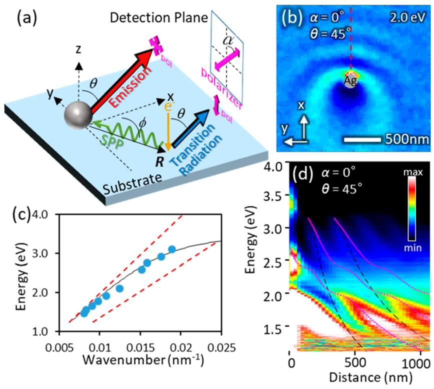

Figure 4. Interference of transition radiation and SPP-mediated particle emission for a 135 nm Ag sphere on a 10 nm SiO_2/Ag substrate. (a) Schematic illustration of the angle- and polarization-resolved measurement with SPP-mediated particle excitation. Measurements in panels b−d correspond to a polarization angle $\alpha = 0°$ and detection angle $\theta = 45°$. (b) Photon map at 2.0 eV photon energy. (c) Measured dispersion relation of the SPPs (symbols) compared with the calculated dispersion (solid curve). The light lines in the vacuum and SiO_2 are shown for reference (dashed lines). (d) Line profile along the dotted line in panel b. The pink (black) broken curves correspond to the calculated constructive interference profiles with (without) considering the phase associated with SPP particle scattering.

tal results, such as the perpendicular dipole around 1 eV, the in-plane bonding mode around 1.75 eV, the in-plane antibonding mode around 2.65 eV, and higher-order modes at larger energies. The resonance energies calculated for different SiO_2 thicknesses and sphere diameters are plotted as square symbols in Figure 2e,f, which match well the experimental results.

To analyze the spatial field distribution and mode symmetry, we plot the z-component of the total electric field at different energies in Figure 3c,d, where the electron beam is passing close to the sphere. While the field on the substrate at 1 eV is approximately rotationally symmetric, showing a perpendicular dipole pattern, a two-fold symmetric pattern around the z-particle axis is observed for the in-plane bonding dipole mode at 1.75 eV. The relative phase between the substrate field and the sphere field starts to flip as the energy increases, reaching the antibonding mode at ~2.65 eV. This phase flip is most clearly visible on the opposite side of the particle relative to the location of the electron beam excitation because the electron beam itself creates a strong field that overshadows the one induced from the particle and the surface.

We now attempt to extract the phase of the substrate-coupled particle modes by taking advantage of SPPs on the substrate. Because the in-plane dipole modes strongly couple to SPPs, it should be possible to excite them through SPPs generated by the electron, even at large distances from the sphere. The electron beam incident on the flat metallic substrate launches SPPs in all directions (i.e., circular SPP waves emanating from the point at which the electron impinges the surface), together with transition radiation (TR), as described in Figures 1a and 4a.[20,29] TR can be intuitively understood as the light generated by the destruction of the effective dipole associated with the electron and its image charge as the electron traverses the metal surface. Fast electrons in the relativistic regime produce TR over a broad spectral range, thus working as a white-like reference light source. The electric field of TR is summarized in eq S1 of the SI. The SPPs generated by the electron beam reach the sphere, where they are partially converted into photons by scattering at the particle. Because all of these processes are coherent, the field scattered from the sphere and the TR field interfere in the far field.[20,30] By the detection angle and polarization selection, we can visualize this interference spatially and spectrally.

For this measurement, we choose 10 nm SiO_2 thickness and a rather large particle (135 nm) because it better shows the energy splitting of in-plane dipole modes, thus providing an ideal target for phase analysis. Figure 4b shows the interference mapping with p polarization ($\alpha = 0°$) and a detection angle $\theta = 45°$ at 2.0 eV photon energy. TR is also p-polarized (see eq S1 in the SI), and hence interference effects are expected to appear if we filter p-polarized light to obtain the CL signal.[25,29] With this detection configuration and energy selection, the dominant mode of the sphere is the in-plane dipole with charge oscillation along the x axis.[31] (See also the SI.) This interference pattern is similar to the one created with oblique-incidence light and particle scattering.[13,32] We note that the slightly inhomogeneous contrast on the flat substrate area could be due to the roughness of the substrate surface, although no significant scattering from the substrate surface alone is observed. From the spatial line profile (taken along the red line in Figure 4b) of the interference pattern at different energies, we extract the dispersion relation of the SPPs, as shown in Figure 4c. (See SI for details of profile fitting.) The

DOI: 10.1021/acs.nanolett.9b04335
Nano Lett. 2020, 20, 592−598

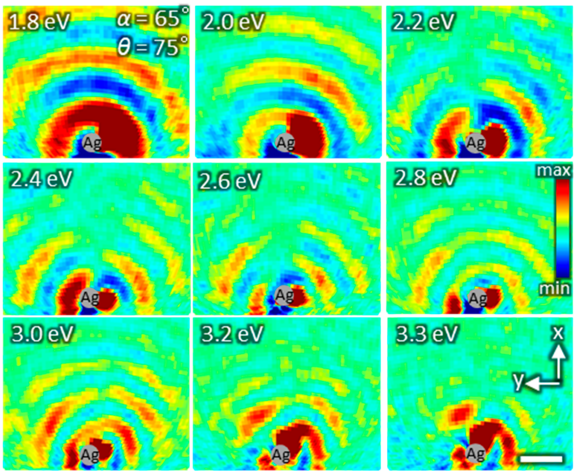

Figure 5. Conformal mappings of CL photon maps measured at polarization angle $\alpha = 65°$ and detection angle $\theta = 75°$ for different photon energies (see labels). The scale bar corresponds to 500 nm in the conformal space.

obtained dispersion relation matches well the calculated one for a vacuum/10 nm SiO_2/Ag layered system.

The complete spectroscopic line profile along the red line in Figure 4b clearly shows an interference pattern, encompassing constructive interference *bump* lines around 2 eV photon energy. This represents the phase flip of the split mode around its resonance. The high-intensity lines correspond to different orders of constructive interference between TR and the SPP scattering emission from the sphere. The constructive interference condition as a function of electron-sphere distance R along the substrate surface is described through the expression[20]

$$R = \frac{\Phi_{osc} + 2m\pi}{k_{spp} + k \sin\theta \cos\phi} + \Delta \tag{1}$$

where Φ_{osc} is the phase of the field scattered by the particle, m is an integer number, k_{spp} is the SPP wave vector, k is the free-space light wave vector, ϕ is the in-plane azimuthal angle defined in Figure 4a, and Δ stands for an additional phase delay associated with the interaction distance of the SPP with the sphere. The black dashed curves in Figure 4d show interference curves calculated from eq 1 without considering the phase change produced by the particle ($\Phi_{osc} = 0$, $\Delta = 0$), which obviously do not match the experimental profiles. By introducing the scatterer phase Φ_{osc} based on a coupled oscillator model with normal mode splitting[33−35] and the interaction distance $\Delta = 0.15\lambda_{spp}$ using the SPP wavelength λ_{spp}, the experimental profiles are well reproduced by eq 1, as shown as the pink dotted curves in Figure 4d. We note that only the in-plane dipole makes a contribution in the 2.0 to 3.0 eV photon-energy range for a 135 nm sphere. Using the normal-mode splitting model, we determine the value Δ to best fit the experimental results. (See details in the SI.) The double phase flip of the split-mode resonances reasonably reproduces the *bumps* around 2 eV. The observed slight deviation at lower and higher energies seems to arise from the contribution of the perpendicular dipole and higher-order modes, respectively.

Using this interference method, we can also extract the symmetry of the coupled SPPs, including the phase. For this purpose, we introduce a conformal mapping of the interference photon map so that the oscillating profile matches the SPP wavelength. To do so, the original position $\mathbf{R}$ from the sphere is conformally mapped into the $\mathbf{R}' = M\mathbf{R}$ space using a magnification factor M, which can be calculated using the SPP wave vector as

$$M = 1 + \frac{k}{k_{spp}} \sin\theta \cos\phi \tag{2}$$

This conformal mapping scheme is illustrated in the SI. Besides the change in spatial coordinates, the intensity is also normalized as $I' = I/M$ taking into consideration the SPP propagation. The intrinsic SPP decay length is not taken into account in the current mapping scale and energy range because SPPs have long propagation lengths on Ag compared with the distances involved in our samples.

For this mapping, we selectively extract the dipole along the y axis by setting the detection angle close to grazing with respect to the substrate ($\theta = 75°$) and the polarization angle ($\alpha = 65°$) between s and p polarizations. Under these conditions, within the 2.2 to 2.6 eV photon-energy range, the interference between the in-plane dipole along the y axis and TR is maximally captured. Because radiation from this dipole is mainly s-polarized, whereas TR is p-polarized, the radiation to be detected is elliptically or linearly polarized depending on the relative phase of the TR and scattering contributions. For a certain relative phase, the linear component in this polarization direction gives rise to maxima in the intensity, thus generating constructive interfering profiles. Figure 5 shows the conformally mapped interference patterns. Between 2.2 and 2.6

DOI: 10.1021/acs.nanolett.9b04335
Nano Lett. 2020, 20, 592−598

eV, the dipolar *radiation* pattern with opposite phases on the right and left halves of the plot is visualized. A spatial phase flip at the center ($y = 0$) is clearly observable. Below 2.0 eV, the influence of the perpendicular dipole becomes more dominant, giving rise to a circular pattern. At higher energies above 3.2 eV, a quadrupole-like pattern starts to emerge, although its profile is not very clear due to the short propagation of SPPs at this energy. These patterns reveal phase maps that are similar to those obtained by pump−probe SNOM.[36] However, the presented interference CL method has clear advantages over SNOM because it provides simultaneous spectroscopic data by a single measurement that enables the extraction of phase information from frequency space with better spatial resolution. Consequently, this interference method can be used to extract the phase produced by the scatterer using TR as a reference.

In conclusion, we have demonstrated interference measurements of silver spheres coupled to a metallic substrate using a STEM-CL setup, where strong fields are produced at the gap between the particle and the substrate. Because of coupling to the substrate, the dipole mode of the silver particle splits into antibonding and bonding modes with opposite induced surface-charge schemes. These split modes and their interaction with the surface are well reproduced by numerical electromagnetic simulations with the electron acting as a source.

Coupling to the induced substrate charges directly implies coupling to SPPs. This allows particle modes to be excited through SPPs that are launched at a distance by the incident electron beam on the metal substrate, which also produces TR. Because the electromagnetic fields associated with electron-generated SPPs and TR, as well as those of light produced by SPP-particle scattering, are all coherent, they produce interference resulting in fringe patterns in the spectral, angular, and electron-beam-position dependence of the emitted CL intensity. By analyzing these fringe patterns, we have extracted the phase associated with SPP-particle-mode coupling. Interestingly, we could reproduce the spatial SPP field distribution including the phase through conformally mapping the obtained spectral images. Through this approach, we have resolved mode symmetry and spectroscopic phase flips of the SPP-coupled modes, revealing the interaction of the plasmonic particle and SPPs. This method offers simultaneous spectroscopic and nanoscopic spatial phase mappings over a broad spectral range, without the need for time-consuming energy scans used in other techniques such as phase measurement by SNOM, and also offers a more direct comparison with theory, without the inherent complication introduced by the presence of tips. Additionally, in terms of spatial resolution, the presented technique based on a focused electron beam provides one order of magnitude higher spatial resolution than SNOM; therefore it can reveal complex nanoscopic near-field distributions in plasmonic nanostructures.

■ ASSOCIATED CONTENT

Ⓢ Supporting Information

The Supporting Information is available free of charge at https://pubs.acs.org/doi/10.1021/acs.nanolett.9b04335.

> Mode identification for samples with various silica-spacer thicknesses, surface roughness of silica-coated silver substrates, mode splitting of in-plane dipole, radiation of electric dipole, excitation of particle mode by SPPs, normal-mode splitting, interference pattern of transition radiation and particle scattering through SPPs, calculated interference patterns, and conformal mapping of the interference pattern (PDF)

■ AUTHOR INFORMATION

Corresponding Author

*E-mail: sannomiya.t.aa@m.titech.ac.jp.

ORCID

Takumi Sannomiya: 0000-0001-7079-2937
Andrea Konečná: 0000-0002-7423-5481
F. Javier García de Abajo: 0000-0002-4970-4565

Author Contributions

The manuscript was written through contributions of all authors. All authors have given approval to the final version of the manuscript.

Funding

JST PRESTO (#JPMJPR17P8), ERC (advanced grant 789104-eNANO), the Spanish MINECO (MAT2017-88492-R and SEV2015-0522), the Catalan CERCA, and Fundació Privada Cellex.

Notes

The authors declare no competing financial interest.

■ ACKNOWLEDGMENTS

We thank Dr. H. Saito for the fruitful discussions. A part of the calculations was performed using the RIKEN HOKUSAI GreatWave Facility.

■ REFERENCES

(1) Atwater, H. A.; Polman, A. Plasmonics for improved photovoltaic devices. *Nat. Mater.* **2010**, *9* (3), 205−213.

(2) Danckwerts, M.; Novotny, L. Optical frequency mixing at coupled gold nanoparticles. *Phys. Rev. Lett.* **2007**, *98* (2), 026104.

(3) Anker, J. N.; Hall, W. P.; Lyandres, O.; Shah, N. C.; Zhao, J.; Van Duyne, R. P. Biosensing with plasmonic nanosensors. *Nat. Mater.* **2008**, *7* (6), 442−453.

(4) Mkhitaryan, V.; Meng, L. J.; Marini, A.; García de Abajo, F. J. Lasing and Amplification from Two-Dimensional Atom Arrays. *Phys. Rev. Lett.* **2018**, *121* (16), 163602.

(5) Tame, M. S.; McEnery, K. R.; Ozdemir, S. K.; Lee, J.; Maier, S. A.; Kim, M. S. Quantum plasmonics. *Nat. Phys.* **2013**, *9* (6), 329−340.

(6) Clavero, C. Plasmon-induced hot-electron generation at nanoparticle/metal-oxide interfaces for photovoltaic and photocatalytic devices. *Nat. Photonics* **2014**, *8* (2), 95−103.

(7) Chen, W.; Zhang, S. P.; Kang, M.; Liu, W. K.; Ou, Z. W.; Li, Y.; Zhang, Y. X.; Guan, Z. Q.; Xu, H. X. Probing the limits of plasmonic enhancement using a two-dimensional atomic crystal probe. *Light: Sci. Appl.* **2018**, *7*, 56.

(8) Chikkaraddy, R.; de Nijs, B.; Benz, F.; Barrow, S. J.; Scherman, O. A.; Rosta, E.; Demetriadou, A.; Fox, P.; Hess, O.; Baumberg, J. J. Single-molecule strong coupling at room temperature in plasmonic nanocavities. *Nature* **2016**, *535* (7610), 127−130.

(9) Kongsuwan, N.; Demetriadou, A.; Chikkaraddy, R.; Benz, F.; Turek, V. A.; Keyser, U. F.; Baumberg, J. J.; Hess, O. Suppressed Quenching and Strong-Coupling of Purcell-Enhanced Single-Molecule Emission in Plasmonic Nanocavities. *ACS Photonics* **2018**, *5* (1), 186−191.

(10) Hajisalem, G.; Nezami, M. S.; Gordon, R. Probing the Quantum Tunneling Limit of Plasmonic Enhancement by Third Harmonic Generation. *Nano Lett.* **2014**, *14* (11), 6651−6654.

DOI: 10.1021/acs.nanolett.9b04335
Nano Lett. 2020, 20, 592−598

(11) Oulton, R. F.; Sorger, V. J.; Zentgraf, T.; Ma, R. M.; Gladden, C.; Dai, L.; Bartal, G.; Zhang, X. Plasmon lasers at deep subwavelength scale. *Nature* **2009**, *461* (7264), 629−632.
(12) Ding, F.; Yang, Y. Q.; Deshpande, R. A.; Bozhevolnyi, S. I. A review of gap-surface plasmon metasurfaces: fundamentals and applications. *Nanophotonics* **2018**, *7* (6), 1129−1156.
(13) Huber, A. J.; Ocelic, N.; Hillenbrand, R. Local excitation and interference of surface phonon polaritons studied by near-field infrared microscopy. *J. Microsc.* **2008**, *229* (3), 389−395.
(14) Zhang, S. P.; Bao, K.; Halas, N. J.; Xu, H. X.; Nordlander, P. Substrate-Induced Fano Resonances of a Plasmonic: Nanocube: A Route to Increased-Sensitivity Localized Surface Plasmon Resonance Sensors Revealed. *Nano Lett.* **2011**, *11* (4), 1657−1663.
(15) Lei, D. Y.; Fernandez-Dominguez, A. I.; Sonnefraud, Y.; Appavoo, K.; Haglund, R. F.; Pendry, J. B.; Maier, S. A. Revealing Plasmonic Gap Modes in Particle-on-Film Systems Using Dark-Field Spectroscopy. *ACS Nano* **2012**, *6* (2), 1380−1386.
(16) Yu, B. X.; Woo, J.; Kong, M.; O'Carroll, D. M. Mode-specific study of nanoparticle-mediated optical interactions in an absorber/metal thin film system. *Nanoscale* **2015**, *7* (31), 13196−13206.
(17) Yamamoto, N.; Ohtani, S.; García de Abajo, F. J. Gap and Mie Plasmons in Individual Silver Nanospheres near a Silver Surface. *Nano Lett.* **2011**, *11* (1), 91−95.
(18) Guzzinati, G.; Beche, A.; Lourenco-Martins, H.; Martin, J.; Kociak, M.; Verbeeck, J. Probing the symmetry of the potential of localized surface plasmon resonances with phase-shaped electron beams. *Nat. Commun.* **2017**, *8*, 14999.
(19) Feist, A.; Echternkamp, K.; Schauss, J.; Yalunin, S.; Schafer, S.; Ropers, C. Quantum coherent optical phase modulation in an ultrafast transmission electron microscope. *Nature* **2015**, *521* (7551), 200−203.
(20) Yamamoto, N.; Suzuki, T. Conversion of surface plasmon polaritons to light by a surface step. *Appl. Phys. Lett.* **2008**, *93* (9), 093114.
(21) Kociak, M.; Zagonel, L. Cathodoluminescence in the scanning transmission electron microscope. *Ultramicroscopy* **2017**, *174*, 50−50.
(22) Kociak, M.; Stephan, O. Mapping plasmons at the nanometer scale in an electron microscope. *Chem. Soc. Rev.* **2014**, *43* (11), 3865−3883.
(23) Polman, A.; Kociak, M.; García de Abajo, F. J. Electron-beam spectroscopy for nanophotonics. *Nat. Mater.* **2019**, *18* (11), 1158−1171.
(24) Sannomiya, T.; Saito, H.; Junesch, J.; Yamamoto, N. Coupling of Plasmonic Nanopore Pairs: Facing Dipoles Attract Each Other. *Light: Sci. Appl.* **2016**, *5*, No. e16146.
(25) Yamamoto, N. Development of high-resolution cathodoluminescence system for STEM and application to plasmonic nanostructures. *Microscopy* **2016**, *65* (4), 282−295.
(26) Fischer, U. C.; Pohl, D. W. Observation of Single-Particle Plasmons by Near-Field Optical Microscopy. *Phys. Rev. Lett.* **1989**, *62* (4), 458−461.
(27) Mills, D. L. Attenuation of surface plaritons by surface-roughness. *Phys. Rev. B* **1975**, *12* (10), 4036−4046.
(28) Kolomenski, A.; Kolomenskii, A.; Noel, J.; Peng, S. Y.; Schuessler, H. Propagation length of surface plasmons in a metal film with roughness. *Appl. Opt.* **2009**, *48* (30), 5683−5691.
(29) García de Abajo, F. J. Optical excitations in electron microscopy. *Rev. Mod. Phys.* **2010**, *82* (1), 209−275.
(30) Kuttge, M.; Vesseur, E. J. R.; Koenderink, A. F.; Lezec, H. J.; Atwater, H. A.; García de Abajo, F. J.; Polman, A. Local density of states, spectrum, and far-field interference of surface plasmon polaritons probed by cathodoluminescence. *Phys. Rev. B: Condens. Matter Mater. Phys.* **2009**, *79* (11), 113405.
(31) Thollar, Z.; Wadell, C.; Matsukata, T.; Yamamoto, N.; Sannomiya, T. Three-Dimensional Multipole Rotation in Spherical Silver Nanoparticles Observed by Cathodoluminescence. *ACS Photonics* **2018**, *5* (7), 2555−2560.
(32) Kuhler, P.; García de Abajo, F. J.; Solis, J.; Mosbacher, M.; Leiderer, P.; Afonso, C. N.; Siegel, J. Imprinting the Optical Near Field of Microstructures with Nanometer Resotution. *Small* **2009**, *5* (16), 1825−1829.
(33) Zhang, S.; Genov, D. A.; Wang, Y.; Liu, M.; Zhang, X. Plasmon-induced transparency in metamaterials. *Phys. Rev. Lett.* **2008**, *101* (4), No. 047401.
(34) Farhang, A.; Bigler, N.; Martin, O. J. F. Coupling of multiple LSP and SPP resonances: interactions between an elongated nanoparticle and a thin metallic film. *Opt. Lett.* **2013**, *38* (22), 4758−4761.
(35) Koppens, F. H. L.; Chang, D. E.; García de Abajo, F. J. Graphene Plasmonics: A Platform for Strong Light-Matter Interactions. *Nano Lett.* **2011**, *11* (8), 3370−3377.
(36) Rindzevicius, T.; Alaverdyan, Y.; Sepulveda, B.; Pakizeh, T.; Kall, M.; Hillenbrand, R.; Aizpurua, J.; García de Abajo, F. J. Nanohole plasmons in optically thin gold films. *J. Phys. Chem. C* **2007**, *111* (3), 1207−1212.

DOI: 10.1021/acs.nanolett.9b04335
Nano Lett. 2020, 20, 592−598

ACS Photonics
pubs.acs.org/journal/apchd5
Article

Nanoscale Nonlinear Spectroscopy with Electron Beams

Andrea Konečná, Valerio Di Giulio, Vahagn Mkhitaryan, Claus Ropers, and F. Javier García de Abajo*

Cite This: ACS Photonics 2020, 7, 1290−1296
Read Online
ACCESS | Metrics & More | Article Recommendations | Supporting Information

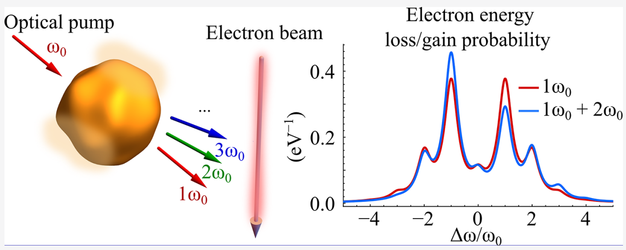

ABSTRACT: We theoretically demonstrate the ability of electron beams to probe the nonlinear photonic response with nanometer spatial resolution, well beyond the capabilities of existing optical techniques. Although the interaction of electron beams with photonic modes is generally weak, the use of optical pumping produces stimulated electron−light interactions that can exceed order-unity probabilities in photon-induded near field electron microscopy (PINEM). Here, we demonstrate that PINEM can locally and quantitatively probe the nonlinear optical response. Specifically, we predict a dependence of PINEM electron spectra on the sample nonlinearity that can reveal the second-harmonic (SH) response of optical materials with nanometer resolution, observed through asymmetries between electron energy losses and gains. We illustrate this concept by showing that PINEM spectra are sensitive to the SH near field of centrosymmetric structures and by finding substantial spectral asymmetries in geometries for which the linear interaction is reduced.

KEYWORDS: *photon-induced near field electron microscopy (PINEM), electron energy-loss spectroscopy (EELS), nonlinear optics, second-harmonic generation, ultrafast optics*

Electron microscope spectroscopies have evolved into a powerful set of techniques capable of providing structural and dynamical information on materials with nanometer/femtosecond/meV space/time/energy resolution.[1−23] In particular, low-loss electron energy-loss spectroscopy (EELS) can nowadays access local spectral information on plasmons in metallic nanostructures,[24−29] excitons in semiconductors,[30] phonons in ionic crystals[5,14] and graphene,[31] and atomic vibrations in molecules.[22,32] Additionally, ultrafast temporal resolution is achieved in PINEM by synchronizing the time of arrival of femtosecond electron and optical pulses at the sample.[2−4,6−12,15−21] Recent proposals further extend light−matter interactions in PINEM to produce attosecond electron pulses,[15,33] electron entanglement,[34] probe photon statistics,[35] and perform quantum computations.[36]

The high spatial resolution enabled by electron beams could also find application in the mapping of the nonlinear optical response in nanostructures, which is important from both fundamental and applied viewpoints to better understand and improve the performance of nonlinear nanophotonic devices.[37−39] However, despite the widespread use of electron-beam spectroscopies to characterize the linear response of nanomaterials, the higher-order nonlinear response is generally considered unreachable because of the weak interaction between individual beamed electrons and sample excitations. This scenario is substantially changed in PINEM, where sample modes are populated through external optical pumping to high occupation numbers that can yield scattering probabilities exceeding order unity, effectively resulting in multiple quanta exchanges between the electron probe and the optical field, observed to generate up to hundreds of loss and gain orders.[20,21] Additionally, the femtosecond duration of both electron and optical pulses allows employing high light intensities that can trigger substantial nonlinearities without damaging the sample. The prospects are therefore excellent for

Received: February 29, 2020
Published: April 9, 2020

https://dx.doi.org/10.1021/acsphotonics.0c00326
ACS Photonics 2020, 7, 1290−1296

ACS Photonics pubs.acs.org/journal/apchd5 Article

the use of PINEM to probe the nonlinear optical response of materials at length scales determined by the subnanometer transversal size of focused electron beams, for example to help unveil fundamental aspects of high-harmonic generation, such as its interplay with nonlocal and quantum-confinement effects at metallic sample boundaries.[40] PINEM could thus lead to a radical improvement in terms of noninvasiveness, intrinsic phase sensitivity, and spatial resolution compared to existing nonlinear characterization techniques relying on either far-[41,42] or near-field[41,43−47] optics.

In this Article, we theoretically demonstrate the potential of PINEM to quantitatively probe the nonlinear optical response with nanometer spatial resolution. Specifically, we focus on the sampling of SH fields, which are revealed as asymmetries in the PINEM spectra. We illustrate this concept by first considering spherical gold nanoparticles, which, despite their centrosymmetry, display an evanescent SH near field that gives rise to substantially modified transmission electron spectra under attainable ultrafast illumination intensities below the damage threshold. We further explore the interaction with nanorods as an example of configuration in which linear-field coupling is strongly reduced, further increasing the spectral asymmetry to the 10% level. Our results support PINEM performed with variable illumination frequency as a nonlinear optical characterization technique with unsurpassed combination of spatial and spectral resolution.

Energy-momentum mismatch prevents absorption or emission of photons by electrons in free space. In contrast, translational-symmetry breaking in illuminated nanostructures enables such coupling,[48,49] which is mediated by near-field components that give rise to multiple exchanges of photons between the electron and the optical field (Figure 1). More precisely, when neglecting nonlinear optical fields, the electron−light interaction is fully captured by the parameter[3,4,50] $\beta_1 = (e/\hbar\omega_0)\int dz\, E_z^{(1)} e^{-i\omega_0 z/v}$, where $E_z^{(1)}$ is the linear electric field component along the direction of the electron velocity $\mathbf{v} = v\hat{\mathbf{z}}$ (i.e., for illumination with a time-dependent external light field $\mathbf{E}^{ext}(t) = 2\mathrm{Re}\{\mathbf{E}^{ext} e^{-i\omega_0 t}\}$), integrated over positions z along the electron trajectory, and ω_0 is the light frequency. The transmitted electron spectrum is then characterized by loss ($l < 0$) and gain ($l > 0$) peaks (electron energy change $l\hbar\omega_0$) of integrated probability $P_l = J_l^2(2|\beta_1|)$ defined in terms of Bessel functions J_l (Figure 1, red curve). We remark that, although multiple peaks are produced in the spectrum (i.e., electron−light interaction is nonlinear), the interaction is fully controlled by the single parameter β_1, which is linear in the electric field (i.e., light−sample interaction is linear).

As we show below, the nonlinear response associated with the nanostructure can produce near fields at frequencies that are multiples of ω_0 and result in asymmetries of the electron spectrum (Figure 1, blue curve) like those observed under external illumination consisting of superimposed harmonics.[15] In what follows, we focus on gold nanoparticles, in which the bulk second-order nonlinear response cancels due to inversion symmetry of the crystal lattice, while the surface SH response is relatively large compared with other materials[42,51−54] and can be substantially enhanced due to field amplification mediated by surface plasmons.[37−39] For simplicity, we neglect higher-order nonlinear terms, which should be comparatively smaller under the conditions considered below.

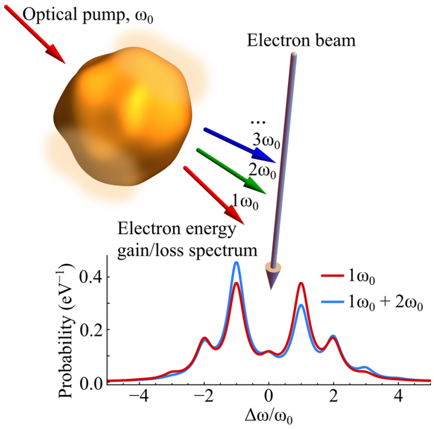

Figure 1. Nanoscale sampling of the nonlinear optical response. An optical pump at the sampling frequency ω_0 illuminates a nanoparticle in coincidence with the arrival of a focused electron. If the particle responds linearly, the EELS spectrum presents a symmetric distribution of stimulated loss ($\omega > 0$) and gain ($\omega < 0$) features (red curve). Nonlinear response in the particle generally produces harmonic optical fields at multiples of ω_0, which are revealed through an asymmetric EELS spectrum (blue curve). We illustrate this effect by taking $|\beta_1| = 1$, $|\beta_2| = 0.1$, $\delta = 0$, $\hbar\omega_0 = 1$ eV, and a Lorentzian broadening of 0.6 eV fwhm (see main text).

RESULTS AND DISCUSSION

Theoretical Description of Nonlinear PINEM. We extend previously developed PINEM theory[3,4,50] to incorporate both the fundamental and SH fields in the electron−light interaction. While previous works have already considered superimposing fundamental and higher-harmonic excitation fields in PINEM,[15] we now focus on the intrinsic fundamental and SH response generated in the sample itself. In our theoretical approach, we consider an incident electron with small energy and momentum spread relative to central values E_0 and $\hbar\mathbf{k}_0$, so that its wave function can be written as $\psi(\mathbf{r},t) = e^{i(\mathbf{k}_0\cdot\mathbf{r}-E_0 t/\hbar)}\phi_0(\mathbf{r},t)$ in terms of a smooth function $\phi_0(\mathbf{r}, t)$ that undergoes only small variations over each optical period. After PINEM interaction, the transmitted electron wave function is given by this expression with ϕ_0 replaced by $\phi = \phi_0 \sum_l f_l e^{il\omega_0(z/v-t)}$, where the electron is taken to move along z and the sum extends over components associated with an effective number of exchanged photons l (>0 for gain and <0 for loss). The amplitudes of these components are found to be (see Supporting Information (SI))

$$f_l = e^{il\arg\{-\beta_1\}} \sum_{n=-\infty}^{\infty} e^{-in\delta} J_{l+2n}(2|\beta_1|) J_n(2|\beta_2|)$$

where

$$\beta_j = \frac{e}{\hbar j\omega_0}\int_{-\infty}^{\infty} dz\, E_z^{(j)}(\mathbf{R}_0, z) e^{-ij\omega_0 z/v} \tag{1}$$

describes the interaction with the fundamental ($j = 1$) and SH ($j = 2$) fields of frequency $j\omega_0$,

https://dx.doi.org/10.1021/acsphotonics.0c00326
ACS Photonics 2020, 7, 1290−1296

ACS Photonics pubs.acs.org/journal/apchd5 Article

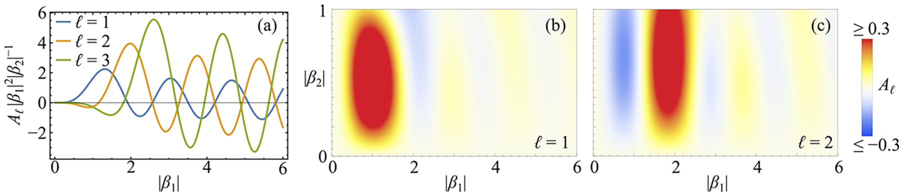

Figure 2. Second-harmonic-induced asymmetry in the PINEM spectra. We plot the asymmetry parameter A_l (eq 4) in the $|\beta_2| \ll 1$ limit (a) and for larger values of this parameter (b). We consider selected sideband orders l and take $\delta = 0$.

$$\delta = \arg\{\beta_2\} - 2\arg\{\beta_1\} \tag{2}$$

captures the dependence on the relative phase of both j fields, and the impact parameter $\mathbf{R}_0 = (x_0, y_0)$ defines the position of the electron beam under the assumption that its transversal size is small compared with the optical fields under consideration. The probability associated with an electron energy change $l\hbar\omega_0$ is simply given by $P_l = |f_l|^2$, which obviously depends on the coupling strengths $|\beta_j|$, but also on the phase difference δ. Incidentally, eqs 1 and 2 predict a phase δ independent of any displacement in the position z of the field relative to the electron wave function.

In practice, we expect to deal with small values of the SH coupling coefficient $|\beta_2|$, for which the probability of the sideband l reduces to

$$P_l = J_l^2(2|\beta_1|) + |\beta_2| C_l(2|\beta_1|)\cos\delta \tag{3}$$

where $C_l(x) = 2J_l(x)[J_{l+2}(x) - J_{l-2}(x)]$ (see SI). This expression shows that P_l deviates maximally from the linear PINEM regime when δ is a multiple of π, a result that is also maintained for arbitrarily large values of $|\beta_2|$ (see SI). Importantly, SH components enter the PINEM probability through a linear correction in the SH field amplitude instead of its intensity, thus facilitating the determination of the nonlinear material response for the expected low values of $|\beta_2|$. Additionally, when the linear PINEM coefficient vanishes ($\beta_1 = 0$), one obtains a regular PINEM spectrum with sidebands separated by $2\hbar\omega_0$, as determined by the SH coupling coefficient β_2, which for $|\beta_2| \ll 1$ produces probabilities $P_l \approx |\beta_2|^{2l}/l!^2$.

As a way of capturing the spectral asymmetry observed in Figure 1 due to nonlinear interactions, we define the parameter

$$A_l = P_l - P_{-l} \tag{4}$$

(difference between gain and loss probabilities in sidebands l and $-l$), which for small $|\beta_2|$, using eq 3, becomes $A_l \propto |\beta_2/\beta_1^2|$, with a coefficient of proportionality $2|\beta_1|^2 C_l(|\beta_1|)\cos\delta$ that depends on the illumination intensity. Obviously, the ratio $|\beta_2/\beta_1^2|$ is independent of light intensity, therefore facilitating the determination of the nonlinear SH response upon direct inspection of the asymmetry parameters A_l. Additionally, the order l that is best suited to resolve the nonlinear behavior depends on the range of $|\beta_1|$, as shown in Figure 2a for small $|\beta_2|$ and Figure 2b,c for a larger range of this parameter.

In what follows, we calculate the SH field by considering a distribution of surface dipoles oriented along the local surface normal $\hat{\mathbf{n}}_s$ with a polarizability per unit area at each surface position $\mathbf{s}$ given by[55]

$$\mathbf{P}_s^{(2)} = \chi_{\perp\perp\perp}[\hat{\mathbf{n}}_s \cdot \mathbf{E}^{(1)}(\mathbf{s})]^2 \hat{\mathbf{n}}_s \tag{5}$$

where $\chi_{\perp\perp\perp}$ is the dominant component of the SH surface susceptibility (other tensor components are negligible in metals[55−58]), and the linear field $\mathbf{E}^{(1)}$ needs to be evaluated for the illumination frequency ω_0 at a point immediately inside the metal. We obtain $\mathbf{E}^{(1)}$ by solving Maxwell's equations with a light plane wave as a source and the gold described through its tabulated frequency-dependent dielectric function.[59] From here, we obtain the SH field $\mathbf{E}^{(2)}$ by again solving those equations with the surface dipole distribution (eq 5) as a source. These fields are then inserted into eq 1 to produce the coupling parameters β_j. Incidentally, the SH field entering β_2 is equivalently obtained using the reciprocity theorem from the field produced by the passing electron at frequency $2\omega_0$ on the particle surface, which results in a substantial reduction of computation time (see SI).

Probing the Second-Harmonic Near Field in Centrosymmetric Structures. Although inversion symmetry prevents far-field SH generation, an evanescent field at frequency $2\omega_0$ can still exist in the vicinity of such illuminated nanostructures and interact with a passing electron to produce PINEM asymmetries. We illustrate this possibility by considering a spherical gold nanoparticle (Figure 3) based on an analytical solution of this problem in the quasistatic limit (see details in SI), which, given the small diameter of the particle under consideration (20 nm), we find to be in excellent agreement with numerically obtained retarded calculations. As expected,[60−62] the linear near field exhibits a characteristic dipolar pattern oriented along the incident polarization, while the SH field displays a quadrupolar profile (Figure 3a). Additionally, a prominent ∼2.4 eV particle plasmon is observed in the spectral dependence of both linear and SH near fields (Figure 3b), with maximum intensity at the sphere poles.

For a 100 keV electron passing 2 nm away from the upper pole, we obtain a regular PINEM spectral profile describable through the probabilities $J_l^2(2|\beta_1|)$ when neglecting nonlinear effects (Figure 3c), while inclusion of SH response produces a substantial asymmetry (Figure 3d), thus corroborating that the electron can indeed sample SH near fields despite the symmetry of the particle. Considering a typical laser fluence damage threshold $\sim 10^2$ J/m^2 for small Au nanoparticles,[63] we estimate feasible laser pulse durations down to 100 fs. We also note that larger spheres could be interesting samples to investigate the interplay between high-harmonic generation and excitation of high-order plasmonic modes, which can be efficiently probed by a tightly focused electron beam passing close to the sphere surface.

https://dx.doi.org/10.1021/acsphotonics.0c00326
ACS Photonics 2020, 7, 1290−1296

ACS Photonics pubs.acs.org/journal/apchd5 Article

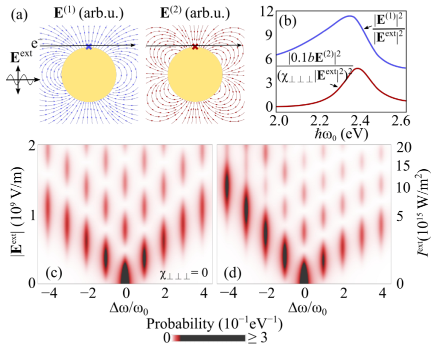

Figure 3. PINEM sampling of the second-harmonic near field in a gold sphere. (a) A linearly polarized light plane wave (external field $\mathbf{E}^{\rm ext}$, frequency ω_0) excites a gold sphere (20 nm diameteter) giving rise to induced fields $\mathbf{E}^{(1)}$ and $\mathbf{E}^{(2)}$ at the fundamental (ω_0) and SH ($2\omega_0$) frequencies, respectively. We show electric field lines outside the particle in the plane defined by the light polarization and propagation directions for $\hbar\omega_0$ = 2.4 eV. (b) Spectral dependence of the linear (blue curve) and SH (red curve) near-field intensity at the position of the crosses (distance b = 2 nm from the surface), normalized by using $|\mathbf{E}^{\rm ext}|$, the SH susceptibility $\chi_{\perp\perp\perp}$, and the distance b. (c) Spectral and light-field-amplitude (left vertical scale) and intensity (right scale) dependence of the PINEM electron probability for $\hbar\omega_0$ = 2.4 eV in the absence of nonlinear particle response ($\chi_{\perp\perp\perp}$ = 0) for 100 keV electrons passing 2 nm outside the surface along the trajectory indicated by the black arrows in (a). (d) Same as (c), but including SH fields for a typical nonlinear susceptibility[S6,S7] $\chi_{\perp\perp\perp}$ = 10^{-18} m^2/V. We introduce in (c,d) a Lorentzian broadening of 0.6 eV fwhm that represents a finite energy spread of the electron beam already demonstrated in PINEM;[13] Figure S2 in SI further demonstrates that the spectral asymmetry is still clearly discernible even with 2 eV fwhm broadening.

Effect of Cancellation of Linear PINEM. By virtue of symmetry, β_1 should vanish for an electron passing through the center of a gold nanorod under the orientation and illumination conditions shown in Figure 4a. By numerically calculating the β_j coefficients as described above (from retarded field simulations), we indeed observe a vanishing of β_1 for the central trajectory (Figure 4b,c), while $|\beta_2|$ takes sizable values even for a moderate, experimentally feasible incident light amplitude $<10^8$ V/m (i.e., light intensity $\lesssim 5 \times 10^{13}$ W/m^2).[7] When moving the electron beam away from the rod center, the coupling coefficients change significantly, but in all cases display a prominent $\approx$1.63 eV spectral feature associated with the rod dipolar plasmon (Figure 4b). In the central trajectory, although $\beta_1 = 0$, the nonzero β_2 produces a symmetric spectrum with small integrated inelastic probability $\propto |\beta_2|^2$ (see above). It is therefore convenient to have a suitable nonzero value of $|\beta_1|$ to better observe nonlinear effects (see Figure 2). Such a regime can be reached for beam positions slightly off the rod center, as shown in Figure 4c as the electron beam is scanned along the rod for illumination on resonance with the dipolar rod plasmon. Remarkably, the resulting spectral asymmetry reaches $A_1 \sim -10\%$ in the first sideband (Figure 4d) under the considered realistic conditions.

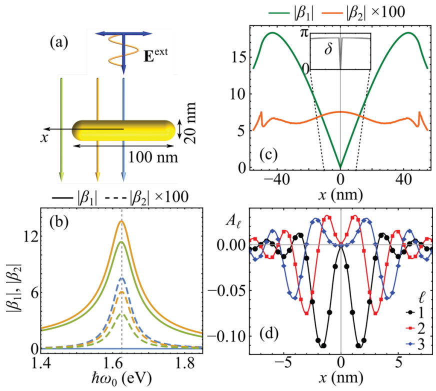

Figure 4. Spatial dependence of nonlinear PINEM. (a) We consider a gold nanorod (100 nm long, 20 nm thick, hemispherical caps) illuminated with polarization along the particle axis. (b) Absolute values of the coupling coefficients $|\beta_1|$ (solid curves) and $|\beta_2|$ (dashed curves) as a function of light frequency ω_0 for electron beams (100 keV) crossing the rod axis at the positions indicated by the color-coordinated downward arrows in (a), external field amplitude $|\mathbf{E}^{\rm ext}|$ = 5×10^7 V/m (i.e., light intensity 1.3×10^{13} W/m^2), and SH surface susceptibility $\chi_{\perp\perp\perp}$ = 10^{-18} m^2/V. (c) Electron-beam-position dependence of $|\beta_1|$ (green) and $|\beta_2|$ (orange) for $\hbar\omega_0 \approx 1.63$ eV on resonance with the dipolar rod plasmon. The inset shows the phase δ close to the rod center. (d) Asymmetry parameter A_ℓ extracted from (c) near the rod center.

CONCLUDING REMARKS

In summary, our results support the use of stimulated light-electron interactions near nanostructures to locally and quantitatively probe the nonlinear response of the materials forming them. This idea can directly be implemented through careful analysis of PINEM data using existing microscope setups. Importantly, signatures of the second-harmonic response appear as contributions to the electron spectra scaling linearly with the nonlinear field amplitude, rather than its intensity. Further study is needed to explore the ability of resolving higher-order nonlinear processes. Improvements in the nonlinear detection efficiency could arise by making the electron interact with additional illuminated structures, whereby the linear coupling coefficient β_1 could be manipulated to better resolve the nonlinear contribution β_2.

Combined with tomography through sample and light beam rotation and spatial sampling of the near field, more detailed information on the spatial dependence of the nonlinear response could be also obtained. Exploiting these methods, an interesting possibility is offered by quantum nonlinearites present in Jaynes-Cummings coupling[64] of quantum optical emitters in optical cavities. Nonlinear response from a substrate in the sample could also play a role that needs to be ellucidated. The interplay between nonlinear and quantum-confinement effects could also be investigated with the required spatial resolution enabled by electron beams in order to elucidate anharmonic behavior of conduction electrons near metal surfaces, as well as the role played by nonlocal screening, particularly when high-order modes of

https://dx.doi.org/10.1021/acsphotonics.0c00326
ACS Photonics 2020, 7, 1290−1296

short spatial wavelength are involved. In brief, tightly focused electron beams can facilitate the determination of the optical nonlinear response for small amounts of material with unprecedented spatial resolution using currently available ultrafast electron microscopes.

■ ASSOCIATED CONTENT

Supporting Information

The Supporting Information is available free of charge at https://pubs.acs.org/doi/10.1021/acsphotonics.0c00326.

> Sections S1–S4: Details on the theory of nonlinear PINEM, including an analytical derivation of the β_1 and β_2 coefficients for a spherical particle in the quasistatic limit and a comparison with retarded numerical simulations. Figure S1: Comparison of analytical and numerical solutions for the coupling coefficients corresponding to the spherical particle from Figure 3. Figure S2: Influence of initial electron energy broadening on PINEM spectra (PDF)

■ AUTHOR INFORMATION

Corresponding Author

F. Javier García de Abajo – *ICFO-Institut de Ciencies Fotoniques, The Barcelona Institute of Science and Technology, 08860 Castelldefels, Barcelona, Spain; ICREA-Institució Catalana de Recerca i Estudis Avançats, 08010 Barcelona, Spain;* orcid.org/0000-0002-4970-4565; Email: javier.garciadeabajo@nanophotonics.es

Authors

Andrea Konečná – *ICFO-Institut de Ciencies Fotoniques, The Barcelona Institute of Science and Technology, 08860 Castelldefels, Barcelona, Spain;* orcid.org/0000-0002-7423-5481

Valerio Di Giulio – *ICFO-Institut de Ciencies Fotoniques, The Barcelona Institute of Science and Technology, 08860 Castelldefels, Barcelona, Spain*

Vahagn Mkhitaryan – *ICFO-Institut de Ciencies Fotoniques, The Barcelona Institute of Science and Technology, 08860 Castelldefels, Barcelona, Spain*

Claus Ropers – *fourth Physical Institute-Solids and Nanostructures, University of Gottingen, Göttingen 37077, Germany*

Complete contact information is available at: https://pubs.acs.org/10.1021/acsphotonics.0c00326

Notes

The authors declare no competing financial interest.

■ ACKNOWLEDGMENTS

We thank A. Feist, K. E. Priebe, and S.V. Yalunin for stimulating discussions. This work has been supported in part by ERC (Advanced Grant 789104-eNANO), the Spanish MINECO (MAT2017-88492-R and SEV2015-0522), the Catalan CERCA Program, Fundació Privada Cellex, and the Deutsche Forschungsgemeinschaft (SFB 1073, Project A05). V.D.G. acknowledges support from the EU through a Marie Skłodowska-Curie grant (COFUND-DP, H2020-MSCA-CO-FUND-2014, GA n 665884).

■ REFERENCES

(1) Egerton, R. F. *Electron Energy-Loss Spectroscopy in the Electron Microscope*; Plenum Press: New York, 1996.

(2) Barwick, B.; Flannigan, D. J.; Zewail, A. H. Photon-Induced Near-Field Electron Microscopy. *Nature* **2009**, *462*, 902–906.

(3) García de Abajo, F. J.; Asenjo Garcia, A.; Kociak, M. Multiphoton Absorption and Emission by Interaction of Swift Electrons with Evanescent Light Fields. *Nano Lett.* **2010**, *10*, 1859–1863.

(4) Park, S. T.; Lin, M.; Zewail, A. H. Photon-Induced Near-Field Electron Microscopy (PINEM): Theoretical and Experimental. *New J. Phys.* **2010**, *12*, 123028.

(5) Krivanek, O. L.; Lovejoy, T. C.; Dellby, N.; Aoki, T.; Carpenter, R. W.; Rez, P.; Soignard, E.; Zhu, J.; Batson, P. E.; Lagos, M. J.; Egerton, R. F.; Crozier, P. A. Vibrational Spectroscopy in the Electron Microscope. *Nature* **2014**, *514*, 209–214.

(6) Kirchner, F. O.; Gliserin, A.; Krausz, F.; Baum, P. Laser Streaking of Free Electrons at 25 keV. *Nat. Photonics* **2014**, *8*, 52–57.

(7) Feist, A.; Echternkamp, K. E.; Schauss, J.; Yalunin, S. V.; Schäfer, S.; Ropers, C. Quantum Coherent Optical Phase Modulation in an Ultrafast Transmission Electron Microscope. *Nature* **2015**, *521*, 200–203.

(8) Piazza, L.; Lummen, T. T. A.; Quiñonez, E.; Murooka, Y.; Reed, B.; Barwick, B.; Carbone, F. Simultaneous Observation of the Quantization and the Interference Pattern of a Plasmonic Near-Field. *Nat. Commun.* **2015**, *6*, 6407.

(9) Echternkamp, K. E.; Feist, A.; Schäfer, S.; Ropers, C. Ramsey-Type Phase Control of Free-Electron Beams. *Nat. Phys.* **2016**, *12*, 1000–1004.

(10) Ryabov, A.; Baum, P. Electron Microscopy of Electromagnetic Waveforms. *Science* **2016**, *353*, 374–377.

(11) Vanacore, G. M.; Fitzpatrick, A. W. P.; Zewail, A. H. Four-Dimensional Electron Microscopy: Ultrafast Imaging, Diffraction and Spectroscopy in Materials Science and Biology. *Nano Today* **2016**, *11*, 228–249.

(12) Kozák, M.; McNeur, J.; Leedle, K. J.; Deng, H.; Schönenberger, N.; Ruehl, A.; Hartl, I.; Harris, J. S.; Byer, R. L.; Hommelhoff, P. Optical Gating and Streaking of Free Electrons with Sub-Optical Cycle Precision. *Nat. Commun.* **2017**, *8*, 14342.

(13) Feist, A.; Bach, N.; Rubiano da Silva, N.; Danz, T.; Moller, M.; Priebe, K. E.; Domrose, T.; Gatzmann, J. G.; Rost, S.; Schauss, J.; Strauch, S.; Bormann, R.; Sivis, M.; Schafer, S.; Ropers, C. Ultrafast Transmission Electron Microscopy Using a Laser-Driven Field Emitter: Femtosecond Resolution with a High Coherence Electron Beam. *Ultramicroscopy* **2017**, *176*, 63–73.

(14) Lagos, M. J.; Trügler, A.; Hohenester, U.; Batson, P. E. Mapping Vibrational Surface and Bulk Modes in a Single Nanocube. *Nature* **2017**, *543*, 529–532.

(15) Priebe, K. E.; Rathje, C.; Yalunin, S. V.; Hohage, T.; Feist, A.; Schäfer, S.; Ropers, C. Attosecond Electron Pulse Trains and Quantum State Reconstruction in Ultrafast Transmission Electron Microscopy. *Nat. Photonics* **2017**, *11*, 793–797.

(16) Pomarico, E.; Madan, I.; Berruto, G.; Vanacore, G. M.; Wang, K.; Kaminer, I.; García de Abajo, F. J.; Carbone, F. meV Resolution in Laser-Assisted Energy-Filtered Transmission Electron Microscopy. *ACS Photonics* **2018**, *5*, 759–764.

(17) Vanacore, G. M.; Madan, I.; Berruto, G.; Wang, K.; Pomarico, E.; Lamb, R. J.; McGrouther, D.; Kaminer, I.; Barwick, B.; García de Abajo, F. J.; Carbone, F. Attosecond Coherent Control of Free-Electron Wave Functions Using Semi-Infinite Light Fields. *Nat. Commun.* **2018**, *9*, 2694.

(18) Vanacore, G. M.; Berruto, G.; Madan, I.; Pomarico, E.; Biagioni, P.; Lamb, R. J.; McGrouther, D.; Reinhardt, O.; Kaminer, I.; Barwick, B.; Larocque, H.; Grillo, V.; Karimi, E.; García de Abajo, F. J.; Carbone, F. Ultrafast Generation and Control of an Electron Vortex Beam via Chiral Plasmonic Near Fields. *Nat. Mater.* **2019**, *18*, 573–579.

(19) Wang, K.; Dahan, R.; Shentcis, M.; Kauffmann, Y.; Tsesses, S.; Kaminer, I. Coherent Interaction between Free Electrons and Cavity Photons. *arXiv:1908.06206* **2019**, na.

(20) Kfir, O.; Lourenço-Martins, H.; Storeck, G.; Sivis, M.; Harvey, T. R.; Kippenberg, T. J.; Feist, A.; Ropers, C. Controlling Free Electrons with Optical Whispering-Gallery Modes. *arXiv:1910.09540* **2019**, na.

(21) Dahan, R.; Nehemia, S.; Shentcis, M.; Reinhardt, O.; Adiv, Y.; Wang, K.; Beer, O.; Kurman, Y.; Shi, X.; Lynch, M. H.; Kaminer, I. Observation of the Stimulated Quantum Cherenkov Effect. *arXiv:1909.00757* **2019**, na.

(22) Hachtel, J. A.; Huang, J.; Popovs, I.; Jansone-Popova, S.; Keum, J. K.; Jakowski, J.; Lovejoy, T. C.; Dellby, N.; Krivanek, O. L.; Idrobo, J. C. Identification of Site-Specific Isotopic Labels by Vibrational Spectroscopy in the Electron Microscope. *Science* **2019**, *363*, 525−528.

(23) Polman, A.; Kociak, M.; García de Abajo, F. J. Electron-Beam Spectroscopy for Nanophotonics. *Nat. Mater.* **2019**, *18*, 1158−1171.

(24) García de Abajo, F. J. Optical Excitations in Electron Microscopy. *Rev. Mod. Phys.* **2010**, *82*, 209−275.

(25) Rossouw, D.; Botton, G. A. Plasmonic Response of Bent Silver Nanowires for Nanophotonic Subwavelength Waveguiding. *Phys. Rev. Lett.* **2013**, *110*, 066801.

(26) Kociak, M.; Stephan, O. Mapping Plasmons at the Nanometer Scale in an Electron Microscope. *Chem. Soc. Rev.* **2014**, *43*, 3865−3883.

(27) Horl, A.; Trugler, A.; Hohenester, U. Full Three-Dimensonal Reconstruction of the Dyadic Green Tensor from Electron Energy Loss Spectroscopy of Plasmonic Nanoparticles. *ACS Photonics* **2015**, *2*, 1429−1435.

(28) Guzzinati, G.; Beche, A.; Lourenco-Martins, H.; Martin, J.; Kociak, M.; Verbeeck, J. Probing the Symmetry of the Potential of Localized Surface Plasmon Resonances with Phase-Shaped Electron Beams. *Nat. Commun.* **2017**, *8*, 14999.

(29) Krehl, J.; Guzzinati, G.; Schultz, J.; Potapov, P.; Pohl, D.; Martin, J.; Verbeeck, J.; Fery, A.; Büchner, B.; Lubk, A. Spectral Field Mapping in Plasmonic Nanostructures with Nanometer Resolution. *Nat. Commun.* **2018**, *9*, 4207.

(30) Tizei, L. H. G.; Lin, Y.-C.; Mukai, M.; Sawada, H.; Lu, A.-Y.; Li, L.-J.; Kimoto, K.; Suenaga, K. Exciton Mapping at Subwavelength Scales in Two-Dimensional Materials. *Phys. Rev. Lett.* **2015**, *114*, 107601.

(31) Senga, R.; Suenaga, K.; Barone, P.; Morishita, S.; Mauri, F.; Pichler, T. Position and Momentum Mapping of Vibrations in Graphene Nanostructures in the Electron Microscope. *Nature* **2019**, *573*, 247−250.

(32) Rez, P.; Aoki, T.; March, K.; Gur, D.; Krivanek, O. L.; Dellby, N.; Lovejoy, T. C.; Wolf, S. G.; Cohen, H. Damage-Free Vibrational Spectroscopy of Biological Materials in the Electron Microscope. *Nat. Commun.* **2016**, *7*, 10945.

(33) Morimoto, Y.; Baum, P. Diffraction and Microscopy with Attosecond Electron Pulse Trains. *Nat. Phys.* **2018**, *14*, 252−256.

(34) Kfir, O. Entanglements of Electrons and Cavity Photons in the Strong-Coupling Regime. *Phys. Rev. Lett.* **2019**, *123*, 103602.

(35) Di Giulio, V.; Kociak, M.; García de Abajo, F. J. Probing Quantum Optical Excitations with Fast Electrons. *Optica* **2019**, *6*, 1524−1534.

(36) Reinhardt, O.; Mechel, C.; Lynch, M.; Kaminer, I. Free-Electron Qubits. *arXiv:1907.10281* **2019**, na.

(37) Kauranen, M.; Zayats, A. V. Nonlinear Plasmonics. *Nat. Photonics* **2012**, *6*, 737−748.

(38) Panoiu, N. C.; Sha, W. E. I.; Lei, D. Y.; Li, G.-C. Nonlinear Optics in Plasmonic Nanostructures. *J. Opt.* **2018**, *20*, 083001.

(39) Butet, J.; Brevet, P.-F.; Martin, O. J. F. Optical Second Harmonic Generation in Plasmonic Nanostructures: From Fundamental Principles to Advanced Applications. *ACS Nano* **2015**, *9*, 10545−10562.

(40) Krasavin, A. V.; Ginzburg, P.; Zayats, A. V. Free-electron Optical Nonlinearities in Plasmonic Nanostructures: A Review of the Hydrodynamic Description. *Laser Photonics. Rev.* **2018**, *12*, 1700082.

(41) Bozhevolnyi, S. I.; Pedersen, K.; Skettrup, T.; Zhang, X.; Belmonte, M. Far- and Near-Field Second-Harmonic Imaging of Ferroelectric Domain Walls. *Opt. Commun.* **1998**, *152*, 221−224.

(42) Boyd, R. W. *Nonlinear Opt.*, 3rd ed.; Academic Press: Amsterdam, 2008.

(43) Zayats, A. V.; Sandoghdar, V. Apertureless Scanning Near-Field Second-Harmonic Microscopy. *Opt. Commun.* **2000**, *178*, 245−249.

(44) Bouhelier, A.; Beversluis, M.; Hartschuh, A.; Novotny, L. Near-Field Second-Harmonic Generation Induced by Local Field Enhancement. *Phys. Rev. Lett.* **2003**, *90*, 013903.

(45) Zavelani-Rossi, M.; Celebrano, M.; Biagioni, P.; Polli, D.; Finazzi, M.; Duo, L.; Cerullo, G.; Labardi, M.; Allegrini, M.; Grand, J.; Adam, P.-M. Near-Field Second-Harmonic Generation in Single Gold Nanoparticles. *Appl. Phys. Lett.* **2008**, *92*, 093119.

(46) Neacsu, C. C.; van Aken, B. B.; Fiebig, M.; Raschke, M. B. Second-Harmonic Near-Field Imaging of Ferroelectric Domain Structure of $YMnO_3$. *Phys. Rev. B: Condens. Matter Mater. Phys.* **2009**, *79*, No. 100107.

(47) Metzger, B.; Hentschel, M.; Giessen, H. Probing the Near-Field of Second-Harmonic Light Around Plasmonic Nanoantennas. *Nano Lett.* **2017**, *17*, 1931−1937.

(48) Howie, A. Electrons and Photons: Exploiting the Connection. *Inst. Phys. Conf. Ser.* **1999**, *161*, 311−314.

(49) García de Abajo, F. J.; Kociak, M. Electron Energy-Gain Spectroscopy. *New J. Phys.* **2008**, *10*, 073035.

(50) García de Abajo, F. J.; Barwick, B.; Carbone, F. Electron Diffraction by Plasmon Waves. *Phys. Rev. B: Condens. Matter Mater. Phys.* **2016**, *94*, No. 041404.

(51) Bloembergen, N.; Chang, R. K.; Jha, S. S.; Lee, C. H. Optical Second-Harmonic Generation in Reflection from Media with Inversion Symmetry. *Phys. Rev.* **1968**, *174*, 813−822.

(52) Simon, H. J.; Mitchell, D. E.; Watson, J. G. Optical Second-Harmonic Generation with Surface Plasmons in Silver Films. *Phys. Rev. Lett.* **1974**, *33*, 1531−1534.

(53) Sipe, J. E.; So, V. C. Y.; Fukui, M.; Stegeman, G. I. Analysis of Second-Harmonic Generation at Metal Surfaces. *Phys. Rev. B: Condens. Matter Mater. Phys.* **1980**, *21*, 4389−4402.

(54) Galanty, M.; Shavit, O.; Weissman, A.; Aharon, H.; Gachet, D.; Segal, E.; Salomon, A. Second Harmonic Generation Hotspot on a Centrosymmetric Smooth Silver Surface. *Light: Sci. Appl.* **2018**, *7*, 49.

(55) Bachelier, G.; Butet, J.; Russier-Antoine, I.; Jonin, C.; Benichou, E.; Brevet, P.-F. Origin of Optical Second-Harmonic Generation in Spherical Gold Nanoparticles: Local Surface and Nonlocal Bulk Contributions. *Phys. Rev. B: Condens. Matter Mater. Phys.* **2010**, *82*, 235403.

(56) Krause, D.; Teplin, C. W.; Rogers, C. T. Optical Surface Second Harmonic Measurements of Isotropic Thin-Film Metals: Gold, Silver, Copper, Aluminum, and Tantalum. *J. Appl. Phys.* **2004**, *96*, 3626−3634.

(57) Wang, F. X.; Rodríguez, F. J.; Albers, W. M.; Ahorinta, R.; Sipe, J. E.; Kauranen, M. Surface and Bulk Contributions to the Second-Order Nonlinear Optical Response of a Gold Film. *Phys. Rev. B: Condens. Matter Mater. Phys.* **2009**, *80*, 233402.

(58) Timbrell, D.; You, J. W.; Kivshar, Y. S.; Panoiu, N. C. A Comparative Analysis of Surface and Bulk Contributions to Second-Harmonic Generation in Centrosymmetric Nanoparticles. *Sci. Rep.* **2018**, *8*, 3586.

(59) Johnson, P. B.; Christy, R. W. Optical Constants of the Noble Metals. *Phys. Rev. B* **1972**, *6*, 4370−4379.

(60) Dadap, J. I.; Shan, J.; Eisenthal, K. B.; Heinz, T. F. Second-Harmonic Rayleigh Scattering from a Sphere of Centrosymmetric Material. *Phys. Rev. Lett.* **1999**, *83*, 4045−4048.

(61) Dadap, J. I.; Shan, J.; Heinz, T. F. Theory of Optical Second-Harmonic Generation from a Sphere of Centrosymmetric Material: Small-Particle Limit. *J. Opt. Soc. Am. B* **2004**, *21*, 1328−1347.

https://dx.doi.org/10.1021/acsphotonics.0c00326
ACS Photonics 2020, 7, 1290−1296

(62) Russier-Antoine, I.; Benichou, E.; Bachelier, G.; Jonin, C.; Brevet, P. F. Multipolar Contributions of the Second Harmonic Generation from Silver and Gold Nanoparticles. *J. Phys. Chem. C* **2007**, *111*, 9044−9048.

(63) Fales, A. W.; Vogt, W. C.; Pfefer, T. J.; Ilev, I. K. Quantitative Evaluation of Nanosecond Pulsed Laser-Induced Photomodification of Plasmonic Gold Nanoparticles. *Sci. Rep.* **2017**, *7*, 15704.

(64) Jaynes, E.; Cummings, F. Comparison of Quantum and Semiclassical Radiation Theories with Application to the Beam Maser. *Proc. IEEE* **1963**, *51*, 89−109.

4 Electron beam shaping with light

A possible solution to overcome some drawbacks and bring new applications of STEM-EELS is to perform electron beam shaping. We can employ electron phase plates (EPPs) that can be inserted in an electron microscope [see the scheme in FIGURE 4.1(a)] to prepare an electron wave function with on-demand amplitude and phase profile. Such shaping could also compensate for a phase distortion introduced by the other electron-optics elements and thus eliminate the need for expensive aberration correctors. A conceptually well-known EPP design is a diffraction grating used as a beam splitter[63] or a generator of vortex electron beams (VEBs)[64,65], see FIGURE 4.1(b). Another option to imprint the phase varying transversely to the beam axis is to let an extended beam transmit through a thin film with a nontrivial thickness profile. Sculpted thin films have been successfully used to compensate for a spherical aberration[66] or VEB generation[67]. However, these EPPs have a major drawback: they cannot be modified or tuned when plugged into the microscope.

So far, several designs of tunable EPPs have been proposed. The first design relies on an array of micron-scale einzel lenses whose voltage and thus the relative phase of electrons transmitted through different lenses can be adjusted independently. Preliminary proof-of-concept experiments with the einzel-lens modulator (ELM)[68] demonstrated the successful generation of variously shaped electron beams (SEBs). An example of an ELM featuring six einzel lenses and the corresponding phase profile of the transmitted electron wave function is shown in FIGURE 4.1(c). Another microelectronics-based EPP relies on metallic electrodes forming a non-trivial electrostatic potential around the edges of an aperture. Here we suggest two alternatives based on the electron-photon interaction, such as the scheme shown in FIGURE 4.1(d).

Light modulation in free space

García de Abajo, F. J. & Konečná, A. Optical Modulation of Electron Beams in Free Space. *Phys. Rev. Lett.* **126,** 123901 (12 2021).

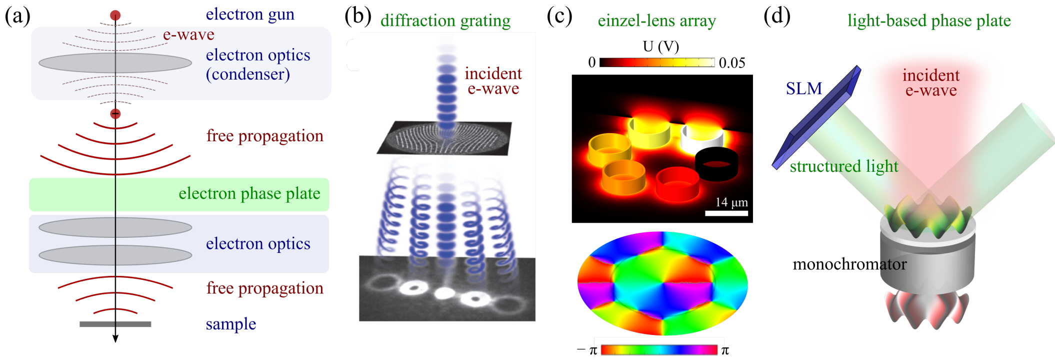

Figure 4.1: Electron phase plates. (a) A simplified scheme of an electron microscope with an electron phase plate. (b) Diffraction grating for generation of electron vortex beams (taken from Ref.[64]). (c) An array of six einzel lenses representing a tunable EPP. (d) PINEM-based EPP.

The optical free-electron modulator (OFEM) is based on the interaction of fast electrons with optical fields in free space. The free-space interaction is due to an electron-photon momentum mismatch typically very inefficient but still feasible if an intense laser field is involved. If the optical field features a tailored amplitude and phase profile, achieved, *e.g.*, by incorporating a spatial light modulator (SLM), the electron wave function exhibits a nontrivial spatial variation after the interaction. Our theoretical suggestion was recently reproduced experimentally[23], confirming the predictions.

Light modulation using PINEM approach

Konečná, A. & García de Abajo, F. J. Electron Beam Aberration Correction Using Optical Near Fields. *Phys. Rev. Lett.* **125,** 030801 (3 2020).

The SLM is also used in the second possible design when tailored light is reflected off a thin film opaque for light but transparent for electrons. The presence of the film makes the electron-photon interaction more efficient, which is well known from other PINEM experiments[71]. The PINEM-based EPP, which we exploited theoretically, could be straightforwardly used for correcting electron-microscope aberrations or for reaching on-demand electron beam shapes. Recent experimental realization confirmed our predictions and demonstrated the generation of Laguerre-Gauss beams in a setup very similar to the theoretically proposed one[72].

PHYSICAL REVIEW LETTERS **125,** 030801 (2020)

Electron Beam Aberration Correction Using Optical Near Fields

Andrea Konečná[1] and F. Javier García de Abajo[1,2,*]

[1]ICFO-Institut de Ciencies Fotoniques, The Barcelona Institute of Science and Technology, 08860 Castelldefels (Barcelona), Spain

[2]ICREA-Institució Catalana de Recerca i Estudis Avançats, Passeig Lluís Companys 23, 08010 Barcelona, Spain

(Received 24 April 2020; accepted 1 July 2020; published 17 July 2020)

The interaction between free electrons and optical near fields is attracting increasing attention as a way to manipulate the electron wave function in space, time, and energy. Relying on currently attainable experimental capabilities, we design optical near-field plates to imprint a lateral phase on the electron wave function that can largely correct spherical aberration without the involvement of electric or magnetic lenses in the electron optics, and further generate on-demand lateral focal spot profiles. Our work introduces a disruptive and powerful approach toward aberration correction based on light-electron interactions that could lead to compact and versatile time-resolved free-electron microscopy and spectroscopy.

DOI: 10.1103/PhysRevLett.125.030801

The development and widespread use of spatial light modulators have revolutionized optics by enabling an increasing degree of control over light beam propagation. Likewise, the extension of this concept to electron optics could provide the means for controlling the electron wave function and its interactions with atomic-scale samples. Electron microscopes already reach precise spatial and temporal control over the amplitude and phase of the wave function of beam electrons employed as sample probes. Over the last decades, costly and sophisticated arrangements of magnetostatic and electrostatic lenses have been engineered to eliminate electron-optics aberrations [1,2], making it possible to focus electron beams with subangstrom precision in state-of-the-art scanning transmission electron microscopes. These capabilities are crucial for atomic-scale imaging and spectroscopy [3,4].

Parallel efforts have led to the development of amplitude and phase reconstruction techniques such as ptychography [5] or electron tomography and holography [6], which have proved useful in both imaging low-contrast samples [7,8] and acquiring additional information on the sample, such as electric or magnetic field distributions [9–11]. An alternative approach has consisted in preparing electron beams with on-demand focal spot phase and intensity distributions designed to introduce phase contrast and selectively interact with targeted types of excitations such as plasmons of specific multipolar symmetry [12] or chiral modes and materials magnetic properties [13,14]. Such phase-shaped electron beams can be obtained through diffraction by a static phase plate [12,15–17] or ingenious use of lens aberrations [18,19]. A recent work also demonstrates programmable electron phase plates based on arrays of electrically biased transmission elements [20].

The interaction of free electrons with optical near fields in illuminated nanostructures opens exciting possibilities as a further mechanism to control the electron wave function. This phenomenon has been exploited to develop the so-called photon-induced near-field electron microscopy [21], which has been the subject of intense experimental [21–40] and theoretical [41–48] efforts. By synchronizing the arrival of ultrashort electron and laser pulses near the sample, the former can undergo stimulated absorption or emission of up to hundreds of photons [39,40]. This technique has been predicted to imprint optical phase on the lateral electron wave function [45], which has been demonstrated to generate vortex electron beams via photon-to-electron angular momentum transfer [37]. The synergetic combination of spatial light modulators and ultrafast electron microscopy constitutes a powerful platform for the control of free-electron wave functions, including the possibility of compensating beam aberrations and shaping the focal spot. While other alternatives to traditional electron-optics components have been suggested, such as using nanofabricated structures or thin films for wave front shaping and correction [49,50], our target is to introduce a more versatile and tunable solution.

In this Letter, we theoretically demonstrate the correction of spherical aberration in an electron beam upon transmission through an illuminated thin film, where light-electron phase transfer compensates for the undesired deviation of the transverse electron wave function from a spherical wave front, thereby resulting in nearly unaberrated focusing down to subangstrom focal spots. The proposed implementation of this type of photonic aberration corrector (PAC) in an electron microscope is schematically depicted in Fig. 1, where the new element is placed after the condenser along the electron optical path in order to imprint the required phase on the electron wave function to compensate for the aberration produced by subsequent electron-optics focusing elements. The PAC consists of an optically opaque electron-transparent thin film (e.g., a metal film deposited on a Si_3N_4 membrane, as

PHYSICAL REVIEW LETTERS **125,** 030801 (2020)

already used in photon-induced near-field electron microscopy studies [25,35], but we discuss additional options in Sec. S3 of the Supplemental Material [51]) on which a lateral optical pattern is projected with diffraction-limited spatial resolution. Electron interaction with semi-infinite light fields [35] in this film then produces energy sidebands in the transmitted electrons that can be optimized to accommodate $\sim 1/3$ of the electrons in the first sideband (i.e., electrons that have gained one photon energy). A monochromator inserted right after the PAC removes the rest of the energy sidebands before entering an electron-optics module for focusing at the sample. Aberration correction is thus performed through the PAC phase plate, which represents an alternative to traditional aberration correctors. This type of design inherits the flexibility of light patterning through spatial light modulators, here demonstrated for aberration correction, but also enabling arbitrary shaping of the electron focal spot.

Electron beam propagation through the electron microscope.—We represent fast electrons by their space- and time-dependent wave function $\psi_z(\mathbf{R})e^{-i\mathcal{E}_0 t}$, where we consider monochromatic electrons of energy $\mathcal{E}_0$ that depend on transverse coordinates $\mathbf{R} = (x, y)$ at each propagation plane determined by z. Free propagation from z' to z is described by the expression [44,52]

$$\psi_z(\mathbf{R}) = \int\int \frac{d^2\mathbf{Q}d^2\mathbf{R}'}{(2\pi)^2} e^{i[\mathbf{Q}\cdot(\mathbf{R}-\mathbf{R}')+q_z(z-z')]}\psi_{z'}(\mathbf{R}'),$$

where the outer integral extends over transverse wave vectors $\mathbf{Q}$, $q_z = \sqrt{q_0^2 - Q^2}$ is the longitudinal wave vector, $\hbar\mathbf{q}_0 = m_e\mathbf{v}\gamma$ and $\mathbf{v}$ are the average electron momentum and velocity vectors, respectively, $\gamma = 1/\sqrt{1 - v^2/c^2}$ is the Lorentz factor, m_e is the electron rest mass, and c is the speed of light in vacuum. In what follows, we focus on electron beams of well-defined chirality, characterized by an azimuthal orbital quantum number m, such that the wave function takes the form $\psi_z(\mathbf{R}) = \psi_z(R)e^{im\varphi}$, where (R, φ) are polar coordinates. Additionally, electrons in microscopes are collimated and therefore safely described in the paraxial approximation, for which $q_z \approx q_0 - Q^2/2q_0$. These considerations allow us to carry out some of the above integrals to find [51]

$$\begin{aligned}\psi_z(R) &= (\mathcal{F}^m_{z-z'} \cdot \psi_{z'})|_R \\ &\equiv (-i)^{m+1}\xi_{z-z'}e^{iq_0(z-z')} \\ &\quad\times \int_0^\infty R'dR'J_m(\xi_{z-z'}RR')e^{i\xi_{z-z'}(R^2+R'^2)/2}\psi_{z'}(R'),\end{aligned} \tag{1}$$

where $\xi_{z-z'} = q_0/(z - z')$, J_m is a Bessel function, and we implicitly define the free-propagation operator $\mathcal{F}^m$ using matrix notation with a dot standing for integration over the radial coordinate R.

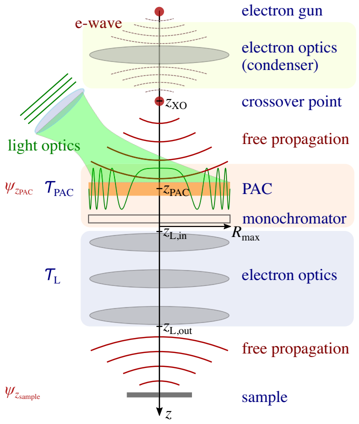

FIG. 1. Proposed experimental arrangement incorporating a photonic aberration corrector (PAC) to mitigate electron spherical aberration through an electron optical phase plate. The PAC module (light orange frame) is placed just before the electron-optics focusing module (electromagnetic lenses inside the light blue frame) at a distance $z_{L,\rm in} - z_{\rm xo}$ from the crossover point. A coherent electron wave is prepared by condenser lenses placed after an electron gun. Both the transmitted beam and the light wave prepared by a spatial light modulator are restricted by a circular aperture of radius $R_{\rm max}$.

Transmission through the microscope sketched in Fig. 1 results in an electron wave function at the sample given by

$$\psi_{z_{\rm sample}} = \mathcal{F}^m_{z_{\rm sample}-z_{L,\rm out}} \cdot \mathcal{T}_L \cdot \mathcal{F}^m_{z_{L,\rm in}-z_{\rm PAC}} \cdot \mathcal{T}_{\rm PAC} \cdot \psi_{z_{\rm PAC}}, \tag{2}$$

where $\psi_{z_{\rm PAC}}$ represents the electron incident on the plane of the corrector at $z_{\rm PAC}$, while $\mathcal{T}_{\rm PAC}$ and $\mathcal{T}_L$ account for transmission through the PAC and electron lenses (orange and blue frames in Fig. 1, respectively). For a thin lens, the latter is well described by [53,54]

$$\mathcal{T}_L|_{RR'} = \delta(R - R')e^{i\chi(\theta)}e^{-iq_0R^2/2f}\Theta(R_{\rm max} - R), \tag{3}$$

where f is the focal distance, a pupil blocks propagation above a radial distance $R_{\rm max}$, and the phase $\chi(\theta)$ accounts for aberrations in the lenses as a function of exit angle $\theta = R/(z_{\rm sample} - z_{L,\rm out})$. Here, we concentrate on spherical aberration, so we express $\chi(\theta) = C_3q_0\theta^4/4$ in terms of the (length) coefficient C_3 [52,55]. For simplicity, in what follows we consider a spherical wave $\psi_{z_{\rm PAC}}(R) \propto e^{iq_0R^2/2(z_{\rm PAC}-z_{\rm xo})}$ with $m = 0$ emerging from a perfect point-like crossover that can be produced by another set of condenser lenses placed after the electron source and

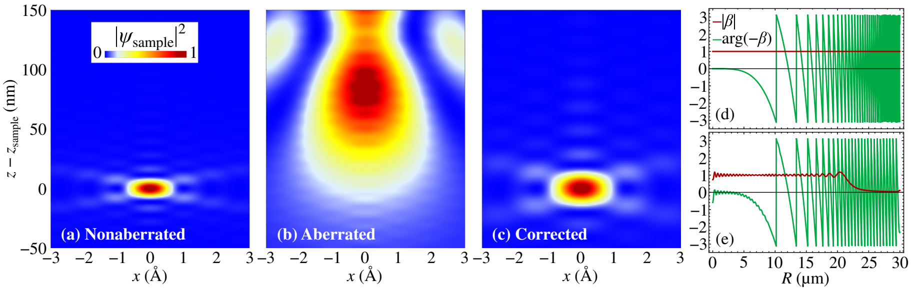

FIG. 2. Spatial dependence of the electron intensity focus at the sample. We plot the normalized beam electron density $|\psi_{\mathrm{sample}}|^2$ [Eq. (2)] obtained through (a) aberration-free electron optics; (b) electron optics introducing spherical aberration with $C_3 = 1$ mm; and (c) same as (b) including a PAC module. We consider 60-keV electrons, a focal distance $f = 1$ mm, $z_L - z_{\mathrm{xo}} = 40f$, and an aperture $R_{\max} = 30\ \mu$m. The corrected beam profile in (c) is calculated by using a realistic spatial dependence of the coupling parameter β as a function of radial distance R in the PAC [panel (e), obtained from Eqs. (6) and (8) with $\lambda_0 = 500$ nm light wavelength], which differs from the ideal β that is needed to perfectly correct the aberration [panel (d), Eq. (7)].

preceding the PAC. In practice, the condenser lenses together with collimating apertures provide lateral coherence of the electron beam over the aperture restricted by $R_{\max}$, as needed for a correct performance of the PAC. We note that the PAC can also correct for aberrations introduced by the preceding lenses, but for demonstration purposes, here we only consider the electron-optics aberration produced by the objective lens placed after the PAC. Additionally, we take the PAC to coincide with the near and far sides of the optical lenses at the virtual plane $z = z_L$.

In the absence of aberrations ($\chi = 0$), $\psi_{z_{\mathrm{sample}}}$ is focused at a position $z = z_{\mathrm{sample}}$ determined by the lens formula $1/(z_{\mathrm{sample}} - z_L) + 1/(z_L - z_{\mathrm{xo}}) = 1/f$ [51]. This is illustrated in Fig. 2(a) for 60-keV electrons (∼5 pm wavelength) with $z_L - z_{\mathrm{xo}} = 40f$ (implying $z_{\mathrm{xo}} - z_L \approx f$), $f = 1$ mm, and $R_{\max} = 30\ \mu$m. The focal spot is limited by diffraction at the aperture, yielding a $\psi_{z_{\mathrm{sample}}} \sim J_1(R/\Delta)$ transverse profile of subangstrom width $\sim\Delta = f/q_0 R_{\max} = 0.26$ Å. In contrast, a typical spherical aberration corresponding to $C_3 = 1$ mm produces a substantially broadened and shifted focus [Fig. 2(b)], accompanied by satellite foci along the optical axis.

Electron optical phase plate.—We intend to cancel the aberration phase χ by imprinting an additional phase on the electron wave function through the interaction with an optical near field [35,44,45]. For this purpose, we consider an optically opaque electron-transparent film subject to external illumination, a configuration that has been demonstrated to produce large coupling to the electrons [35]. We assume that inelastic scattering due to interaction with the film material can be neglected, while the additional phase acquired through this interaction should only contribute as a position-independent overall factor. The condition of weak inelastic scattering is met by thin metal films with thickness < 10 nm, well below the electron inelastic mean free path [51,56]. Alternatively, a thin dielectric membrane can be used together with more intense optical illumination, as we demonstrate in Sec. S3 of the Supplemental Material [51].

The transmitted electron wave function consists of sidebands of energies $\mathcal{E}_0 + \hbar\ell\omega_0$ separated from the incident energy by multiples ℓ (<0 for loss, >0 for gain) of the photon energy $\hbar\omega_0$. In the nonrecoil approximation, the wave function associated with each transmitted sideband ℓ consists of the incident wave function times a multiplicative factor accounted for by the operator [35,46]

$$\mathcal{T}_{\mathrm{PAC}}|_{RR'} = \delta(R - R') J_\ell(2|\beta|) e^{i\ell \arg\{-\beta\}}, \tag{4}$$

where the coupling coefficient

$$\beta(\mathbf{R}) = \frac{e}{\hbar\omega_0} \int_{-\infty}^{\infty} dz\, E_z(\mathbf{R}, z) e^{-i\omega_0 z/v} \tag{5}$$

captures the electron-light interaction through the (along-the-beam) E_z component of the optical electric-field amplitude, which bears a dependence on transverse coordinates $\mathbf{R}$ that can be controlled through a spatial light modulator. We first consider axially symmetric illumination [implying $m = 0$ in Eq. (2)] and express the incident optical field $E_z = \int_0^{k_0} dk_\parallel J_0(k_\parallel R) e^{ik_z z} \alpha_{k_\parallel}$ as a combination of cylindrical Bessel waves with in- and out-of-plane wave vector components $k_\parallel$ and $k_z = \sqrt{k_0^2 - k_\parallel^2}$, respectively, limited by the free-space light wave vector $k_0 = \omega_0/c$. Upon insertion of this field into Eq. (5), we find

$$\beta(R) = \int_0^{k_0} k_\parallel dk_\parallel J_0(k_\parallel R)\beta_{k_\parallel}, \tag{6}$$

where the coefficient $\beta_{k_\parallel}$ is proportional to $\alpha_{k_\parallel}$ and also includes light components reflected at the film [35]; we stress that $\beta_{k_\parallel}$ can therefore be controlled through the applied angular light profile $\alpha_{k_\parallel}$.

Design of the PAC field profile.—We now design the PAC based on an electron optical phase plate in which $\ell = 1$ is selected, while other sidebands ($\ell \neq 1$) are filtered out by a monochromator (Fig. 1), using for example a Wien filter [1] (easily capable of separating peaks with an energy difference $\hbar\omega_0 \sim 1$ eV). The aberration phase χ introduced through $\mathcal{T}_L$ [Eq. (3)] can then be eliminated from Eq. (2) by setting

$$\arg\{-\beta(R)\} = -\chi(\theta) \tag{7}$$

in $\mathcal{T}_{\rm PAC}$ [Eq. (4)], where $R = \theta(z_{\rm sample} - z_L)$. We can maximize the current by imposing $|\beta| = \beta_0 \approx 0.92$, which yields an absolute maximum fraction of the $\ell = 1$ sideband $J_1^2(2\beta_0) \approx 34\%$ [51]. The PAC then involves a reduction in electron current by a factor of $\sim 2/3$, which, together with beam losses due to interaction with the PAC material, represents a drawback compared to traditional solutions for aberration correction in which most of the beam current is transmitted. The spatial dependence of $\beta = -\beta_0 e^{-i\chi}$ required to produce perfect aberration correction and maximum $\ell = 1$ current is presented in Fig. 2(d) according to Eq. (7) for $\mathcal{E}_0 = 60$ keV and $f = C_3 = 1$ mm. However, optical diffraction at the used finite light wavelength $\lambda_0 = 2\pi/k_0$ limits the profile of β that can be achieved in practice using far-field illumination. We find a nearly optimum realistic profile by setting $\beta = -\beta_0 e^{-i\chi}$ in Eq. (6) and approximately inverting this equation to yield

$$\beta_{k_\parallel} = -\beta_0 \int_0^{R_{\rm max}} RdRJ_0(k_\parallel R)e^{-i\chi[R/(z_{\rm sample}-z_L)]} \tag{8}$$

(this inversion is only exact in the $k_0 R_{\rm max} \gg 1$ limit). The coupling coefficient obtained by inserting Eq. (8) back into Eq. (6) is plotted in Fig. 2(e) for a photon wavelength $\lambda_0 = 500$ nm, which resembles the perfect-correction coefficient of Fig. 2(d) up to $R \sim 20$ μm, but deviates substantially from that target value at larger R (i.e., where the phase χ exhibits rapid variations over a distance $\sim\lambda_0$). Although the resulting corrected beam profile plotted in Fig. 2(c) is not perfect, it still provides an impressive improvement in electron focusing compared to the aberrated spot shown in Fig. 2(b) [51]. We note that the degree of correction increases when λ_0 is made smaller relative to $R_{\rm max}$, as we show in Fig. 3, which further predicts a remarkable aberration compensation using blue light. We also verified that aberration correction by the PAC does not introduce any undesired beam tails (see Fig. S5 in the Supplemental Material [51]).

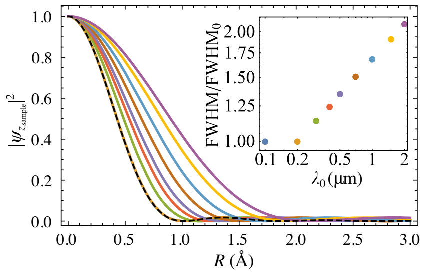

FIG. 3. Approaching perfect aberration correction. We show the focal spot profile obtained with the same parameters as in Fig. 2(c) using light of different wavelength λ_0. The inset shows the spot FWHM normalized to the unaberrated one (FWHM$_0$, corresponding to the dashed black curve in the main plot) and provides a color legend for the main plot.

The PAC can be fed using light with definite chirality m [i.e., $E_z(\mathbf{R}, z) = E_z(R, z)e^{im\varphi_{\mathbf{R}}}$, which directly translates through Eqs. (4) and (5) into $\mathcal{T}_{\rm PAC} \propto e^{im\varphi_{\mathbf{R}}}$], still described by Eqs. (6) and (8) with J_0 substituted by J_m. Results for the transverse profile of the electron focus using chiral PACs with $m = 1$ and 3 are compared with the $m = 0$ profile in Fig. 4, revealing the formation of donuts

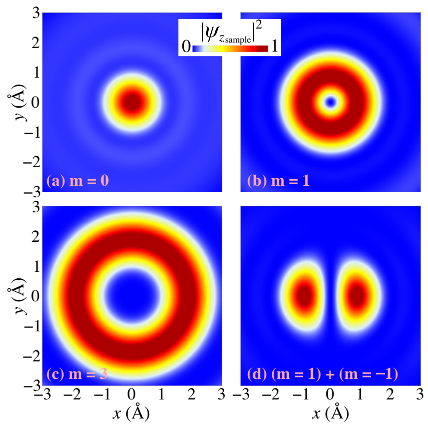

FIG. 4. Manipulation of the focal spot profile. Transverse cuts of electron focal spots obtained by correcting spherical aberration under the same conditions as in Fig. 2(c) but using light fields with the indicated symmetry: $e^{im\varphi}$ azimuthal dependence in (a)–(c) and $\cos\varphi$ in (d).

associated with an electron wave function of $e^{im\varphi}$ azimuthal symmetry. More complex profiles are possible, which should be reachable using a spatial light modulator to project light on the PAC. For example, Fig. 4(d) shows the result obtained by projecting a symmetric combination of $m = 1$ and $m = -1$ light.

Conclusion.—In summary, we propose the use of electron optical phase plates as a way of tailoring the amplitude and phase of the electron-transverse wave function in an electron beam. Specifically, we theoretically demonstrate correction of spherical aberration without the involvement of complex electron-optics elements. This concept can be straightforwardly applied to eliminate any undesired distortions introduced by electron optics in both standard and ultrafast electron microscopes. Although we apply analytical methods to produce a proof-of-principle design, improvement in the capabilities of such phase plates could be gained through machine learning, which should enable the design of more complex electron spot shapes or correction of a general combination of aberrations following the example of light optics [57]. Ultimately, iterative improvement of the PAC could be attained through a feedback loop involving measurement of the electron spot and modification of the projected light profile. Additionally, temporal manipulation of the imprinted optical phase offers interesting possibilities for the exploration of sample dynamics through time-varying electron spot profiles. The versatility and compactness of electron optical phase plates hold potential for active control of electron wave functions beyond the present application in aberration correction.

We thank Mathieu Kociak, Albert Polman, and Claus Ropers for helpful and enjoyable discussions. This work has been supported in part by ERC (Advanced Grant 789104-eNANO), the Spanish MINECO (MAT2017-88492-R and SEV2015-0522), the Catalan CERCA Program, and Fundació Privada Cellex.

---

[*]Corresponding author.
javier.garciadeabajo@nanophotonics.es

[1] P. Hawkes and J. Spence, *Springer Handbook of Microscopy* (Springer Nature, Switzerland, AG, 2019).
[2] M. Haider, H. Rose, S. Uhlemann, E. Schwan, B. Kabius, and K. Urban, Ultramicroscopy **75**, 53 (1998).
[3] P. E. Batson, N. Dellby, and O. L. Krivanek, Nature (London) **418**, 617 (2002).
[4] D. A. Muller, L. Fitting Kourkoutis, M. Murfitt, J. H. Song, H. Y. Hwang, J. Silcox, N. Dellby, and O. L. Krivanek, Science **319**, 1073 (2008).
[5] Y. Jiang, Z. Chen, Y. Han, P. Deb, H. Gao, S. Xie, P. Purohit, M. W. Tate, J. Park, S. M. Gruner *et al.*, Nature (London) **559**, 343 (2018).
[6] P. A. Midgley and R. E. Dunin-Borkowski, Nat. Mater. **8**, 271 (2009).
[7] H.-W. Fink, H. Schmid, E. Ermantraut, and T. Schulz, J. Opt. Soc. Am. A **14**, 2168 (1997).
[8] F. S. Yasin, T. R. Harvey, J. J. Chess, J. S. Pierce, C. Ophus, P. Ercius, and B. J. McMorran, Nano Lett. **18**, 7118 (2018).
[9] M. R. McCartney, N. Agarwal, S. Chung, D. A. Cullen, M.-G. Han, K. He, L. Li, H. Wang, L. Zhou, and D. J. Smith, Ultramicroscopy **110**, 375 (2010).
[10] O. Nicoletti, F. de la Peña, R. K. Leary, D. J. Holland, C. Ducati, and P. A. Midgley, Nature (London) **502**, 80 (2013).
[11] K. Shibata, A. Kovács, N. S. Kiselev, N. Kanazawa, R. E. Dunin-Borkowski, and Y. Tokura, Phys. Rev. Lett. **118**, 087202 (2017).
[12] G. Guzzinati, A. Beche, H. Lourenco-Martins, J. Martin, M. Kociak, and J. Verbeeck, Nat. Commun. **8**, 14999 (2017).
[13] S. M. Lloyd, M. Babiker, G. Thirunavukkarasu, and J. Yuan, Rev. Mod. Phys. **89**, 035004 (2017).
[14] J. Rusz and S. Bhowmick, Phys. Rev. Lett. **111**, 105504 (2013).
[15] J. Verbeeck, H. Tian, and P. Schattschneider, Nature (London) **467**, 301 (2010).
[16] B. J. McMorran, A. Agrawal, I. M. Anderson, A. A. Herzing, H. J. Lezec, J. J. McClelland, and J. Unguris, Science **331**, 192 (2011).
[17] R. Shiloh, Y. Lereah, Y. Lilach, and A. Arie, Ultramicroscopy **144**, 26 (2014).
[18] P. Schattschneider, M. Stöger-Pollach, and J. Verbeeck, Phys. Rev. Lett. **109**, 084801 (2012).
[19] L. Clark, A. Béché, G. Guzzinati, A. Lubk, M. Mazilu, R. Van Boxem, and J. Verbeeck, Phys. Rev. Lett. **111**, 064801 (2013).
[20] J. Verbeeck, A. Béché, K. Müller-Caspary, G. Guzzinati, M. A. Luong, and M. Den Hertog, Ultramicroscopy **190**, 58 (2018).
[21] B. Barwick, D. J. Flannigan, and A. H. Zewail, Nature (London) **462**, 902 (2009).
[22] F. O. Kirchner, A. Gliserin, F. Krausz, and P. Baum, Nat. Photonics **8**, 52 (2014).
[23] L. Piazza, T. T. A. Lummen, E. Quiñonez, Y. Murooka, B. Reed, B. Barwick, and F. Carbone, Nat. Commun. **6**, 6407 (2015).
[24] A. Feist, K. E. Echternkamp, J. Schauss, S. V. Yalunin, S. Schäfer, and C. Ropers, Nature (London) **521**, 200 (2015).
[25] T. T. A. Lummen, R. J. Lamb, G. Berruto, T. LaGrange, L. D. Negro, F. J. García de Abajo, D. McGrouther, B. Barwick, and F. Carbone, Nat. Commun. **7**, 13156 (2016).
[26] K. E. Echternkamp, A. Feist, S. Schäfer, and C. Ropers, Nat. Phys. **12**, 1000 (2016).
[27] C. Kealhofer, W. Schneider, D. Ehberger, A. Ryabov, F. Krausz, and P. Baum, Science **352**, 429 (2016).
[28] A. Ryabov and P. Baum, Science **353**, 374 (2016).
[29] G. M. Vanacore, A. W. P. Fitzpatrick, and A. H. Zewail, Nano Today **11**, 228 (2016).
[30] Y. Morimoto and P. Baum, Nat. Phys. **14**, 252 (2018).
[31] M. Kozák, J. McNeur, K. J. Leedle, H. Deng, N. Schönenberger, A. Ruehl, I. Hartl, J. S. Harris, R. L. Byer, and P. Hommelhoff, Nat. Commun. **8**, 14342 (2017).
[32] A. Feist, N. Bach, T. D. N. Rubiano da Silva, M. Mäller, K. E. Priebe, T. Domräse, J. G. Gatzmann, S. Rost, J. Schauss, S. Strauch *et al.*, Ultramicroscopy **176**, 63 (2017).

[33] K. E. Priebe, C. Rathje, S. V. Yalunin, T. Hohage, A. Feist, S. Schäfer, and C. Ropers, Nat. Photonics **11**, 793 (2017).
[34] E. Pomarico, I. Madan, G. Berruto, G. M. Vanacore, K. Wang, I. Kaminer, F. J. García de Abajo, and F. Carbone, ACS Photonics **5**, 759 (2018).
[35] G. M. Vanacore, I. Madan, G. Berruto, K. Wang, E. Pomarico, R. J. Lamb, D. McGrouther, I. Kaminer, B. Barwick, F. J. García de Abajo, and F. Carbone, Nat. Commun. **9**, 2694 (2018).
[36] Y. Morimoto and P. Baum, Phys. Rev. A **97**, 033815 (2018).
[37] G. M. Vanacore, G. Berruto, I. Madan, E. Pomarico, P. Biagioni, R. J. Lamb, D. McGrouther, O. Reinhardt, I. Kaminer, B. Barwick *et al.*, Nat. Mater. **18**, 573 (2019).
[38] K. Wang, R. Dahan, M. Shentcis, Y. Kauffmann, S. Tsesses, and I. Kaminer, Nature (London) **582**, 50 (2020).
[39] S. Nehemia, R. Dahan, M. Shentcis, O. Reinhardt, Y. Adiv, K. Wang, O. Beer, Y. Kurman, X. Shi, M. H. Lynch, and I. Kaminer, arXiv:1909.00757.
[40] O. Kfir, H. Lourenço-Martins, G. Storeck, M. Sivis, T. R. Harvey, T. J. Kippenberg, A. Feist, and C. Ropers, Nature (London) **582**, 46 (2020).
[41] F. J. García de Abajo, A. Asenjo Garcia, and M. Kociak, Nano Lett. **10**, 1859 (2010).
[42] S. T. Park, M. Lin, and A. H. Zewail, New J. Phys. **12**, 123028 (2010).
[43] S. T. Park and A. H. Zewail, J. Phys. Chem. A **116**, 11128 (2012).
[44] F. J. García de Abajo, B. Barwick, and F. Carbone, Phys. Rev. B **94**, 041404(R) (2016).
[45] W. Cai, O. Reinhardt, I. Kaminer, and F. J. García de Abajo, Phys. Rev. B **98**, 045424 (2018).
[46] V. Di Giulio, M. Kociak, and F. J. García de Abajo, Optica **6**, 1524 (2019).
[47] O. Kfir, Phys. Rev. Lett. **123**, 103602 (2019).
[48] O. Reinhardt, C. Mechel, M. Lynch, and I. Kaminer, arXiv:1907.10281.
[49] V. Grillo, A. H. Tavabi, E. Yucelen, P.-H. Lu, F. Venturi, H. Larocque, L. Jin, A. Savenko, G. C. Gazzadi, R. Balboni *et al.*, Opt. Express **25**, 21851 (2017).
[50] R. Shiloh, R. Remez, P.-H. Lu, L. Jin, Y. Lereah, A. H. Tavabi, R. E. Dunin-Borkowski, and A. Arie, Ultramicroscopy **189**, 46 (2018).
[51] See Supplemental Material at http://link.aps.org/supplemental/10.1103/PhysRevLett.125.030801 for a derivation of Eq. (1), a calculation of the coupling coefficient β for thin films, additional elements of the simulation with the PAC and the electron lenses at the same virtual plane, further details on the PAC, and a comparison of electron spot profiles with and without aberration correction.
[52] L. J. Allen, M. P. Oxley, and D. Paganin, Phys. Rev. Lett. **87**, 123902 (2001).
[53] P. Hawkes, B. Lencová, and M. Lenc, J. Microsc. **179**, 145 (1995).
[54] R. F. Egerton, *Physical Principles of Electron Microscopy: An Introduction to TEM, SEM, and AEM* (Springer, New York, 2005).
[55] D. M. Paganin, T. C. Petersen, and M. A. Beltran, Phys. Rev. A **97**, 023835 (2018).
[56] H. Shinotsuka, S. Tanuma, C. J. Powell, and D. R. Penn, Surf. Interface Anal. **47**, 871 (2015).
[57] O. Albert, L. Sherman, G. Mourou, T. B. Norris, and G. Vdovin, Opt. Lett. **25**, 52 (2000).

PHYSICAL REVIEW LETTERS **126,** 123901 (2021)

Editors' Suggestion

Optical Modulation of Electron Beams in Free Space

F. Javier García de Abajo[1,2,*] and Andrea Konečná[1]

[1]ICFO-Institut de Ciencies Fotoniques, The Barcelona Institute of Science and Technology, 08860 Castelldefels (Barcelona), Spain

[2]ICREA-Institució Catalana de Recerca i Estudis Avançats, Passeig Lluís Companys 23, 08010 Barcelona, Spain

(Received 7 November 2020; accepted 16 February 2021; published 22 March 2021)

We exploit free-space interactions between electron beams and tailored light fields to imprint on-demand phase profiles on the electron wave functions. Through rigorous semiclassical theory involving a quantum description of the electrons, we show that monochromatic optical fields focused in vacuum can be used to correct electron beam aberrations and produce selected focal shapes. Stimulated elastic Compton scattering is exploited to imprint the required electron phase, which is proportional to the integral of the optical field intensity along the electron path and depends on the transverse beam position. The required light intensities are attainable in currently available ultrafast electron microscope setups, thus opening the field of free-space optical manipulation of electron beams.

DOI: 10.1103/PhysRevLett.126.123901

Electron microscopy has experienced impressive advances over the last decades thanks to the design of sophisticated magnetostatic and electrostatic lenses that reduce electron optics aberrations [1–3] and are capable of focusing electron beams (e-beams) with subångstrom precision [4,5]. In addition, the availability of more selective monochromators [6] enables the exploration of sample excitations down to the midinfrared regime [7–10]. Such accurate control over e-beam shape and energy is crucial for atomic-scale imaging and spectroscopy [1–10].

The focused e-beam profile ultimately depends on the phase acquired by the electron along its passage through the microscope column. By imprinting an on-demand transverse phase profile on the electron wave function, one can shape the e-beam density distribution at the specimen, creating, for example, multifocal configurations to study atomic structures and delocalized optical modes through elastic [11] and inelastic [12] holography, respectively. Additionally, temporal control over the phase and the resulting focal shape in the subpicosecond domain would grant us access into structural and excitation dynamics, suggesting the use of coherent control techniques [13] to optimize the phase for the desired application.

Besides electron optics lenses, several physical elements have been demonstrated to control transverse e-beam shaping. In particular, biprisms based on biased wires provide a dramatic example of laterally varying phase imprinting that is commonly used for e-beam splitting in electron holography [11], along with applications such as symmetry-selected plasmon excitation in metallic nanowires [14]. In a related context, vortex e-beams have been realized using a magnetic pseudomonopole [15]. Recently, plates with individually biased perforations have been developed to enable position-selective control over the electric Aharonov-Bohm phase stamped on the electron wave function [16], while passive carved plates have been employed as amplitude filters to produce highly chiral electron vortices [17–19] and aberration correctors [20,21].

The electron phase can also be modified by the ponderomotive force associated with the interaction between e-beams and optical fields. In particular, periodic light standing waves were predicted to produce electron diffraction [22], which was eventually observed in a challenging experiment [23–25] that had to circumvent the weak free-space electron-photon coupling associated with an energy-momentum mismatch [26]. Such a mismatch forbids single photon emission or absorption processes by free electrons, consequently limiting electron-light coupling to second-order interactions that concatenate an even number of virtual photon events. This type of interaction has been recently exploited to produce attosecond free-electron pulses [27,28].

Interestingly, the presence of material structures introduces scattered optical fields that can supply momentum and break the mismatch, thus enabling the occurrance of real photon processes [26] used, for example, in laser-driven electron accelerators [29,30]. Because the strength of scattered fields reflects the nanoscale optical response of the materials involved, this phenomenon was speculated to enable electron energy-gain spectroscopy as a way to dramatically improve spectral resolution in electron microscopes [31–33], as later corroborated in experiment [34]. By synchronizing the arrival of electron and light pulses at the sample, photon-induced near-field electron microscopy (PINEM) was demonstrated to exert temporal control over the electron wave function along the beam direction [35–58]. Additionally, modulation of the transverse wave function can be achieved in PINEM by laterally shaping the employed light [59], which results in the transfer of linear [49,60] and angular [53,61] momentum between photons and electrons.

PHYSICAL REVIEW LETTERS **126,** 123901 (2021)

Recently, we have proposed to use PINEM to imprint on-demand transverse e-beam phase profiles [62], thus relying on ultrafast e-beam shaping as an alternative approach to aberration correction. This method enables fast active control over the modulated e-beam at the expense of retaining only $\sim 1/3$ of monochromatic electrons and potentially introducing decoherence through inelastic interactions with the light scatterer. An approach to phase molding in which no materials are involved and the electron energy is preserved would then be desirable.

In this Letter, we propose an optical free-space electron modulator (OFEM) in which a phase profile is imprinted on the transverse electron wave function by means of the stimulated elastic Compton scattering associated with the A^2 term in the light-electron coupling Hamiltonian. The absence of material structures prevents electron decoherence and enables the use of high light intensities, as required to activate ponderomotive forces. We present a simple, yet rigorous semiclassical theory that supports applications of OFEM in aberration correction and transverse e-beam shaping. While optical e-beam phase stamping has been demonstrated in tour-de-force experiments using continuous-wave lasers [63–65], we envision pulsed illumination as a more feasible route to implement an OFEM, exploiting recent advances in ultrafast electron transmission microscopes (UTEMs), particularly in systems that incorporate light injection with a high numerical aperture [52] for diffraction-limited patterning of the optical field.

Free-space optical phase imprinting.—We study the free-space interaction between an e-beam and a light field represented by its vector potential $\mathbf{A}(\mathbf{r},t)$, working in a gauge in which the electric potential vanishes. With the e-beam propagation direction taken along z, it is convenient to write the electron wave function as $\psi(\mathbf{r},t)=\mathrm{e}^{iq_0z-iE_0t/\hbar}\phi(\mathbf{r},t)$, where we separate the slowly varying envelope $\phi(\mathbf{r},t)$ from the fast oscillations imposed by the central wave vector q_0 and energy E_0. Under the typical conditions met in electron microscopes, and assuming that interaction with light only produces small variations in the electron energy compared to E_0, we can adopt the nonrecoil approximation to reduce the Dirac equation in the minimal coupling scheme to an effective Schrödinger equation (see Sec. S1 in the Supplemental Material (SM) [66]),

$$(\partial_t+\mathbf{v}\cdot\nabla)\phi(\mathbf{r},t)=\frac{-i}{\hbar}\mathcal{H}'(\mathbf{r},t)\phi(\mathbf{r},t),$$

where

$$\mathcal{H}'=\frac{e}{c}\mathbf{v}\cdot\mathbf{A}+\frac{e^2}{2m_\mathrm{e}c^2\gamma}\left(A_x^2+A_y^2+\frac{1}{\gamma^2}A_z^2\right) \quad (1)$$

is the interaction Hamiltonian, $\mathbf{v}=v\hat{\mathbf{z}}$ is the electron velocity, and $\gamma=1/\sqrt{1-v^2/c^2}$ introduces relativistic corrections to the A^2 term. This equation admits the analytical solution

$$\phi(\mathbf{r},t)=\phi_0(\mathbf{r}-\mathbf{v}t)\exp\left[\frac{-i}{\hbar}\int_{-\infty}^{t}dt'\mathcal{H}'(\mathbf{r}-\mathbf{v}t+\mathbf{v}t',t')\right],$$

where $\phi_0(\mathbf{r}-\mathbf{v}t)$ is the incident electron wave function.

We consider that the light field acts on the electron over a sufficiently short path length L as to neglect any transverse variation in its wave function during the interaction (e.g., $L\lesssim D/\theta_e\sim 1$ mm for an e-beam diameter $D\sim 1\ \mu$m and a divergence angle $\theta_e\sim 1$ mrad). We also note that the $\mathbf{v}\cdot\mathbf{A}$ term in Eq. (1) does not contribute to the final electron state because it represents real photon absorption or emission events, which are kinematically forbidden (see Sec. S2 in the SM [66]). Likewise, following a similar argument, under monochromatic illumination with light of frequency ω, the time-varying components in A^2 ($\propto \mathrm{e}^{\pm 2\mathrm{i}\omega t}$), which describe two-photon emission or absorption, also produce vanishing contributions. The remaining terms $\propto \mathrm{e}^{\pm\mathrm{i}\omega t\mp\mathrm{i}\omega t}$ represent stimulated elastic Compton scattering, a second-order process that combines virtual absorption and emission of photons, amplified by the large population of their initial and final states. An alternative description of this effect is provided by the ponderomotive force acting on a classical point-charge electron and giving rise to diffraction in the resulting effective potential [25]. As we are interested in imprinting a phase on the electron wave function without altering its energy, we consider spectrally narrow external illumination that can be effectively regarded as monochromatic, such as that produced by laser pulses of much longer duration than the electron pulse. Writing the light vector potential as $\mathbf{A}(\mathbf{r},t)=2\mathrm{Re}\{\mathbf{A}(\mathbf{r})\mathrm{e}^{-\mathrm{i}\omega t}\}$ so that the electric field amplitude reads $\mathbf{E}(\mathbf{r})=(\mathrm{i}\omega/c)\mathbf{A}(\mathbf{r})$, we find the transmitted wave function to reduce to

$$\psi(\mathbf{r},t)=\psi_0(\mathbf{r}-\mathbf{v}t)\mathrm{e}^{\mathrm{i}\varphi(\mathbf{R})},$$

where

$$\varphi(\mathbf{R})=\frac{-1}{\mathcal{M}\omega^2}\int_{-\infty}^{\infty}dz\left[|E_x(\mathbf{r})|^2+|E_y(\mathbf{r})|^2+\frac{1}{\gamma^2}|E_z(\mathbf{r})|^2\right] \quad (2)$$

is an imprinted phase that depends on the transverse coordinates $\mathbf{R}=(x,y)$. Also, we define the scaled mass $\mathcal{M}=m_\mathrm{e}\gamma v/c\alpha$ with $\alpha\approx 1/137$ denoting the fine structure constant, and t is taken such that $\psi_0(\mathbf{r}-\mathbf{v}t)$ has already passed the interaction region, which after a change of variables ($z-vt+vt'\to z$) allows us to extend the integral to $z=\infty$.

Description of an OFEM.—We envision an OFEM placed right before the objective lens of an electron microscope [Fig. 1(a)] in a region where the e-beam spans a large diameter ($\gtrsim$100 times the light wavelength). The OFEM could consist of a combination of planar and parabolic

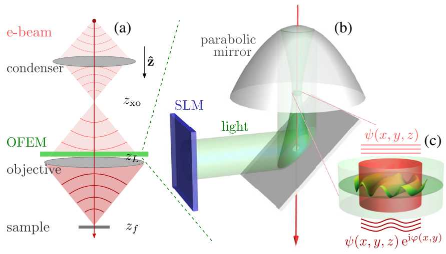

FIG. 1. Optical free-space electron modulator (OFEM). (a) The proposed element is placed in the electron microscope column right before the objective lens. (b) The OFEM incorporates a parabolic mirror that focuses light with a high numerical aperture on a vacuum region that intersects the electron beam. The electric field distribution at the optical focal spot is patterned by using a far-field spatial light modulator (SLM). (c) A phase is imprinted on the electron wave function, whose dependence on transverse coordinates $\mathbf{R}$ is proportional to the field intensity integrated along z.

mirrors with drilled holes that allow the e-beam to pass through the optical focal region [Fig. 1(b)]. The electron is then exposed to intense fields that can be shaped with diffraction-limited lateral resolution through a spatial light modulator and a high numerical aperture in the parabolic mirror. This results in a controlled position-dependent phase, as prescribed by Eq. (2) [Fig. 1(c)]. Considering a monochromatic e-beam and omitting for simplicity an overall $e^{-iE_0t/\hbar}$ time-dependent factor, free propagation of the electron wave function between planes z and z_f is described by

$$\psi(\mathbf{r}_f) = \iint \frac{d^2\mathbf{q}_\perp d^2\mathbf{R}}{(2\pi)^2} e^{i\mathbf{q}_\perp\cdot(\mathbf{R}_f-\mathbf{R})+iq_z(z_f-z)}\psi(\mathbf{r}) \propto \int d^2\mathbf{R}\, e^{iq_0|\mathbf{R}_f-\mathbf{R}|^2/2(z_f-z)}\psi(\mathbf{r}), \quad (3)$$

where the second line is obtained by performing the $\mathbf{q}_\perp = (q_x, q_y)$ integral in the paraxial approximation (i.e., $q_z = \sqrt{q_0^2 - q_\perp^2} \approx q_0 - q_\perp^2/2q_0$), and we are interested in exploring positions $r_f = (\mathbf{R}_f, z_f)$ near the electron focal point. In a simplified microscope model, we take $z = z_L$ at the entrance of the objective lens where the OFEM is also placed, and the incident electron is a spherical wave $\psi(\mathbf{R}, z_L) \propto e^{iq_0R^2/2(z_L-z_{\rm xo})}$ emanating from the crossover point $\mathbf{r} = (0, 0, z_{\rm xo})$ following the condenser lens. Introducing in Eq. (3) the phase $e^{-iq_0R^2/2f}$ produced by an objective lens with focal distance f and aperture radius $R_{\rm max}$, we have (see Sec. S3 in the SM [66])

$$\psi(\mathbf{r}_f) \propto \int d^2\vec{\theta}\, e^{-iq_0\vec{\theta}\cdot\mathbf{R}_f} e^{i\chi(\vec{\theta})+i\varphi(\mathbf{R})} e^{iq_0R^2\Delta/2}, \quad (4)$$

where $\vec{\theta} = \mathbf{R}/(z_f - z_L)$. Also, we define $\Delta = 1/(z_f - z_L) + 1/(z_L - z_{\rm xo}) - 1/f$, the phases χ and φ are produced by aberrations and the OFEM [Eq. (2)], respectively, and the integral is restricted to $\theta < R_{\rm max}/(z_f - z_L)$. In what follows, we study the electron wave function profile $\psi(\mathbf{r}_f)$ as given by Eq. (4) at the focal plane z_f, defined by the condition $\Delta = 0$.

Required light intensity.—From Eq. (2), the imprinted phase shift scales with the light intensity $I_0 = c|E|^2/2\pi$ roughly as $\varphi/I_0 \sim -2\pi L/\mathcal{M}c\omega^2$, where L is the effective length of the light-electron interaction region, which depends on the focusing conditions of the external illumination. For example, for an electron moving along the axis of an optical paraxial vortex beam of azimuthal angular momentum number $m = 1$ and wavelength $\lambda_0 = 2\pi c/\omega$, we have $L \approx 2\lambda_0/\theta_L^2$, where θ_L is the light beam divergence half-angle (see Sec. S5 in the SM [66]). Under these conditions, a phase $\varphi = 2\pi$ is achieved with a light power $\mathcal{P} = 2\mathcal{M}c^2\omega \sim 40$ kW for 60 keV electrons and $\lambda_0 = 500$ nm; this result is independent of θ_L, emphasizing the important role of phase accumulation along a large interaction region in a loosely focused light beam. Perhaps more relevant is the power required to imprint an average phase $\langle\varphi\rangle \sim \pi$ [i.e., $\langle I_0\rangle \sim \mathcal{M}c\omega^2/2L$ from Eq. (2)] over the area $\pi R_{\rm max}^2$ of the objective lens aperture; taking $R_{\rm max}/\lambda_0 = 20$, a conservative interaction length $L \sim 1$ μm, and 60 keV electrons, we find a total beam power $\mathcal{P} = \pi R_{\rm max}^2\langle I_0\rangle \sim 40$ MW, which could be distributed in a quasimonochromatic 10 ps pulse to act on sub-ps electron pulses using UTEM technology. We note that the phase scaling $\varphi \propto I_0/(v\gamma\omega^2)$ [see Eq. (2)] leaves some room for improvement by placing the OFEM in low-energy regions of the e-beam to reduce the optical power demand.

Aberration correction.—As an application of lateral phase molding, we explore the conditions needed to compensate for the third-order spherical aberration, which corresponds to [71,72] $\chi(\theta) = C_3q_0\theta^4/4$ in Eq. (4), where C_3 is a length coefficient. Upon examination of the phase profile imprinted by paraxial light vortex beams (see Sec. S4 in the SM [66]), we find that an azimuthal number $m = 3$ produces the required radial dependence $\varphi(R) = -(\pi^5\mathcal{P}/12\mathcal{M}c^2\omega)(\theta_L R/\lambda_0)^4$ under the condition $R \ll \lambda_0/2\pi\theta_L$. For typical microscope parameters $C_3 = f = 1$ mm, 60 keV electrons, $R_{\rm max} = 30$ μm, and $\lambda_0 = 500$ nm, the above condition is satisfied with $\theta_L \ll 0.15°$. Then, the compensation of spherical aberration (i.e., $\varphi = -\chi$) is realized with a beam power $\mathcal{P} = (6\hbar c^2/\pi^4\alpha)C_3q_0^2\lambda_0^3/\theta_L^4(z_f - z_L)^4 \gg 4 \times 10^8$ W, which is attainable using femtosecond laser pulses in UTEMs [41,49,57,58].

Transverse e-beam shaping.—The production of on-demand electron spot profiles involves a two-step process comprising the determination of the necessary phase pattern $\varphi(\mathbf{R})$ and from there the required optical beam parameters that generate that phase. While this is a complex task in general, we can find an approximate analytical solution for one-dimensional systems, assuming translational invariance along a direction y perpendicular to the electron velocity. We therefore consider an optical beam characterized by an electric field $\mathbf{E}(\mathbf{r}) = E(x,z)\hat{\mathbf{y}}$ and explore the generation of focal electron shapes defined by a wave function $\psi(x,z)$ independent of y. For light propagating along positive z directions, we can write without loss of generality $E(x,z) = \int_{-k_0}^{k_0} (dk_x/2\pi) e^{i(k_x x + k_z z)} \beta_{k_x}$ with $k_z = \sqrt{k_0 - k_x^2}$ and $k_0 = 2\pi/\lambda_0$ in terms of the expansion coefficients β_{k_x}. Inserting this expression into Eq. (2), we find (see Sec. S6 in the SM [66]) $\varphi(x) = \varphi_0 - (1/2\pi\mathcal{M}\omega^2) \int_{-k_0}^{k_0} dk_x e^{2ik_x x} (k_z/|k_x|) \beta_{k_x} \beta^*_{-k_x}$, where φ_0 is a global phase. Given a target profile $\varphi^{\rm target}(x)$, we can then use the approximation $\beta_{k_x}\beta^*_{-k_x} \approx -2\mathcal{M}\omega^2(|k_x|/k_z) \int dx\, e^{-2ik_x x} \varphi^{\rm target}(x)$ to generate the needed light beam coefficients. A particular solution is obtained by imposing $\beta_{k_x} = \beta^*_{-k_x}$, which renders β_{k_x} as the square root of the right-hand side in the above expression. For any solution, combining these two integral expressions and dismissing φ_0, we find

$$\varphi(x) = \frac{1}{\pi} \int_{-R_{\rm max}}^{R_{\rm max}} dx' \frac{\sin[4\pi(x-x')/\lambda_0]}{x-x'} \varphi^{\rm target}(x'), \quad (5)$$

which yields a diffraction-limited phase profile.

We explore this strategy in Fig. 2, where the left panels present the OFEM phase and the right ones show the corresponding color-matched wave functions obtained by inserting that phase into Eq. (4) without aberrations ($\chi = 0$) and with the integral over θ_y yielding a trivial overall constant factor. Broken curves in Figs. 2(a), 2(b) and red curves in Figs. 2(c)–2(f) stand for target profiles, whereas the rest of the curves are obtained by accounting for optical diffraction [i.e., by transforming the target phase as prescribed by Eq. (5)]. In-plane OFEM and focal coordinates x and x_f are normalized as explained in the caption, thus defining universal curves for a specific choice of the ratio between the objective aperture radius and the light wavelength $R_{\rm max}/\lambda_0 = 12.5$. Linear phase profiles [Fig. 2(a)], which are well reproduced by diffraction-limited illumination, give rise to peaked electron wave functions [Fig. 2(b)] centered at positions $x_f = (A/2\pi)\lambda_{e\perp}$ that depend on the slope of the phase $\varphi = Ax/R_{\rm max} + B$, with the offset value B determining the focal peak phase. The situation is more complicated when aiming to produce two electron peaks, which can be achieved with an intermittent phase profile that combines two different slopes, either without [Figs. 2(c) and 2(d)] or with [Figs. 2(e) and 2(f)] offset to generate symmetric or antisymmetric wave functions, respectively. Light diffraction reduces the contrast of the obtained focal shapes but still tolerates well-defined intensity peaks [Figs. 2(b), 2(d), 2(f), light curves], which become sharper when $R_{\rm max}/\lambda_0$ is increased (see Fig. S1 in the SM [66]).

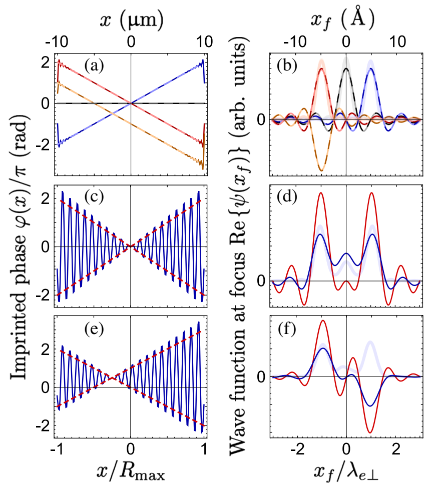

FIG. 2. 1D electron focus shaping. We plot the OFEM-imprinted electron phase [(a),(c),(e)] and the corresponding wave function at the focal plane [(b),(d),(f)]. Dashed curves in (a),(b) and red curves in (c)–(f) correspond to ideal target profiles, while solid curves in (a),(b) and blue curves in (c)–(f) stand for the result obtained by introducing optical diffraction in the OFEM illumination. We consider a linear phase variation (a) leading to single-peak wave functions (b), as well as more complex phase patterns (c),(e) producing symmetric (d) and antisymmetric (f) double-peak wave functions. We take a ratio of the objective-lens semiaperture to the light wavelength $R_{\rm max}/\lambda_0 = 12.5$. The in-plane OFEM and focal coordinates x and x_f are normalized to $R_{\rm max}$ and the projected electron Abbe wavelength $\lambda_{e\perp} = \lambda_e/{\rm NA}$, respectively, where $\lambda_e = 2\pi/q_0$ is the electron wavelength and ${\rm NA} = R_{\rm max}/(z_f - z_L)$ is the microscope numerical aperture. The electron probability density $|\psi|^2$ is shown as color-matching thick-light curves in (b),(d),(f). Upper horizontal scales correspond to 60 keV electrons, $R_{\rm max} = 10\ \mu$m, and ${\rm NA} = 0.01$.

For actual two-dimensional beams, using the consolidated results of image compression theory [67,68], we can find approximate contour spot profiles by setting the OFEM phase to the argument of the Fourier transform of solid shapes filling those contours. This is illustrated in Fig. 3, where panel (b) represents the phase of the object in (a), while panel (c) is the actual diffraction-limited phase obtained by convoluting (b) with a point spread function $J_1(2\pi R/\lambda_0)/R\lambda_0$ (see Sec. S7 in the SM [66]), which produces a blurred but still discernible electron focal image.

Conclusion.—In brief, shaped optical fields can modulate the electron wave function in free space to produce

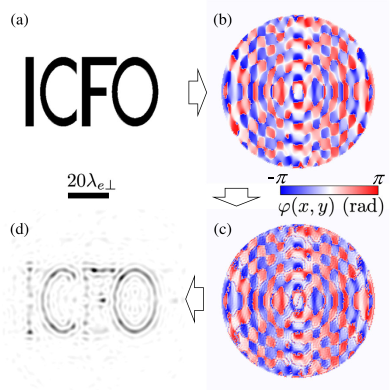

FIG. 3. 2D electron focus shaping. (a) Designated focal shape. (b) Phase of the Fourier transform of (a) (target phase). (c) Diffraction-limited phase to be imprinted by OFEM assuming $R_{\max}/\lambda_0 = 30$. (d) Finally obtained focal profile. The bar shows the scale of (a),(d) in units of $\lambda_{e\perp}$. The phase plots have a radius $R_{\max}$.

on-demand e-beam focal profiles. The required light intensities are reachable using pulsed illumination that is currently available in UTEMs. We have illustrated this idea with simple examples of target optical profiles, but a higher degree of control over the transverse electron wave function should benefit from machine learning techniques [73] for the well-defined problem of finding the optimum light beam angular profile that better fits the desired e-beam spot shape. In combination with spatiotemporal light shaping, the proposed OFEM element should enable the exploration of nanoscale nonlocal correlations in the dynamics of the specimen.

We thank Mathieu Kociak and Ido Kaminer for helpful and enjoyable discussions. This work has been supported in part by European Research Council (Advanced Grant No. 789104eNANO), the European Commission (Horizon 2020 Grants No. FET-Proactive 101017720-EBEAM and No. FET-Open 964591-SMART-electron), the Spanish MINECO (MAT2017-88492-R and SEV2015-0522), the Catalan CERCA Program, and Fundació Privada Cellex.

[*]Corresponding author.
javier.garciadeabajo@nanophotonics.es

[1] M. Haider, H. Rose, S. Uhlemann, E. Schwan, B. Kabius, and K. Urban, Ultramicroscopy **75**, 53 (1998).
[2] P. E. Batson, N. Dellby, and O. L. Krivanek, Nature (London) **418**, 617 (2002).
[3] P. Hawkes and J. Spence, *Springer Handbook of Microscopy* (Springer Nature Switzerland AG, 2019).
[4] P. D. Nellist, M. F. Chisholm, N. Dellby, O. L. Krivanek, M. F. Murfitt, Z. S. Szilagyi, A. R. Lupini, A. Borisevich, W. H. Sides, Jr., and S. J. Pennycook, Science **305**, 1741 (2004).
[5] D. A. Muller, L. Fitting Kourkoutis, M. Murfitt, J. H. Song, H. Y. Hwang, J. Silcox, N. Dellby, and O. L. Krivanek, Science **319**, 1073 (2008).
[6] O. L. Krivanek, T. C. Lovejoy, N. Dellby, T. Aoki, R. W. Carpenter, P. Rez, E. Soignard, J. Zhu, P. E. Batson, M. J. Lagos *et al.*, Nature (London) **514**, 209 (2014).
[7] M. J. Lagos, A. Trügler, U. Hohenester, and P. E. Batson, Nature (London) **543**, 529 (2017).
[8] F. S. Hage, R. J. Nicholls, J. R. Yates, D. G. McCulloch, T. C. Lovejoy, N. Dellby, O. L. Krivanek, K. Refson, and Q. M. Ramasse, Sci. Adv. **4**, eaar7495 (2018).
[9] F. S. Hage, D. M. Kepaptsoglou, Q. M. Ramasse, and L. J. Allen, Phys. Rev. Lett. **122**, 016103 (2019).
[10] J. A. Hachtel, J. Huang, I. Popovs, S. Jansone-Popova, J. K. Keum, J. Jakowski, T. C. Lovejoy, N. Dellby, O. L. Krivanek, and J. C. Idrobo, Science **363**, 525 (2019).
[11] G. Möllenstedt and H. Düker, Z. Phys. **145**, 377 (1956).
[12] J. Verbeeck, G. Bertoni, and P. Schattschneider, Ultramicroscopy **108**, 263 (2008).
[13] C. Bäuerle, D. C. Glattli, T. Meunier, F. Portier, P. Roche, P. Roulleau, S. Takada, and X. Waintal, Rep. Prog. Phys. **81**, 056503 (2018).
[14] G. Guzzinati, A. Beche, H. Lourenco-Martins, J. Martin, M. Kociak, and J. Verbeeck, Nat. Commun. **8**, 14999 (2017).
[15] A. Béché, R. Van Boxem, G. Van Tendeloo, and J. Verbeeck, Nat. Phys. **10**, 26 (2014).
[16] J. Verbeeck, A. Béché, K. Müller-Caspary, G. Guzzinati, M. A. Luong, and M. D. Hertog, Ultramicroscopy **190**, 58 (2018).
[17] J. Verbeeck, H. Tian, and P. Schattschneider, Nature (London) **467**, 301 (2010).
[18] B. J. McMorran, A. Agrawal, I. M. Anderson, A. A. Herzing, H. J. Lezec, J. J. McClelland, and J. Unguris, Science **331**, 192 (2011).
[19] R. Shiloh, Y. Lereah, Y. Lilach, and A. Arie, Ultramicroscopy **144**, 26 (2014).
[20] V. Grillo, A. H. Tavabi, E. Yucelen, P.-H. Lu, F. Venturi, H. Larocque, L. Jin, A. Savenko, G. C. Gazzadi, R. Balboni *et al.*, Opt. Express **25**, 21851 (2017).
[21] R. Shiloh, R. Remez, P.-H. Lu, L. Jin, Y. Lereah, A. H. Tavabi, R. E. Dunin-Borkowski, and A. Arie, Ultramicroscopy **189**, 46 (2018).
[22] P. L. Kapitza and P. A. M. Dirac, Proc. Cambridge Philos. Soc. **29**, 297 (1933).
[23] D. L. Freimund, K. Aflatooni, and H. Batelaan, Nature (London) **413**, 142 (2001).
[24] D. L. Freimund and H. Batelaan, Phys. Rev. Lett. **89**, 283602 (2002).
[25] H. Batelaan, Rev. Mod. Phys. **79**, 929 (2007).
[26] F. J. García de Abajo, Rev. Mod. Phys. **82**, 209 (2010).
[27] M. Kozák, N. Schönenberger, and P. Hommelhoff, Phys. Rev. Lett. **120**, 103203 (2018).
[28] M. Kozák, Phys. Rev. Lett. **123**, 203202 (2019).

[29] D. S. Black, U. Niedermayer, Y. Miao, Z. Zhao, O. Solgaard, R. L. Byer, and K. J. Leedle, Phys. Rev. Lett. **123**, 264802 (2019).
[30] N. Schönenberger, A. Mittelbach, P. Yousefi, J. McNeur, U. Niedermayer, and P. Hommelhoff, Phys. Rev. Lett. **123**, 264803 (2019).
[31] A. Howie, Inst. Phys. Conf. Ser. **161**, 311 (1999).
[32] F. J. García de Abajo and M. Kociak, New J. Phys. **10**, 073035 (2008).
[33] A. Howie, Microsc. Microanal. **15**, 314 (2009).
[34] E. Pomarico, I. Madan, G. Berruto, G. M. Vanacore, K. Wang, I. Kaminer, F. J. García de Abajo, and F. Carbone, ACS Photonics **5**, 759 (2018).
[35] B. Barwick, D. J. Flannigan, and A. H. Zewail, Nature (London) **462**, 902 (2009).
[36] F. J. García de Abajo, A. Asenjo-Garcia, and M. Kociak, Nano Lett. **10**, 1859 (2010).
[37] S. T. Park, M. Lin, and A. H. Zewail, New J. Phys. **12**, 123028 (2010).
[38] S. T. Park and A. H. Zewail, J. Phys. Chem. A **116**, 11128 (2012).
[39] F. O. Kirchner, A. Gliserin, F. Krausz, and P. Baum, Nat. Photonics **8**, 52 (2014).
[40] L. Piazza, T. T. A. Lummen, E. Quiñonez, Y. Murooka, B. Reed, B. Barwick, and F. Carbone, Nat. Commun. **6**, 6407 (2015).
[41] A. Feist, K. E. Echternkamp, J. Schauss, S. V. Yalunin, S. Schäfer, and C. Ropers, Nature (London) **521**, 200 (2015).
[42] T. T. A. Lummen, R. J. Lamb, G. Berruto, T. LaGrange, L. D. Negro, F. J. García de Abajo, D. McGrouther, B. Barwick, and F. Carbone, Nat. Commun. **7**, 13156 (2016).
[43] K. E. Echternkamp, A. Feist, S. Schäfer, and C. Ropers, Nat. Phys. **12**, 1000 (2016).
[44] A. Ryabov and P. Baum, Science **353**, 374 (2016).
[45] G. M. Vanacore, A. W. P. Fitzpatrick, and A. H. Zewail, Nano Today **11**, 228 (2016).
[46] M. Kozák, J. McNeur, K. J. Leedle, H. Deng, N. Schönenberger, A. Ruehl, I. Hartl, J. S. Harris, R. L. Byer, and P. Hommelhoff, Nat. Commun. **8**, 14342 (2017).
[47] A. Feist, N. Bach, T. D. N. Rubiano da Silva, M. Mäller, K. E. Priebe, T. Domräse, J. G. Gatzmann, S. Rost, J. Schauss, S. Strauch *et al.*, Ultramicroscopy **176**, 63 (2017).
[48] K. E. Priebe, C. Rathje, S. V. Yalunin, T. Hohage, A. Feist, S. Schäfer, and C. Ropers, Nat. Photonics **11**, 793 (2017).
[49] G. M. Vanacore, I. Madan, G. Berruto, K. Wang, E. Pomarico, R. J. Lamb, D. McGrouther, I. Kaminer, B. Barwick, F. J. García de Abajo *et al.*, Nat. Commun. **9**, 2694 (2018).
[50] Y. Morimoto and P. Baum, Phys. Rev. A **97**, 033815 (2018).
[51] Y. Morimoto and P. Baum, Nat. Phys. **14**, 252 (2018).
[52] P. Das, J. D. Blazit, M. Tencé, L. F. Zagonel, Y. Auad, Y. H. Lee, X. Y. Ling, A. Losquin, O. S. C. Colliex, F. J. García de Abajo *et al.*, Ultramicroscopy **203**, 44 (2019).
[53] G. M. Vanacore, G. Berruto, I. Madan, E. Pomarico, P. Biagioni, R. J. Lamb, D. McGrouther, O. Reinhardt, I. Kaminer, B. Barwick *et al.*, Nat. Mater. **18**, 573 (2019).
[54] O. Kfir, Phys. Rev. Lett. **123**, 103602 (2019).
[55] V. Di Giulio, M. Kociak, and F. J. García de Abajo, Optica **6**, 1524 (2019).
[56] N. Talebi, Phys. Rev. Lett. **125**, 080401 (2020).
[57] O. Kfir, H. Lourenço-Martins, G. Storeck, M. Sivis, T. R. Harvey, T. J. Kippenberg, A. Feist, and C. Ropers, Nature (London) **582**, 46 (2020).
[58] K. Wang, R. Dahan, M. Shentcis, Y. Kauffmann, A. B. Hayun, O. Reinhardt, S. Tsesses, and I. Kaminer, Nature (London) **582**, 50 (2020).
[59] F. J. García de Abajo, B. Barwick, and F. Carbone, Phys. Rev. B **94**, 041404(R) (2016).
[60] A. Feist, S. V. Yalunin, S. Schäfer, and C. Ropers, Phys. Rev. Research **2**, 043227 (2020).
[61] W. Cai, O. Reinhardt, I. Kaminer, and F. J. García de Abajo, Phys. Rev. B **98**, 045424 (2018).
[62] A. Konečná and F. J. García de Abajo, Phys. Rev. Lett. **125**, 030801 (2020).
[63] H. Müller, J. Jin, R. Danev, J. Spence, H. Padmore, and R. M. Glaeser, New J. Phys. **12**, 073011 (2010).
[64] O. Schwartz, J. J. Axelrod, S. L. Campbell, C. Turnbaugh, R. M. Glaeser, and H. Müller, Nat. Methods **16**, 1016 (2019).
[65] J. J. Axelrod, S. L. Campbell, O. Schwartz, C. Turnbaugh, R. M. Glaeser, and H. Müller, Phys. Rev. Lett. **124**, 174801 (2020).
[66] See Supplemental Material, which includes Refs. [38,55, 67–70], at http://link.aps.org/supplemental/10.1103/PhysRevLett.126.123901 for additional results, including derivations of Eqs. (1), (4), and (5).
[67] M. Hayes, J. Lim, and A. Oppenheim, IEEE Trans. Acoustics Speech Signal Process. **28**, 672 (1980).
[68] D. Aiger and H. Talbot, in *2010 IEEE Computer Society Conference on Computer Vision and Pattern Recognition* (IEEE, San Francisco, 2010), pp. 295–302.
[69] A. Messiah, *Quantum Mechanics* (North-Holland, New York, 1966).
[70] W. H. Press, S. A. Teukolsky, W. T. Vetterling, and B. P. Flannery, *Numerical Recipes* (Cambridge University Press, New York, 1992).
[71] L. J. Allen, M. P. Oxley, and D. Paganin, Phys. Rev. Lett. **87**, 123902 (2001).
[72] D. M. Paganin, T. C. Petersen, and M. A. Beltran, Phys. Rev. A **97**, 023835 (2018).
[73] S. R. Spurgeon, C. Ophus, L. Jones, A. Petford-Long, S. V. Kalinin, M. J. Olszta, R. E. Dunin-Borkowski, N. Salmon, K. Hattar, W.-C. D. Yang *et al.*, Nat. Mater. **20**, 274 (2020).

5 Applications of shaped electron beams

The shaped electron beams introduced in the previous chapters offer many applications. As already shown, the rapidly tunable EPPs, such as those based on electron-light interaction, can eliminate aberrations of conventional electro- and magnetostatic electron lenses and serve as aberration correctors. However, the EPPs could be used to introduce previously impossible approaches in imaging and spectroscopy.

Single-pixel imaging with electron beams

Konečná, A., Rotunno, E., Grillo, V., García de Abajo, F. J. & Vanacore, G. M. Single-Pixel Imaging in Space and Time with Optically Modulated Free Electrons. *ACS Photonics* **10,** 1463–1472 (2023).

In light optics, the detection of light reflected off or transmitted through a sample is typically done using detectors with multiple pixels. Such detectors are however relatively slow and cannot operate at all wavelengths. Imaging with a detector featuring only one pixel was developed to overcome these drawbacks. Of course, a single pixel only carries information on the integrated intensity of the transmitted or reflected light, and we would lack spatial resolution. The sample morphology is therefore reconstructed using variable illumination with differently shaped incoming light beams.

We studied if the same approach is suitable for electron microscopy. We found that by tailoring the electron wave function amplitude with the PINEM-based EPP, we can reconstruct the structure of amplitude objects even when considering limitations of a realistic setup. We have also suggested that the same reconstruction algorithm could be used in time instead of the spatial domain to reconstruct the temporal evolution of a reversible event modifying the sample image contrast.

Entangling electrons and optical excitations

Konečná, A., Iyikanat, F. & García de Abajo, F. J. Entangling free electrons and optical excitations. *Sci. Adv.* **8,** eabo7853 (2022).

It can be shown that the interaction of fast electrons with a sample featuring optical modes results in an entangled electron-sample state which we describe in terms of excited sample states and final electron scattering directions. We formulate an inverse problem when we target a specific final entangled state, which can be achieved by precisely shaping and positioning the incident electron wave function with respect to the sample.

We study two specific cases of a plasmonic nanotriangle with localized surface plasmon modes and a hBN-like molecule supporting vibrational excitations. In both scenarios we can find suitable shapes of incident electron wave functions to achieve the desired final entangled states within a specific energy and momentum window (*i.e.*, we need to perform energy and momentum post-filtering). It is also possible to target excitation of only one sample mode and eliminate the electron interaction with other modes. In such case, we can achieve a selective excitation similar to shown previously[75].

ACS Photonics
pubs.acs.org/journal/apchd5 Article

Single-Pixel Imaging in Space and Time with Optically Modulated Free Electrons

Andrea Konečná,[#] Enzo Rotunno,[#] Vincenzo Grillo, F. Javier García de Abajo,* and Giovanni Maria Vanacore*

Cite This: ACS Photonics 2023, 10, 1463−1472 Read Online

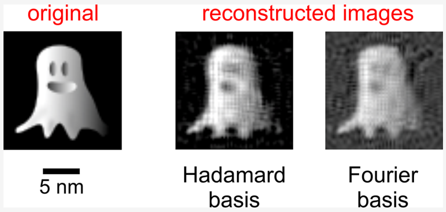

ABSTRACT: Single-pixel imaging, originally developed in light optics, facilitates fast three-dimensional sample reconstruction as well as probing with light wavelengths undetectable by conventional multi-pixel detectors. However, the spatial resolution of optics-based single-pixel microscopy is limited by diffraction to hundreds of nanometers. Here, we propose an implementation of single-pixel imaging relying on attainable modifications of currently available ultrafast electron microscopes in which optically modulated electrons are used instead of photons to achieve subnanometer spatially and temporally resolved single-pixel imaging. We simulate electron beam profiles generated by interaction with the optical field produced by an externally programmable spatial light modulator and demonstrate the feasibility of the method by showing that the sample image and its temporal evolution can be reconstructed using realistic imperfect illumination patterns. Electron single-pixel imaging holds strong potential for application in low-dose probing of beam-sensitive biological and molecular samples, including rapid screening during in situ experiments.

KEYWORDS: *single-pixel imaging, electron microscopy, electron beam shaping, electron−light interaction, ultrafast dynamics*

INTRODUCTION

Single-pixel imaging (SPI) is a key application of structured-wave illumination. This method, which has been recently developed in the context of optical imaging, relies on the interrogation of a certain object using a number of spatially modulated illumination patterns while synchronously measuring the total intensity of the scattered light captured by a single-pixel detector.[1−4] Key elements in this method are (i) a spatial light modulator (SLM), which provides the spatial encoding of the illumination patterns that is necessary for image reconstruction and (ii) the inherent "sparsity" of typical real-space images such that the bulk of the information is only contained in a limited number of pixels, and consequently, compressed sensing (CS) can be used.[5−8] CS uses prior knowledge of sparsity in the coefficient domain, making the reconstruction of the image possible by using a smaller number of measurements. Specifically, $O(K \log(N))$ measurements are typically needed if the information is K-sparse and has N pixels.

The idea behind SPI is to perform a number of sequential measurements with specific illumination patterns expressed on a sufficiently complete basis that can be either incoherent (random patterns) or spatially correlated (such as Hadamard or Fourier bases) with the object to be imaged. The ensemble of M measurements, identified by the vector χ, is then correlated to the image T (sample transmission function) with a number of pixels N_{pix} (in which one usually has $M \ll N_{pix}$) through the $M \times N_{pix}$ measurement matrix H, which contains the employed SLM patterns, such that $\chi = HT$. An image reconstruction algorithm is then used to retrieve a reconstructed image T^*.

In optical microscopy, the SPI technique is well-established and its unique measurement scheme has demonstrated far superior performance with respect to conventional imaging. This is because the illumination patterns used for sampling can be custom-tailored to maximize the amount of information acquired during the measurement, whereas in conventional imaging, information gathering is bound to stochastic processes. Different aspects of this idea have been the topic of recent relevant literature in the field of SPI. In particular, several groups have demonstrated that the ordering of Hadamard patterns, for instance, is of primary importance to maximize the effectiveness of CS algorithms. Different orderings based on the significance of the patterns (i.e., different *a priori* knowledge) have been proposed, such as, to mention a few, the "Russian Dolls" ordering,[9] the "cake

Received: January 12, 2023
Published: April 19, 2023

https://doi.org/10.1021/acsphotonics.3c00047
ACS Photonics 2023, 10, 1463−1472

ACS Photonics pubs.acs.org/journal/apchd5 Article

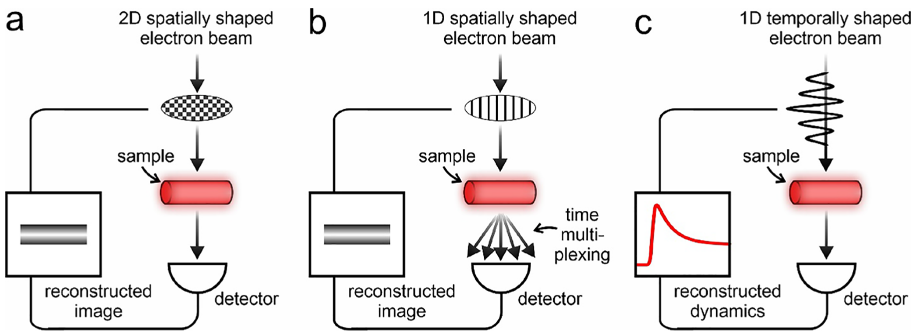

Figure 1. Single-pixel imaging with electrons. Schematic representation of different single-pixel schemes that are amenable to implementation in a transmission electron microscope for 2D spatial imaging (a), 1D spatial imaging (b), and 1D temporal reconstruction (c).

cutting" ordering,[10] the "origami pattern" ordering,[11] and an ordering based on the total variation of the Hadamard basis.[12] This concept can be pushed to its ultimate limit when deep learning (DL) is used to gather *a priori* information and identify the best set of illumination patterns.[13] In this way, it has been demonstrated that, in a limiting scenario in which an object must be identified within a restricted pool of choices, the task can be accomplished without even needing to reconstruct the image,[14] but just after a single SPI measurement. Incidentally, compressed sensing approaches have recently been used in a transmission electron microscope (TEM) for encoding temporal dynamics in electron imaging with a 10 kHz frame rate (100 μs resolution).[15]

In SPI, the number of illumination patterns required for high-quality imaging increases proportionally with the total number of pixels. However, CS methods and, more recently, DL approaches have been considered to substantially reduce the number of measurements necessary for the reconstruction of an image with respect to the total number of unknown pixels. This is an extremely interesting aspect for electron microscopy since it would entail a lower noise, faster response time, and lower radiation dose with respect to conventional imaging. DL approaches, which have already demonstrated superior performances with respect to CS in terms of speed and sampling ratio, can be organized into three categories: (i) improving the quality of reconstructed images;[16−19] (ii) identifying the best illumination strategy by exploiting the features learned during training;[13,14] and (iii) reconstructing the target image directly from the measured signals.[19−23] Also, a reduction in the sampling rate well below the Nyquist limit (down to 6%) has been demonstrated using DL.

Such advantages would be particularly appealing in the context of electron imaging of nano-objects in their biological and/or chemical natural environment, for which the minimization of the electron dose is critical[24,25] to avoid sample damage. Initial attempts have been made using MeV electrons with beam profiles controlled by laser image projection on a photocathode.[26] This method is, however, incompatible with the subnanometer resolution achieved in TEMs through electron collimation stages. Subnanometer resolution for SPI thus requires patterning of high-quality coherent beams. In TEMs, SPI has never been proposed and adopted before, mainly due to the lack of fast, versatile, and reliable electron modulators that would be able to generate the required rapidly changing structured electron patterns.

Here, we propose to implement electron SPI (ESPI) in TEMs by illuminating the specimen using structured electron beams created by a photonic free-electron modulator (here referred as PELM). The PELM is based on properly synthesized localized electromagnetic fields that are able to create an efficient electron modulation for programmable time/energy and space/momentum control of electron beams. Our approach adopts optical field patterns to imprint on the phase and amplitude profile of the electron wave function, an externally controlled well-defined modulation varying both in time and space while the electron pulse crosses the light field. The PELM concept relies on the ability to modulate electrons with optical fields[27−31] down to attosecond timescales[32−36] and along its transverse coordinates.[37−40] In essence, we overcome the problem of designing and fabricating complicated electron optics elements by resorting to shaping light beams, which has been proven a much easier task to perform, while in addition, it enables fast temporal modulation. Indeed, a critical advantage of our approach with respect to existing methods lies on the possibility of achieving an unprecedented ultrafast switching and an extreme flexibility of electron manipulation, which can also open new quantum microscopy applications.[41,42]

A suitable platform for generating the required light field configurations is represented by a light-opaque, yet electron-transparent thin film on which an externally controlled optical pattern is projected from an SLM. The SLM provides an out-of-plane electric field, $E_z(x,y)$, with a customized transverse configuration that embodies the required laterally changing phase and amplitude profiles. In such a configuration, the spatial pattern imprinted on the incident light field by the SLM is directly transferred onto the transverse profile of the electron wavepacket, as recently shown both theoretically[43,44] and experimentally.[45,46] Different portions of the electron wave profile experience a different phase modulation as dictated by the optical pattern. We can thus obtain an externally programmable electron beam with a laterally changing encoded modulation. Moreover, the ability to modulate the electron phase and amplitude has the potential to overcome Poisson noise,[47,48] which is a key aspect that renders the SPI

1464 https://doi.org/10.1021/acsphotonics.3c00047
ACS Photonics 2023, 10, 1463−1472

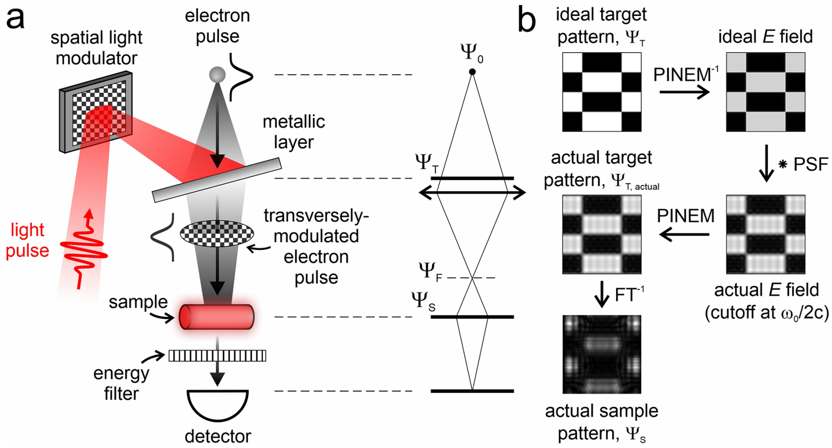

Figure 2. Electron single-pixel imaging (ESPI) via light-mediated electron modulation. (a) Schematic representation of the experimental layout considered for the single-pixel imaging method, implemented by using structured electron beams that are in turn created via light-based manipulation. In our configuration, the spatial pattern imprinted on the incident light field by a programmable spatial light modulator is transferred on the transverse profile of the electron wavepacket by electron−light interaction. (b) Sequence of operations used to calculate the transverse distribution of the electron beam arriving on the sample either when starting from an ideal target pattern or when considering realistic non-ideal conditions. We take a pattern from a Hadamard basis for this example.

method not only feasible but also advantageous in terms of low-dose imaging.

A synchronized intensity measurement followed by a CS or DL reconstruction could then be used to retrieve the sample image. Of course, the possibility to use CS or DL algorithms strictly relies on the amount of *a priori* information known about the object under investigation.[7] This is particularly relevant for ESPI, which can benefit from such *a priori* information, especially in terms of optimal discrimination, more than conventional imaging. In fact, standard TEM imaging is generally object-independent and any *a priori* information is applied only after acquisition to interpret the image, something that can be understood as a denoising procedure. Instead, SPI allows one to optimize the acquisition strategy even before starting the experiment and, thus, holds a direct advantage when using the appropriate pattern basis (see the Supporting Information for a direct example).

In Figure 1a−c, we present different single-pixel schemes that can be implemented in an electron microscope for 2D spatial imaging (Figure 1a), 1D spatial imaging (Figure 1b), and 1D temporal reconstruction (Figure 1c). Specifically, 2D spatial imaging involves the use of a basis of modulation patterns changing in both transverse directions x and y (for instance, a Hadamard basis) for full 2D image reconstruction. Instead, 1D spatial imaging involves the use of modulation patterns changing only along one direction (such as a properly chosen Fourier basis) coupled to temporal multiplexing of the electron beam on the detector, which should enable a simpler and faster 1D image reconstruction.

The third scenario of temporal reconstruction is conceptually novel. Importantly, the 1D single-pixel reconstruction algorithm works for any dependent variable of the system phase space. This implies that, by choosing a well-defined basis of temporally changing modulation functions, such as a series of monochromatic periodic harmonics, it would be possible to reconstruct the time dynamics of a sample. The nature of the method would also allow us to reconstruct the dynamical evolution on a temporal scale much smaller than the electron pulse duration because the resolution depends only on the different frequency components of the basis and not on the length of the electron wavepacket. In principle, this approach could even be implemented with a continuous electron beam.

■ RESULTS

Principles of Single-Pixel Imaging. Single-pixel imaging relies on pre-shaped illumination intensity patterns $H^m(\mathbf{R}_S)$ that are transmitted through a sampled specimen described by a spatially dependent amplitude transmission function $T(\mathbf{R}_S)$, defining the sample image, such that the intensity collected at the detector and associated with the m^{th} illumination pattern is

$$\chi^m = \int d^2\mathbf{R}_S T(\mathbf{R}_S) H^m(\mathbf{R}_S) \tag{1}$$

where we integrate over the sample plane and χ^m are the elements of the measurement vector. The target is to reconstruct the sample transmission function

$$T(\mathbf{R}_S) = \sum_m t^m H^m(\mathbf{R}_S) \tag{2}$$

in terms of coefficients t^m. Now, we assume that the overlap between the illumination patterns is described by

$$\int d^2\mathbf{R}_S H^m(\mathbf{R}_S) H^{m'}(\mathbf{R}_S) = S^{mm'} \tag{3}$$

where $S^{mm'}$ are real-valued coefficients. Then, by substituting eq 2 in eq 1, we retrieve

https://doi.org/10.1021/acsphotonics.3c00047
ACS Photonics 2023, 10, 1463−1472

$$\int d^2\mathbf{R}_S \sum_m t^m H^m(\mathbf{R}_S) H^{m'}(\mathbf{R}_S) = \chi^{m'} \tag{4}$$

We note that if the illumination patterns form an orthonormal basis, then we immediately recover $t^m = \chi^m$ (i.e., the intensities recorded at the detector can directly serve as the expansion coefficients). However, in the general case, where eq 3 produce nonzero nondiagonal elements, the expansion coefficients are

$$t^m = \sum_{m'} \chi^{m'} (S^{-1})^{mm'} \tag{5}$$

By substituting the coefficients back in eq 2, we find the general formula

$$T(\mathbf{R}_S) = \sum_m \sum_{m'} \chi^{m'} (S^{-1})^{mm'} H^m(\mathbf{R}_S) \tag{6}$$

for the reconstruction of the transmission function of the specimen. It is worth noting that, besides our current choice, many different orthogonalization algorithms have been implemented in the literature (see for instance ref 49), which can also be used in combination with our ESPI scheme.

Single-Pixel Imaging in TEM via a Photonic Electron Modulator. We now proceed to analytically describe the scheme utilized to implement the SPI method in an electron microscope. This is shown in Figure 2, where the sample illumination is performed using structured electron beams created via light-induced manipulation. Efficient and versatile phase and intensity modulation of a free electron can be achieved using a PELM device. In our configuration, the spatial pattern imprinted on the incident light field by a programmable SLM is transferred on the transverse profile of the electron wavepacket by electron−light interaction.[45] This is generally dubbed as the photon-induced near-field electron microscopy (PINEM) effect,[27,28,50] although in our configuration, we actually exploit the breaking of translational symmetry induced by a thin film (inverse transition radiation), as described in detail in refs 35 51, and 52, rather than a confined near field induced by a nanoscale structure. The shaped electron wavepacket is then propagated through the TEM column toward the sample.

The electron−light interaction under consideration admits a simple theoretical description:[35,43] starting with an electron wave function ψ_0 incident on the PELM, after the interaction with the light field has taken place, the electron wave function is inelastically scattered into mutually coherent quantized components of amplitude

$$\begin{aligned}\psi_l^m(\mathbf{R}_{\mathrm{PELM}}) &= \psi_0(\mathbf{R}_{\mathrm{PELM}}) J_l(2|\beta^m(\mathbf{R}_{\mathrm{PELM}})|) \\ &\quad \exp(il \arg\{-\beta^m(\mathbf{R}_{\mathrm{PELM}})\}) \\ &= \psi_0(\mathbf{R}_{\mathrm{PELM}}) \mathcal{F}\{\beta^m(\mathbf{R}_{\mathrm{PELM}})\}\end{aligned} \tag{7}$$

corresponding to electrons that have gained ($l > 0$) or lost ($l < 0$) l quanta of photon energy $\hbar\omega$. Here, $\mathcal{F}\{...\}$ represents the PINEM operator, which depends on the imprinted variation of the transverse profile, governed by the coupling coefficient

$$\beta^m(\mathbf{R}) = \frac{e}{\hbar\omega} \int dz E_z^m(\mathbf{R}) \exp(-i\omega z/v) \tag{8}$$

where $\hbar$ is the reduced Planck constant, e is the elementary charge, and the light illumination is further characterized by the electric field $\mathbf{E}^m$ (see the Supporting Information for a detailed calculation of β^m in a metallic thin film). We assume that beam electrons have velocity $\mathbf{v} \parallel \hat{z}$. Due to the inelastic nature of the PINEM interaction, post-interaction electrons gain or lose different numbers of quanta, associated with kinetic energy changes $l\hbar\omega$. In addition, the corresponding contributions to the wave function in eq 7 have different spatial distributions of amplitude and phase. For our purpose, it would be beneficial to place a simple energy filter after the PELM, selecting, for example, the $l = 1$ component only (i.e., electrons gaining one photon energy quantum).

The energy filter needs to efficiently separate a given sideband of the electron energy distribution from the rest of the spectrum. The higher the filter efficiency, the larger the contrast in the modulation pattern, also resulting in a more reduced noise in the final image. However, a relatively modest reduction should be sufficient as we estimate that ∼34% of the electron signal can be placed in the first (gain or loss) sideband. In addition, as we are interested in intensity patterns, the first gain or loss sidebands both deliver the same pattern, and thus, 68% of the electrons are contributing by simultaneously filtering both bands. As a possible improvement, light patterns could be also engineered to eventually remove the need for energy filtering. These possibilities are in fact enabled by properly tuning the light field intensity and, thus, the resulting modulation of the electron beam and its energy distribution.[35]

A practical approach toward the design of the structured beam sample illumination is to define a suitable ψ_l^m and thus also β^m, study the propagation of the wave function to the plane of the specimen, and then find optimal settings for the aperture size, beam energy, and focal distance in such a way that $H^m(\mathbf{R}_S)$ mimics the optical illumination pattern. For ESPI, we thus impose the inelastically scattered electron wave function, ψ_l^m, to be equal to the target pattern, ψ_T, defined within the chosen basis ($\psi_l^m = \psi_T$). Once this is defined, we can retrieve the coupling coefficient, β^m, and, therefore, the light field, E_z^m, to be implemented on the SLM by applying an inverse PINEM transformation, $\mathcal{F}^{-1}\{...\}$, to the target pattern ψ_T (see Figure 2 and also Figure S1 for a Hadamard basis and Figure S2 for a Fourier basis).

Particularly important is to demonstrate the feasibility of the method also under realistic, non-ideal conditions. We do this by applying a momentum cutoff (ω_0/nc, where n = 1,2, and 3) on the retrieved light field defined by a momentum-dependent point spread function (PSF) to take into account the finite illumination wavelength and limited numerical aperture. This produces the actual light field, $E_z^m|_{\mathrm{actual}}$, from which we can calculate the actual coupling coefficient, $\beta^m|_{\mathrm{actual}}$. By applying the PINEM transformation, $\mathcal{F}\{...\}$, we can in turn find the actual target pattern, $\psi_T|_{\mathrm{actual}}$.

The sequence of operations is defined in eq 9 below and visually shown in Figure 2 and Figures S1 and S2:

$$\begin{aligned}&\psi_l^m = \psi_T \rightarrow \beta^m = \mathcal{F}^{-1}\{\psi_T\} \rightarrow \beta^m \\ &|_{\mathrm{actual}} = \beta^m \times \mathrm{PSF}_n \rightarrow \psi_T|_{\mathrm{actual}} = \mathcal{F}\{\beta^m|_{\mathrm{actual}}\}\end{aligned} \tag{9}$$

To maximize the efficiency of the electron amplitude and phase modulation, it is beneficial to place the PELM onto a plane along the microscope column where the beam is extended to diameters much larger than the wavelength of the optical illumination. In such a scenario, we can achieve the

https://doi.org/10.1021/acsphotonics.3c00047
ACS Photonics 2023, 10, 1463−1472

ACS Photonics pubs.acs.org/journal/apchd5 Article

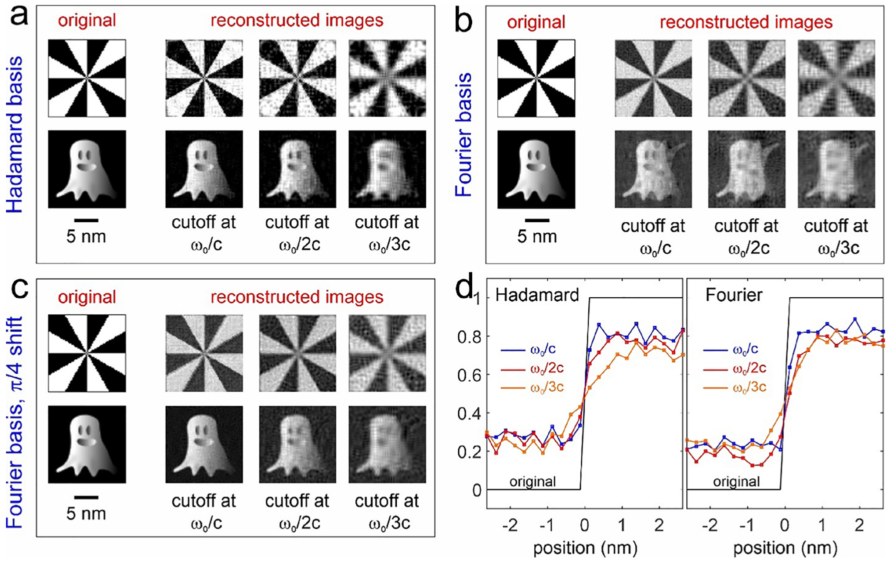

Figure 3. ESPI imaging using Hadamard and Fourier bases. We discuss image reconstruction of a Siemens star and a ghost image performed using a Hadamard basis (a), Fourier basis (b), and Fourier basis with a $\pi/4$ phase shift (c). Reconstructed images are shown for different momentum cutoffs (ω_0/nc, where n = 1,2, and 3) on the retrieved light field. The field of view of all images if 16×16 nm^2. (d) Spatial profiles obtained at the sharp edge of the Siemens star when using a Hadamard basis (left) and a Fourier basis (right). The black curve represents the original image, while the blue, red, and orange curves are associated with frequency cutoffs of ω_0/c, $\omega_0/2c$, and $\omega_0/3c$, respectively. The spatial resolution is estimated by taking the 10:90 value of the error function fit for each curve. We obtain the following resolutions: 0.29 nm at a cutoff of ω_0/c, 0.49 nm at a cutoff of $\omega_0/2c$, and 1.43 nm at a cutoff of $\omega_0/3c$ for the Hadamard-reconstructed images; 0.25 nm at a cutoff of ω_0/c, 0.63 nm at a cutoff of $\omega_0/2c$, and 1.01 nm at a cutoff of $\omega_0/3c$ for the Fourier-reconstructed images.

desired detail in the variation of the transverse wave function profile. However, we then have to rely on electron lenses to focus the beam on the sample.

The focusing action together with the free propagation of the electron wave function between the PELM and the sample planes is described, within the paraxial approximation, as[43]

$$\psi_S^m(\mathbf{R}_S, z_S) \approx \frac{-i\xi}{2\pi}\exp[iq_0(z_S - z_{\mathrm{PELM}})]\exp(-i\xi R_S^2/2)\int d^2\mathbf{R}_{\mathrm{PELM}}\psi_T|_{\mathrm{actual}}(\mathbf{R}_{\mathrm{PELM}})P(\mathbf{R}_{\mathrm{PELM}}) \times \exp\left[iq_0 R_{\mathrm{PELM}}^2/2\left(\frac{1}{z_S - z_{\mathrm{PELM}}} - \frac{1}{f}\right)\right]\exp[-i\xi(x_{\mathrm{PELM}}x_S + y_{\mathrm{PELM}}y_S)] \tag{10}$$

where we have defined $\xi = q_0/(z_S - z_{\mathrm{PELM}})$ with q_0 as the electron wave vector that varies with acceleration voltage and the coordinates $\mathbf{R}_S = (x_S, y_S)$ evolving in the sample $z = z_S$ plane. In addition, $P(\mathbf{R}_{\mathrm{PELM}})$ is a transmission (pupil) function, which becomes 1 if the electron beam passes through an effective aperture placed in the PELM plane and 0 otherwise. We have also replaced the focusing action of all subsequent lenses by a single aberration-free thin lens with a focal distance f placed virtually just after the PELM. The illumination intensity at the sample resulting from eq 10 is

$$I^m(\mathbf{R}_S) = |\psi_S^m(\mathbf{R}_S, z_S)|^2 \propto \frac{\xi^2}{4\pi^2}\left|\int d^2\mathbf{R}_{\mathrm{PELM}} J_1(2|\beta^m(\mathbf{R}_{\mathrm{PELM}})|)\exp(i\arg\{-\beta^m(\mathbf{R}_{\mathrm{PELM}})\}) \times \exp\left[iq_0 R_{\mathrm{PELM}}^2/2\left(\frac{1}{z_S - z_{\mathrm{PELM}}} - \frac{1}{f}\right)\right]\exp[-i\xi(x_{\mathrm{PELM}}x_S + y_{\mathrm{PELM}}y_S)]\right|^2 \tag{11}$$

In Figure 2b and Figures S1 and S2, we show the realistic sample patterns obtained for a Hadamard pattern and a Fourier pattern, chosen as examples when using the following parameters: 200 keV electrons, lens focal distance f = 1 mm,

https://doi.org/10.1021/acsphotonics.3c00047
ACS Photonics 2023, 10, 1463−1472

ACS Photonics pubs.acs.org/journal/apchd5 Article

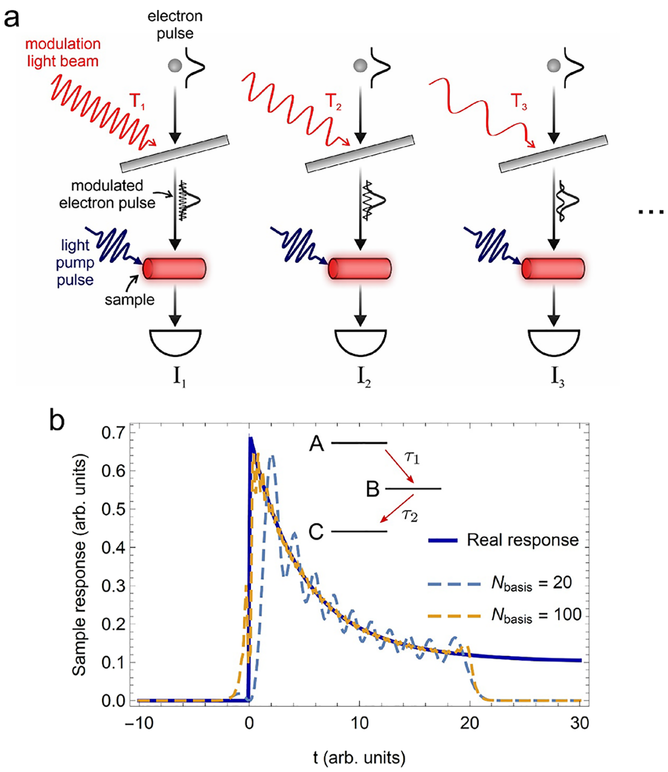

Figure 4. Temporal electron single-pixel imaging. 1D temporal single-pixel reconstruction of a material dynamics. (a) A sequence of long light pulses with varying periods T_j couple to the electron pulse via inverse transition radiation mediated by a metallic plate. We show three different periods: $T_1 < T_2 < T_3$. The longitudinally modulated electron pulse then interacts with the sample in its excited state, and for each period T_j, a scattered intensity I_j is measured. The full temporal evolution of the sample is finally reconstructed from a Fourier-like transformation of the measured signals (see main text for details). (b) Simulated temporal dynamics of a system comprising three states (A, B, and C) according to the diagram in the inset. In the plot, the real response of the system (blue curve), obtained from a rate equation model, is compared with the results of temporal Fourier reconstructions using either 20 basis functions (dashed blue curve) or 100 basis functions (dashed orange curve), as defined in eq S16.

$z_{\mathrm{PELM}} = 0$, $z_{\mathrm{S}} = 1.0008$ mm (defocus of 0.8 μm), and PELM area of $10 \times 10\ \mu\mathrm{m}^2$.

It is important to mention that the ESPI method here proposed is based on electron intensity modulation, rather than phase modulation. Therefore, there are no stringent constraints or requirements on the transverse coherence of the electron beam for the method to work properly. This is what makes this technique readily available in many different experimental configurations where, for instance, one would favor electron current density over coherence to increase the signal-to-noise ratio of the measurements. Of course, if the transverse coherence of the electron beam is commensurate with the spatial scale at the PELM plane in which a significant phase change of the interaction strength β^m takes place, then phase modulation effects could be visible. Under such conditions, the method could take advantage of the possibility to imprint also a phase modulation—besides an amplitude modulation—on the electron transverse profile. This aspect would not only largely increase the number of patterns forming the basis used for the reconstruction, but it could also potentially allow us to image phase objects via the ESPI method in analogy to optical SPI.[53]

An efficient reconstruction can be achieved with a binary illumination using the Hadamard basis, where N sample pixels (e.g., a set of discrete $\mathbf{R}_{\mathrm{S}}$ points) can be reconstructed with N patterns.[54] However, because the Hadamard basis adopts +1 and −1 values to ensure orthogonality, in our case, non-orthonormality issues might arise from the fact that we are working with intensity patterns that are never negative. This aspect, together with the imperfect illumination under realistic, non-ideal conditions (see Figure 2), implies that the actual sample patterns no longer represent an orthonormal basis, and

1468 https://doi.org/10.1021/acsphotonics.3c00047 ACS Photonics 2023, 10, 1463−1472

therefore, the reconstructed sample transmission function, $T(\mathbf{R}_S)$, has to the corrected as described in eqs 5 and 6 via the overlap matrix $S^{mm'}$. The latter and its inverse are shown in Figure S3 for the Hadamard basis. Another option for a basis is to use Fourier-like intensity patterns (Fourier basis), which are defined as

$$H(\mathbf{R}_S, \mathbf{K}, \varphi) = a + b\cos(\mathbf{K}\cdot\mathbf{R}_S + \varphi) \tag{12}$$

where $\mathbf{K}$ are spatial frequencies, a and b are constants, and φ is a phase.

DISCUSSION

Image Reconstruction Using Hadamard and Fourier Bases. We show next several examples of image reconstruction using different bases. For illustration, we consider a Siemens star and a ghost image. The former is a binary {0,1} image with sharp transitions, whereas the latter presents small features, is asymmetric, and shows a gradual intensity variation from 0 to 1. This allows us to test in full the capabilities of the method.

In Figure 3a, we plot the ideal and reconstructed Siemens star and ghost image considering different cutoffs for a Hadamard basis. Clearly, the reconstructions reproduce all the main features of the original images, although we also encounter some noise and even a few negative values, which should not appear. The latter are due to ill-conditioned matrix inversion that we need to use for the reconstruction to compensate for the non-orthonormality of the involved patterns. In Figure 3b, we plot the results of image reconstruction using a Fourier basis. Although for the Siemens star reconstruction, the Fourier basis is performing similarly as the Hadamard basis, for the ghost image, it is clear that the Fourier basis with the same number of patterns (64×64) yields artifacts: a faint mirror-reflected ghost is superimposing on the actual one. The reconstruction with the Fourier basis becomes considerably better when taking into account a phase offset so that the Fourier pattern would no longer be symmetric with respect to the origin. In Figure 3c, we consider an offset of $\varphi = \pi/4$ for the corresponding reconstructed sample images. As a result, the reconstructed ghost image no longer exhibits the faint mirror-reflected artifact that was visible in Figure 3b.

Based on the results of Figure 3, we perform additional quantitative analysis on the images to compare the different reconstruction algorithms and bases. We extract the peak signal-to-noise ratio (PSNR) for both the Siemens star and ghost images for the two bases and three different cutoff frequencies used. From these calculations, we conclude that the reconstruction with a Fourier basis provides values of the PSNR about 10% better than the Hadamard basis for all cutoffs. This is probably due to the fact the Hadamard basis is composed of binary patterns, which are extremely sensitive to distortions caused by diffractive effects during electron propagation, whereas such effects are mitigated for Fourier patterns, which are characterized by gradual, smooth variations. The better quality of the images reconstructed via Fourier patterns directly implies a better image resolution. This is visible in Figure 3d, where we show the effect of the reconstruction on the spatial shape of a particularly sharp feature of the Siemens star. As expected, we observe an increasing broadening when smaller cutoff frequencies are considered. The estimated spatial resolution (for a 10:90 fit of the error function) varies from 0.29 nm at a cutoff of ω_0/c to 1.43 nm at a cutoff of $\omega_0/3c$ for the Hadamard-reconstructed images, whereas the Fourier basis provides slightly better values ranging from 0.25 nm at a cutoff of ω_0/c to 1.01 nm at a cutoff of $\omega_0/3c$.

It is important to mention that the ESPI method that we propose here is intended to be applied to imaging amplitude objects. In fact, in TEMs, a huge amount of information is contained in amplitude-contrast mechanisms, such as mass-thickness contrast, Z-contrast, and bright-field and dark-field imaging as well as electron energy-loss spectroscopy (EELS) and energy-dispersive X-ray spectroscopy (EDX). In a standard TEM, single-pixel detectors are in fact already present. This is for instance the case of the high-angle annular dark-field (HAADF) detector used for performing Z-contrast imaging in STEM mode, which can also provide an experimental verification of the proposed configurations. Besides their use as single-pixel detectors, STEM detectors are also able to gather signals in different angular regimes. Such capability is generally used to access simultaneously more information about the sample (typically chemical information). In the SPI context, we can anticipate a more complex partition of the detector—exploiting its angular detection capability—bridging the gap with other techniques such as integrated differential phase contrast (iDPC) or ptychography.

Temporal Electron Single-Pixel Imaging. As a final aspect, we present a possible implementation of the 1D temporal ESPI reconstruction scheme. The basic idea is to be able to reconstruct the dynamic behavior of a specimen—for instance, its dielectric response to an optically induced electronic excitation—using a sequence of temporally modulated electron pulses with varying periodicity. In Figure 4a, we show the schematics of the experiment, where a sequence of long light pulses with varying periods T_j couple to the electron pulse via inverse transition radiation as mediated by the aforementioned metallic plate. The longitudinally modulated electron pulse then interacts with the sample in its excited state, and for each period T_j, a signal I_j is measured. In terms of the single-pixel formalism, this means that we are choosing a one-dimensional Fourier-like basis for the evolution of the incident electron current as a function of delay time with respect to the pumping time:

$$H^m(t) = e^{-\left(t-\frac{t_{\max}+t_{\min}}{2}\right)^2/2\sigma^2}\sin^2[\pi mt/(t_{\max} - t_{\min})] \tag{13}$$

where $t_{\min}$ and $t_{\max}$ determine the boundaries of the sampling time interval and σ^2 is the variance of the envelope of the probing electron wave function.

As discussed in detail in the Supporting Information, we have simulated the dynamics of a system comprising three states (A, B, and C) according to the diagram in Figure 4b. At time zero, the system is taken to be pumped to an excited state A, from which it decays in a cascade fashion to B and then to C. The time evolution of the populations of the three states within our model system is governed by three rate equations. In Figure 4b, we show the results of a temporal Fourier reconstruction using the basis functions defined in eq 13 in an analogous way to the spatial domain and, again, taking into account the non-orthogonality of the illumination basis. We demonstrate that, already with 20 basis functions, the gross features of the temporal response of the system are retrieved.

It is important to note that the temporal resolution of the measurement no longer depends on the duration of the electron and light pulses but only on the frequency bandwidth of the light field used for electron modulation. This aspect is

https://doi.org/10.1021/acsphotonics.3c00047
ACS Photonics 2023, 10, 1463−1472

extremely interesting because it opens the possibility of using continuous electron and light beams, provided that an efficient electron−light coupling is achieved.[55−59] A possible technological implementation of such a scheme can be realized by using an optical parametric amplifier (OPA) coupled to a difference frequency generator (DFG). This type of configuration would provide light fields with periods in the 0.8−50 fs range, making our approach invaluable to investigate sample dynamics with a temporal resolution that is far below that of state-of-the-art ultrafast electron microscopy, and equally combined with the atomic spatial resolution provided by electron beams.

CONCLUSIONS

In this work, we have proposed the implementation of single-pixel imaging in electron microscopy and predicted that such a method can provide image reconstruction with subnanometer resolution as well as temporal dynamics reconstruction with a precision of a few femtoseconds while benefiting from *a priori* information, especially in terms of optimal discrimination. This potential is examined here when using fast and versatile optically induced electron beam modulation, although it can also be applied to other schemes of electron beam shaping using, for example, electrostatic and magnetostatic devices.[60−64] Finally, the possibility of using deep learning approaches in the reconstruction algorithm can substantially reduce, by more than one order of magnitude,[18] the number of measurements necessary to form an image, thus making such a method suitable for high-spatiotemporal-resolution, low-dose probing of beam-sensitive biological and molecular samples.

ASSOCIATED CONTENT

Supporting Information

The Supporting Information is available free of charge at https://pubs.acs.org/doi/10.1021/acsphotonics.3c00047.

> Section S1: Determination of the coupling coefficient β for a homogeneous thin film; Section S2: detailed description of the analytical calculations behind the temporal electron single-pixel imaging approach; Section S3: additional notes on optimal discrimination and use of *a priori* information in single-pixel imaging and conventional imaging (PDF)

AUTHOR INFORMATION

Corresponding Authors

F. Javier García de Abajo − *ICFO-Institut de Ciencies Fotoniques, The Barcelona Institute of Science and Technology, Barcelona 08860, Spain; ICREA-Institució Catalana de Recerca i Estudis Avançats, 08010 Barcelona, Spain;* orcid.org/0000-0002-4970-4565; Email: javier.garciadeabajo@nanophotonics.es

Giovanni Maria Vanacore − *Laboratory of Ultrafast Microscopy for Nanoscale Dynamics (LUMiNaD), Department of Materials Science, University of Milano-Bicocca, 20121 Milano, Italy;* orcid.org/0000-0002-7228-7982; Email: giovanni.vanacore@unimib.it

Authors

Andrea Konečná − *ICFO-Institut de Ciencies Fotoniques, The Barcelona Institute of Science and Technology, Barcelona 08860, Spain; Central European Institute of Technology, Brno University of Technology, 612 00 Brno, Czech Republic;* orcid.org/0000-0002-7423-5481

Enzo Rotunno − *Centro S3, Istituto di Nanoscienze-CNR, 41125 Modena, Italy;* orcid.org/0000-0003-1313-3884

Vincenzo Grillo − *Centro S3, Istituto di Nanoscienze-CNR, 41125 Modena, Italy;* orcid.org/0000-0002-0389-7664

Complete contact information is available at: https://pubs.acs.org/10.1021/acsphotonics.3c00047

Author Contributions

[#]A.K. and E.R. contributed equally. G.M.V., V.G., and F.J.G.d.A. conceived the idea. A.K. and F.J.G.d.A. performed the PINEM calculations. A.K., E.R., and V.G. performed the SPI calculations. G.M.V., E.R., and A.K. performed the data analysis. All authors participated in interpreting the results, data discussion, and manuscript preparation.

Funding

This work is part of the SMART-electron project that has received funding from the European Union's Horizon 2020 Research and Innovation Programme under grant agreement no. 964591. We also acknowledge partial support by the European Research Council (advanced grant no. 789104-eNANO), the Spanish MINECO (Severo Ochoa CEX2019-000910-S), and the ESF under the project CZ.02.2.69/0.0/0.0/20_079/0017436.

Notes

The authors declare no competing financial interest.

REFERENCES

(1) Edgar, M. P.; Gibson, G. M.; Padgett, M. J. Principles and prospects for single-pixel imaging. *Nat. Photon.* **2019**, *13*, 13.

(2) Duarte, M. F.; et al. Single-pixel imaging via compressive sampling. *IEEE Signal Process. Mag.* **2008**, *25*, 83−91.

(3) Gibson, G. M.; Johnson, S. D.; Padgett, M. J. Single-pixel imaging 12 years on: a review. *Opt. Express* **2020**, *28*, 28190−28208.

(4) Osorio Quero, C. A.; Durini, D.; Rangel-Magdaleno, J.; Martinez-Carranza, J. Single-pixel imaging: An overview of different methods to be used for 3D space reconstruction in harsh environments. *Rev. Sci. Instrum.* **2021**, *92*, 111501.

(5) Candes, E. J.; Romberg, J.; Tao, T. *IEEE Trans. Inf. Theory* **2006**, *52*, 489.

(6) Katz, O.; Bromberg, Y.; Silberberg, Y. *Appl. Phys. Lett.* **2009**, *95*, 131110.

(7) Kovarik, L.; Stevens, A.; Liyu, A.; Browning, N. D. Implementing an accurate and rapid sparse sampling approach for low-dose atomic resolution STEM imaging. *Appl. Phys. Lett.* **2016**, *109*, 164102.

(8) Schwartz, J.; Zheng, H.; Hanwell, M.; Jiang, Y.; Hovden, R. Dynamic compressed sensing for real-time tomographic reconstruction. *Ultramicroscopy* **2020**, *219*, No. 113122.

(9) Sun, M.-J.; Meng, L.-T.; Edgar, M. P.; Padgett, M. J.; Radwell, N. A Russian Dolls ordering of the Hadamard basis for compressive single-pixel imaging. *Sci. Rep.* **2017**, *7*, 3464.

(10) Yu, W.-K. Super Sub-Nyquist Single-Pixel Imaging by Means of Cake-Cutting Hadamard Basis Sort. *Sensors* **2019**, *19*, 4122.

(11) Yu, W.-K.; Liu, Y.-M. Single-Pixel Imaging with Origami Pattern Construction. *Sensors* **2019**, *19*, 5135.

(12) Yu, X.; Stantchev, R. I.; Yang, F.; Pickwell-MacPherson, E. Super Sub-Nyquist Single-Pixel Imaging by Total Variation Ascending Ordering of the Hadamard Basis. *Sci. Rep.* **2020**, *10*, 9338.

(13) Higham, C. F.; Murray-Smith, R.; Padgett, M. J.; Edgar, M. P. Deep learning for real-time single-pixel video. *Sci. Rep.* **2018**, *8*, 2369.

(14) Zhang, Z.; Li, X.; Zheng, S.; Yao, M.; Zheng, G.; Zhong, J. Image-free classification of fast-moving objects using "learned" structured illumination and single-pixel detection. *Opt. Express* **2020**, *28*, 13269−13278.

(15) Reed, B. W.; Moghadam, A. A.; Bloom, R. S.; Park, S. T.; Monterrosa, A. M.; Price, P. M.; Barr, C. M.; Briggs, S. A.; Hattar, K.; McKeown, J. T.; Masiel, D. J. Electrostatic subframing and compressive-sensing video in transmission electron microscopy. *Struct. Dyn.* **2019**, *6*, No. 054303.
(16) Shimobaba, T.; Endo, Y.; Nishitsuji, T.; Takahashi, T.; Nagahama, Y.; Hasegawa, S.; Sano, M.; Hirayama, R.; Kakue, T.; Shiraki, A.; Ito, T. Computational ghost imaging using deep learning. *Opt. Commun.* **2018**, *413*, 147.
(17) Lyu, M.; Wang, W.; Wang, H.; Wang, H.; Li, G.; Chen, N.; Situ, G. Deep-learning-based ghost imaging Meng Lyu. *Sci. Rep.* **2017**, *7*, 17865.
(18) He, Y.; Gao, W.; Dong, G.; Zhu, S.; Chen, H.; Zhang, A.; Xu, Z. Ghost Imaging Based on Deep Learning. *Sci. Rep.* **2018**, *8*, 6469.
(19) Wang, F.; Wang, C.; Deng, C.; Han, S.; Situ, G. Single-pixel imaging using physics enhanced deep learning. *Photon. Res.* **2022**, *10*, 104−110.
(20) Liu, S.; Meng, X.; Yin, Y.; Wu, H.; Jiang, W. Computational ghost imaging based on an untrained neural network. *Opt. Lasers Eng.* **2021**, *147*, 106744.
(21) He, Y.; Duan, S.; Yuan, Y.; Chen, H.; Li, J.; Xu, Z. Ghost Imaging Based on Recurrent Neural Network. *Opt. Express* **2022**, *30*, 23475−23484.
(22) Wang, F.; Wang, H.; Wang, H.; Li, G.; Situ, G. Learning from simulation: An end-to-end deep-learning approach for computational ghost imaging. *Opt. Express* **2019**, *27*, 25560−25572.
(23) Wu, H.; Wang, R.; Zhao, G.; Xiao, H.; Wang, D.; Liang, J.; Tian, X.; Cheng, L.; Zhang, X. Ruizhou Wang, Genping Zhao, Huapan Xiao, Daodang Wang, Jian Liang, Xiaobo Tian, Lianglun Cheng, and Xianmin Zhang, Sub-Nyquist computational ghost imaging with deep learning. *Opt. Express* **2020**, *28*, 3846−3853.
(24) Chen, Q.; Dwyer, C.; Sheng, G.; Zhu, C.; Li, X.; Zheng, C.; Zhu, Y. Imaging Beam-Sensitive Materials by Electron Microscopy. *Adv. Mater.* **2020**, *32*, 1907619.
(25) Egerton, R. F. Radiation damage to organic and inorganic specimens in the TEM. *Micron* **2019**, *119*, 72−87.
(26) Li, S.; Cropp, F.; Kabra, K.; Lane, T. J.; Wetzstein, G.; Musumeci, P.; Ratner, D. Electron Ghost Imaging. *Phys. Rev. Lett.* **2018**, *121*, No. 114801.
(27) Barwick, B.; Flannigan, D. J.; Zewail, A. H. Photon-induced near-field electron microscopy. *Nature* **2009**, *462*, 902−906.
(28) Feist, A.; Echternkamp, K. E.; Schauss, J.; Yalunin, S. V.; Schäfer, S.; Ropers, C. Quantum coherent optical phase modulation in an ultrafast transmission electron microscope. *Nature* **2015**, *521*, 200−203.
(29) Vanacore, G. M.; Madan, I.; Carbone, F. Spatio-temporal shaping of a free-electron wave function via coherent light−electron interaction. *La Rivista del Nuovo Cimento* **2020**, *43*, 567−597.
(30) Di Giulio, V.; Kociak, M.; García de Abajo, F. J. Probing quantum optical excitations with fast electrons. *Optica* **2019**, *6*, 1524−1534.
(31) Reinhardt, O.; Kaminer, I. Theory of shaping electron wavepackets with light. *ACS Photon.* **2020**, *7*, 2859.
(32) Priebe, K. E.; Rathje, C.; Yalunin, S. V.; Hohage, T.; Feist, A.; Schäfer, S.; Ropers, C. Attosecond electron pulse trains and quantum state reconstruction in ultrafast transmission electron microscopy. *Nat. Photon.* **2017**, *11*, 793.
(33) Kozák, M.; Schönenberger, N.; Hommelhoff, P. Ponderomotive generation and detection of attosecond free-electron pulse trains. *Phys. Rev. Lett.* **2018**, *120*, No. 103203.
(34) Morimoto, Y.; Baum, P. Diffraction and microscopy with attosecond electron pulse trains. *Nat. Phys.* **2018**, *14*, 252.
(35) Vanacore, G. M.; et al. Attosecond coherent control of free-electron wave functions using semi-infinite light fields. *Nat. Commun.* **2018**, *9*, 2694.
(36) Tsarev, M.; Ryabov, A.; Baum, P. Free-electron qubits and maximum-contrast attosecond pulses via temporal Talbot revivals. *Phys. Rev. Res.* **2021**, *3*, No. 043033.
(37) Kealhofer, C.; Schneider, W.; Ehberger, D.; Ryabov, A.; Krausz, F.; Baum, P. All-optical control and metrology of electron pulses. *Science* **2016**, *352*, 429.
(38) Vanacore, G. M.; et al. Ultrafast generation and control of an electron vortex beam via chiral plasmonic near fields. *Nat. Mater.* **2019**, *18*, 573−579.
(39) Feist, A.; Yalunin, S. V.; Schäfer, S.; Ropers, C. High-purity free-electron momentum states prepared by three-dimensional optical phase modulation. *Phys. Rev. Research* **2020**, *2*, No. 043227.
(40) Schwartz, O.; Axelrod, J. J.; Campbell, S. L.; Turnbaugh, C.; Glaeser, R. M.; Müller, H. Laser phase plate for transmission electron microscopy. *Nat. Methods* **2019**, *16*, 1016−1020.
(41) Madan, I.; Vanacore, G. M.; Gargiulo, S.; LaGrange, T.; Carbone, F. The quantum future of microscopy: Wave function engineering of electrons, ions, and nuclei. *App. Phys. Lett.* **2020**, *116*, 230502.
(42) Konečná, A.; Iyikanat, F.; García de Abajo, F. J. Entangling free electrons and optical excitations. *Sci. Adv.* **2022**, *8*, eabo7853.
(43) Konečná, A.; García de Abajo, F. J. Electron beam aberration correction using optical near fields. *Phys. Rev. Lett.* **2020**, *125*, No. 030801.
(44) García de Abajo, F. J.; Konečná, A. Optical modulation of electron beams in free space. *Phys. Rev. Lett.* **2021**, *126*, No. 123901.
(45) Madan, I.; Leccese, V.; Mazur, A.; Barantani, F.; LaGrange, T.; Sapozhnik, A.; Tengdin, P. M.; Gargiulo, S.; Rotunno, E.; Olaya, J.-C.; Kaminer, I.; Grillo, V.; García De, F. J.; Carbone, F.; Vanacore, G. M. Ultrafast Transverse Modulation of Free Electrons by Interaction with Shaped Optical. *ACS Photonics* **2022**, *9*, 3215−3224.
(46) Mihaila, M. C. C.; Weber, P.; Schneller, M.; Grandits, L.; Nimmrichter, S.; Juffmann, T. Transverse Electron Beam Shaping with Light. *Phys. Rev. X* **2022**, *12*, No. 031043.
(47) Sekia, T.; Ikuhara, Y.; Shibata, N. Theoretical framework of statistical noise in scanning transmission electron microscopy. *Ultramicroscopy* **2018**, *193*, 118−125.
(48) Mevenkamp, N.; Binev, P.; Dahmen, W.; Voyles, P. M.; Yankovich, A. B.; Berkels, B. Poisson noise removal from high-resolution STEM images based on periodic block matching. *Adv. Struct. Chem. Imaging* **2015**, *1*, 1.
(49) Kallepalli, A.; Viani, L.; Stellinga, D.; Rotunno, E.; Bowman, R.; Gibson, G. M.; Sun, M.-J.; Rosi, P.; Frabboni, S.; Balboni, R.; Migliori, A.; Grillo, V.; Padgett, M. J. Challenging Point Scanning across Electron Microscopy and Optical Imaging using Computational Imaging. *Intell. Comput.* **2022**, *2022*, DOI: 10.34133/icomputing.0001.
(50) Piazza, L.; et al. Simultaneous observation of the quantization and the interference pattern of a plasmonic near-field. *Nat. Commun.* **2015**, *6*, 6407.
(51) Madan, I.; et al. Holographic imaging of electromagnetic fields via electron-light quantum interference. *Sci. Adv.* **2019**, *5*, No. eaav8358.
(52) Morimoto, Y.; Baum, P. Attosecond control of electron beams at dielectric and absorbing membranes. *Phys. Rev. A* **2018**, *97*, No. 033815.
(53) Hu, X.; Zhang, H.; Zhao, Q.; Yu, P.; Li, Y.; Gong, L. Hao Zhang, Qian Zhao, Panpan Yu, Yinmei Li, and Lei Gong, Single-pixel phase imaging by Fourier spectrum sampling. *Appl. Phys. Lett.* **2019**, *114*, No. 051102.
(54) Zhang, Z.; Wang, X.; Zheng, G.; Zhong, J. Hadamard single-pixel imaging versus Fourier single-pixel imaging. *Opt. Express* **2017**, *25*, 19619−19639.
(55) Kfir, O.; Lourenço-Martins, H.; Storeck, G.; Sivis, M.; Harvey, T. R.; Kippenberg, T. J.; Feist, A.; Ropers, C. Controlling free electrons with optical whispering-gallery modes. *Nature* **2020**, *582*, 46−49.
(56) Wang, K.; Dahan, R.; Shentcis, M.; Kauffmann, Y.; Tsesses, S.; Kaminer, I. Coherent Interaction between Free Electrons and Cavity Photons. *Nature* **2020**, *582*, 50.
(57) Dahan, R.; Nehemia, S.; Shentcis, M.; Reinhardt, O.; Adiv, Y.; Shi, X.; Be'er, O.; Lynch, M. H.; Kurman, Y.; Wang, K.; Kaminer, I.

Resonant phase-matching between a light wave and a free-electron wavefunction. *Nat. Phys.* **2020**, *16*, 1123−1131.
(58) Dahan, R.; Gorlach, A.; Haeusler, U.; Karnieli, A.; Eyal, O.; Yousefi, P.; Segev, M.; Arie, A.; Eisenstein, G.; Hommelhoff, P.; Kaminer, I. Imprinting the quantum statistics of photons on free electrons. *Science* **2021**, *373*, 1309−1310.
(59) Henke, J.-W.; Sajid Raja, A.; Feist, A.; Huang, G.; Arend, G.; Yang, Y.; Kappert, F. J.; Ning Wang, R.; Möller, M.; Pan, J.; Liu, J.; Kfir, O.; Ropers, C.; Kippenberg, T. J. Integrated photonics enables continuous-beam electron phase modulation. *Nature* **2021**, *600*, 653−658.
(60) Béché, A.; Van Boxem, R.; Van Tendeloo, G.; Verbeeck, J. Magnetic monopole field exposed by electrons. *Nat. Phys.* **2014**, *10*, 26−29.
(61) Verbeeck, J.; Béché, A.; Müller-Caspary, K.; Guzzinati, G.; Luong, M. A.; Den Hertog, M. Hertog, demonstration of a 2×2 programmable phase plate for electrons. *Ultramicroscopy* **2018**, *190*, 58.
(62) Pozzi, G.; Grillo, V.; Lu, P.-H.; Tavabi, A. H.; Karimi, E.; Dunin-Borkowski, R. E. Design of electrostatic phase elements for sorting the orbital angular momentum of electrons. *Ultramicroscopy* **2020**, *208*, No. 112861.
(63) Tavabi, A. H.; Rosi, P.; Rotunno, E.; Roncaglia, A.; Belsito, L.; Frabboni, S.; Pozzi, G.; Gazzadi, G. C.; Lu, P.-H.; Nijland, R.; Ghosh, M.; Tiemeijer, P.; Karimi, E.; Dunin-Borkowski, R. E.; Grillo, V. Experimental Demonstration of an Electrostatic Orbital Angular Momentum Sorter for Electron Beams. *Phys. Rev. Lett.* **2021**, *126*, No. 094802.
(64) Schachinger, T.; Hartel, P.; Lu, P.-H.; Löffler, S.; Obermair, M.; Dries, M.; Gerthsen, D.; Dunin-Borkowski, R. E.; Schattschneider, P. Experimental realization of a $\pi/2$ vortex mode converter for electrons using a spherical aberration corrector. *Ultramicroscopy* **2021**, *229*, No. 113340.

https://doi.org/10.1021/acsphotonics.3c00047
ACS Photonics 2023, 10, 1463−1472

SCIENCE ADVANCES | RESEARCH ARTICLE

PHYSICS

Entangling free electrons and optical excitations

Andrea Konečná[1,2], Fadil Iyikanat[1], F. Javier García de Abajo[1,3]*

The inelastic interaction between flying particles and optical nanocavities gives rise to entangled states in which some excitations of the latter are paired with momentum changes in the former. Specifically, free-electron entanglement with nanocavity modes opens appealing opportunities associated with the strong interaction capabilities of the electrons. However, the achievable degree of entanglement is currently limited by the lack of control over the resulting state mixtures. Here, we propose a scheme to generate pure entanglement between designated optical-cavity excitations and separable free-electron states. We shape the electron wave function profile to select the accessible cavity modes and simultaneously associate them with targeted electron scattering directions. This concept is exemplified through theoretical calculations of free-electron entanglement with degenerate and nondegenerate plasmon modes in silver nanoparticles and atomic vibrations in an inorganic molecule. The generated entanglement can be further propagated through its electron component to extend quantum interactions beyond existing protocols.

INTRODUCTION

Although entangled states in the context of quantum optics are generally relying on photons (*1*, *2*), the exploration of entanglement with other types of information carriers could open a wealth of possibilities to find previously unexplored phenomena and materialize disruptive protocols for quantum metrology and microscopy (*3*–*5*). In particular, free electrons are advantageous candidates because they can undergo substantial inelastic scattering by nanostructures (*6*), which is an attribute enabling electron energy-loss spectroscopy (EELS) performed in electron microscopes to reveal the presence, strength, and spatial distribution of optical excitations down to the atomic scale (*7*–*13*). Actually, low-loss EELS has been extensively used to study atomic vibrations in low-dimensional materials (*14*, *15*) and molecules (*16*–*19*), collective excitations such as plasmons (*20*–*24*) and phonon polaritons (*11*, *25*–*27*), and photon confinement in optical cavities (*28*–*30*).

In momentum-resolved EELS, each excitation event produced by a traversing electron is individually identified through an electron measurement as a function of the deflection angle and energy loss (*31*–*33*), and therefore, this configuration already generates entanglement between electron states with different energy/momentum and excitations in the sampled structure. Consequently, the post-interaction electron-sample state has the form

$$|\Psi_f\rangle = \sum_n \int d^2\mathbf{Q}_f \, \alpha^f_{\mathbf{Q}_f,n} \, |\mathbf{Q}_f\rangle \otimes |n\rangle \qquad (1)$$

where n and $\mathbf{Q}_f$ run over final sample and electron-wave-vector states, respectively, and $\alpha^f_{\mathbf{Q}_f,n}$ are complex scattering amplitudes (*13*). In some simple scenarios, such as the interaction with translationally invariant structures supporting surface polaritons, the excitation of these modes is associated with the transfer of definite amounts of energy and momentum, thus producing electron entanglement with a continuum of optical modes, which reveals their dispersion relation when measuring the electrons as a function of energy loss and deflection angle (*31*, *33*–*36*). Entangled states produced by interaction with a polaritonic band in a translationally invariant specimen can even include the creation of multiple surfaces modes (*32*, *37*, *38*), as reported in the first experimental evidence of surface plasmons (*37*). However, for localized modes and, generally, in the interaction with photonic cavities, the resulting electron-specimen mixture of states is too complex to be of practical interest for quantum technologies.

Free-electron waves can be manipulated with great precision thanks to an impressive series of advances that occurred in electron microscopy over the past decades. Now, electron beams (e-beams) can be collimated and focused with sub-ångstrom spatial precision (*39*), as well as monochromatized and energy-filtered within a few millielectronvolt energy resolution (*11*, *25*). In addition to traditional electron-optics elements such as lenses (*40*) and beam splitters (*41*–*43*), electron waves can be laterally shaped into on-demand profiles through static (*44*, *45*) and programmable (*46*) plates, as well as through interaction with spatially modulated optical fields (*47*–*51*). The manipulation of the longitudinal electron wave function component is also possible in ultrafast electron microscopes (*52*), which enable temporal electron-pulse compression down to attosecond (*53*–*55*) time scales, and further endows free electrons with the ability to transfer quantum coherence among different systems (*56*, *57*). The field is thus ripe for the exploitation of free electrons as additional elements in the quantum technology Lego, but as impressive as these advances may seem, they have not yet been leveraged to generate pure entanglement between light and free electrons in which only a few quantum states are involved in Eq. 1.

Here, we demonstrate through rigorous quantum theory that pure entanglement between electrons and confined optical modes can be generated by suitably patterning the transverse incident electron wave function. As schematically illustrated in Fig. 1A, the electron undergoes a change in the direction of propagation after being inelastically scattered by a specimen, and we prepare the incident electron wave profile (amplitude and phase) in such a way that only a few sample excitations are accessible (two in the figure), leading to separable transmission directions (transverse wave vectors $\mathbf{Q}_1$ and $\mathbf{Q}_2$). The two possible excitations created by the electron together with their different associated scattering directions form an entangled state. In essence, we specify a finite volume in the configuration space of transmitted electrons defined by an energy-loss window $\Delta\hbar\omega$ and a transverse momentum area $\Delta\hbar\mathbf{Q}_f$ in which the final state only

[1]ICFO-Institut de Ciencies Fotoniques, The Barcelona Institute of Science and Technology, Castelldefels, Barcelona 08860, Spain. [2]Central European Institute of Technology, Brno University of Technology, Brno 61200, Czech Republic. [3]ICREA-Institució Catalana de Recerca i Estudis Avançats, Passeig Lluís Companys 23, 08010 Barcelona, Spain.
*Corresponding author. Email: javier.garciadeabajo@nanophotonics.es

SCIENCE ADVANCES | RESEARCH ARTICLE

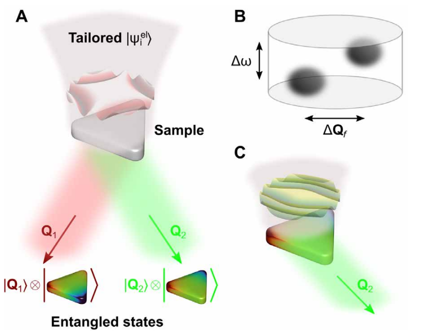

Fig. 1. Proposed scheme for the generation of entangled electron–cavity states. (**A**) A preshaped electron interacts with a nanostructure (a triangular plasmonic cavity) supporting well-defined optical or vibrational modes. The incident electron wave function $|\psi_i^{el}\rangle$ is tailored such that we obtain entangled states after interaction, correlating different specimen excitations (colored triangles) with separated electron scattering directions (final electron state having components of transverse wave vectors $\mathbf{Q}_1$ and $\mathbf{Q}_2$). A maximally entangled electron-specimen state is thus produced as the sample is in a superposition of excited states correlated with different electron scattering directions. (**B**) Electrons are emerging along separate spots within a finite region of size $\Delta\hbar\omega \times \Delta\hbar\mathbf{Q}_f$ in the configuration space of energy-loss and transverse-momentum transfers. (**C**) Momentum filtering at the electron detector allows us to project on the desired sample mode and eventually explore its dynamics through subsequent interrogation, for example, by exposure to a synchronized light pulse.

populates two well-defined spots (Fig. 1B). As we demonstrate below, this approach can also be used to create heralded single sample excitations (Fig. 1C). In addition, manipulation of the electron component in electron–sample entangled states through, for example, electron interference could be used to process quantum information and imprint it on other (eventually macroscopic) objects via subsequent interactions.

RESULTS

Free-electron interaction with confined optical modes

We intend to synthesize an electron–sample state, as described by Eq. 1, with the free-electron component piled up at separate regions in momentum–energy space (Fig. 1B) and a different sample excitation associated with each of those regions. The starting point is the initial combined state

$$|\Psi_i\rangle = |\psi_i^{el}\rangle \otimes |0\rangle$$

where the specimen is in its ground state $|0\rangle$ and the incident electron wave function, whose spatial dependence is given by

$$\psi_i^{el}(\mathbf{R}) = \int d^2\mathbf{Q}_i\, \alpha^i_{\mathbf{Q}_i} (e^{i\mathbf{Q}_i\cdot\mathbf{R}}/2\pi) \qquad (2)$$

is prepared as a combination of momentum states with coefficients $\alpha^i_{\mathbf{Q}_i}$ determined through the use of customized transmission masks (*44*, *45*, *58*) or phase imprinting based on electrostatic (*46*) and optical (*47*, *49*) fields. We consider incident monochromatic electrons, such that the dependence of the electron wave function on two-dimensional (2D) transverse coordinates $\mathbf{R}$ and its decomposition in 2D wave vectors $\mathbf{Q}_i$ is everything we need to describe the electron in the interaction region without loss of generality.

The electron–specimen interaction operates a linear transformation relating the final coefficients $\alpha^f_{\mathbf{Q}_f,n}$ in Eq. 1 to $\alpha^i_{\mathbf{Q}_i}$ in Eq. 2. More precisely,

$$\alpha^f_{\mathbf{Q}_f,n} = \int d^2\mathbf{Q}_i\, M_{\mathbf{Q}_f-\mathbf{Q}_i,n}\, \alpha^i_{\mathbf{Q}_i} \qquad (3)$$

where $M_{\mathbf{Q}_f-\mathbf{Q}_i,n}$ only depends on the momentum transfer $\hbar(\mathbf{Q}_i - \mathbf{Q}_f)$ for each excited state n (see Methods).

A connection can be readily established to EELS experiments, in which electron counts are recorded as a function of the energy loss $\hbar\omega$, thus yielding a frequency- and momentum-resolved loss probability $\Gamma_{EELS}(\mathbf{Q}_f, \omega) = \sum_n |\alpha^f_{\mathbf{Q}_f,n}|^2\, \delta(\omega - \omega_n)$, where $\hbar\omega_n$ is the excitation energy of the sample mode n. Within first-order perturbation theory and further adopting the electrostatic and nonrecoil approximations, the angle-resolved EELS probability can be expressed in terms of mode-dependent dimensionless spectral functions $g_n(\omega)$ as

$$\Gamma_{EELS}(\mathbf{Q}_f, \omega) = \frac{e^2}{4\pi^3 \hbar v^2} \sum_n g_n(\omega) \times \left| \int d^2\mathbf{R}\, \psi_i^{el}(\mathbf{R})\, e^{-i\mathbf{Q}_f\cdot\mathbf{R}}\, w_n(\mathbf{R}, \omega) \right|^2 \qquad (4)$$

where v is the electron velocity and

$$w_n(\mathbf{R}, \omega) \propto \int d^2\mathbf{Q}\, e^{i\mathbf{Q}\cdot\mathbf{R}}\, M_{\mathbf{Q},n} \qquad (5)$$

describes the spatial profile of mode n [see details in Methods, including expressions for the quantities $g_n(\omega)$ and $w_n(\mathbf{R}, \omega)$ associated with plasmons and atomic vibrations].

Here, we are interested in determining the incident electron wave function profile (i.e., the momentum-dependent coefficients $\alpha^i_{\mathbf{Q}_i}$) such that different sample modes n are associated with final wave function coefficients $\alpha^f_{\mathbf{Q}_f,n}$ within well-separated regions in momentum space (see Fig. 1B). To demonstrate the feasibility of this concept in the synthesis of electron–sample entanglement, we invert Eq. 3 with a predetermined choice of $\alpha^f_{\mathbf{Q}_f,n}$, which we set to designated values for each sample excitation n within a targeted finite-size region in $\mathbf{Q}_f$ space (see details in Methods). This simple procedure is sufficient for the proof-of-principle demonstration that we pursue in this work. However, in one of the examples, we present further improvement of the results when using an iterative method. Other schemes for incident electron wave function optimization could rely on neural-network training (*59*).

Selected excitation of individual plamons

As a preliminary step before addressing electron–sample entanglement, we tackle the problem of selectively exciting a single plasmon in a metallic nanoparticle. Although this can be achieved through post-selection of a small range of scattered electron wave vectors (*42*), we formulate a solution in which the plasmon-exciting electrons emerge within a relatively large region in momentum space, and this solution is generalized below to create entanglement. We consider a silver triangle that sustains five plasmon modes in the spectral region between 2.4 and 3.7-eV spectral region (*60*): two sets of doubly degenerate dipolar (blue curve and circles, $n = 1,2$) and quadrupolar (red, $n = 4,5$) plasmons and one nondegenerate hexapolar mode (green, $n = 3$), as revealed by the spatial and spectral functions plotted in Fig. 2 (A and B) (see details of the calculation in Methods). We then optimize the incident electron wave function over a finite $\mathbf{Q}_i$ region discretized with 1257 pixels and defined by a convergence half-angle $\varphi_i = 1.5$ mrad, such that either $n = 1,2$ or $n = 3$ is the only mode excited when the scattered electrons are collected over a $\mathbf{Q}_f$ region spanning a half-angle $\varphi_f = 0.75$ mrad (discretized with 49 pixels) and energy-filtered between 2.4 and 3.3 eV. Incidentally, modes $n = 1$ and 2 are dipolar, so they can be effectively excited in the aloof configuration, while mode $n = 3$ is hexapolar and requires the electron to pass closer to the particle to be excited.

The resulting real-space profiles of $\psi_i^{\rm el}(\mathbf{R})$ are shown in the insets of Fig. 2C (circular color plots; see also fig. S6A for the incident electron wave functions in $\mathbf{Q}_i$ space), along with the color-matched EELS probability curves obtained from Eq. 4 by collecting only electrons that emerge within the indicated $\mathbf{Q}_f$ and energy region. In a typical experimental scenario with an unshaped electron beam, multiple modes are excited by the incident electron because they have overlapping spatial distributions (Fig. 2A), and the EELS probability integrated over all possible $\mathbf{Q}_f$'s is rigorously given by the incoherent average over incident electron positions $\mathbf{R}$, weighted by the electron probability $|\psi_i^{\rm el}(\mathbf{R})|^2$ (see Methods) (*6*, *61*). However, our simple optimization procedure is capable of placing the weight of the excitation of either $n = 1,2$ or $n = 3$ mode preferably inside the $\mathbf{Q}_f$ region defined by a collection half-angle $\varphi_f = 0.75$ mrad. Such an optimization can be performed for smaller or larger convergence and collection angles as shown in fig. S1.

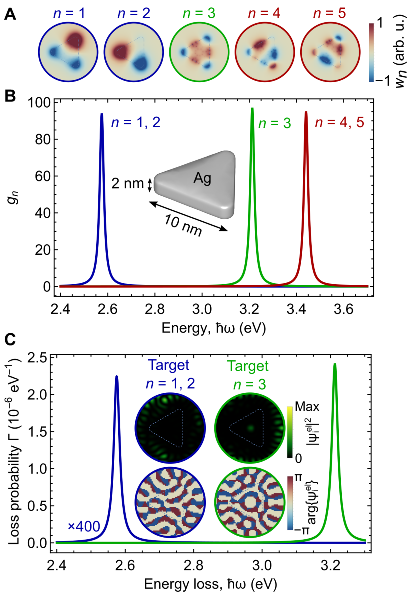

Fig. 2. Selective excitation of plasmon modes in a silver nanotriangle. (**A** and **B**) Spatial profiles (A) and spectral functions (B) associated with plasmons in a silver nanotriangle with a thickness of 2 nm and a side length of 10 nm. We find two sets of degenerate modes (blue and red peaks) and one nondegenerate mode (green; see color labels matched with the index n). (**C**) Electron energy-loss spectra for two optimized incident electron wave function profiles $\psi_i^{\rm el}(\mathbf{R})$. The insets show maps of the probability density and phase of the incident wave functions in the space of transverse coordinates $\mathbf{R}$, framed in color-matched circumferences. The optimization is carried out for 100 keV electrons, an electron detector consisting of 49 pixels, an incident convergence half-angle $\varphi_i = 1.5$ mrad, and a collection half-angle $\varphi_f = 0.75$ mrad. The nanotriangle contour is indicated by thin dashed lines in (A) and (C).

Generation of electron–plasmon entangled states

We now apply the principle of $\psi_i^{\rm el}$ shaping to demonstrate the generation of electron–sample entanglement for the same triangular particle as considered above. Specifically, we focus on the lowest-energy degenerate plasmons $n = 1,2$ (i.e., we consider post-selection of these final states by an energy filter) and aim at correlating these excitations with final electron momentum states along separate $\mathbf{Q}_f$ directions (Fig. 3A). By maximizing the fraction of the signal associated with the targeted excitation in each respective $\mathbf{Q}_f$ direction through the steepest-descent method, we find the optimized electron wave function shown in real space in Fig. 3B (and in momentum space in fig. S6B), from which we obtain the actual scattered electron distribution plotted in Fig. 3C in $\mathbf{Q}_f$ space for components corresponding to the excitation of $n = 1$ (top) and $n = 2$ (bottom) modes.

When examining the resulting degree of entanglement, we express the final electron–sample state after energy filtering and momentum post-selection by two apertures defined by the orange circles in Fig. 3C as

$$\begin{aligned} |\Psi_f\rangle = & \ (p_{11}|\mathbf{Q}_1\rangle + p_{12}|\mathbf{Q}_2\rangle) \otimes |1\rangle \\ & + (p_{22}|\mathbf{Q}_2\rangle + p_{21}|\mathbf{Q}_1\rangle) \otimes |2\rangle \end{aligned} \quad (6)$$

where we assume that the apertures are small enough so that each of them captures coherently scattered electrons characterized by a well-defined state $|\mathbf{Q}_f\rangle$ with $f = 1,2$ (in practice, each of them can be a coherent superposition of plane waves transmitted through the finite solid angle region spanned by each aperture). To achieve pure entanglement, we require $p_{nm} \to 0$ for $n \neq m$ terms in Eq. 6, which happens after the noted numerical optimization: We obtain values $p_{11}^2/(p_{11}^2 + p_{21}^2) = 0.999991$ and $p_{22}^2/(p_{22}^2 + p_{12}^2) = 0.999779$, confirming a high degree of entanglement (*62*). Incidentally, a more direct inversion procedure without optimization still yields a level of entanglement exceeding 90% (fig. S2).

We note that the symmetry of the selected degenerate plasmons plays a similar role as photon polarization in light-based entanglement schemes (*1*). In the present instance, the electron wave function profiles are strongly affected by the threefold symmetry of the plasmonic nanoparticles and the choice of correlated electron output angles. Optimized profiles for more symmetric nanoparticles also become more symmetric, as shown for silver disks in fig. S3, where a high degree of entanglement (>99% mode separation) is achieved by direct inversion.

Electron entanglement with atomic vibrational states

The electron–sample entanglement scheme under consideration can be applied to sample excitations of different nature. We illustrate this versatility by considering atomic vibrations in a hexagonal boron

SCIENCE ADVANCES | RESEARCH ARTICLE

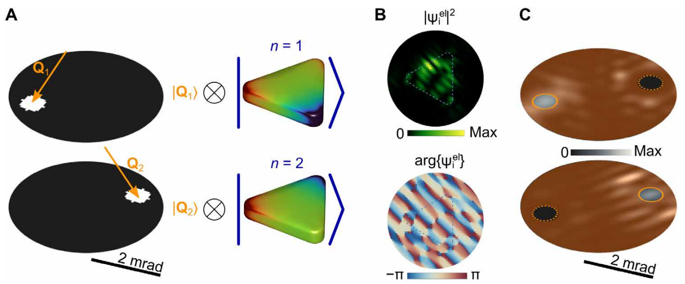

Fig. 3. Creation of electron–sample states with a high degree of entanglement. (**A**) Pursued electron–sample entangled state, consisting of the superposition of selected (by means of two apertures) electron momentum states within the white pixels in $\mathbf{Q}_f$ space (left) and correlated degenerate dipolar plasmons in the silver nanotriangle sample considered in Fig. 2 (right). (**B**) Spatial profile of the optimized incident wave function $\psi_i^{el}(\mathbf{R})$ required to produce the final state in (A). The contour of the triangular nanoparticle is indicated with dashed lines. (**C**) Resulting probability distributions $|\langle \mathbf{Q}_f, n|\Psi_f\rangle|^2$ with $n = 1$ (top) and $n = 2$ (bottom) in $\mathbf{Q}_f$ space, where each aperture (small circles) transmits nearly 100% of the targeted excitation n. The area outside the apertures (intended to be masked) is colored to emphasize the selected momentum regions of interest. The optimization is carried out for 100 keV electrons, 81 pixels in each of the detector apertures, $\varphi_i = 4$ mrad, and $\varphi_f = 2$ mrad.

nitride (hBN) molecule (Fig. 4), which we simulate from first principles (see Methods) (*63*) assuming passivation of the edges with hydrogen atoms. This structure supports a number of vibrational excitations up to energies ~450 meV, including a set of triply degenerate N—H bond-stretching modes at 440 meV (see EELS spectrum in fig. S4), on which we focus our analysis. We again optimize the incident electron wave function to achieve entanglement between final electron states and vibrational modes of the molecule [see the resulting $\psi_i^{el}(\mathbf{R})$ and $\psi_i^{el}(\mathbf{Q}_i)$ profiles in figs. S5 and S6C]. Because of the strong spatial confinement of vibrational modes, the angular ranges that need to be used for the incident and scattered electron wave functions are now considerably larger than for plasmons (cf. angle scales in Figs. 3 and 4). The achieved electron–sample state, illustrated in Fig. 4B, exhibits a decent degree of entanglement when selecting electrons scattered along the colored circles in $\mathbf{Q}_f$ space, also revealed through the partial probabilities contributed by each of the three vibrational modes to each of the regions enclosed by those circles (see table in Fig. 4C).

DISCUSSION

By entangling the transverse momenta of free electrons with localized optical excitations in a nanostructure, we could selectively measure one of the corresponding outgoing electron directions, thus providing a way to herald the creation of single designated excitations in the studied specimen. This should allow us to follow the dynamics of the latter and gain insight into the state-dependent decay pathways, for example, by subsequently probing the evolution of the specimen through scattering of laser pulses that are synchronized with the electron in an electron-pump/photon-probe approach. An additional possibility is offered by correlating the angle-resolved electron signal with traces originating in the decay of excited states of the specimen (e.g., an electrical signal produced by coupling to electron-hole pairs in a proximal semiconductor or also the polarization- and angle-resolved cathodoluminescence emission associated with radiative decay). The present scheme could further be extended to incorporate gain processes similar to those in photon-induced near-field electron microscopy (PINEM) (*54*) upon illumination of the sample with symmetry-matched optical pulses that can simultaneously excite a subset of its supported excitations.

We remark that the proposed approach holds elements of novelty with respect to traditional quantum optics methods because one of the entangled particles (the free electron) can be highly energetic and, therefore, capable of undergoing subsequent strong collisions with other objects. These collisions could, for instance, trigger chemical reactions that would then be entangled with optical modes in the specimen with which the electron has previously interacted.

Although we have illustrated some possibilities based on heuristic electron wave function designs and a straightforward application of the steepest-descent maximization method, improved solutions to the problem of entanglement optimization could be obtained through neural-network training (*59*), possibly combined with iterative physical improvement of the wave function profile based on currently explored tunable electron phase plates (*46*–*51*). As an alternative to the use of aloof interaction with the optical modes of the sampled nanostructure to avoid strong electron collisions with atomic potentials, this type of adaptive improvement could potentially be used to compensate for the effect of these potentials and morphological imperfections. In addition to the investigated examples of plasmons in nanoparticles and atomic vibrations in molecules, we envision the entanglement of free electrons with optical modes in dielectric cavities (*30*) and photons guided along optical waveguides (*64*), which together configure a vast range of possibilities for leveraging the quantum nature of free electrons in the design of improved microscopy and metrology schemes.

METHODS

Transfer matrix for inelastic electron–sample scattering

The time-dependent electron–sample system can be generally described by a wave function of the form $|\psi(t)\rangle = \sum_n \int d^3\mathbf{q}\, \alpha_{\mathbf{q},n}(t)\, e^{-i(\epsilon_\mathbf{q}+\omega_n)t} |\mathbf{q}\rangle \otimes |n\rangle$, where $|\mathbf{q}\rangle$ and $|n\rangle$ are electron and sample eigenstates of the noninteracting Hamiltonian with energies $\hbar\varepsilon_q$ and $\hbar\omega_n$, respectively. In particular, electron states are labeled by the 3D

Konečná *et al.*, *Sci. Adv.* **8**, eabo7853 (2022) 25 November 2022 **4 of 8**

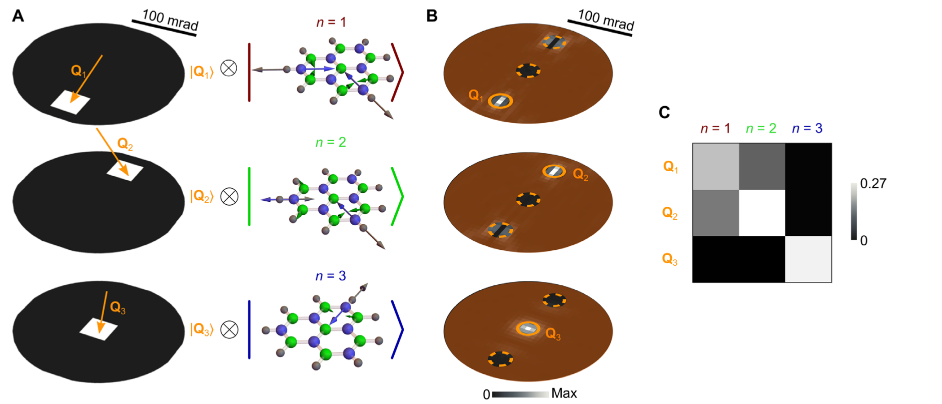

Fig. 4. Entanglement of free electrons and atomic vibrations. (**A**) Pursued electron–sample entangled state, consisting of the superposition of selected (by means of three apertures) electron-momentum states within the white pixels in $\mathbf{Q}_f$ space (left) and correlated triply degenerate 440-meV vibrational modes of an hBN molecule (right). (**B**) Resulting probability distributions $|\langle Q_f, n|\Psi_f\rangle|^2$ with $n = 1$ (top), $n = 2$ (middle), and $n = 3$ (bottom) in $\mathbf{Q}_f$ space. The area outside the apertures (small circles) is colored to emphasize the selected momentum regions of interest. (**C**) Probability matrix showing the fractional contribution associated with the excitation of each of the three vibrational modes $n = 1$ to 3 to the energy-filtered electron signal contained within the three selected circular areas around final transverse wave vectors $\mathbf{Q}_1$, $\mathbf{Q}_2$, and $\mathbf{Q}_3$ in (A). The sum of the nine matrix elements is normalized to one. We consider 60 keV electrons, 29 detector pixels, and $\varphi_i = \varphi_f = 100$ mrad.

momentum $\hbar\mathbf{q}$ and satisfy the orthonormality relation $\langle\mathbf{q}|\mathbf{q}'\rangle = \delta(\mathbf{q}-\mathbf{q}')$. The expansion coefficients $\alpha_{\mathbf{q},n}(t)$ are determined by solving the Schrödinger equation with an electron–sample interaction Hamiltonian $\hat{\mathcal{H}}_1$, which is generally weak for the energetic electrons that are typically used in electron microscopes, so we can work within first-order perturbation theory. Then, taking the sample to be initially prepared in its ground state $n = 0$, the post-interaction wave function has coefficients $\alpha_{\mathbf{q},n}(\infty) = (-2\pi i/\hbar)\int d^3\mathbf{q}'\ \delta(\epsilon_\mathbf{q} - \epsilon_{\mathbf{q}'} + \omega_n)\langle n|\langle\mathbf{q}|\hat{\mathcal{H}}_1|\mathbf{q}'\rangle|0\rangle\,\alpha_{\mathbf{q}',0}(-\infty)$, where we set $\omega_0 = 0$ without loss of generality. We further adopt the nonrecoil approximation (*13*) $\epsilon_\mathbf{q} - \epsilon_{\mathbf{q}'} \approx (\mathbf{q}-\mathbf{q}')\cdot\mathbf{v}$ under the assumption that the transverse electron energy is negligible compared with the longitudinal energy along the e-beam direction defined by the average electron velocity $\mathbf{v}$. This condition is commonly satisfied in electron microscopes. In this approximation, the energy $\hbar\omega_n$ transferred from the electron to the sample is fully absorbed by a change in the longitudinal electron wave vector given by $-\omega_n/v$, so for monochromatic incident electrons, the initial and final longitudinal components of the electron wave function play a trivial role and can be disregarded in the description of the present problem. Consequently, we can expand the final wave function as shown in Eq. 1, with coefficients $\alpha^f_{\mathbf{Q}_f,n} \equiv \alpha_{\mathbf{q},n}(\infty)$ that only depend on the transverse electron wave vector $\mathbf{Q}_f$ for each sample excitation n and are determined from the incident electron wave function coefficients $\alpha^i_{\mathbf{Q}_i} \equiv \alpha_{\mathbf{q},0}(-\infty)$ through the linear relation $\alpha^f_{\mathbf{Q}_f,n} = \int d^2\mathbf{Q}_i\, M_{\mathbf{Q}_f-\mathbf{Q}_i,n}\,\alpha^i_{\mathbf{Q}_i}$ (Eq. 3) with

$$M_{\mathbf{Q}_f-\mathbf{Q}_i,n} = \frac{-2\pi i}{\hbar v}\langle n|\langle\mathbf{q}_f|\hat{\mathcal{H}}_1|\mathbf{q}_i\rangle|0\rangle \qquad (7)$$

We remark that the transfer matrix elements defined in Eq. 7 involve just the difference between incident and scattered transverse wave vectors. In what follows, we develop a formalism to relate $M_{\mathbf{Q}_f-\mathbf{Q}_i,n}$ to the EELS probability and obtain specific expressions for plasmonic and atomic-vibration modes.

EELS with shaped electron beams

We consider the configuration of Fig. 1A and assume the electron velocity and sample dimensions to be small enough as to neglect retardation effects and work in the electrostatic regime. Further adopting the aforementioned nonrecoil approximation, we can disregard the longitudinal component of the electron wave function and only consider the dependence on transverse coordinates $\mathbf{R} = (x, y)$ (i.e., taking the electron velocity $\mathbf{v}$ along z). We can then write a general expression for the EELS probability $\Gamma_{\rm EELS}(\omega)$ in terms of the energy loss $\hbar\omega$, the transverse wave vector $\mathbf{Q}_f \perp \hat{z}$ of the final (f) electron state (corresponding to a wave function $\propto e^{i\mathbf{Q}_f\cdot\mathbf{R}}$), and the transverse component of the initial (i) electron wave function, $\psi_i(\mathbf{R})$. More precisely, using equation 17 of (*6*), we have $\Gamma_{\rm EELS}(\omega) = \int d^2\mathbf{Q}_f\Gamma_{\rm EELS}(\mathbf{Q}_f,\omega)$, where

$$\Gamma_{\rm EELS}(\mathbf{Q}_f,\omega) = \frac{e^2}{4\pi^3\hbar v^2}\int d^2\mathbf{R}\int d^2\mathbf{R}'\,\psi_i(\mathbf{R})\,\psi_i^*(\mathbf{R}')\times e^{i\mathbf{Q}_f\cdot(\mathbf{R}'-\mathbf{R})}\mathcal{W}(\mathbf{R},\mathbf{R}',\omega) \qquad (8)$$

is the momentum-resolved probability and

$$\mathcal{W}(\mathbf{R},\mathbf{R}',\omega) = \int_{-\infty}^{\infty}dz\int_{-\infty}^{\infty}dz'\,e^{i\omega(z-z')/v}\times{\rm Im}\{-W(\mathbf{r},\mathbf{r}',\omega)\} \qquad (9)$$

is a transverse screened interaction obtained from the full screened interaction $W(\mathbf{r},\mathbf{r}',\omega)$. The latter stands for the Coulomb potential created at $\mathbf{r}$ by a point charge of magnitude $e^{-i\omega t}$ placed at $\mathbf{r}'$, including the effect of screening by the environment. Now, as we show below for plasmonic and phononic structures, the transverse screened interaction in Eq. 9 is separable as

$$\mathcal{W}(\mathbf{R},\mathbf{R}',\omega) = \sum_n g_n(\omega)\,w_n(\mathbf{R},\omega)\,w_n^*(\mathbf{R}',\omega) \qquad (10)$$

where n runs over excitation modes characterized by spatial profiles $w_n(\mathbf{R}, \omega)$ and dimensionless spectral functions $g_n(\omega)$. Finally, inserting Eq. 10 into Eq. 8, we readily find Eq. 4 in the main text. Incidentally, the angle-integrated inelastic electron signal (i.e., the integral of Eq. 8 over $\mathbf{Q}_f$) reduces to $\Gamma_{\rm EELS}(\omega) = (e^2/\pi\hbar v^2)\Sigma_n g_n(\omega) \int d^2\mathbf{R}\,|\psi_i(\mathbf{R})|^2\,|w_n(\mathbf{R}, \omega)|^2$, which is an average over transverse positions $\mathbf{R}$ weighted by both the incident electron probability (*6*, *61*) and the mode spatial profile, and consequently, because the e-beam can generally excite different modes n, the optimization scheme that we pursue here to produce entanglement essentially consists in rearranging the $\mathbf{Q}_f$ distribution of the scattered electron components associated with the excitation of each of those modes.

We note that the spectral functions in this formalism can be generally approximated by Lorentzians

$$g_n(\omega) \approx \mathrm{Im}\left\{\frac{G_n/\pi}{\omega_n - \omega - i\gamma_n/2}\right\}$$

peaked at the mode energies $\hbar\omega_n$ and having areas G_n and widths γ_n (see below) that determine the spectral positions and strengths of the EELS features.

Numerical determination of $|\psi_i^{\rm el}\rangle$ for creating selected excitations and entangled electron–sample states

Given a desired final state defined through the coefficients $\alpha^f_{\mathbf{Q}_f,n}$, we numerically obtain $\alpha^i_{\mathbf{Q}_i}$ by inverting Eq. 3 upon discretization of $\mathbf{Q}_i$ using a finite number of points and pixels at the electron analyzer in the Fourier plane $\mathbf{Q}_f$, as noted in the main text. More precisely, we follow a simple procedure consisting in specifying target values of $\alpha^f_{\mathbf{Q}_f,n}$ within a region $Q < Q_{f,\max}$ (effectively setting it to zero outside it) and obtain $\alpha^i_{\mathbf{Q}_i}$ for $Q_i < Q_{i,\max}$ through the aforementioned numerical inversion method. The wave vector ranges are related to the maximum incidence|collection half-angle $\varphi_{i|f}$ through $Q_{i|f,\max} = (m_e v/\hbar)\sin\varphi_{i|f}$. In this scheme, to select a single sample excitation $n = n_0$ (Fig. 2), we set $\alpha^f_{\mathbf{Q}_f,n} = C\delta_{nn_0}\Theta(Q_{f,\max} - Q_f)$, where C is a constant and Θ is the step function. However, to produce electron–sample entanglement involving two (Fig. 3) or three (Fig. 4) sample states n_j correlated with final electron wave vectors $\mathbf{Q}_j$ (see Fig. 1B), we set $\alpha^f_{\mathbf{Q}_f,n_j}$ to a constant at the $\mathbf{Q}_f$ space pixel that contains $\mathbf{Q}_j$ and zero elsewhere. We then construct $|\psi_i^{\rm el}\rangle$ from the obtained coefficients $\alpha^i_{\mathbf{Q}_i}$ (also setting them to zero for $Q_i > Q_{i,\max}$) and insert this input wave function in Eq. 4 to generate the actual final probability distributions, plotted in the figures with a finer discretization in $\mathbf{Q}_f$ space.

Transfer matrix from the spectral and spatial mode functions

An expression for the EELS probability analogous to Eq. 4 can be readily obtained from Eq. 3 as

$$\Gamma_{\rm EELS}(\mathbf{Q}_f, \omega) = \sum_n \left|\int d^2\mathbf{Q}_i\, M_{\mathbf{Q}_f - \mathbf{Q}_i,n}\,\alpha^i_{\mathbf{Q}_i}\right|^2 \delta(\omega - \omega_n) \quad (11)$$

The connection between Eqs. 4 and 11 is established by adding finite mode widths γ_n to the latter and expanding the incident electron wave function in the former as an integral over momentum components, as indicated in Eq. 2. Comparing the two resulting expressions, we find

$$M_{\mathbf{Q},n} = \frac{e}{4\pi^2 v}\sqrt{\frac{G_n}{\pi\hbar}}\int d^2\mathbf{R}\, e^{-i\mathbf{Q}\cdot\mathbf{R}}\, w_n(\mathbf{R}, \omega) \quad (12)$$

which provides a prescription to obtain the transfer matrix coefficients defined in Eq. 7 directly from the screened interaction, thus bypassing the need for a detailed specification of the interaction Hamiltonian. Then, the spatial profiles in Eq. 5 are simply given by the inverse Fourier transform of Eq. 12.

Transfer matrix and transverse screened interaction for plasmonic nanoparticles

In the electrostatic limit under consideration, we can recast the response of an arbitrarily shaped homogeneous nanoparticle into an eigenvalue problem (*65*, *66*). We then need to find the real eigenvalues λ_n and eigenvectors $\sigma_n(\mathbf{s})$ of the integral equation $2\pi\lambda_n\sigma_n(\mathbf{s}) = \oint d\mathbf{s}'\, F(\mathbf{s}, \mathbf{s}')\sigma_n(\mathbf{s}')$, where $\mathbf{s}$ and $\mathbf{s}'$ run over particle surface coordinates, $F(\mathbf{s}, \mathbf{s}') = -\hat{\mathbf{n}}\cdot(\mathbf{s} - \mathbf{s}')/|\mathbf{s} - \mathbf{s}'|^3$, and $\hat{\mathbf{n}}$ is the outer surface normal. Here, we solve this eigensystem for triangular particles using the MNPBEM toolbox (*67*) based on a finite boundary element discretization of the particle surface. Then, the spectral functions in Eq. 10 reduce to (*65*, *66*)

$$g_n(\omega) = \mathrm{Im}\left\{\frac{-2}{\epsilon(1 + \lambda_n) + (1 - \lambda_n)}\right\}$$

whereas the spatial profiles become

$$w_n(\mathbf{R}, \omega) = 2\oint d\mathbf{s}\, \sigma_n(\mathbf{s})\, e^{-i\omega s_z/v} K_0\left(\frac{\omega|\mathbf{R} - \mathbf{S}|}{v}\right)$$

with $\mathbf{s} = \mathbf{S} + s_z\hat{\mathbf{z}}$. This expression neglects the contribution of bulk modes, which should be a reasonable approximation at loss energies well below the bulk plasmon. Inserting it into Eq. 12, the transfer matrix elements reduce to

$$M_{\mathbf{Q},n} \approx \frac{e}{\pi v}\sqrt{\frac{G_n}{\pi\hbar}}\,\frac{1}{Q^2 + \omega_n^2/v^2}\oint d\mathbf{s}\, \sigma_n(\mathbf{s}) e^{-i(\mathbf{Q} + \hat{\mathbf{z}}\omega_n/v)\cdot\mathbf{s}}$$

where we have approximated $\omega \approx \omega_n$. For silver, we model the dielectric function as (*6*) $\epsilon = \epsilon_b - \omega_p^2/\omega(\omega + i\gamma)$ with $\epsilon_b = 4.0$, $\hbar\omega_p = 9.17$ eV, and $\hbar\gamma = 21$ meV, yielding mode frequencies $\omega_n = \omega_p/\sqrt{\epsilon_b + (1 - \lambda_n)/(1 + \lambda_n)}$, flat widths $\gamma_n \approx \gamma$, and spectral weights $G_n = \pi\omega_n^3/[\omega_p^2(1 + \lambda_n)]$.

Transfer matrix and transverse screened interaction for atomic vibrations

For molecules or nanoparticles whose mid-infrared response is dominated by atomic vibrations, we find the spectral and spatial dependence of the modes in Eq. 10 to be governed by (*63*, *68*).

$$g_n(\omega) = \mathrm{Im}\left\{\frac{\omega_n^2}{\omega_n^2 - \omega(\omega + i\gamma)}\right\} \quad (13)$$

and

$$w_n(\mathbf{R}, \omega) = \frac{2}{\omega_n}\sum_l \frac{1}{\sqrt{M_l}}\int d^3\mathbf{r}'\, K_0(\omega|\mathbf{R} - \mathbf{R}'|/v)\, e^{i\omega z'/v}\,[\mathbf{e}_{nl}\cdot\vec{\rho}_l(\mathbf{r}')]$$

where n now runs over vibrational modes, ω_n and $\mathbf{e}_{nl}$ are the corresponding real frequencies and normalized atomic displacement vectors ($\Sigma_l\, \mathbf{e}_{nl}\cdot\mathbf{e}_{n'l} = \delta_{nn'}$), respectively, the l sum extends over the atoms in the structure, M_l is the mass of atom l, $\vec{\rho}_l(\mathbf{r})$ denotes the gradient of the charge distribution associated with displacements of that atom, and we have incorporated a phenomenological damping rate γ (here set to $\hbar\gamma = 1$ meV). From Eq. 13, we have $\gamma_n \approx \gamma$ for all modes and $G_n \approx \pi\omega_n/2$. Following (*63*), we use density functional theory (DFT) to calculate $\vec{\rho}_l(\mathbf{r})$, ω_n, and $\boldsymbol{e}_{nl}$ (see below). The prescription $|\mathbf{R}-\mathbf{R}'| \rightarrow \sqrt{|\mathbf{R}-\mathbf{R}'|^2+\Delta^2}$ is also adopted with $\Delta = 0.2$ Å to approximately account for a cutoff $\sim\hbar/\Delta$ in momentum transfer (*6*) and so avoid the unphysical divergence associated with close electron-atom encounters.

First-principles description of atomic vibrations

We use DFT and the projector augmented wave method (*69*) as implemented in the Vienna Ab initio Simulation Package (*70–72*) with the Perdew-Burke-Ernzerhof–generalized gradient approximation for electron exchange and correlation (*73*). This method is applied to describe hBN flakes with hydrogen-passivated edges using a plane wave cutoff energy of 500 eV and a sufficient amount of vacuum spacing in all directions around the structure to avoid interaction among the periodic images. Atomic equilibrium positions are found by minimizing the total energy using the conjugate gradient method with convergence criteria between consecutive iteration steps set to 10^{-5} eV for the total energy and 0.02 eV/Å for the atomic forces. Vibrational frequencies and eigenmodes are found by diagonalizing the dynamical matrix, which is calculated for 0.01-Å displacements. The corresponding gradients $\vec{\rho}_l(\mathbf{r})$ of the charge distribution are obtained by treating core electrons and nuclei as point particles, while the contribution coming from valence electrons is directly taken from DFT using a dense grid.

SUPPLEMENTARY MATERIALS

Supplementary material for this article is available at https://science.org/doi/10.1126/sciadv.abo7853

REFERENCES AND NOTES

1. R. Horodecki, P. Horodecki, M. Horodecki, K. Horodecki, Quantum entanglement. *Rev. Mod. Phys.* **81**, 865–942 (2009).
2. E. Togan, Y. Chu, A. S. Trifonov, L. Jiang, J. Maze, L. Childress, M. V. G. Dutt, A. S. Sörensen, P. R. Hemmer, A. S. Zibrov, M. D. Lukin, Quantum entanglement between an optical photon and a solid-state spin qubit. *Nature* **466**, 730–734 (2010).
3. O. Kfir, Entanglements of electrons and cavity photons in the strong-coupling regime. *Phys. Rev. Lett.* **123**, 103602 (2019).
4. V. Di Giulio, M. Kociak, F. J. García de Abajo, Probing quantum optical excitations with fast electrons. *Optica* **6**, 1524–1534 (2019).
5. O. Reinhardt, C. Mechel, M. Lynch, I. Kaminer, Free-electron qubits. *Ann. Phys.* **533**, 2000254 (2021).
6. F. J. García de Abajo, Optical excitations in electron microscopy. *Rev. Mod. Phys.* **82**, 209–275 (2010).
7. R. F. Egerton, *Electron Energy-Loss Spectroscopy in the Electron Microscope* (Plenum Press, 1996).
8. R. F. Egerton, New techniques in electron energy-loss spectroscopy and eneorgy-filtered imaging. *Micron* **34**, 127–139 (2003).
9. R. Erni, N. D. Browning, Valence electron energy-loss spectroscopy in monochromated scanning transmission electron microscopy. *Ultramicroscopy* **104**, 176–192 (2005).
10. R. Brydson, *Electron Energy Loss Spectroscopy* (BIOS Scientific Publishers, 2001).
11. O. L. Krivanek, T. C. Lovejoy, N. Dellby, T. Aoki, R. W. Carpenter, P. Rez, E. Soignard, J. Zhu, P. E. Batson, M. J. Lagos, R. F. Egerton, P. A. Crozier, Vibrational spectroscopy in the electron microscope. *Nature* **514**, 209–212 (2014).
12. O. L. Krivanek, N. Dellby, J. A. Hachtel, J.-C. Idrobo, M. T. Hotz, B. Plotkin-Swing, N. J. Bacon, A. L. Bleloch, G. J. Corbin, M. V. Hoffman, C. E. Meyer, T. C. Lovejoy, Progress in ultrahigh energy resolution EELS. *Ultramicroscopy* **203**, 60–67 (2019).
13. F. J. García de Abajo, V. Di Giulio, Optical excitations with electron beams: Challenges and opportunities. *ACS Photonics* **8**, 945–974 (2021).
14. F. S. Hage, G. Radtke, D. M. Kepaptsoglou, M. Lazzeri, Q. M. Ramasse, Single-atom vibrational spectroscopy in the scanning transmission electron microscope. *Science* **367**, 1124–1127 (2020).
15. X. Yan, C. Liu, C. A. Gadre, L. Gu, T. Aoki, T. C. Lovejoy, N. Dellby, O. L. Krivanek, D. G. Schlom, R. Wu, X. Pan, Single-defect phonons imaged by electron microscopy. *Nature* **589**, 65–69 (2021).
16. P. Rez, T. Aoki, K. March, D. Gur, O. L. Krivanek, N. Dellby, T. C. Lovejoy, S. G. Wolf, H. Cohen, Damage-free vibrational spectroscopy of biological materials in the electron microscope. *Nat. Commun.* **7**, 10945 (2016).
17. D. M. Haiber, P. A. Crozier, Nanoscale probing of local hydrogen heterogeneity in disordered carbon nitrides with vibrational electron energy-loss spectroscopy. *ACS Nano* **12**, 5463–5472 (2018).
18. J. R. Jokisaari, J. A. Hachtel, X. Hu, A. Mukherjee, C. Wang, A. Konečná, T. C. Lovejoy, N. Dellby, J. Aizpurua, O. L. Krivanek, J.-C. Idrobo, R. F. Klie, Vibrational spectroscopy of water with high spatial resolution. *Adv. Mater.* **12**, 430–436 (2018).
19. J. A. Hachtel, J. Huang, I. Popovs, S. Jansone-Popova, J. K. Keum, J. Jakowski, T. C. Lovejoy, N. Dellby, O. L. Krivanek, J. C. Idrobo, Identification of site-specific isotopic labels by vibrational spectroscopy in the electron microscope. *Science* **363**, 525–528 (2019).
20. M. Bosman, V. J. Keast, M. Watanabe, A. I. Maaroof, M. B. Cortie, Mapping surface plasmons at the nanometre scale with an electron beam. *Nanotechnology* **18**, 165505 (2007).
21. J. Nelayah, M. Kociak, O. Stéphan, F. J. García de Abajo, M. Tencé, L. Henrard, D. Taverna, I. Pastoriza-Santos, L. M. Liz-Marzán, C. Colliex, Mapping surface plasmons on a single metallic nanoparticle. *Nat. Phys.* **3**, 348–353 (2007).
22. D. Rossouw, G. A. Botton, Plasmonic response of bent silver nanowires for nanophotonic subwavelength waveguiding. *Phys. Rev. Lett.* **110**, 066801 (2013).
23. S. F. Tan, L. Wu, J. K. W. Yang, P. Bai, M. Bosman, C. A. Nijhuis, Quantum plasmon resonances controlled by molecular tunnel junctions. *Science* **343**, 1496–1499 (2014).
24. V. Mkhitaryan, K. March, E. Tseng, X. Li, L. Scarabelli, L. M. Liz-Marzán, S.-Y. Chen, L. H. G. Tizei, O. Stéphan, J.-M. Song, M. Kociak, F. J. García de Abajo, A. Gloter, Can copper nanostructures sustain high-quality plasmons? *Nano Lett.* **21**, 2444–2452 (2021).
25. M. J. Lagos, A. Trügler, U. Hohenester, P. E. Batson, Mapping vibrational surface and bulk modes in a single nanocube. *Nature* **543**, 529–532 (2017).
26. A. A. Govyadinov, A. Konečná, A. Chuvilin, S. Vélez, I. Dolado, A. Y. Nikitin, S. Lopatin, F. Casanova, L. E. Hueso, J. Aizpurua, R. Hillenbrand, Probing low-energy hyperbolic polaritons in van der Waals crystals with an electron microscope. *Nat. Commun.* **8**, 95 (2017).
27. N. Li, X. Guo, X. Yang, R. Qi, T. Qiao, Y. Li, R. Shi, Y. Li, K. Liu, Z. Xu, L. Liu, F. J. García de Abajo, Q. Dai, E.-G. Wang, P. Gao, Direct observation of highly confined phonon polaritons in suspended monolayer hexagonal boron nitride. *Nat. Mater.* **20**, 43–48 (2020).
28. O. Kfir, H. Lourenço-Martins, G. Storeck, M. Sivis, T. R. Harvey, T. J. Kippenberg, A. Feist, C. Ropers, Controlling free electrons with optical whispering-gallery modes. *Nature* **582**, 46–49 (2020).
29. K. Wang, R. Dahan, M. Shentcis, Y. Kauffmann, A. Ben Hayun, O. Reinhardt, S. Tsesses, I. Kaminer, Coherent interaction between free electrons and a photonic cavity. *Nature* **582**, 50–54 (2020).
30. Y. Auad, C. Hamon, M. Tencé, H. Lourenço-Martins, V. Mkhitaryan, O. Stéphan, F. J. García de Abajo, L. H. G. Tizei, M. Kociak, Unveiling the coupling of single metallic nanoparticles to whispering-gallery microcavities. *Nano Lett.* **22**, 319–327 (2022).
31. R. B. Pettit, J. Silcox, R. Vincent, Measurement of surface-plasmon dispersion in oxidized aluminum films. *Phys. Rev. B* **11**, 3116–3123 (1975).
32. O. L. Krivanek, Y. Tanishiro, K. Takayanagi, K. Yagi, Electron energy loss spectroscopy in glancing reflection from bulk crystals. *Ultramicroscopy* **11**, 215–222 (1983).
33. F. S. Hage, R. J. Nicholls, J. R. Yates, D. G. McCulloch, T. C. Lovejoy, N. Dellby, O. L. Krivanek, K. Refson, Q. M. Ramasse, Nanoscale momentum-resolved vibrational spectroscopy. *Sci. Adv.* **4**, eaar7495 (2018).
34. P. Shekhar, M. Malac, V. Gaind, N. Dalili, A. Meldrum, Z. Jacob, Momentum-resolved electron energy loss spectroscopy for mapping the photonic density of states. *ACS Photonics* **4**, 1009–1014 (2017).
35. C. Mechel, Y. Kurman, A. Karnieli, N. Rivera, A. Arie, I. Kaminer, Quantum correlations in electron microscopy. *Optica* **8**, 70–78 (2021).
36. Y. Adiv, H. Hu, S. Tsesses, R. Dahan, K. Wang, Y. Kurman, A. Gorlach, H. Chen, X. Lin, G. Bartal, I. Kaminer, Observation of 2D Cherenkov radiation, https://arxiv.org/abs/2203.01698 (2022).
37. C. J. Powell, J. B. Swan, Origin of the characteristic electron energy losses in aluminum. *Phys. Rev.* **115**, 869–875 (1959).
38. P. Schattschneider, F. Födermayr, D. S. Su, Coherent double-plasmon excitation in aluminum. *Phys. Rev. Lett.* **59**, 724–727 (1987).
39. P. E. Batson, N. Dellby, O. L. Krivanek, Sub-ångstrom resolution using aberration corrected electron optics. *Nature* **418**, 617–620 (2002).
40. L. Clark, A. Béché, G. Guzzinati, A. Lubk, M. Mazilu, R. Van Boxem, J. Verbeeck, Exploiting lens aberrations to create electron-vortex beams. *Phys. Rev. Lett.* **111**, 064801 (2013).
41. G. Möllenstedt, H. Düker, Beobachtungen und Messungen an Biprisma-Interferenzen mit Elektronenwellen. *Z. Phys.* **145**, 377–397 (1956).
42. G. Guzzinati, A. Beche, H. Lourenço-Martins, J. Martin, M. Kociak, J. Verbeeck, Probing the symmetry of the potential of localized surface plasmon resonances with phase-shaped electron beams. *Nat. Commun.* **8**, 14999 (2017).
43. C. W. Johnson, A. E. Turner, B. J. McMorran, Scanning two-grating free electron Mach-Zehnder interferometer. *Phys. Rev. Res.* **3**, 043009 (2021).

44. J. Verbeeck, H. Tian, P. Schattschneider, Production and application of electron vortex beams. *Nature* **467**, 301–304 (2010).
45. B. J. McMorran, A. Agrawal, I. M. Anderson, A. A. Herzing, H. J. Lezec, J. J. McClelland, J. Unguris, Electron vortex beams with high quanta of orbital angular momentum. *Science* **331**, 192–195 (2011).
46. J. Verbeeck, A. Béché, K. Müller-Caspary, G. Guzzinati, M. A. Luong, M. D. Hertog, Demonstration of a 2 × 2 programmable phase plate for electrons. *Ultramicroscopy* **190**, 58–65 (2018).
47. A. Konečná, F. J. García de Abajo, Electron beam aberration correction using optical near fields. *Phys. Rev. Lett.* **125**, 030801 (2020).
48. O. Schwartz, J. J. Axelrod, S. L. Campbell, C. Turnbaugh, R. M. Glaeser, H. Müller, Laser phase plate for transmission electron microscopy. *Nat. Methods* **16**, 1016–1020 (2019).
49. F. J. García de Abajo, A. Konečná, Optical modulation of electron beams in free space. *Phys. Rev. Lett.* **126**, 123901 (2021).
50. M. C. C. Mihaila, P. Weber, M. Schneller, L. Grandits, S. Nimmrichter, T. Juffmann, Transverse electron-beam shaping with light. *Phys. Rev. X* **12**, 031043 (2022).
51. I. Madan, V. Leccese, A. Mazur, F. Barantani, T. LaGrange, A. Sapozhnik, P. M. Tengdin, S. Gargiulo, E. Rotunno, J.-C. Olaya, I. Kaminer, V. Grillo, F. J. García de Abajo, F. Carbone, G. M. Vanacore, Ultrafast transverse modulation of free electrons by interaction with shaped optical fields. *ACS Photonics* **10**, 3215–3224 (2022).
52. S. A. Aseyev, E. A. Ryabov, B. N. Mironov, A. A. Ischenko, The development of ultrafast electron microscopy. *Crystals* **10**, 452 (2020).
53. P. Baum, A. H. Zewail, Attosecond electron pulses for 4D diffraction and microscopy. *Proc. Natl. Acad. Sci. U.S.A.* **104**, 18409–18414 (2007).
54. K. E. Priebe, C. Rathje, S. V. Yalunin, T. Hohage, A. Feist, S. Schäfer, C. Ropers, Attosecond electron pulse trains and quantum state reconstruction in ultrafast transmission electron microscopy. *Nat. Photonics* **11**, 793–797 (2017).
55. Y. Morimoto, P. Baum, Diffraction and microscopy with attosecond electron pulse trains. *Nat. Phys.* **14**, 252–256 (2018).
56. O. Kfir, V. Di Giulio, F. J. García de Abajo, C. Ropers, Optical coherence transfer mediated by free electrons. *Sci. Adv.* **7**, eabf6380 (2021).
57. V. Di Giulio, O. Kfir, C. Ropers, F. J. García de Abajo, Modulation of cathodoluminescence emission by interference with external light. *ACS Nano* **15**, 7290–7304 (2021).
58. M. Uchida, A. Tonomura, Generation of electron beams carrying orbital angular momentum. *Nature* **464**, 737–739 (2010).
59. S. R. Spurgeon, C. Ophus, L. Jones, A. Petford-Long, S. V. Kalinin, M. J. Olszta, R. E. Dunin-Borkowski, N. Salmon, K. Hattar, W.-C. D. Yang, R. Sharma, Y. Du, A. Chiaramonti, H. Zheng, E. C. Buck, L. Kovarik, R. L. Penn, D. Li, X. Zhang, M. Murayama, M. L. Taheri, Towards data-driven next-generation transmission electron microscopy. *Nat. Mater.* **20**, 274–279 (2021).
60. F. P. Schmidt, H. Ditlbacher, F. Hofer, J. R. Krenn, U. Hohenester, Morphing a plasmonic nanodisk into a nanotriangle. *Nano Lett.* **14**, 4810–4815 (2014).
61. R. H. Ritchie, A. Howie, Electron excitation and the optical potential in electron microscopy. *Philos. Mag.* **36**, 463–481 (1977).
62. A. F. Abouraddy, B. E. A. Saleh, A. V. Sergienko, M. C. Teich, Degree of entanglement for two qubits. *Phys. Rev. A* **64**, 050101 (2001).
63. A. Konečná, F. Iyikanat, F. J. García de Abajo, Theory of atomic-scale vibrational mapping and isotope identification with electron beams. *ACS Nano* **15**, 9890–9899 (2021).
64. X. M. Bendaña, A. Polman, F. J. García de Abajo, Single-photon generation by electron beams. *Nano Lett.* **11**, 5099–5103 (2011).
65. F. J. García de Abajo, J. Aizpurua, Numerical simulation of electron energy loss near inhomogeneous dielectrics. *Phys. Rev. B* **56**, 15873–15884 (1997).
66. G. Boudarham, M. Kociak, Modal decompositions of the local electromagnetic density of states and spatially resolved electron energy loss probability in terms of geometric modes. *Phys. Rev. B* **85**, 245447 (2012).
67. U. Hohenester, A. Trügler, MNPBEM - A matlab toolbox for the simulation of plasmonic nanoparticles. *Comput. Phys. Commun.* **183**, 370–381 (2012).
68. J. R. M. Saavedra, F. J. García de Abajo, Phonon excitation by electron beams in nanographenes. *Phys. Rev. B* **92**, 115449 (2015).
69. P. E. Blöchl, Projector augmented-wave method. *Phys. Rev. B* **50**, 17953–17979 (1994).
70. G. Kresse, J. Furthmüller, Efficient iterative schemes for ab initio total-energy calculations using a plane-wave basis set. *Phys. Rev. B* **54**, 11169–11186 (1996a).
71. G. Kresse, J. Hafner, *Ab initio* molecular dynamics for liquid metals. *Phys. Rev. B* **47**, 558–561 (1993).
72. G. Kresse, J. Furthmüller, Efficiency of ab-initio total energy calculations for metals and semiconductors using a plane-wave basis set. *Comput. Mater. Sci.* **6**, 15–50 (1996).
73. J. P. Perdew, K. Burke, M. Ernzerhof, Generalized gradient approximation made simple. *Phys. Rev. Lett.* **77**, 3865–3868 (1996).

Acknowledgments

Funding: This work has been supported in part by the European Research Council (Advanced grant 789104-eNANO), the Spanish MICINN (PID2020-112625GB-I00 and Severo Ochoa CEX2019-000910-S), the Catalan CERCA Program, and Fundaciós Cellex and Mir-Puig. A.K. was supported by the ESF under the project CZ.02.2.69/0.0/0.0/20_079/0017436. **Author contributions:** F.J.G.d.A. conceived the project. A.K. and F.J.G.d.A. developed the theoretical formalism. A.K. performed theoretical calculations for all figures using DFT input generated by F.I. **Competing interests:** The authors declare that they have no competing interests. **Data and materials availability:** All data needed to evaluate the conclusions in the paper are present in the paper and/or the Supplementary Materials.

Submitted 24 February 2022
Accepted 7 October 2022
Published 25 November 2022
10.1126/sciadv.abo7853

6 Conclusion and Outlook

This habilitation thesis can be divided into two main parts: I) CHAPTER 2 and CHAPTER 3 summarize works applying already existing imaging and spectroscopic techniques in electron microscopy to solid-state nanosystems. We discussed the coupling of fast electrons with the confined optical fields over a broad spectral range, which makes the electron beams ideal in probing phonon and plasmon polaritons or excitons in nanostructures. II) In CHAPTER 4 and CHAPTER 5, we demonstrated the high potential of non-trivially shaped electron beams to improve already existing microscopes or develop entirely new microscopic and spectroscopic methods, for which we can seek inspiration in light optics.

I foresee a range of research directions I would like to deal with in the upcoming years. Some of the research topics listed below are already included in the "Junior Star" grant proposal, awarded for years 2023 – 2027 by the Czech Science Foundation to start a new research group.

6.1 Improvements in instrumentation

Development of light-based phase plates

We discussed two possible designs of light-based phase plates in CHAPTER 4. However, many modifications or other options could be adapted, such as polariton-based phase plate[76] or shaping through the interaction of fields confined at edges of an aperture[71], schematically shown in FIGURE 6.1. Further research is also required for solving inverse problems related to using such light-based phase plates, *e.g.*, for a given desired shaped electron wave function, we need to find the needed optical field. We will also focus on a technologically simple, robust, and easy-to-use solution suitable for experimental implementation.

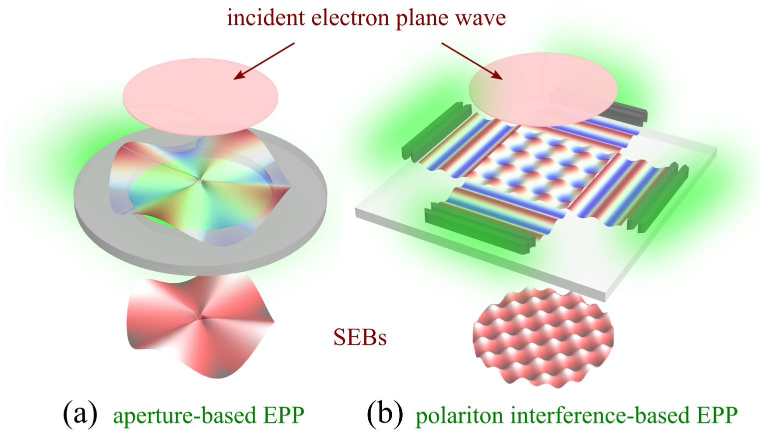

Figure 6.1: Light-based electron phase plates. Two possible schemes for shaping the electron wave function with light. (a) Interaction of electrons with optical field confined at edges of an aperture. (b) Electron beam shaping via the interaction with interfering polaritons.

Generation of electron beams modulated in time

Information on the temporal evolution of the sample morphology or response is another important piece for understanding the basic physical properties and functionalities of nanostructures and nanodevices. Some of the current technological solutions offering temporal resolution in electron microscopy rely on generating well-defined electron pulses. We could, however, think about the possibility of generating other types of temporal modulation of the beam, which could be used for the reconstruction technique as suggested in Ref.[73].

Improvements in spectral resolution in electron energy-loss spectroscopy

The current spectral resolution of a few meV in EELS might still be improved by studying mechanisms that are limiting it. One such limitation could arise due to both elastic and inelastic thermally-induced interactions of the beam with liner tubes through which the electrons are propagating. Calculations should reveal if these limitations play an essential role, and if yes, find materials and geometries to reduce them.

6.2 New applications and methodology of electron micro-spectroscopy

Probing beam-sensitive samples

One of the most difficult challenges in electron microscopy is probing organic or other beam-sensitive samples. In such samples, a high dose of electrons causes damage to bonds through ionization, or light atoms can be completely removed from the sample due to the impact of energetic electrons. To overcome this drawback, we can probe many representatives (samples) of the same system, as utilized, *e.g.*, for reconstructing protein structure in "single-particle analysis"[77]. Another approach for probing the sensitive samples is to control and reduce the electron dose significantly. As most of the beam-sensitive samples are phase objects, it is thus also desirable to enhance the contrast without increasing the dose. This could be done by taking advantage of shaped or even pulsed and shaped electron beams in connection with reconstruction algorithms, as suggested in Figure 6.2(a).

It has been shown that electron energy-loss spectroscopy of sensitive samples can be performed remotely at the expense of losing some spatial resolution[26,28,30,78]. With some prior knowledge of the sample morphology, we could also apply reconstruction algorithms together with shaped electron beams to EELS of molecular samples.

Optical properties of phase-changing materials at the nanoscale

Due to the tunability of their optical, thermal, or electrical properties, phase-changing materials represent interesting platforms for designing switchable nanodevices. One such material is vanadium dioxide (VO_2), which exhibits insulator-to-metal transition relatively close to room temperature at around 335 K. Electron spectro-microscopy with in-situ heating is a very suitable technique for correlating local composition (through X-ray and core-loss EELS signals), optical and thermal properties (low-loss EELS) with the change in crystallinity or shape (diffraction and (high-resolution) imaging), everything as a function of applied temperature. Such experiments would reveal the relation between the phase transition and relevant physical properties at the truly microscopic level. They could complement other measurements often done with bulk samples or nanoparticle assemblies, where some effects are averaged out.

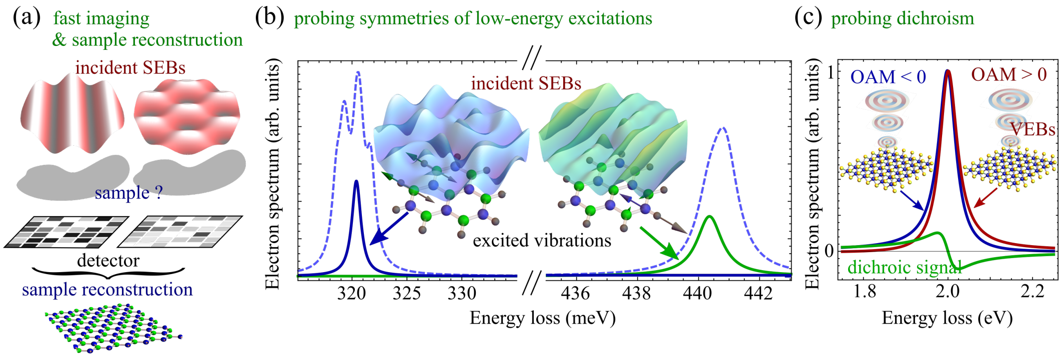

Figure 6.2: Applications of shaped electron beams in microscopy and spectroscopy. (a) Fast imaging and (3D) reconstruction of sample structure with the aid of SEBs. Extended SEBs interact with an unknown sample while the corresponding intensities of the transmitted waves are collected at a multi-pixel detector. The intensities associated with different incident SEBs are then used to reconstruct sample structure down to the atomic scale. (b) SEBs featuring different symmetries can selectively excite specific vibrational modes of a molecule as demonstrated in the S-EEL spectra (dashed curve corresponds to the spectrum acquired with a conventional beam). Such information can be used to reconstruct the localisation and symmetry of the modes with a low electron dose. (c) Dichroic signal is acquired when probing chiral nanostructures, lattices (here we show an example of monolayer MoS_2) and molecules with VEBs having positive and negative OAM.

Nanoscale thermometry

EELS with meV resolution can detect not only energy losses but also energy gains which can the electron beam experience when interacting with a sample at non-zero temperature. If we know occupation statistics of low-energy sample excitations (typically Bose-Einstein for vibrations and phonons), we can determine the local temperature at the sample from the ratio of the energy loss and gain peaks[79,80]. We could study potential of this technique to explore samples with inhomogeneous temperature spread or study radiative near-field thermal transport.

Optical dichroism

Detecting chiral samples' dichroic optical and vibrational response is essential in many fields. In pharmacy, different molecular enantiomers often play a role in drug effectiveness and safety. At the same time, chiral centres in inorganic materials emerging due to atomic defects or a specific band structure (as in some TMDs) find applications in information storage and processing. At the atomic or nanoscale level, dichroism could be studied with a particular class of shaped electron beams, vortex electron beams (VEBs), featuring a non-zero orbital angular momentum (OAM), as schematically shown in Figure 6.2(c). So far, only several theoretical works suggest the feasibility of energy- and OAM-filtered EELS to reveal the optical dichroic signal[81–83], but first experimental attempts have been inconclusive[84]. We will explore the robustness of the dichroic signal concerning the exact beam-sample geometry and suggest practical schemes for reliable and practical measurement schemes.

Controlling excitations in nanophotonics systems

We have already shown in Chapter 5 that by controlling the incident beam shape, we can selectively excite only desired excitations in the sample[75,83], see also Figure 6.2(b). We will further explore the applications of the shaped electron beams and reconstruction schemes in energy-loss spectroscopy to acquire information on excitations' localisation or symmetries with increased spatial or spectral resolution.

7 References

1. Knoll, M. & Ruska, E. Das elektronenmikroskop. *Zeitschrift für Physik* **78,** 318–339 (1932).
2. Batson, P. E., Dellby, N. & Krivanek, O. L. Sub-ångstrom resolution using aberration corrected electron optics. *Nature* **418,** 617 (2002).
3. Ryabov, A., Thurner, J. W., Nabben, D., Tsarev, M. V. & Baum, P. Attosecond metrology in a continuous-beam transmission electron microscope. *Sci. Adv.* **6,** eabb1393 (2020).
4. Lovejoy, T., Corbin, G., Dellby, N., Hoffman, M. & Krivanek, O. L. Advances in Ultra-High Energy Resolution STEM-EELS. *Microsc. Microanal.* **24,** 446–447 (2018).
5. Egerton, R. F. *Electron Energy-loss Spectroscopy in the Electron Microscope* (Plenum Press, New York, 1996).
6. Krivanek, O. L., Lovejoy, T. C., Dellby, N., Aoki, T., Carpenter, R. W., Rez, P., Soignard, E., Zhu, J., Batson, P. E., Lagos, M. J., Egerton, R. F. & Crozier, P. A. Vibrational spectroscopy in the electron microscope. *Nature* **514,** 209–214 (2014).
7. García de Abajo, F. J. Optical excitations in electron microscopy. *Rev. Mod. Phys.* **82,** 209–275 (1 2010).
8. Batson, P. E. Simultaneous STEM imaging and electron energy-loss spectroscopy with atomic-column sensitivity. *Nature* **366,** 727–728 (1993).
9. Haider, M., Hartel, P., Müller, H., Uhlemann, S. & Zach, J. Current and future aberration correctors for the improvement of resolution in electron microscopy. *Philosophical Transactions of the Royal Society A: Mathematical, Physical and Engineering Sciences* **367,** 3665–3682 (2009).
10. Tonomura, A. Applications of electron holography. *Rev. Mod. Phys.* **59,** 639–669 (1987).

11. Malac, M., Hettler, S., Hayashida, M., Kano, E., Egerton, R. F. & Beleggia, M. Phase plates in the transmission electron microscope: operating principles and applications. *Microscopy* **70,** 75–115 (2021).

12. Jiang, Y., Chen, Z., Han, Y., Deb, P., Gao, H., Xie, S., Purohit, P., Tate, M. W., Park, J., Gruner, S. M., Elser, V. & Muller, D. A. Electron ptychography of 2D materials to deep sub-ångström resolution. *Nature* **559,** 343–349 (2018).

13. Pelton, M., Aizpurua, J. & Bryant, G. Metal-nanoparticle plasmonics. *Laser Photonics Rev.* **2,** 136–159 (2008).

14. Fuchs, R. & Kliewer, K. L. Optical modes of vibration in an ionic crystal slab. *Phys. Rev.* **140,** A2076–A2088 (1965).

15. Stockman, M. I. Nanofocusing of optical energy in tapered plasmonic waveguides. *Phys. Rev. Lett.* **93,** 137404 (2004).

16. Li, P., Lewin, M., Kretinin, A. V., Caldwell, J. D., Novoselov, K. S., Taniguchi, T., Watanabe, K., Gaussmann, F. & Taubner, T. Hyperbolic phonon-polaritons in boron nitride for near-field optical imaging and focusing. *Nat. Commun.* **6,** 7507 (2015).

17. Moreno, E., Rodrigo, S. G., Bozhevolnyi, S. I., Martín-Moreno, L. & García-Vidal, F. J. Guiding and focusing of electromagnetic fields with wedge plasmon polaritons. *Phys. Rev. Lett.* **100,** 023901 (2008).

18. Lenert, A., Bierman, D. M., Nam, Y., Chan, W. R., Celanović, I., Soljačić, M. & Wang, E. N. A nanophotonic solar thermophotovoltaic device. *Nat. Nanotechnol.* **9,** 126–130 (2014).

19. Altug, H., Oh, S.-H., Maier, S. A. & Homola, J. Advances and applications of nanophotonic biosensors. *Nature nanotechnology* **17,** 5–16 (2022).

20. Lukin, D. M., Guidry, M. A. & Vu čkovi ć, J. Integrated Quantum Photonics with Silicon Carbide: Challenges and Prospects. *PRX Quantum* **1,** 020102 (2020).

21. Amenabar, I., Poly, S., Nuansing, W., Hubrich, E. H., Govyadinov, A. A., Huth, F., Krutokhvostov, R., Zhang, L., Knez, M., Heberle, J., Bittner, A. M. & Hillenbrand, R. Structural analysis and mapping of individual protein complexes by infrared nanospectroscopy. *Nat..* **4,** 2890 (2013).

22. Lee, J., Crampton, K. T., Tallarida, N. & Apkarian, V. A. Visualizing vibrational normal modes of a single molecule with atomically confined light. *Nature* **568,** 78–82 (2019).

23. Chirita Mihaila, M. C., Weber, P., Schneller, M., Grandits, L., Nimmrichter, S. & Juffmann, T. Transverse Electron-Beam Shaping with Light. *Phys. Rev. X* **12,** 031043 (2022).

24. Hachtel, J. A., Lupini, A. R. & Idrobo, J. C. Exploring the capabilities of monochromated electron energy loss spectroscopy in the infrared regime. *Sci. Rep.* **8,** 5637 (2018).

25. Konečná, A., Iyikanat, F. & García de Abajo, F. J. Theory of Atomic-Scale Vibrational Mapping and Isotope Identification with Electron Beams. *ACS Nano* **15,** 9890–9899 (2021).

26. Rez, P., Aoki, T., March, K., Gur, D., Krivanek, O. L., Dellby, N., Lovejoy, T. C., Wolf, S. G. & Cohen, H. Damage-free vibrational spectroscopy of biological materials in the electron microscope. *Nat. Commun.* **7,** 10945 (2016).

27. Radtke, G., Taverna, D., Lazzeri, M. & Balan, E. First-Principles Vibrational Electron Energy Loss Spectroscopy of β-Guanine. *Phys. Rev. Lett.* **119,** 027402 (2 2017).

28. Hachtel, J. A., Huang, J., Popovs, I., Jansone-Popova, S., Keum, J. K., Jakowski, J., Lovejoy, T. C., Dellby, N., Krivanek, O. L. & Idrobo, J. C. Identification of site-specific isotopic labels by vibrational spectroscopy in the electron microscope. *Science* **363,** 525–528 (2019).

29. Haiber, D. M. & Crozier, P. A. Nanoscale probing of local hydrogen heterogeneity in disordered carbon nitrides with vibrational electron energy-loss spectroscopy. *ACS Nano* **12,** 5463–5472 (2018).

30. Jokisaari, J. R., Hachtel, J. A., Hu, X., Mukherjee, A., Wang, C., Konecna, A., Lovejoy, T. C., Dellby, N., Aizpurua, J., Krivanek, O. L., Idrobo, J.-C. & Klie, R. F. Vibrational spectroscopy of water with high spatial resolution. *Adv. Mater.* **30,** 1802702 (2018).

31. Maciel-Escudero, C., Konečná, A., Hillenbrand, R. & Aizpurua, J. Probing and steering bulk and surface phonon polaritons in uniaxial materials using fast electrons: Hexagonal boron nitride. *Phys. Rev. B* **102,** 115431 (2020).

32. Konečná, A., Li, J., Edgar, J. H., García de Abajo, F. J. & Hachtel, J. A. Revealing Nanoscale Confinement Effects on Hyperbolic Phonon Polaritons with an Electron Beam. *Small* **17,** 2103404 (2021).

33. Caldwell, J. D., Lindsay, L., Giannini, V., Vurgaftman, I., Reinecke, T. L., Maier, S. A. & Glembocki, O. J. Low-loss, infrared and terahertz nanophotonics using surface phonon polaritons. *Nanophotonics* **4,** 44–68 (2015).

34. Dwyer, C., Aoki, T., Rez, P., Chang, S. L. Y., Lovejoy, T. C. & Krivanek, O. L. Electron-Beam Mapping of Vibrational Modes with Nanometer Spatial Resolution. *Phys. Rev. Lett.* **117,** 256101 (2016).

35. Lucas, A. A. & Kartheuser, E. Energy-loss spectrum of fast electrons in a dielectric slab. I. nonretarded losses and cherenkov bulk loss. *Phys. Rev. B* **1,** 3588–3598 (1970).

36. Konečná, A., Venkatraman, K., March, K., Crozier, P. A., Hillenbrand, R., Rez, P. & Aizpurua, J. Vibrational electron energy loss spectroscopy in truncated dielectric slabs. *Phys. Rev. B* **98,** 205409 (2018).

37. Venkatraman, K., Rez, P., March, K. & Crozier, P. A. The influence of surfaces and interfaces on high spatial resolution vibrational EELS from SiO2. *Microscopy* **67,** i14–i23 (2018).

38. Li, Y.-H., Wu, M., Qi, R.-S., Li, N., Sun, Y.-W., Shi, C.-L., Zhu, X.-T., Guo, J.-D., Yu, D.-P. & Gao, P. Probing lattice vibrations at SiO2/Si surface and interface with nanometer resolution. *Chin. Phys. Lett.* **36,** 026801 (2019).

39. Lagos, M. J., Trügler, A., Hohenester, U. & Batson, P. E. Mapping vibrational surface and bulk modes in a single nanocube. *Nature* **543,** 529–532 (2017).

40. Qi, R., Wang, R., Li, Y., Sun, Y., Chen, S., Han, B., Li, N., Zhang, Q., Liu, X., Yu, D., *et al.* Probing Far-Infrared Surface Phonon Polaritons in Semiconductor Nanostructures at Nanoscale. *Nano Lett.* **19,** 5070–5076 (2019).

41. Dai, S., Fei, Z., Ma, Q., Rodin, A. S., Wagner, M., McLeod, A. S., Liu, M. K., Gannett, W., Regan, W., Watanabe, K., Taniguchi, T., Thiemens, M., Dominguez, G., Neto, A. H. C., Zettl, A., Keilmann, F., Jarillo-Herrero, P., Fogler, M. M. & Basov, D. N. Tunable phonon polaritons in atomically thin van der waals crystals of boron nitride. *Science* **343,** 1125–1129 (2014).

42. Govyadinov, A. A., Konečná, A., Chuvilin, A., Vélez, S., Dolado, I., Nikitin, A. Y., Lopatin, S., Casanova, F., Hueso, L. E., Aizpurua, J. & Hillenbrand, R. Probing low-energy hyperbolic polaritons in van der Waals crystals with an electron microscope. *Nat. Commun.* **8,** 95 (2017).

43. Yang, H., Konečná, A., Xu, X., Cheong, S.-W., Garfunkel, E., García de Abajo, F. J. & Batson, P. E. Low-Loss Tunable Infrared Plasmons in the High-Mobility Perovskite (Ba, La) SnO3. *Small* **18,** 2106897 (2022).

44. Yang, H., Konečná, A., Xu, X., Cheong, S.-W., Batson, P. E., García de Abajo, F. J. & Garfunkel, E. Simultaneous Imaging of Dopants and Free Charge Carriers by Monochromated EELS. *ACS Nano* **16,** 18795–18805 (2022).

45. Smith, K. C., Olafsson, A., Hu, X., Quillin, S. C., Idrobo, J. C., Collette, R., Rack, P. D., Camden, J. P. & Masiello, D. J. Direct Observation of Infrared Plasmonic Fano Antiresonances by a Nanoscale Electron Probe. *Phys. Rev. Lett.* **123,** 177401 (2019).

46. Wu, Y., Hu, Z., Kong, X.-T., Idrobo, J. C., Nixon, A. G., Rack, P. D., Masiello, D. J. & Camden, J. P. Infrared plasmonics: STEM-EELS characterization of Fabry-Pérot resonance damping in gold nanowires. *Phys. Rev. B* **101,** 085409 (8 2020).

47. Yang, H., Garfunkel, E. L. & Batson, P. E. Probing free carrier plasmons in doped semiconductors using spatially resolved electron energy loss spectroscopy. *Phys. Rev. B* **102,** 205427 (20 2020).

48. Gallina, P., Konečná, A., Liška, J., Idrobo, J. C. & Šikola, T. Strongly Coupled Plasmon and Phonon Polaritons as Seen by Photon and Electron Probes. *Phys. Rev. Appl.* **19,** 024042 (2023).

49. Prodan, E., Radloff, C., Halas, N. J. & Nordlander, P. Hybridization model for the plasmon response of complex nanostructures. *Science* **302,** 419–422 (2003).

50. Novotny, L. Strong coupling, energy splitting, and level crossings: A classical perspective. *Am. J. Phys.* **78,** 1199–1202 (2010).

51. Nordlander, P., Oubre, C., Prodan, E., Li, K. & Stockman, M. I. Plasmon hybridizaton in nanoparticle dimers. **4,** 899–903 (2004).

52. Huck, C., Vogt, J., Neuman, T., Nagao, T., Hillenbrand, R., Aizpurua, J., Pucci, A. & Neubrech, F. Strong coupling between phonon-polaritons and plasmonic nanorods. *Opt. Express* **24,** 25528–25539 (2016).

53. Lu, G., Gubbin, C. R., Nolen, J. R., Folland, T., Tadjer, M. J., De Liberato, S. & Caldwell, J. D. Engineering the Spectral and Spatial Dispersion of Thermal Emission via Polariton–Phonon Strong Coupling. *Nano Lett.* **21,** 1831–1838 (2021).

54. Cherqui, C., Wu, Y., Li, G., Quillin, S. C., Busche, J. A., Thakkar, N., West, C. A., Montoni, N. P., Rack, . D., Camden, J. P. & Masiello, D. J. STEM/EELS Imaging of Magnetic Hybridization in Symmetric and Symmetry-Broken Plasmon Oligomer Dimers and All-Magnetic Fano Interference. *Nano Lett.* **16,** 6668–6676 (2016).

55. Quillin, S. C., Cherqui, C., Montoni, N. P., Li, G., Camden, J. P. & Masiello, D. J. Imaging Plasmon Hybridization in Metal Nanoparticle Aggregates with Electron Energy-Loss Spectroscopy. **120,** 20852–20859 (2016).

56. Křápek, V., Konečná, A., Horák, M., Ligmajer, F., Stöger-Pollach, M., Hrtoň, M., Babocký, J. & Šikola, T. Independent engineering of individual plasmon modes in plasmonic dimers with conductive and capacitive coupling. *Nanophotonics* **9,** 623–632 (2020).

57. Tizei, L. H. G., Mkhitaryan, V., Lourenço-Martins, H., Scarabelli, L., Watanabe, K., Taniguchi, T., Tencé, M., Blazit, J. D., Li, X., Gloter, A., Zobelli, A., Schmidt, F. P., Liz-Marzán, L. M., García de Abajo, F. J., Stéphan, O. & Kociak, M. Tailored nanoscale plasmon-enhanced vibrational electron spectroscopy. *Nano Lett.* **20,** 2973–2979 (2020).

58. Lagos, M. J., Batson, P. E., Lyu, Z. & Hohenester, U. Imaging Strongly Coupled Plasmon–Phonon Modes in Mid-Infrared Double Antennas. *ACS Photonics* **8,** 1293–1300 (2021).

59. Reidy, K., Majchrzak, P. E., Haas, B., Thomsen, J. D., Konečná, A., Park, E., Klein, J., Jones, A. J. H., Volckaert, K., Biswas, D., Watson, M. D., Cacho, C., Narang, P., Koch, C. T., Ulstrup, S., Ross, F. M. & Idrobo, J. C. Direct Visualization of Subnanometer Variations in the Excitonic Spectra of 2D/3D Semiconductor/Metal Heterostructures. *Nano Lett.* **23,** 1068–1076 (2023).

60. Sannomiya, T., Konečná, A., Matsukata, T., Thollar, Z., Okamoto, T., García de Abajo, F. J. & Yamamoto, N. Cathodoluminescence Phase Extraction of the Coupling between Nanoparticles and Surface Plasmon Polaritons. *Nano Lett.* **20,** 592–598 (2020).

61. Lei, D. Y., Fernández-Domínguez, A. I., Sonnefraud, Y., Appavoo, K., Haglund, R. F. J., Pendry, J. B. & Maier, S. A. Revealing Plasmonic Gap Modes in Particle-on-Film Systems Using Dark-Field Spectroscopy. *ACS Nano* **6,** 1380–1386 (2012).

62. Konečná, A., Di Giulio, V., Mkhitaryan, V., Ropers, C. & García de Abajo, F. J. Nanoscale Nonlinear Spectroscopy with Electron Beams. *ACS Photonics* **7,** 1290–1296 (2020).

63. Yasin, F. S., Harvey, T. R., Chess, J. J., Pierce, J. S., Ophus, C., Ercius, P. & McMorran, B. J. Probing Light Atoms at Subnanometer Resolution: Realization of Scanning Transmission Electron Microscope Holography. *Nano Lett.* **18,** 7118–7123 (2018).

64. McMorran, B. J., Agrawal, A., Anderson, I. M., Herzing, A. A., Lezec, H. J., McClelland, J. J. & Unguris, J. Electron Vortex Beams with High Quanta of Orbital Angular Momentum. *Science* **331,** 192–195 (2011).

65. Verbeeck, J., Tian, H. & Schattschneider, P. Production and application of electron vortex beams. *Nature* **467,** 301–304 (2010).

66. Shiloh, R., Remez, R., Lu, P.-H., Jin, L., Lereah, Y., Tavabi, A. H., Dunin-Borkowski, R. E. & Arie, A. Spherical aberration correction in a scanning transmission electron microscope using a sculpted thin film. *Ultramicroscopy* **189,** 46–53 (2018).

67. Uchida, M. & Tonomura, A. Generation of electron beams carrying orbital angular momentum. *Nature* **464,** 737–739 (2010).

68. Verbeeck, J., Béché, A., Müller-Caspary, K., Guzzinati, G., Luong, M. A. & Den Hertog, M. Demonstration of a 2x2 programmable phase plate for electrons. *Ultramicroscopy* **190,** 58–65. ISSN: 0304-3991 (2018).

69. García de Abajo, F. J. & Konečná, A. Optical Modulation of Electron Beams in Free Space. *Phys. Rev. Lett.* **126,** 123901 (12 2021).

70. Konečná, A. & García de Abajo, F. J. Electron Beam Aberration Correction Using Optical Near Fields. *Phys. Rev. Lett.* **125,** 030801 (3 2020).

71. Vanacore, G. M., Berruto, G., Madan, I., Pomarico, E., Biagioni, P., Lamb, R. J., McGrouther, D., Reinhardt, O., Kaminer, I., Barwick, B., Larocque, H., Grillo, V., Karimi, E., García de Abajo, F. J. & Carbone, F. Ultrafast generation and control of an electron vortex beam via chiral plasmonic near fields. *Nat. Materials* **18,** 573–579 (2019).

72. Madan, I., Leccese, V., Mazur, A., Barantani, F., LaGrange, T., Sapozhnik, A., Tengdin, P. M., Gargiulo, S., Rotunno, E., Olaya, J.-C., Kaminer, I., Grillo, V., de Abajo, F. J. G., Carbone, F. & Vanacore, G. M. Ultrafast Transverse Modulation of Free Electrons by Interaction with Shaped Optical Fields. *ACS Photonics* **9,** 3215–3224 (2022).

73. Konečná, A., Rotunno, E., Grillo, V., García de Abajo, F. J. & Vanacore, G. M. Single-Pixel Imaging in Space and Time with Optically Modulated Free Electrons. *ACS Photonics* **10,** 1463–1472 (2023).

74. Konečná, A., Iyikanat, F. & García de Abajo, F. J. Entangling free electrons and optical excitations. *Sci. Adv.* **8,** eabo7853 (2022).

75. Guzzinati, G., Béché, A., Lourenco-Martins, H., Martin, J., Kociak, M. & Verbeeck, J. Probing the symmetry of the potential of localized surface plasmon resonances with phase-shaped electron beams. *Nat. Commun.* **8** (2017).

76. Tsesses, S., Dahan, R., Wang, K., Bucher, T., Cohen, K., Reinhardt, O., Bartal, G. & Kaminer, I. Tunable photon-induced spatial modulation of free electrons. *Nature Materials* **22,** 345–352 (2023).

77. Lyumkis, D. Challenges and opportunities in cryo-EM single-particle analysis. *Journal of Biological Chemistry* **294,** 5181–5197 (2019).

78. Konečná, A., Neuman, T., Aizpurua, J. & Hillenbrand, R. Surface-enhanced molecular electron energy loss spectroscopy. *ACS Nano* **12,** 4775–4786 (2018).

79. Idrobo, J. C., Lupini, A. R., Feng, T., Unocic, R. R., Walden, F. S., Gardiner, D. S., Lovejoy, T. C., Dellby, N., Pantelides, S. T. & Krivanek, O. L. Temperature Measurement by a Nanoscale Electron Probe Using Energy Gain and Loss Spectroscopy. *Phys. Rev. Lett.* **120,** 095901 (2018).

80. Lagos, M. J. & Batson, P. E. Thermometry with subnanometer resolution in the electron microscope using the principle of detailed balancing. *Nano Lett.* **18,** 4556–4563 (2018).

81. Asenjo-Garcia, A. & García de Abajo, F. J. Dichroism in the Interaction between Vortex Electron Beams, Plasmons, and Molecules. *Phys. Rev. Lett.* **113,** 066102 (2014).

82. Zanfrognini, M., Rotunno, E., Frabboni, S., Sit, A., Karimi, E., Hohenester, U. & Grillo, V. Orbital Angular Momentum and Energy Loss Characterization of Plasmonic Excitations in Metallic Nanostructures in TEM. *ACS Photonics* **6,** 620–627 (2019).

83. Lourenço-Martins, H., Gérard, D. & Kociak, M. Optical polarization analogue in free electron beams. *Nat. Physics* **17,** 598–603 (2021).

84. Harvey, T. R., Pierce, J. S., Chess, J. J. & McMorran, B. J. Demonstration of electron helical dichroism as a local probe of chirality. *arXiv preprint arXiv:1507.01810* (2015).